UNIVERSITY OF TRENTO

Doctoral School in Physics - Department of Physics

Doctoral Thesis

Analysis methods for gravitational wave from binary neutron star coalescences: investigation on the post-merger phase

Candidate:
Maria Concetta Tringali
XXIX cycle

Supervisor:
Prof: Giovanni Andrea Prodi

Coordinator:
Dr. Claudia Lazzaro

July 28, 2017

Contents

List of Figures

List of Tables

Introduction

The coalescence of binary neutron stars (BNS) is amongst the most promising sources for advanced gravitational wave (GW) detectors. The forthcoming addition of the advanced Virgo interferometer to the LIGO detector network will greatly improve the estimation of GW characteristics and therefore the capabilities to test features in the GW signal emitted by the coalescence of a NS binary. Such an observation can constrain the equation of state of these stars in at least two ways: by investigating smaller effects on top of the signal from the inspiral phase due to the tidal deformability of the components and by characterizing the emission from the possible highly excited NS remnant after the merger. Both methods promise to probe matter up to yet unknown and unexplored supranuclear densities, provided that the signal-to-noise ratio (SNR) at which the single GW is detected is sufficiently high or that the results from more detections can be combined together. Depending on mass and Equation of State (EoS) of the NS progenitors, the final fate of the merger can produce either a prompt collapse to black hole (BH) or a massive NS remnant. In the latter case, the merger remnant could be a short-lived, hypermassive NS (HMNS) collapsing to a BH within a few tens of ms after merger, or a long-lived NS, which in turn can be either supramassive (SMNS), i.e. collapsing to a BH on much longer timescales of order of seconds, or even a stable NS. These remnants will be highly excited, showing transient nonaxisymmetric deformations and quadrupolar oscillations, which are expected to emit GWs peaked in the frequency range around 2-3 kHz. The observation of these Post Merger (PM) fingerprints, would allow to constrain the EoS and at the same time to estimate combinations of stellar parameters, such as mass and radius of the two objects.

With these motivations, my PhD thesis addressed the development of a new data analysis tool in order to investigate the GW signal emitted during the PM phase following a NS coalescence. The analysis procedure is developed inside the framework of the Coherent Wave Burst (cWB) pipeline which is employed by LIGO and Virgo collaboration to search for burst signals, i.e. it makes minimal assumption on the GW morphology and provides a robust coverage of generic GW transients.

In the following, we summarize the content of this thesis. The *first Chapter* gives an overview of astrophysics of neutron stars and NS mergers. The first part presents briefly the first ideas about these objects and their observations followed by a short description of the NS internal structure, the observed values of mass and radius. Another section deals with description of the NS equation of state, so-called Tolman-Oppenher-Volkoff (TOV) equations which describe the internal dynamics of these stellar objects whose structure is affected by General Relativity. Following section discusses isolated NSs and X-ray binaries and the possible formation paths for a double NS system. Another section overviews the gravitational wave emission by coalescence of binary system, followed by some general comments about the spectral properties and other features related with the EoS describing the BNS system. Finally, last section briefly describes the coalescence of BNSs as engine of short Gamma-Ray Bursts.

The *second Chapter* focuses on general properties of GW interferometric detectors, their spectral and directional sensitivities, and comments on the advantages of performing GW searches with networks of detectors. Indeed, the networks improve the capability to discriminate between GWs and noise, at least three detectors boost the reconstruction of the GW source sky position and ensure a superior sensitivity to both GW polarizations. The noise sources limiting the interferometer sensitivity are briefly illustrated, as well as the noise transients and how they are mitigated. Finally, the results obtained from the first observing run of the Advanced LIGO detectors and the plan for the future observations are reported.

The *third Chapter* describes the coherent WaveBurst pipeline, the data-analysis pipeline developed by the LIGO and Virgo collaboration to search for transient of gravitational radiation without prior assumptions on the signal waveforms. The pipeline identifies coherent events in the data from different GW detectors and estimates the related GW signal using a maximum likelihood analysis.

In the first section of *fourth Chapter*, it is reported a description of the catalog of numerical relativity waveforms analyzed in this thesis to inspire our follow-up method and test its robustness. The catalog collects GW waveforms of coalescing BNS systems whose merger can produce a BH remnant or a NS remnant. The Monte Carlo simulation of software signal injections is then described.

The *fifth Chapter*, is devoted to description of the follow-up method developed in the thesis targeting NS post-merger signals. A two steps selection procedure discriminates the detection or non detection of a NS PM signal. The tool is an additional module of coherentWaveBurst and is based on a wavelet time-frequency representation. The last part of this chapter explain which characteristics of the PM signal are estimated, in primis the dominant frequency peak in its GW spectrum.

The *sixth Chapter* collects the overall results on Gaussian simulated detector noise, starting from the efficiency of detection and the false positive probability for a NS PM signal. The study is perfomed as a function of source distance for each waveform model in the catalog. The posterior probabilities of finding a NS PM signal are computed. The frequencies of the dominant spectral peak are estimated and compared with the correct values.

In the *seventh Chapter* , preliminary results of the same tool on real detector data are shown. The real data are taken from the last observation run of previous generation LIGO and Virgo detectors, S6-VSR3 run, and are scaled to match the design sensitivity of advanced detectors in the frequency range of interest.

In the *Conclusions Chapter*, final remarks and future step are outlined.

Since the development and testing of a new algorithm involves the efforts of several people in a group, I provide here a description of my direct contribution on the following Chapters of the thesis:

- *First Chapter*: my contribution has been to collect bibliographic material to correctly bring the astrophysical context of this work;
- *Fourth Chapter*: I tuned the configuration parameters of coherent Wave Burst pipeline specifically for this use as
- *Fifth Chapter*: I contributed to the development of the methodological ideas and the development of the tool has been performed in close collaboration with Postdoc Claudia Lazzaro;
- *Sixth and Seventh Chapters*: I designed tests and performed all the simulations and post-production analysis reported in these chapters.

Chapter 1

Introduction to the Astrophysics of Neutron Stars

Chapter 1 gives an overview of the astrophysics of NSs and of the GW emission from BNS coalescences. We summarize the basic properties of these compact objects, including a short review on the NS internal structure and on mass and radius constraints from observations. A general description of populations of isolated NSs and X-ray binaries and of the possible formation paths for a BNS system is also provided. In the last part of this chapter, GW emission by compact binary coalescences is discussed. We review the spectral properties of the emitted GW signals depending on the NS EOS. In the last section, we briefly describe gamma ray-bursts and their progenitors and new model for short-gamma ray burst.

1.1 Neutron Star: first ideas and observations

Two years after James Chadwick discovered the neutron in 1932, a German astronomer and a Swiss astrophysicist, Walter Baade and Fritz Zwicky of Mount Wilson Observatory, proposed the existence of *neutron stars* (NSs). These two astronomers, who also coined the term *supernova*, went on to suggest that "*supernovae represent the transition from ordinary stars into neutron stars, which in their final stages consist of extremely closely packed neutrons*". They proposed that the repulsion force between neutrons could support remnant neutron cores, supported by the Pauli principle that prevents neutrons with identical properties from packing too closely together. When neutrons are pressed together, many of them have to move rapidly (so as not to be identical to their

neighbors). This motion provides a pressure, called *neutron degeneracy pressure*, that is predicted to be even greater than electron degeneracy and this allows stellar remnants with masses beyond the Chandrasekhar limit to be stable [20].

Most scientist ignored Zwicky and Baade's theory until 1967. In this year, Antony Hewish from the Cavendish Laboratory of Cambridge had built a radio telescope operating at a frequency of 81.5 MHz. The initial survey included the whole sky in the declination range $-0.8° < \delta < 44°$ and this area was scanned once a week [21]. A large fraction of the sky was thus under regular surveillance. This instrument was designed to investigate the angular structure of compact radio sources by observing the scintillation caused by the irregular structure of the interplanetary medium. Like the stars, whose apparent position on the sky changes erratically because of the air motion in the Earth's atmosphere (scintillation), the position of radio sources can exhibit a similar effect as a result of the solar wind in the interplanetary space. This interplanetary scintillation is stronger for compact than for extended sources, and thus Hewish hoped to identify quasars by looking for strongly scintillating sources [22].
Soon after the instrument was brought into operation, one of his PhD student, Jocelyn Bell, who was analyzing the output of the radio telescope, noticed that signals which appeared at first to be weak sporadic interference were repeatedly observed at a fixed declination and right ascension; this result showed that source could not be terrestrial in origin. Systematic investigations were started in November and high speed records showed that signals consisted of a series of pulses each lasting ~ 0.3 s and with a period of about P=1.337 s Figure 1.1, which was soon found to be maintained with extreme accuracy [21].

Although it seemed extremely unlikely, one of the first discussed explanations was that the signal they had picked up had been sent by another civilization in our Galaxy. Therefore, the source was initially dubbed "LGM" for little green man. However, when observations with another telescope confirmed the emission and further data analysis showed the presence of other periodic signals from different directions, Jocelyn Bell had to exclude a synchronized alien effort to contact the Earth, and the scientific community had to accept that they were confronted with a new class of astrophysical objects.

Neutron stars are one of the possible end states of a massive star. Following current theories on stellar evolution, they are the result of the evolutionary path of massive progenitors ($\sim 8M_{\odot}<M<$20-30 $M_{\odot}$) which are able to burn elements heavier than carbon and oxygen, up to form a core of ^{56}Fe. This is the most stable element in nature,

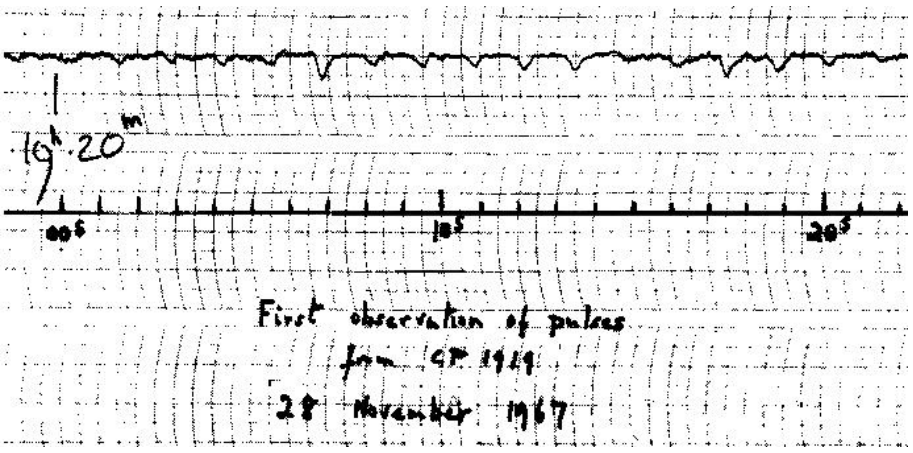

Figure 1.1: The first radio pulsar "CP 1919" (now known as PSR B1919+21), with a pulse period of 1.337 seconds and a pulse width of 0.04 second, was discovered in 1967.

which can not be generated by fusion of lighter ones through exothermic reactions. As the core density increases, the inverse β-decay and the photo-disintegration of the nuclei $\gamma + {}^{56}\mathrm{Fe} \rightarrow 13\,{}^{4}\mathrm{He} + 4\mathrm{n}$, remove energy from the system that supports the subsequent contraction. When the core mass becomes bigger than the Chandrasekhar limit, gravity causes it to collapse, reaching densities typical of nuclear matter $10^{14}\mathrm{g/cm}^3$. It collapses till protons and electrons combine to form neutrons. The core, composed mainly of neutrons, reacts to further compressions producing a shock wave that, aided by neutrino irradiation, ejects all the external shells: the supernova explosion leaves behind a proto-neutron star.

1.1.1 Neutron star structure

The internal structure of a neutron stars is not well determined because of uncertainties in the equation of state of degenerate nuclear matter. The structure of neutron star can be subdivided into different regions: the *surface*, the *crust*, and the *outer* and *inner core* (see figure 1.2). A brief description for each region follows below [22].

Surface

The surface of neutron stars (composed by atmosphere and envelope), has density less than 10^6 g cm^{-3} and it is only a negligible amount of the total mass of the neutron star, although it can be relevant for some observational properties. A 1-cm-thick neutron star atmosphere shapes the emergent photon spectrum and it plays a crucial role for the

interpretation of observations (e.g., to know whether a blackbody spectrum is a good approximation).

Crust

The neutron stars have a strong magnetic surface fields ($\sim 10^{12}$ Gauss) that influences the electron motion inside atoms, compressing electrons into thin, needle-like shapes; such atoms have energy levels much higher than at zero magnetic fields strength.
The envelope which is neighboring layer to atmosphere, indeed, is crucial for the transport properties and the release of the thermal energy at the neutron star surface. The crust is usually separated into *outer* and *inner* crust. It has a tickhness of 1-2 km and contains mainly nuclei. These nuclei undergo attractive nuclear and repulsive Coulomb force and lie in the lowest energy level. Moving toward inner parts of neutron star, the density increases. At low density, $\rho < 10^6$ g cm^{-3}, the dominant nuclei are ^{56}Fe with abundance $Y_e = Z/A = 26/56 = 0.46$. As the density increases, matter becomes ionized, and the atomic nuclei are embedded in a nearly uniform medium of background electrons. The preferred nuclei become more and more neutron rich with $Y_e \sim 0.1-0.2$. Such nuclei are very different from nuclei under terrestrial conditions: they have mass numbers up to several hundred and they arrange in a crystalline form because of the interplay between nuclear and Coulomb forces. At the *neutron drip density*, $\rho_{drip} = 4 \cdot 10^{11}$ g cm^{-3}, the chemical potential of the neutrons inside the nuclei becomes zero and the neutrons start to "drip" out of nuclei, immersing the nuclei in a background sea of neutrons. If the temperatures are low enough, these neutrons can be in a superfluid state: they form a fluid that is characterized by complete absence of viscosity. At even higher density, the geometry of nuclear matter changes through different structures: from spherical ("meatballs"), over nuclear slabs ("lasagna"), to voids embedded in nuclear matter ("Swiss cheese"), and finally, when the density is so high that the nucleons touch, it forms a uniform nuclear fluid ("sauce"). This regime is often referred to as "nuclear pasta".

Core

The core contains about 99% of the mass of the neutron star, and it is divided in two regions:

- The outer core region has a density of $\sim \rho < 10^{14}$ g cm^{-3}, here the nuclei disappear and matter is composed by a homogenous neutron-proton fluid. The outer core, of course, contains also negatively charged leptons, electrons and muons to neutralize the charges of the protons. Again, the neutrons are likely to be superfluid and

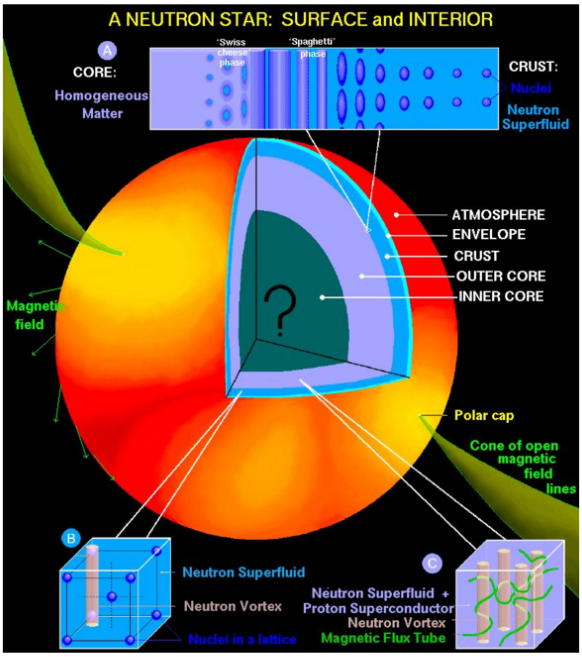

Figure 1.2: Structure of a neutron star.

the protons may be superconducting, which means that they do not exhibit any electrical resistance.

- In the very centre of the neutron star, a core region of very high density, $\rho \geq 3 \cdot 10^{15}$ g cm^{-3}, may or may not exist. The existence of this phase depends upon the behaviour of matter at very high energies and densities. It is not clear if there is a phase transition to quark matter or some other phase of matter quite distinct from the neutron liquid. Many of the models of stable neutron stars do not show the precence of this core region but it is certainly not excluded that exotic forms of matter might exist in the core of massive neutron stars.

1.1.2 Neutron star masses: measurements

Mass is one of the important parameters of a NS. From precise mass measurements we can infer informations about the stellar evolution of its progenitor, nuclear matter composition and its equation of state (EoS) (see the paragraph 1.1.4); mass measurements also provide tests of Einstein's general relativity in the strong gravity regime.

Generally, it is not trivial to measure the masses of isolated neutron stars. About one half of the stars are members of binary stellar system and when a neutron star appears as a pulsar it is easier to estimate the mass of companions using orbital parameters measured via high precision pulse timing observations. The pulsar's orbit can be described in classical gravity by the five Keplerian parameters, see the Figure 1.3: the orbital period of a binary system P, the projection of the pulsar's semimajor axis $a\ \sin(i)$ (where i is the inclination angle of orbital plane with respect of line of sight), the orbital eccentricity e, the longitude of periastron ω and the epoch of periastron passage T_0.
Considering a binary system where m_1 is individual mass of primary (pulsar), m_2 mass of companion star and i inclination angle, the mass function f

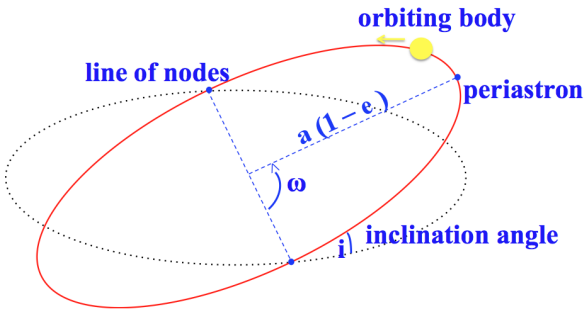

Figure 1.3: Representation of orbital parameters for a binary system.

$$f(m_1, m_2, i) = \frac{(m_2 \sin i)^3}{M^2} = \left(\frac{2\pi}{P}\right)^2 (a \sin i)^3 \tag{1.1}$$

is related to these orbital parameters, where $M = m_1 + m_2$ is the total mass of the system. Although the mass function depends on observable parameters, it is not sufficient to give a measurement of the mass of the pulsar and of its companion and additional information is required. Precise neutron star mass measurements come from radio pulsar timing techniques and rely on the measurement of relativistic effects in the binary orbits.

If general relativistic effects are important, the description of the system requires up to five more post-Keplerian (PK) parameters [23]: advance of periastron $\dot{\omega}$, orbital period decay $\dot{P}$, gravitational redshift (time dilation) γ, the range r and Shapiro delay s, which are related to the component masses, the orbital period, and eccentricity. If all five Keplerian parameters and two or more post-Keplerian parameters are known, the individual mass of binary components and the inclination angle of the orbit with respect to line of sight can be determined [22].

In highly eccentric systems that have been observed repeatedly over a long period of time, the measurement of $\dot{\omega}$ is usually possible and leads to a strong constraint on the total mass of the binary system M.
The measurement of the parameter γ requires similarly eccentric systems and long-term monitoring. In high inclination systems, on the other hand, it is sometimes possible to detect the Shapiro time delay and obtain the parameters r and s.
The measurement of the rate of orbital period decay $\dot{P}$ typically requires the longest monitoring and timing of the pulsar, sometimes over decades. This has been achieved for a handful of pulsars in binaries.
The precision with which the pulsar mass can be determined ultimately depends on the number of PK parameters that are measured for that binary. When two or more PK parameters are known, the pulsar mass is precisely determined. In the category where only one PK parameter is known in addition to the mass function, the mass of each neutron star is not as well constrained. Detailed studies of PK parameters related to different binary system, double neutron stars (NS-NS), neutron star-white dwarf (NS-WD), neutron star with main sequence companions (NS-MS), are reported in [23] [24].

The measured masses are collected into four groups, as displayed in Figure 1.4, each one refers to different evolutionary histories: X-ray binaries, double-neutron star binaries, WD-neutron star binaries, and WD-neutron star binaries found in globular clusters.
Most neutron stars have masses between 1.3 -1.4 $M_{\odot}$, but lower and higher mass exist (see the following sections). The neutron star birthmass seems to depend on progenitor mass, and its accretion can lead to the accumulation of several tenths of a solar mass over a star's life.
The measurements of mass obtained by NS-NS and NS-WD binary systems are close to 1.33 $M_{\odot}$ and 1.55 $M_{\odot}$ respectively [24]. For what concern mass estimations from binary system containing an accreting neutron star emitting X-rays, we have large values characterized by huge errors. For systems containing white dwarf or main-sequences stars, measurements show high uncertainties and so continued observations are necessary to clarify the situation.
There is now ample observational support from pulsars for neutron stars with masses significantly greater than 1.5 $M_{\odot}$. These include PSR J1903+0327, which has a main-sequence companion; the globular cluster pulsars PSR 1748-2446 I and PSR 1748-2446 J, PSR J1748-2021B, PSR B1516+02B, PSR J2043+1711, and PSR J1614-2230, all of which have WD companions; and the black widow pulsar PSRB1957+20. The largest well-measured masses are 2.01±0.04 $M_{\odot}$ of PSR J0348+0432 [25][26] and 1.97±0.04 $M_{\odot}$ of PSR J1614-2230 [27], for which i has been determined by detection of the Shapiro

time delay. This system, with an orbital period of around 8.7 days, is composed by pulsar with a spin period of 3.15 ms and by a companion with 0.5 $M_{\odot}$. For this binary, projected semimajor axis $a \sin i$= 11.3 light seconds and $\sin i = 0.99989$; in other words, this is the most inclined pulsar binary system known at present [25]. The Shapiro time delay amplitude is 48.8 μs. Due to its high accuracy, this mass has become the standard for the minimum value of the neutron star maximum mass.

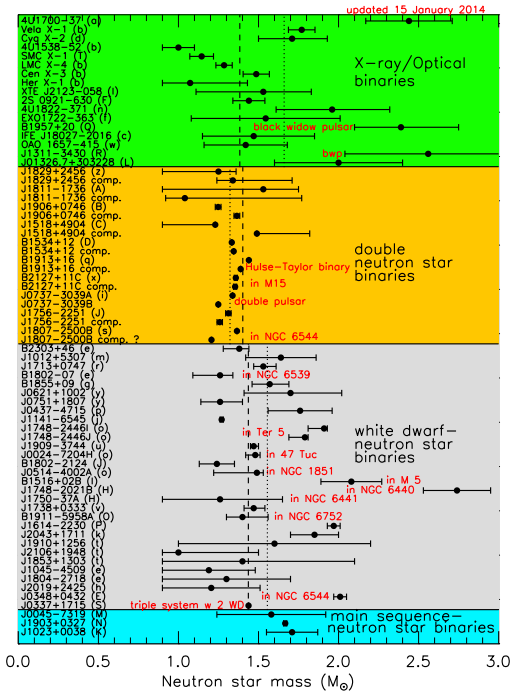

Figure 1.4: Measured and estimated mass of neutron stars in radio binary pulsars (gold, silver and blue regions) and in X-ray accreting binaries (green). For each region the dotted line represent mass averages; weighted averages are shown as dashed lines [1].

1.1.3 Neutron Star Radii

Radius estimates from isolated neutron stars are restricted by distance uncertainties. Moreover, there are many astrophysical observations that could lead to the extraction of neutron star radii, or combined mass and radius constraints; different methods have been proposed, a list is reported in [28].

Among them, thermal emission and X-ray bursts from neutron star surfaces have dominated recent attempts to infer neutron star radii.

After the formation of a proto-neutron star in the aftermath of a gravitational collapse supernova event, cooling of the core proceeds via neutrino emission, leading to temperatures of order 10^9K within years. During this period, the star is not in complete thermal equilibrium due to the relatively long thermal relaxation time of the crust, which is expected to be of order 10 to 100 years. The excess heat of the crust is preferentially transported by electron conduction into the star's isothermal core, dominating radiation by thermal emission from the surface. However, the surface will finally come into thermal equilibrium with the core, causing a reduction in the surface temperature. Depending upon whether or not the core neutrino emission processes are rapid or conventional, the drop in surface temperature will be a factor of 2 (and relatively slow) to 10 (and relatively abrupt). Following this reduction, the surface temperature stabilizes at a value about 100 times the core temperature.
In addition, some accreting neutron stars are observed to undergo long-duration X-ray bursts, sometimes called superbursts, which appear to be powered by thermonuclear He fusion. During the burst, some of the heat is transported into the interior, warming the crust. Observations of quiescent thermal emission following the bursts would therefore probe the thermal relaxation timescale of the crust as well as the rate of core neutrino emission.
Therefore, the observation of thermal emission from neutron star surface at optical and X-ray frequencies, becomes one method to estimate neutron star radius and it is useful to examine the relation between the thermal relaxation time and the structure of neutron stars [29].
To a zeroth approximation, thermal emission from neutron stars is blackbody radiation, so measures of their integrated fluxes and temperatures yield estimates of their angular diameters through Kirchhoff 's laws:

$$F = \frac{L}{4\pi d} = \left(\frac{R}{d}\right)^2 \sigma_B T_{eff}^4 \tag{1.2}$$

where σ_B is the Stefan-Boltzmann constant, T_{eff} the effective temperature, R geometrical radius, d the distance, and F and L represent the flux and luminosity observed at Earth. This equation becomes:

$$F_\infty = \frac{L_\infty}{4\pi d} = \left(\frac{R_\infty}{d}\right)^2 \sigma_B T_{eff,\infty}^4 \tag{1.3}$$

when redshifted at the Earth from the neutron star's surface, where the redshift is given by:

$$z = \frac{1}{1 - 2GM/Rc^2} - 1 \tag{1.4}$$

the quantities R and M are geometrical radius and mass of neutron star, G gravitational constant, c speed of light. Considering redshift, $T_{eff,\infty} = T_{eff}/(1+z)$ and $F_\infty = F_\infty/(1+z)$.

At this point, combining flux F_∞, temperature $T_{eff,\infty}$ and distance d measurements, the quantity inferred from thermal radiation observations of a neutron star's surface is the so-called radiation radius:

$$R_\infty = \frac{R}{\sqrt{1 - 2GM/Rc^2}}. \tag{1.5}$$

R_∞ is a function of mass and radius of the neutron star and an independent measurement of R_∞ and and M gives an estimate of R. The principal uncertainties in extracting radii from thermal emissions involve the distance, the magnitude of interstellar hydrogen (H) absorption, given that most hard UV radiation and an appreciable fraction of X-rays are absorbed between the star and the Earth, the atmospheric composition and magnetic field strength and distribution.

The best-studied isolated neutron star is RX J1856-3754 [30], which is the only one close enough to have an accurate parallactic distance: $d = 120 \pm 8\ pc$ [31]. Values of R_∞ in the range of 13 to 16 km are estimated from fitting data for RX J1856-3754 and various globular cluster soruces [28][29] . It is also possible to obtain upper and lower limits of NS radius from the fact that the sound speed inside a NS has to be lower than the speed of light [32] [33]:

$$R_{min} \simeq 1.5 R_S = \frac{3GM}{c^2} = 6.2\ km\ \left(\frac{M}{1.4M_\odot}\right), \tag{1.6}$$

where R_S is the Schwarzschild radius

$$R_S = \frac{2GM}{c^2} \simeq 4.2\ km \left(\frac{M}{1.4M_\odot}\right), \tag{1.7}$$

and from the maximum linear speed allowed at the surface of a rotating NS:

$$R_{max} \simeq \left(\frac{GMP^2}{4\pi^2}\right)^{1/3} = 16.8\ km \left(\frac{M}{1.4M_\odot}\right)^{1/3} \left(\frac{P}{ms}\right)^{2/3}. \tag{1.8}$$

For the fastest rotating pulsar known, PSR B1937+21, with a period P= 1.56 ms, the latter provides a limit of $R_{max} = 22.6\ km$ for $M = 1.4\ M_{\odot}$.
Most models predict a radius of $R \sim 10 - 12\ km$, consistent with the above theoretical upper and lower limits.

1.1.4 Equation of state of neutron stars

The structure of a star is determined by hydrostatic equilibrium. The equation of hydrostatic equilibrium describes the balance between gravity and the pressure forces, result of the microscopic interactions in the stellar material. Therefore, to calculate a neutron star model, one has to solve the corresponding hydrostatic equilibrium equations in relativistic gravity, the so-called *Tolman-Oppenheimer-Volkoff equations*. We now assume a static, spherically symmetric distribution of matter. The interior solution must match the vacuum Schwarzschild solution at the surface of the spherical mass distribution.

Let us start with the Einstein equations

$$G_{\mu\nu} \equiv R_{\mu\nu} - \frac{1}{2} g_{\mu\nu} R = \frac{8\pi G}{c^4} T_{\mu\nu} \tag{1.9}$$

where on the left side, $G_{\mu\nu}$ is the Einstein tensor describing the curvature space-time, on the right side $T_{\mu\nu}$ is the stress energy tensor, describing matter/energy sources of space-time curvature and $g_{\mu\nu}$ is the metric tensor[1]. One measure of curvature is $R_{\mu\nu}$, so called *Ricci* tensor

$$R_{\mu\nu} = \Gamma^{\alpha}_{\mu\nu,\alpha} - \Gamma^{\alpha}_{\mu\alpha,\nu} + \Gamma^{\alpha}_{\beta\alpha}\Gamma^{\beta}_{\mu\nu} - \Gamma^{\alpha}_{\beta\mu}\Gamma^{\beta}_{\alpha\nu} \tag{1.10}$$

built up from the Christoffel symbols

$$\Gamma^{\mu}_{\alpha\beta} = \frac{1}{2} g^{\mu\nu}[g_{\alpha\nu,\beta} + g_{\beta\nu,\alpha} - g_{\alpha\beta,\nu}]. \tag{1.11}$$

Its contraction or trace, $R = R^{\gamma}_{\ \gamma} = g^{\gamma\delta} R_{\gamma\delta}$ is known as *Ricci curvature scalar.*
The comma denotes differentiation with respect to the coordinate $x^{\mu} = (x^0, x^1, x^2, x^3)$, in spherical coordinates $x^{\mu} = (t, r, \theta, \phi)$

The Schwarzschild exact solution describes a spacetime which is spherically symmet-

[1]The symmetry of Einstein tensor G satisfying properties: the Bianchi identities given by $\nabla_{\mu} G^{\mu\nu} = 0$ and conservation laws derived from $\nabla_{\mu} T^{\mu\nu} = 0$, which combines to give the Einstein equations (1.9).

ric, static[2] and in vacuum[3] [2].

According to Birkhoff's theorem, the Schwarzschild metric is the most general spherically symmetric solution of the Einstein field equations in vacuum. As a result, the Schwarzschild solution is also the solution in the exterior regions of a spherically symmetric relativistic star, quite independently of whether it is static or oscillating radially (Birkhoff, 1923). Introducing spherical coordinates, (t, r, θ, ϕ), the line element of a Schwarzschild spacetime is:

$$ds^2 = -\left(1 - \frac{2GM}{c^2 r}\right) c^2 dt^2 + \left(1 - \frac{2GM}{c^2 r}\right)^{-1} dr^2 + r^2(d\theta^2 + \sin^2\theta d\varphi^2), \tag{1.12}$$

where M is the total mass-energy (i.e., the gravitational mass) of the system, G is gravitational constant and c speed of light. In order to obtain the TOV equations, we consider the matter inside the star as a perfect fluid whose stress-energy tensor is

$$T^{\mu\nu} = (\epsilon + P)u^\mu u^\nu + p g^{\mu\nu} \tag{1.13}$$

with total energy density ϵ, isotropic pressure P, metric $g^{\mu\nu}$ and four-velocity $u^\mu = \left(\frac{dt}{d\tau}, \frac{dr}{d\tau}, \frac{d\theta}{d\tau}, \frac{d\phi}{d\tau}\right) = \gamma(1, \vec{v})$. The total energy density ϵ consists of both the rest mass density of the fluid ρ and the internal energy ε, which in this case represents the thermal motion of the constituent fluid particles:

$$\epsilon = \rho c^2 + \varepsilon \tag{1.14}$$

Using the spherical coordinates for such a problem r, θ and ϕ, the invariant interval ds^2 in a spherical and static spacetime has the form:

$$ds^2 = -e^{2\phi} c^2 dt^2 + e^{2\lambda} dr^2 + r^2(d\theta^2 + \sin^2\theta d\varphi^2), \tag{1.15}$$

where

$$g_{00} = -e^{2\phi},\ g_{11} = e^{2\lambda},\ g_{22} = r^2,\ g_{33} = r^2 \sin^2\theta. \tag{1.16}$$

For a star in hydrostatic equilibrium, we can take ϕ and λ to be dependent on r and not

[2]A static solution of the Einstein equations is one in which the metric components are neither dependent on time nor are affected by a time reversal, i.e., by a coordinate transformation t -> -t.

[3]The word "vacuum" here denotes a region of spacetime where the gravitational effect of any matter present is negligible.

on t and the 4-velocity with null space components (c, 0, 0,0) [34].
Setting G= c =1 (geometrical units), it is useful to introduce a re-parameterisation of the radial metric component g_{rr} by

$$m(r) \equiv \frac{1}{2}r\left(1 - \frac{1}{g_{rr}}\right) = \frac{1}{2}r(1 - e^{-2\lambda}) \tag{1.17}$$

so that

$$g_{rr} = e^{2\lambda} = \left(1 - \frac{2m}{r}\right)^{-1} \tag{1.18}$$

Thus, the stress-energy tensor becomes:

$$T_{\mu\nu} = (\epsilon + P)u^{\mu}u^{\nu} + pg^{\mu\nu} = \begin{pmatrix} -\epsilon e^{2\phi} & 0 & 0 & 0 \\ 0 & (1 - \frac{2m}{r})^{-1}P & 0 & 0 \\ 0 & 0 & r^2P & 0 \\ 0 & 0 & 0 & r^2 sen\theta^2 P \end{pmatrix} \tag{1.19}$$

At this point, we can calculate Christoffel symbols $\Gamma_{\mu\nu}$, the curvature tensor $R_{\mu\nu}$, the Einstein tensor $G_{\mu\nu}$ and stress-energy tensor $T_{\mu\nu}$ [35]. From eq.(1.10), the nonzero, independent components of the Ricci tensor $R_{\mu\nu}$ are (see the [35]):

$$R_{tt} = e^{2\Phi}\left[(\phi'' + \phi')\left(1 - \frac{2m}{r}\right) + \phi'\left(\frac{2r - 3m - rm'}{r^2}\right)\right], \tag{1.20}$$

$$R_{rr} = \left(1 - \frac{2m}{r}\right)^{-1}\left[\frac{(rm' - m)(2 + r\phi')}{r^3}\right] - \phi'' - \phi'^2, \tag{1.21}$$

$$R_{\theta\theta} = cosec^2 R_{\phi\phi} = (2m - r)\phi' + m' + \frac{m}{r}, \tag{1.22}$$

The Ricci scalar is

$$R = g^{\mu\nu}R_{\mu\nu} = 2\left[\frac{2m'}{r^2} + \phi'\left(\frac{3m - 2r + rm'}{r^2}\right) - \left(1 - \frac{2m}{r}\right)(\phi'' + \phi')\right]. \tag{1.23}$$

Thus, the time and radial components of Einstein equation is given by

$$G_{tt} = \frac{2m'e^{2\Phi}}{r^2} = 8\pi\epsilon e^{\Phi} \quad \longrightarrow \boxed{m' = \frac{dm}{dr} = 4\pi r^2\epsilon} \tag{1.24}$$

$$G_{rr} = \frac{2}{r}\left(\Phi' - \frac{m}{1-m/r}\right) = \frac{8\pi P}{1-2m/r} \quad \longrightarrow \boxed{\Phi' = \frac{d\Phi}{dr} = \frac{m + 4\pi r^3 P}{r(r-2m)}} \tag{1.25}$$

$$\begin{aligned} 0 = \nabla_\nu T^{r\nu} &= \frac{\partial T^{r\nu}}{\partial x^\nu} + T^{\sigma\nu}\Gamma^r_{\sigma\nu} + T^{r\sigma}\Gamma^\nu_{r\nu} \\ &= \frac{\partial T^{rr}}{\partial r} + T^{tt}\Gamma^r_{tt} + T^{rr}\Gamma^r_{rr} + T^{\theta\theta}\Gamma^r_{\theta\theta} + T^{\phi\phi}\Gamma^r_{\phi\phi} + T^{rr}\Gamma^\nu_{r\nu} \\ &= \left(1 - \frac{2m}{r}\right)[P' + (P+\epsilon)\Phi'] \quad \longrightarrow \boxed{P' = \frac{dP}{dr} = -(\epsilon + P)\Phi'} \end{aligned} \tag{1.26}$$

Thus, indicating G and c explicitly, *Tolman-Oppenheimer-Volkoff* (TOV) equations of hydrostatic equilibrium, considering equation of state $P = P(\rho, \epsilon)$, are:

$$\frac{dm}{dr} = 4\pi r^2 \epsilon(r), \tag{1.27}$$

$$\frac{dP}{dr} = -\frac{G\epsilon(r)\ m(r)}{c^2 r^2}\left(1 + \frac{P(r)}{\epsilon(r)}\right)\left(1 + \frac{4\pi P(r) r^3}{c^2 m(r)}\right)\left(1 - \frac{2Gm(r)}{c^2 r}\right)^{-1}, \tag{1.28}$$

$$\frac{d\phi}{dr} = -\frac{1}{\epsilon(r)}\frac{dP}{dr}\left(1 + \frac{P(r)}{\epsilon(r)}\right)^{-1}, \tag{1.29}$$

where $\epsilon(r)$ is energy density at the distance r, $m(r)$ is the total mass inside the sphere of radius r and $P(r)$ the pressure at the distance r. Taking $P \ll c^2\epsilon$ and $m \ll c^2 r$, we have the Newtonian limit.

Outside of the star, the solution is the Schwarzschild solution, the quantity m(r) represents the gravitational mass-energy inside a sphere of radius r and includes all contributions to the relativistic mass (baryonic mass, internal energy, and the negative gravitational binding energy). So that, its integral from the centre of the star to infinity is:

$$M = \int_0^\infty 4\pi r^2 \epsilon(r)\ dr = \int_0^R 4\pi r^2 \epsilon(r)\ dr \tag{1.30}$$

where r = R marks the position where $\epsilon(R) = 0$.

Comparing the equations of the stellar structure in the Newtonian case

$$\frac{dm}{dr} = 4\pi r^2 \rho(r) \qquad \textit{mass equation} \tag{1.31}$$

$$\frac{dP}{dr} = -\frac{G\rho(r)m(r)}{r^2} \qquad \textit{momentum equation} \tag{1.32}$$

$$\frac{d\phi}{dr} = -\frac{1}{\rho(r)}\frac{dP}{dr} \qquad \textit{potential equation} \tag{1.33}$$

with eq.s (1.27)-(4.2(d)), we observe that:

- the mass equation look like the Newtonian case;
- the first factor of momentum equation comes from Newtonian one; the second and third factors represent special relativity corrections that arise from the mass-energy relation E=mc^2 and the last factor is a general relativistic correction based on the physical signifcance of the Schwarzschild form of the metric and the meaning of m(r) as the total integrated mass out to a radial distance r.

In eq.(1.28), the last correction factor allow us to understand if the contribution of General Relativity (GR) is important or not. If the factor [22]

$$\eta \equiv \frac{2Gm}{c^2 r} \ll 1 \tag{1.34}$$

the general relativistic effect is negligible (in the geometric unit $\eta = 2m/r$).
For example, let's consider the Sun, a white dwarf (WD) and a neutron star and calculate the η factor in geometric units ($G = c = 1; 1M_\odot = 1.5km$)

- **Sun**: $1M_\odot = 1.5\ km, R_\odot = 7 \cdot 10^5\ km \Rightarrow \eta \approx 4 \cdot 10^{-6}$
- **White Dwarf**: $M_{WD} = 0.6\ M_\odot, R_{WD} \simeq 10^4\ km \Rightarrow \eta \approx 1.8 \cdot 10^{-4}$
- **Neutron Star**: $M_{NS} = 1.4\ M_\odot, R_{NS} \simeq 10\ km \Rightarrow \eta \approx 0.4$

We observe that the Sun is a completly non relativistic object, for a WD the GR corrections can be ignored while for a NS general relativistic effects are important for its structure.

These equations can be solved by numerical integration starting from the center $r = 0$ up to stellar surface $r = R$. A set of boundary conditions and an equation of state

$P = K\rho^{\gamma}$ (K is the polytropic constant and γ is the adiabatic exponent) which relates the density to the pressure are necessary. Generally, it is considered at the origin

$$m(r=0) = 0, \qquad P(r=0) = P_c, \qquad \epsilon_c, \tag{1.35}$$

while at the surface r=R

$$m(R) = M, \qquad P(R) = 0, \qquad \phi(R) = \frac{1}{2}\log\left(1 - \frac{2M}{R}\right) \tag{1.36}$$

The steps to calculate the TOV equations are the following:

1. Pick a value of central density $\epsilon(r=0) = \epsilon_c$ and boundary condition $m(r=0) = 0$. The equation of state gives P_c;

2. Integrate eqs.(1.27) and (1.28) out from r = 0, using the values in step 1 as initial conditions. Each time a new value of P is obtained, the equation of state gives the corresponding value of ρ.

3. The value r = R at which P = 0 is the radius of the star, and m (R)=M.

This procedure can be repeated for a range of different central densities, and we therefore obtain a whole family of stellar models with varying central densities.

The Figure 1.5 shows numerical solutions for a set of TOV equations, with labels referring to different equations of state. In both plots, the horizontal green stripe refers to largest observed mass for a neutron star $M = 2.01 \pm 0.4\ M_{\odot}$ [25][26]. The left panel shows the behaviour of the gravitational mass M as a function of the central rest-mass density ρ_c and its inset reports the difference between M and baryonic mass M_b taking into account a specific EoS. We can note that baryonic mass M_b is always larger. As we can see from the left panel, each curve, corresponding to a sequence of TOV solutions with a given EOS, has a local maximum related to a value of the central density where $dM/d\rho_c = 0$. The value of central density is a turning point because it distinguishes *stable* stars, i.e., with $dM/d\rho_c > 0$ (left), from *unstable* ones, i.e., with $dM/d\rho_c < 0$ (right). To understand this, we consider a stellar configuration with relatively small central density and mass, which is accreting matter. The addition of a small amount of rest mass induces an increase of the central density and of the mass, therefore a new equilibrium for the stellar structure. Of course, this process can not proceed indefinitely

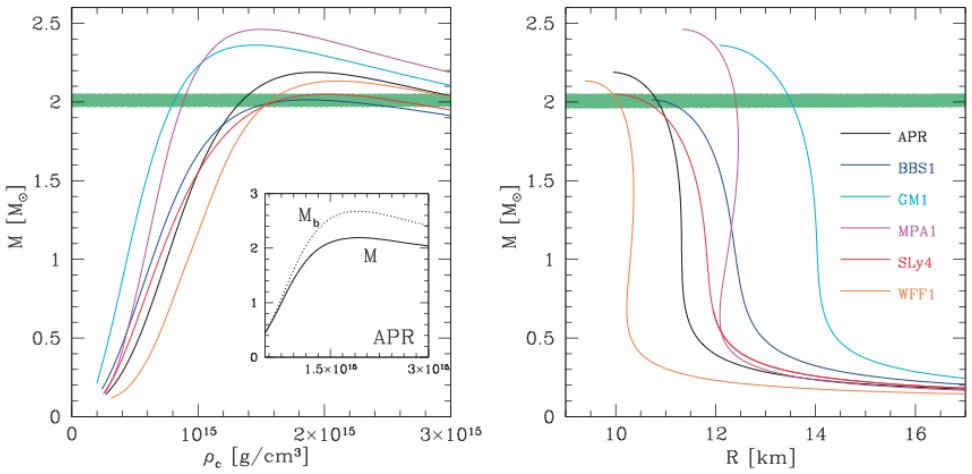

Figure 1.5: Left panel shows the gravitational mass, M, as a function of the central rest-mass density ρ_c for a set of equation of states (EoS). In right panel, it is reported the gravitational mass as a function of the stellar radius. In both plots, the horizontal green belt refers to the range for the largest reported mass for a neutron star [2].

and the addition of a single atom leads the star to evolve dynamically towards a black-hole cofinguration.

The right panel on the other hand, shows the mass as a function of the stellar radius for stable stellar models. Note that the compactness $C = M/R$ increases with the mass.

Rotating stars: supramassive and hypermassive neutron stars

Before going ahead, we want to remind the definitions of *hypermassive* and *supramassive* neutron stars [36].

A sequence of spherical neutron stars has always a maximum mass. Rotation can increase the maximum mass that can be supported. When the angular velocity of a *uniformly* rotating neutron star reaches the angular velocity of a particle in a circular Keplerian orbit at the equator, the spin frequency is such that the star would shed mass if it was span-up even infinitesimally. The corresponding star is then said to be spinning at the *mass-shedding frequency* or *Keplerian frequency* (or *break-up frequency*), Ω_k [2]. As a first approximation, the Keplerian frequency can be estimated to be $\Omega_K \sim (2/3)\sqrt{\pi\bar{\rho}}$ with $\bar{\rho}$ volume-averaged rest-mass density [2][37]. Uniformly rotating neutron stars with rest mass exceeding the maximum rest mass of non-spinning neutron stars for a given EoS but not the mass-shedding one, are called *supramassive* neutron stars (SMNS). This type of stars will eventually collapse to a black hole due to angular momentum losses via dissipative processes. A typical dissipative process is the electromagnetic emission

associated with magnetic dipole radiation.

The merger of binary neutron stars does not produce a uniformly rotating remnant, but a *differentially* rotating one. This can correspond to an enhancement of the centrifugal support, in which case the maximum allowed mass of the remnant can exceed the maximum allowed mass of uniformly rotating NSs for a given EOS. These differentially rotating neutron stars are called hypermassive neutron stars (HMNSs).
A HMNS collapses to a black hole when the differential rotation is lost through GW emission.

1.2 Populations of neutron stars

In this paragraph, I will give a general description both on isolated neutron stars and X-ray binaries and on the possible formation paths for a double neutron star system. See [22] [5] [38] [39][40] for more details about these topics.

1.2.1 Isolated neutron star

Isolated neutron stars or companions of compact objects (see the following section) can appear as radio and/or X-ray *pulsars*. As we seen at beginning of this chapter, they are thought to be born in type II supernovae. The typical event rate for such supernovae in spiral galaxies is of the order of one event every 50-100 years. This means that our Galaxy is populated by at least a few hundred million neutron stars.
A pulsar (pulsating radio source) is a highly magnetized ($B \simeq 10^{12} - 10^{13}\ G$), rotating neutron star (NS), that emits a beam of electromagnetic radiation produced by the acceleration of charged particles along the magnetic field line of neutron star. This radiation can be observed when the cone of emission intersects the line of sight of the observer. This effect is called *lighthouse effect* consequently on Earth we would observe periodic pulses from this object. This sequence pulses has a unique period associated with it, which is the period of rotation of the pulsar; they were found originally at radio wavelengths but have since been observed at optical, X-ray, and gamma-ray energies.

The magnetic dipole model

The magnetic dipole model is a simple model accepted to explain many of observed properties of the pulsars. It assumes the pulsar is a rigid, magnetized sphere which rotates in vacuum; the magnetic field is assumed to be dipolar with the magnetic moment $\vec{m}$

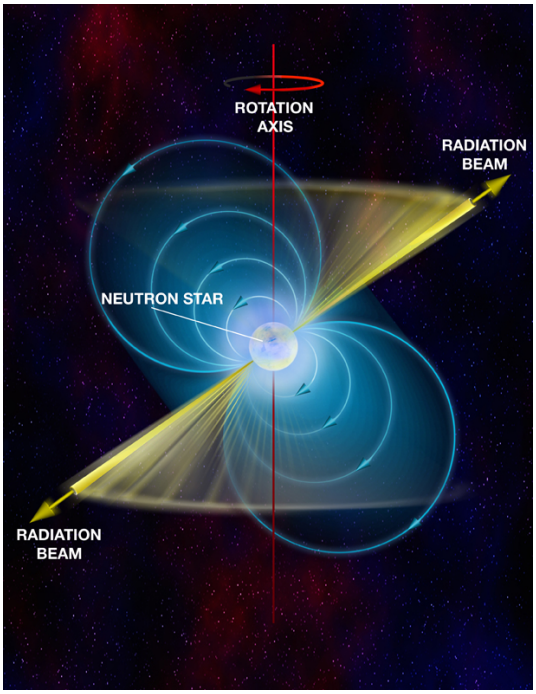

Figure 1.6: Sketch of electromagnetic emission from polar regions of the pulsar. As the pulsar rotates, these beams sweep around 360 degrees like a lighthouse. Radio telescopes receive a regular train of pulses as the beam repeatedly crosses the earth, making the pulsar appear to be a pulsating radio signal [3]

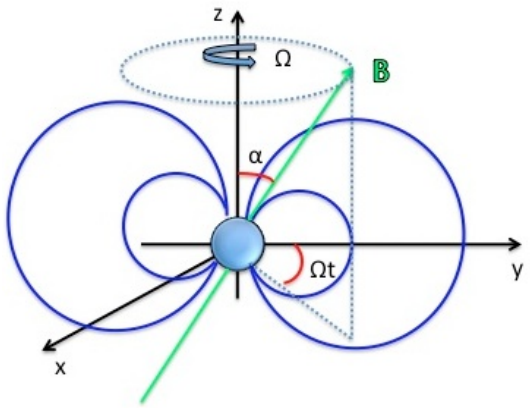

Figure 1.7: Schematic representation of a pulsar. The z axis is the rotation axis and α is the angle between magnetic field $\vec{B}$ and .

and forming an angle α with respect to the rotation axis [39].

Let be a dipolar magnetic field

$$\vec{B}(\vec{r}) = \frac{3\vec{n}(\vec{m}\cdot\vec{n}) - \vec{m}}{r^3} \tag{1.37}$$

where $r = |\vec{r}|$. $\vec{n} = \vec{r}/r$ and $\vec{m}$ is the magnetic dipole moment.
Using $\vec{m} \parallel \vec{n}$, r= R where R is the stellar radius, the magnetic field at the pole is

$$\vec{B}_p = \frac{2\vec{m}}{R^3} \qquad \Rightarrow \vec{m} = \frac{\vec{B}_p R^3}{2} \tag{1.38}$$

Similarly to power emitted by an electric dipole, the power emitted is :

$$\left(\frac{dW}{dt}\right)_{dip} = -\frac{2}{3c^3} \mid \ddot{\vec{d}} \mid^2 \qquad Larmor's formula \tag{1.39}$$

where $\vec{d}$ is electric dipole moment. A time-varying magnetic dipole radiates a power

$$\dot{E}_{md} = \left(\frac{dW}{dt}\right)_{md} = -\frac{2}{3c^3} \mid \ddot{\vec{m}} \mid^2 \tag{1.40}$$

To calculate the second time derivative of $\vec{m}$, we assume that the pulsar rotates with angular frequency ω, $\vec{m}$ that forms and angle α with the rotation z-axis. In the polar coordinate, the magnetic dipole moment is equal to

$$\vec{m} = \frac{1}{2} B_p R^3 (\cos\alpha \widehat{\mathbf{z}} + \sin\alpha\cos(\omega t)\widehat{\mathbf{y}} + \sin\alpha\sin(\omega t)\widehat{\mathbf{x}}) \tag{1.41}$$

and its second time derivative

$$\mid \ddot{\vec{m}} \mid^2 = \frac{1}{4} B_p^2 R^6 \omega^4 \sin^2\alpha \tag{1.42}$$

Putting this expression in eq.(1.40), the total emitted power is

$$\dot{E}_{md} = -\frac{2}{3c^3} \mid \ddot{\vec{m}} \mid^2 = -\frac{B_p^2 R^6 \omega^4 \sin^2\alpha}{6c^3} \tag{1.43}$$

In the dipole model, the emitted energy by the star is to the detriment of pulsar rotational energy

$$E_{rot} = \frac{1}{2} I \omega^2 \tag{1.44}$$

where I is the moment of inertia. Because of the pulsar is assumed to be a rigid sphere (dI/dt=0), the energy variation is given by

$$\frac{dE_{rot}}{dt} = I\omega\dot{\omega}. \tag{1.45}$$

By solving for $\dot{\omega}$ and equating dE_{rot}/dt and $(dW/dt)_{md}$:

$$\dot{\omega} = -\frac{B_p^2 R^6 \omega^3 \sin^2 \alpha}{6c^3 I} < 0 \tag{1.46}$$

This means that the pulsar slows down because of dipole emission.

Pulsar ages

The characteristic timescale for this slowdown is so-called *dipole age of a pulsar* [39]

$$\tau_{dipole} \equiv -\left(\frac{\omega}{2\dot{\omega}}\right) = \frac{3Ic^3}{B_p^2 R^6 \sin^2 \alpha \omega_0^2} \tag{1.47}$$

where the values of angular frequency ω and its time derivative $\dot{\omega}$ can be measured.

Expressing the eq.(1.46) in terms of power law, we have

$$\dot{\omega} = -K\omega^n \tag{1.48}$$

where the exponent n is called *braking index* and K is a proportional constant. Integrating this equation

$$\int_{\omega_0}^{\omega} \frac{d\omega}{\omega^n} = -K \int_{t_0}^{t} dt \tag{1.49}$$

where t_0 refers to the birth time. Setting $t_0 = 0$ and $K = -\dot{\omega}/\omega^n$

$$t = -\frac{1}{n-1}\left(\frac{\omega}{\dot{\omega}}\right)\left[1 - \left(\frac{\omega}{\dot{\omega}}\right)^{n-1}\right] \tag{1.50}$$

If we assume that the observed pulsar is "old" and has spun down since birth, $\omega_0 \gg \omega$, we can neglect the last term in the brackets. So, the expression

$$\tau_{pa} = -\frac{1}{n-1}\left(\frac{\omega}{\dot{\omega}}\right) \tag{1.51}$$

is called *characteristic pulsar age.*
Comparing eq.(1.46) and eq.(1.48), the braking index int the magnetic dipole model is n=3. However, braking indices determineted by observation, are between 2 and 3, this means that dipole emission definitely cannot be the full story.

Magnetic field strenght

Assuming that the dipole model is a fair description of a real pulsar and using $\omega = 2\pi/P$, $dE_{rot}/dt = I\omega\dot{\omega} = (dW/dt)_{md}$ and eq.(1.43), we can solve for $B_p \sin\alpha$:

$$B_p \sin\alpha = \sqrt{\frac{3c^3}{2\pi^2}\frac{I}{R^6}P\dot{P}}. \tag{1.52}$$

If we want a rough estimate, we can insert $\sin\alpha \approx 1$ and we find

$$B_p \approx 3.2 \cdot 10^{19}\ G \left(\frac{P\dot{P}}{1\ s}\right)^{1/2}. \tag{1.53}$$

Using as example the Crab pulsar, we obtain $B_p \approx 10^{12} G$.

P – $\dot{\mathbf{P}}$ diagram

The $P - \dot{P}$ diagram is a cartesian plane with the period on the abscissa and a first time derivative of the period on the ordinate. In the diagram, lines of constant B-field strength ($B_p \propto \sqrt{P\dot{P}}$) are reported. Although the details of the magnetic field evolution are still not fully understood, the B-field generally decay with the age of the pulsar.

From the diagram, we can observe that the pulsars group in two broad classes: *normal* and *millisecond pulsar*.

- *normal pulsar:* young pulsar (associated to supernova remnant), slow rotation period P from $\sim$ 0.1 to 1 s, rapid spin-down of $\sim 10^{-15} s\ s^{-1}$ and high B-field $\sim 10^{12}\ G$,
- *millisecond pulsar:* old pulsar (found in binary system), fast rotation period P from $\sim$ 1.5 to 30 ms, slow spin-down of $\sim 10^{-19} s\ s^{-1}$ and low B-field $\sim 10^{8}\ G$,

Concerning to millisecond pulsars, they are associated to binary system in which the companion star transfers mass and angular momentum to the neutron star. At this point, the neutorn star spins up to fast rotation. These pulsars are called *recycled pulsars*.

1.2.2 Binary neutron stars: astrophysical description

About half of all stars are part of systems consisting of two or more stars, so called binary or multiple stellar system. Binary systems containing a compact object such

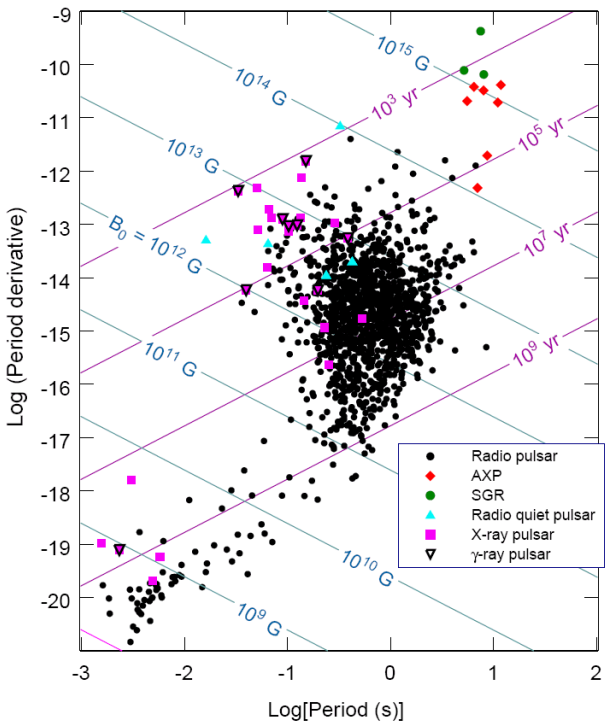

Figure 1.8: *$P - \dot{P}$ diagram for a sample of radio pulsars, radio quite pulsar, SGRs and X-ray pulsars.*

as a white dwarf (WD), a neutron star (NS) or a black hole (BH), are called *compact binary systems*. Obviously, each compact star can have any type of star as companion characterizing the binary systems.

X-ray binaries lie in binary systems where a non-compact star transfers matter to compact companion one which can be a NS or BH. This process occurs either via the so called Roche-lobe overflow or via stellar wind (see Figure 1.9).
According to accretion theory, an accreting compact object emits mainly X-ray radiation. The luminosity produced by accretion process is proportional to $L \propto 1/R$ (see Chap. 8 of [22]); in case of a white dwarf as compact object, this quantity is smaller because a WD radius R is larger, and therefore only systems close to Earth can be observed.

Traditionally, X-ray binaries are classified into two classes according to the mass of companion:

- *High-Mass X-ray Binaries* (HMXBs) where donator star is young and massive ($M \gtrsim 10\ M_{\odot}$) star: usually an O or B star, a Be star, blue supergiant; the X-ray luminosity of the system is less than optical one. O-type stars are massive stars ($> 16 M_{\odot}$) and very hot and extremely luminous while the B-type stars are blue

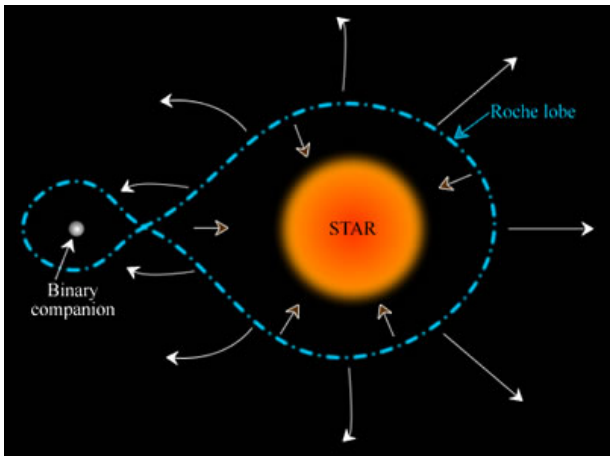

(a) High mass X-ray binary where the compact object is fed by a strong wind.

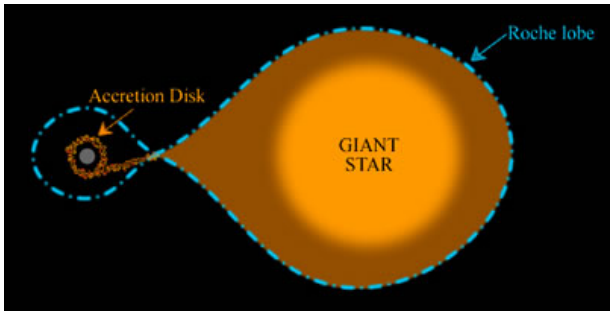

(b) Low mass X-ray binary where the accretion occurs via Roche lobe overflow.

Figure 1.9: Mechanism of mass transfer for HMXB (on the top) and for LMXB (on the bottom) [4]

and energetic but less luminous and massive massive ($> 2.1M_{\odot} - 16M_{\odot}$) then O one. The spectrum of O-type stars is complex but the transition in classification from O-type to B-type lies in absence of He II λ4541.

- *Low-Mass X-ray Binaries* (LMXBs) where donator star is slowly evolving low-mass ($M \lesssim 1.5\ M_{\odot}$) main-sequence star; the X-ray luminosity is larger by about one order of magnitude than the optical luminosity.

Due to the nature of their star companion, LMXB and HMXB systems belong to two different stellar populations. For a star in the main sequence, larger is the mass than lower is the time which is spent by the star in main sequence. Thus, HMXBs with short-lived massive companion star are young system because its companion star is short-lived massive star. They are found near star-forming regions, in particular close to spiral arms in the galactic plane as the figure 1.10 shows. Their orbital periods range from few hours to several hundred days. LMXBs are old systems being associated to a long-lived low-mass stars. They are manly found in the bulge and the globular clusters of our Galaxy. The latter harbor mainly old stars, for this reason LMXBs belong to old stellar population. The orbital periods of LMXB last from few minutes up to several days. The companion is difficult to observe and it can be seen only in systems with a large orbital separation.

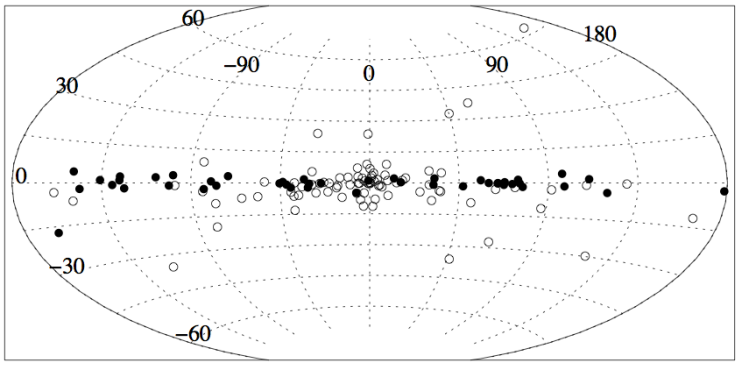

Figure 1.10: The plot shows the distribution of 86 LMXBs (open circles) and 52 HMXBs (filled circles) in the Galaxy [5] .

The accretion system is also different as shown in Figure 1.9. The compact object of HMXB system accretes mass originating from the companion stellar wind. Instead in LMXB systems, accretion is driven by the Roche-lobe overflow of the non compact star: the main sequence star fills its Roche-lobe because of nuclear reactions which produce

an expansion of its structure. At this point, through Lagrange point L1, the matter is transferred to massive, compact object settling into an accretion disk around it. Due to low-mass of non-compact star, its nuclear evolution timescale is long and accretion mechanism can go on for hundreds of millions year.

These differences imply a very different phenomenology. If HMXB system contains a neutron star, the magnetic field can force the infalling matter to corotate with the magnetic field lines. In this way, the matter is channeled by the magnetic field onto the magnetic poles of the neutron star where the X-rays are produced. In general, the magnetic and rotation axes are misaligned, the X-ray luminosity will be modulated in time by neutron star rotation period. These systems appear like X-ray pulsars.
In LMXB case where the matter flows from companion through the Lagrangian point forming a disk around the compact object, the magnetic field is weak and does not channel the material to the poles of the neutron star. Thus, the flux is not strongly modulated by the neutron star spin. The accreting material is mainly form by H and He. In LMXB, every few hours an explosive nuclear fusion reaction occurs and this leads to short bursts of X-ray radiation. These systems are called X-ray bursters.

Double neutron stars: formation channels

There are several formation paths for double neutron stars (DNSs). Before, it is useful to remember the stellar fate for different values of initial mass M_{ini}:

- $M_{ini} \lesssim 8\ M_{\odot}$, the star will end its life as a white dwarf.
- $8\ M_{\odot} \lesssim M_{ini} \lesssim 25\ M_{\odot}$, the star will undergo supernova (SN) explosion and a neutron star will be formed.
- $M_{ini} \gtrsim 25\ M_{\odot}$, a black hole (BH) will form.

The standard scenario for DNS formation is a close ($\sim 1\ AU$), massive binary system where both stars have mass between $(8-25)\ M_{\odot}$ see Figure 1.11. The primary (heavier one), bloats up and evolves toward a giant phase. At this stage, it overflows its Roche lobe transferring mass to lower companion (secondary). The primary ends its lifetime exploding as a core-collapse supernova and forms a neutron star. If the system is not destroyed by explosion, it consists of neutron star with main-sequence star. If the main-sequence star transfers mass to neutron star, the system may be observed as a HMXB system. The secondary continues to evolve further and when bloats up, it overwhelms the NS in a common envelope (CE) phase. During this phase, evolved core of star and

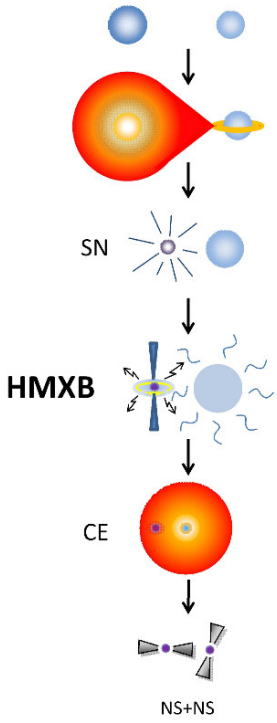

Figure 1.11: Formation of double neutron star system.

neutron star go around each other inside hydrogen envelope of secondary. They lose orbital energy which is deposited in the envelope. This is ejected and system with a naked-core of He of secondary star and neutron star is formed. In turn, the He star will produce a neutron star via SN explosion and if the system will survive the second explosion, then it will be a DNS system.
If the mass of primary and secondary are nearly the same, the initial system has another fate. In this case, the secondary leaves the main-sequence after the primary and before this can explode. Thus, the system has two He-cores orbiting inside a common hydrogen envelope. The orbital energy is released in the envelope leaving behind a close system of two He-cores. Two subsequent supernova (SN) explosions will take place and if the binary system will survive then a close DNS system is formed.

1.2.3 Gravitational wave from compact object mergers

Gravitational waves are a consequence of the theory of General Relativity, published by Albert Einstein in 1916. They are ripples of the gravitational field that propagate at the

speed of light, and are produced when huge masses are accelerated or deformed. This happens in many astrophysical scenarios, including supernova explosions or the gravitational interactions between compact objects such as black holes or neutron stars.
The evolution of merging binary compact objects, containing neutron stars and/or black holes, can be divided roughly into *inspiral*, *merger*, and *ringdown* (or post-merger) phases, each one of which has a distinct signature for detections and numerical models. Let us summarize the main characteristics of these phases.

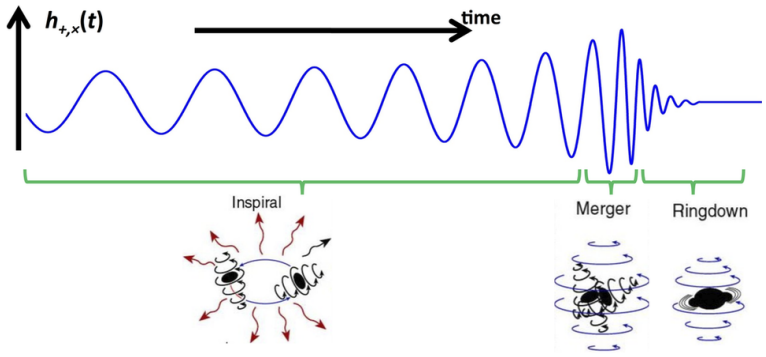

Figure 1.12: Cartoon picture of evolution of coalescence of binary compact object. With blue color is drawn the gravitational wave signal emitted by binary system during the in-spiral, merger and ring-down phases.

Inspiral phase

During this phase, the binary system steadily loses energy emitting GWs; as result, the orbital separation decays over long timescales and the orbital frequency increases. The dynamics of the system can be described in first approximation by Newtonian mechanics until the gravitational radiation timescale becomes comparable to the dynamical timescale, in this case the evolution in time is well-described by Post-Newtonian (PN) expansions [41] [42] [43].

In this section I describe the evolution of in-spiral compact objects. Full description of this topic can be found in [6]. We consider a binary system where the two compact objects, such as neutron stars or black holes, are point-like. Let be m_1, m_2 and $\boldsymbol{r}_1$, $\boldsymbol{r}_2$ masses and positions of two stars. Considering Newtonian case, in the center of mass frame (CM), the system is treated as one-body problem with

$$\mu = \frac{m_1 m_2}{(m_1 + m_2)} \qquad \textit{reduced mass}$$
$$\ddot{\boldsymbol{r}} = -\left(\frac{Gm}{r^3}\right)\boldsymbol{r} \qquad \textit{equation of motion}$$

where $m = m_1 + m_2$ is the total mass of the system and $\boldsymbol{r} = \boldsymbol{r}_2 - \boldsymbol{r}_1$ is the coordinate of relative motion. Examining the case of circular orbits, the orbital frequency of the source ω_s is $\omega_s = v/R$ where v is orbital velocity and R orbital radius and Kepler's third law is:

$$\frac{4\pi^2}{T^2} = \frac{Gm}{a^3} \qquad \longrightarrow \qquad \omega_s^2 = \frac{Gm}{R^3} \tag{1.54}$$

Introducing the *chirp mass*

$$M_c = \mu^{3/5} m^{2/5} = \frac{(m_1 m_2)^{3/5}}{(m_1 + m_2)^{1/5}} \tag{1.55}$$

The two polarization amplitudes h_+, $h_\times$ of the gravitational wave, become:

$$h_+(t) = \frac{4}{r}\left(\frac{GM_c}{c^2}\right)^{5/3}\left(\frac{\pi f_{gw}}{c^2}\right)^{2/3}\frac{1+\cos^2\theta}{2}\cos(2\pi f_{gw} t_{ret} + 2\phi),$$
$$h_\times(t) = \frac{4}{r}\left(\frac{GM_c}{c^2}\right)^{5/3}\left(\frac{\pi f_{gw}}{c^2}\right)^{2/3}\cos\theta\sin(2\pi f_{gw} t_{ret} + 2\phi) \tag{1.56}$$

where the gravitational frequency is related to $f_{gw} = \omega_{gw}/(2\pi)$ and $\omega_{gw} = 2\omega_s$. We can observe that the gravitational amplitudes depend on masses of two stars through their combination in the chirp mass. However, the emission of GWs costs energy. The orbital energy of source is given by sum of kinetic energy and potential energy of the orbit

$$E_{orbit} = E_{kin} + E_{pot} = -\frac{Gm_1 m_2}{2R} \tag{1.57}$$

remembering $E_{kin} = -1/2 E_{pot}$. To compensate the loss of energy via GW emission, R must decreses in time so that E_{orbit} becomes more negative. As the eq. 1.54 shows when R decreases, ω_s increases and if the angular velocity increases also the power radiated in GWs increases. So, on long time- scale, the decrease of R leads to coalescence of two objects. As long as

$$\dot{\omega}_s \ll \omega_s^2, \tag{1.58}$$

we are in the regime called of quasi-circular motion. Under this condition, we compute the back-raction of GWs. Taking into account eq.(1.54) and (1.55), we arrange eq.(1.57) in following way:

$$\begin{aligned} E_{orbit} &= -\frac{Gm_1m_2}{2R} \\ &= -\frac{Gm_1m_2}{2}\ \frac{(w_s)^{2/3}}{(Gm)^{1/3}} = \\ &= -\left(\frac{G^2M_c^5\omega_{gw}^2}{32}\right)^{1/3} \end{aligned} \tag{1.59}$$

The total power radiated in GWs is

$$P = \frac{32}{5}\frac{c^5}{G}\left(\frac{GM_c\omega_{gw}}{2c^3}\right)^{10/3}, \tag{1.60}$$

equating it with derivative of eq. (1.59) -dE_{orbit}/dt

$$-\frac{dE_{orbit}}{dt} = \frac{2}{3}\left(\frac{G^2M_c^5}{32}\right)^{1/3}\omega_{gw}^{-1/3}, \tag{1.61}$$

we obtain:

$$\dot{\omega}_s = \frac{12}{5}2^{1/3}\left(\frac{GM_c}{c^3}\right)^{5/3}\omega_{gw}^{11/3}, \tag{1.62}$$

which in terms of $f_{gw} = \omega_{gw}/(2\pi)$ becomes:

$$\dot{f}_{gw} = \frac{96}{5}\pi^{8/3}\left(\frac{GM_c}{c^3}\right)^{5/3}f_{gw}^{11/3}. \tag{1.63}$$

When the latter equation is integrated, f_{gw} formally diverges at a finite time value denoted with t_{coal} which is the observer time at coalescence. Defining $\tau \equiv t_{coal} - t$ and integrating eq.(1.63) we obtain

$$f_{gw}(\tau) = \frac{1}{\pi}\left(\frac{5}{256}\frac{1}{\tau}\right)^{3/8}\left(\frac{GM_c}{c^3}\right)^{-5/8}, \tag{1.64}$$

and we observe that gravitational frequency f_{gw} formally diverges at a finite value of time, t_{coal}. This divergence is cut off when the orbital separation reaches a value smaller

than critical distance R_{Sch} (Schwarzschild radius) and the two stellar objects merger.

Considering a binary system with two stars each one with mass $M = 1.4\ M_{\odot}$ and corresponding chirp mass of $M_{ch} = 1.21\ M_{\odot}$, the GW frequency is:

$$f_{gw}(\tau) \simeq 134\ Hz \left(\frac{1.21 M_{\odot}}{M_{ch}}\right)^{5/8} \left(\frac{1s}{\tau}\right)^{3/8}. \tag{1.65}$$

From eq.(1.65), we can compute the time to coalescence τ as

$$\tau \simeq 2.18\ s \left(\frac{1.21 M_{\odot}}{M_c}\right)^{5/3} \left(\frac{100 Hz}{f_{gw}}\right)^{8/3}. \tag{1.66}$$

From eq.(1.66), we can compute some value of time to coalescence. For example, at 10 Hz which is lowest frequencies for ground-based interferometers, we receive the radiation emitted at $\tau \simeq 17$ min to coalescence; at 100 Hz we get the radiation from last two seconds and at 1 kHz from last few milliseconds. From third Kepler's law, for $f_{gw} = 1$ kHz and $m_1 = m_2 = 1.4\ M_{\odot}$, the separation R between two stars is $R \simeq 33$ km.This suggests that such small separation is reached only by compact objects such as neutron stars and black holes. From a binary system, it is possible estimate the number of cycles detected in the detector frequency band.
Let be $T(t)$ period of GW slowly varying as function of time, the numbe of cycles in a time interval

$$dN_{cyc} = \frac{dt}{T(t)} = f_{gw}(t)dt \ \longrightarrow\ N_{cyc} = \int_{t_{min}}^{t_{max}} f_{gw}(t)dt = \int_{f_{min}}^{f_{max}} df_{gw} \frac{f_{gw}}{\dot{f}_{gw}}, \tag{1.67}$$

where f_{min}, f_{max} are the detector bandwith. Using the eq.(1.63) to express $\dot{f}_{gw}$ int terms of f_{gw}, we get:

$$\begin{aligned} N_{cyc} &= \frac{1}{32\pi^{8/3}} \left(\frac{GM_c}{c^3}\right)^{-5/3} \left(f_{min}^{-5/3} - f_{max}^{-5/3}\right) \\ &\simeq 1.6 \times 10^4 \left(\frac{10 Hz}{f_{min}}\right)^{5/3} \left(\frac{1.2 M_{\odot}}{M_c}\right)^{5/3}, \end{aligned} \tag{1.68}$$

assuming $f_{min}^{-5/3} - f_{max}^{-5/3} \simeq f_{min}^{-5/3}$. Thus, considering the same values for M_{ch} and m_1, m_2 and $f_{min} \sim 10$ Hz, the interferometer can be follow the evolution of the signal for thousands of cycles.

It is easy to understand that orbital radius decreases when the frequency increases. Starting from eqs. 1.54 and 1.65, the orbital separation of two objects is given by:

$$\frac{\dot{R}}{R} = -\frac{2}{3}\frac{\dot{\omega}_{gw}}{\omega_{gw}} \tag{1.69}$$

which integrates to

$$R(\tau) = R_0\left(\frac{\tau}{\tau_0}\right)^{1/4} = R_0\left(\frac{t_{coal}-t}{t_{coal}-t_0}\right)^{1/4} \tag{1.70}$$

where R_0 is the value of R at initial time t_0 and $\tau_0 = t_{coal} - t_0$. Considering initial time t_0 when $\tau = \tau_0$, from eq.(1.65) and eq.(1.54), the relation between R_0 and time to coalescence τ_0 is given by

$$\tau_0 = \frac{5}{256}\frac{c^5 R_0^4}{G^3 m^2 \mu}. \tag{1.71}$$

Initial radius R_0 ca be related to initial orbital period $T_0 = 2\pi/\omega_s(\tau_0)$ through $R_0^2 = Gm(T_0/2\pi)^2$ and plugging in the numerical values, we have

$$\tau_0 \simeq 9.829 \times 10^6\ yr\ \left(\frac{T_0}{1\ hr}\right)^{8/3}\ \left(\frac{M_\odot}{m}\right)^{2/3}\ \left(\frac{M_\odot}{\mu}\right) \tag{1.72}$$

Thus, considering circular orbits and masses of two stellar components of order $M_\odot$, from the latter we can state that, binary systems at formation with an initial orbital period less than about one day, have coalesced by emission of GWs within the present age of galaxies.

When the two compact objects get close, the effect of gravitational field becomes strong and this reflects on dynamics of the binary system. In particular, it exists a minimum values of the radial distance beyond which the stable circular orbits are not allowed, this is an Inner-most Stable Circular Orbit (ISCO) r_{ISCO}:

$$r_{ISCO} = \frac{6Gm}{c^2} \tag{1.73}$$

m is the total mass of binary system. Therefore, for distance $r \gtrsim r_{ISCO}$, the system undergoes a slow adiabatic inspiral phase through a series of quasi circular orbits followed by GW radiation. When the orbital distance reaches the ISCO, the strong-field effects are dominant and the two objects plunge toward each other and coalesce.
From Kepler's law we have that the in-spiral phase ends when the source frequency is:

$$(f_s)_{ISCO} = \frac{1}{6\sqrt{6}(2\pi)}\frac{c^3}{Gm}, \tag{1.74}$$

with numerical value

$$(f_s)_{ISCO} \simeq 2.2\ kHz\left(\frac{M_\odot}{m}\right). \tag{1.75}$$

Considering a NS system with total mass $m = 2.8\ M_\odot$ ($m_1 = m_2 \simeq 1.4M_\odot$), the coalescence occurs at frequency $(f_s)_{ISCO} \sim 800$ Hz while for BH binary system with total mass $m = 10\ M_\odot$ we have $(f_s)_{ISCO} \sim 200$ Hz. For supermassive BH with $m \sim 10^6\ M_\odot$, $(f_s)_{ISCO}$ is in the mHz band.

The flux of energy per unit area per unit frequency interval is given by (see eq.(1.159) of [6])

$$\frac{dE}{dAdf} = \frac{\pi c^3}{2G} f^2\big(|\tilde{h}_+(f)|^2 + |\tilde{h}_\times(f)|^2\big), \tag{1.76}$$

Writing $dA = r^2 d\Omega$

$$\frac{dE}{df} = \frac{\pi c^3}{2G} f^2 r^2 \int d\Omega\ \big(|\tilde{h}_+(f)|^2 + |\tilde{h}_\times(f)|^2\big), \tag{1.77}$$

integrating over a sphere surrounding the source and being, in the case of a binary system, the sum in the bracket is given by [43]

$$\big(|\tilde{h}_+(f)|^2 + |\tilde{h}_\times(f)|^2\big) = \frac{G^{5/3}}{c^3}\frac{\pi}{12}\frac{M)ch^{5/3}}{r^2}\frac{1}{(\pi f)^{7/3}}, \tag{1.78}$$

the energy spectrum dE/df in the inspiral phase is

$$\frac{dE}{df} = \frac{\pi^{2/3}}{3G}(GM_c)^{5/3} f^{-1/3}. \tag{1.79}$$

Integrating up to GW maximum frequency of the inspiral phase, the total energy radiated during the inspiral phase is :

$$\Delta E_{rad} \sim \frac{\pi^{2/3}}{2G}(GM_c)^{5/3} f_{max}^{2/3}, \tag{1.80}$$

inserting the numerical values,

$$\Delta E_{rad} \sim 4.2 \times 10^{-2} M_\odot c^2 \left(\frac{M_c}{1.21 M_\odot}\right)^{5/3} \left(\frac{f_{max}}{1\ kHz}\right)^{2/3}, \tag{1.81}$$

Setting $f_{max} = 2(f_s)_{ISCO}$ (as appropriate for quadrupole radiation) and using eq.1.55 for chirp mass and eq.1.75 for f_{ISCO}, the total energy radiated during the in-spiral phase depends on reduced mass of the system:

$$\Delta E_{rad} \sim 8 \times 10^{-2} \mu c^2. \tag{1.82}$$

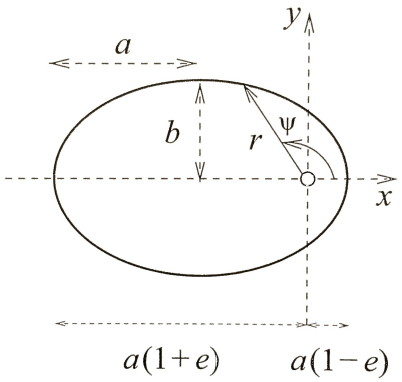

Figure 1.13: The plot reports the parameters of elliptic orbit. The polar coordinates (r, ψ) and Cartesian coordiantes (x, y) are centered on the focus of ellipse (black circle). The angle ψ is measured counterclock-wise from x axis. The semimajor axis is divided in two segments $a(1+e)$ and $a(1-e)$ [6].

The problem of two masses in elliptic Keplerian orbit reduces to a one-body problem for a particle of reduced mass μ subject to an acceleration $\ddot{\boldsymbol{r}} = -\big(Gm/r^2\big)\hat{\boldsymbol{r}}$. This equation of motion for elliptic orbit, has two first integrals of motion, the angular momentum $\boldsymbol{L}$ and the energy E. The conservation of $\boldsymbol{L}$ implies that the orbit lies in a plane with origin in center of mass. The equation of the orbit is [6][44]

$$r = \frac{a(1-e^2)}{1 + e\cos\psi} \tag{1.83}$$

where a is the semimajor axis of elliptical orbit, e the eccentricity and ψ the angular coordinate in the plane of the orbit (see the figure 1.13).
If the plane of the motion and position of the orbit in the plane is specified, then there are two parameters necessary to describe the orbit: the semimajor axis a and the eccentricity e. These parameters are related to the total energy E and the relative angular momentum L through the following equations:

$$a = \frac{Gm\mu}{2|E|}$$
$$L^2 = Gm\mu^2 a(1-e^2) \tag{1.84}$$

We can observe that the orbits with same energy have same semimajor axis a.
The energy radiated by the system averaging over one period of elliptical motion is given by eqs.(16) and (17) of [44]

$$P = \frac{32G^4\mu^2m^3}{5c^5a^5}f(e), \tag{1.85}$$

with factor $f(e)$

$$f(e) = \frac{1}{(1-e^2)^{7/2}}\left(1+\frac{73}{24}e^2+\frac{37}{96}e^4\right). \tag{1.86}$$

In the Newtonian theory, semimajor axis a and the eccentricity e are constants of the motion. In the general theory of gravitation, indeed, the binary system loses energy and angular momentum of the orbital motion producing a secular changes in semimajor axis and in its ellipticity until the two compact objects collapse. So, the eccentricity decreases and the effect of the back-reaction of GW emission is to circularize the orbit.
Thus, the energy E and angular momentum L of the orbit averaged over one period, evolve as [6] [44] [45]:

$$\frac{dE}{dt} = \frac{32}{5}\frac{G^4\mu^2m^3}{c^5a^5}\frac{1}{(1-e^2)^{7/2}}\left(1+\frac{73}{24}e^2+\frac{37}{96}e^4\right), \tag{1.87}$$

$$\frac{dL}{dt} = -\frac{32}{5}\frac{G^{7/2}\mu^2m^{5/2}}{c^5a^{7/2}}\frac{1}{(1-e^2)^2}\left(1+\frac{7}{8}e^2\right). \tag{1.88}$$

The evolution of semimajor axis a and eccentricity e are:

$$\frac{da}{dt} = -\frac{64}{5}\frac{G^3\mu m^2}{c^5a^3}\frac{1}{(1-e^2)^{7/2}}\left(1+\frac{73}{24}e^2+\frac{37}{96}e^4\right), \tag{1.89}$$

$$\frac{de}{dt} = -\frac{304}{15}\frac{G^3\mu m^2}{c^5a^4}\frac{e}{(1-e^2)^{5/2}}\left(1+\frac{121}{304}e^2\right). \tag{1.90}$$

We see from equation (1.90) that if the orbit is a circular orbit $e = 0$, then $de/dt = 0$. This means that circular orbit remains circular orbit. Another way to see this is to consider equations (1.87) and (1.88) which became for $e = 0$:

$$\frac{dE}{dt} = \omega_0 \frac{dL}{dt}, \tag{1.91}$$

where $\omega_0 = (Gm/a^3)^{1/2}$ is the frequency of circular motion (for more details see the equations (4.59), (4.119)-(4.122) of [6]). For ellipitc orbits with $e > 0$, equation (1.90) gives $de/dt < 0$ and therefore because of GW emission, an elliptical orbit becomes more and more circular.

The time to coalescence $\tau(a_0, e_0)$, of a binary system with semimajor axis a_0, eccentricity e_0, at time $t_0 = 0$ is given by (in terms of orbital period):

$$\tau_0(a_0, e_0) \simeq 9.829 \times 10^6 \ yr \left(\frac{T_0}{1 \ hr}\right)^{8/3} \left(\frac{M_\odot}{m}\right)^{2/3} \left(\frac{M_\odot}{\mu}\right) F(e_0), \tag{1.92}$$

$$F(e_0) = \frac{48}{19} \frac{1}{g^4(e_0)} \int_0^{e_0} de \frac{g^4(e)(1-e^2)^{5/2}}{e(1+\frac{121}{304}e^2)},$$

$$g(e) = \frac{e^{12/19}}{1-e^2}\left(1 + \frac{121}{304}e^2\right)^{870/2209} \tag{1.93}$$

Taking the Hulse-Taylor binary system pulsar ($m_1 = m_2 \simeq 1.4 M_\odot$) as example, with $e_0 \simeq 0.617$ and $F(e_0) \simeq 0.184$ and period $T_0 \simeq 7.75$ hr, we obtain that the time to coalescence of Hulse-Taylor binary pulsar is $\tau_0(a_0, e_0) \simeq 300$ Myr.

Merger phase

Merger phase begins when the orbital evolution is so rapid that the adiabatic evolution in no longer a good approximation and the masses come into contact with each other. The two masses go through a violent dynamical phase, that leads to the formation of a black hole (BH) or the formation of a stable or quasi-stable NS remnant which may or may not collapse to a black hole. At this point, the Post-Newtonian approximation is not able to describe evolution of the system. To understand its dynamics, full General Relativity simulations is required, as the problem involves strong relativistic gravity and tidal deformation and disruption. This phase produces the maximum GW amplitude predicted by numerical simulations. However the merger phase in the case of binary

NSs is still not well understood due to many unknown physical effects, such as the equation of state describing NS structure and the effect of their magnetic fields. In case of NS merger, GW emission during the merger encodes important information about EoS (which is unknown at nuclear densities), particularly the GW frequency cut at which the binary orbit becomes unstable resulting in a characteristic cutoff in GW emission at those frequencies[41]. The timescale of the merger phase is very short: from seconds down to a few ms in the case of the heaviest systems.

Ring-down phase

During the ring-down phase the emitted radiation can be computed using perturbation theory (or numerical simulation in case of NS remnant) and it consists of a superposition of quasi-normal modes of remnant formed right after merger. The remnant oscillations carry the signature of progenitor objects: in case of BH as remnant, these modes depend on mass and spin angular momentum; indeed, iin the case of a NS remnant, there is also a tight relation with EoS of progenitors. Also in this phase, the signal lasts for a very short time interval: GWs are emitted for a few ms to seconds, depending on the mass of the final object.

1.3 Binary neutron star coalescences

Coalescence of binary neutron stars is one of the most promising source of gravitational wave detectors advanced LIGO and Virgo. Detection of gravitational waves from merger of neutron stars allow us to extract informations on matter and its EoS, mass, spin and radius of the two objects. After the merger of two neutron stars, two scenarios take place: *prompt collapse* to black hole, if the total mass is large enough and if not, *delayed collapse* to black hole, with the formation of massive neutron star (MNS).

The Figure 1.14 from [2], shows different evolution scenarios of binary neutron star system. The time is reported on the horizontal axis while on the vertical axis, the ratio between the mass of the binary, M, and the the maximum mass of an isolated spherical star, M_{max}. For each evolution stage, it is reported the frequencies at which gravitational waves should be emitted. The binary system evolves on the radiation-reaction time-scale, i.e., on the time-scale due to loss of energy and angular momentum via gravitational radiation. For all cases, in-spiral phase could last for millions of years before the binary reaches a separation small enough that the changes in the orbits take place on a time-scale of a few seconds (finite-size effects and relativistic regimes become

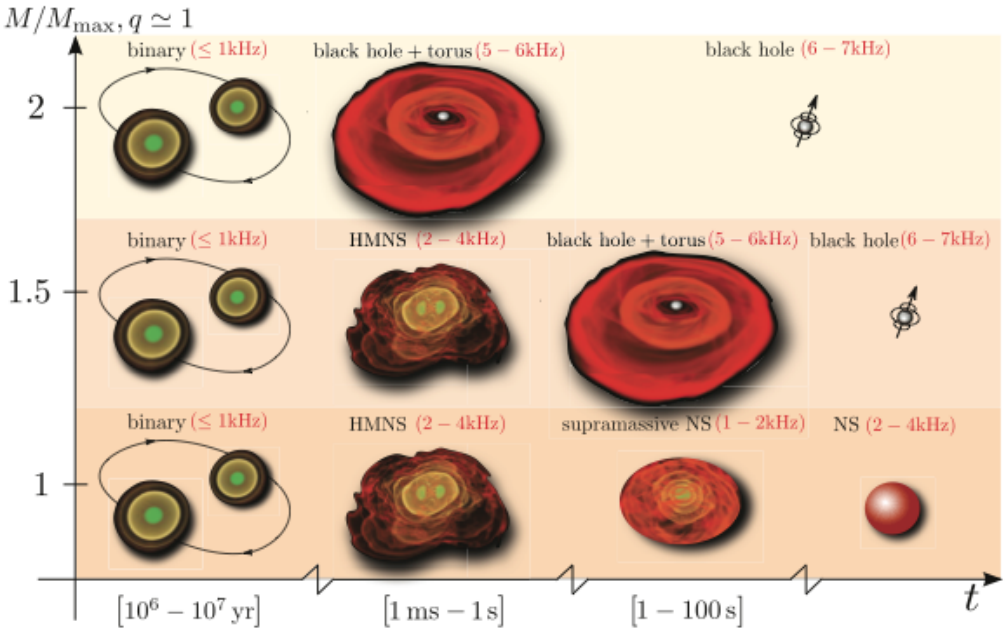

Figure 1.14: Cartoon illustrates the different evolution scenarios of equal-mass binary neutron star system, showing how the dynamics changes in time as a function of the initial mass of the binary. Depending on the initial mass, the binary can either collapse promptly to a black hole surrounded by a torus, or produce a HMNS which ultimately collapses to a black hole and torus, or for small values of masses, lead to a HMNS which eventually generates a supramassive neutron star [2]. For each object formed during the various stages, in red, are indicating the typical frequencies at which gravitational waves should be emitted [7].

dominant and numerical solution of the equations of relativistic hydrodynamics in fully dynamical spacetimes is necessary to describe the system).

From the cartoon, after the coalescence of two neutron stars, we see that, taking into account $M/M_{max} \gtrsim 1.5$, the binary system can either collapse promptly (over time-scale of a few ms) to black-hole surrounded by a torus or, in case of $1 \lesssim M/M_{max} \lesssim 1.5$, can form a HMNS (hyper massive neutron star) which eventually collapse to back hole with a torus (over time-scale of 10-1000 ms). In both cases, the torus accrete matter onto the black hole on a time-scale of the order of 1-100 or more. In general, the duration of this phase is due to most efficient process removing angular momentum, i.e., gravitational radiation, magnetic fields or viscous processes. At the same time, its value is very uncertain because it is not easy to perform accurate numerical simulation for these very long time-scales. If neutron star masses are small $M/M_{max} \lesssim 1$, the remnant of the merger loses much of its angular momentum and differential rotation, eventually becoming a hot, axisymmetric and supramassive neutron star (SMNS). When SMNS

will have lost all of its rotational energy due to dissipative or radiative losses, its only possible fate will be the collapse to a black hole [2].

1.3.1 Gravitational wave spectral properties

In section 1.3, we discussed about the the fate of coalescence of binary neutron stars. The GW signal coming from NS merger, carries important information on system and on the equation state of matter at several times nuclear density ($\rho = 2.7 \times 10^{14}$ g/cm^3). When the two neutron stars get closer, the tidal effects became dominant leaving a signature on EoS describing the phase evolution of GW waveform of the system.

If a merger of double neutron stars does not form a BH right after their coalescence (*prompt scenario*), a massive ($M > 2M_{\odot}$), differentially rotating oscillating neutron star may form before collapsing to BH (*delayed scenario*). The post-merger neutron star (PMNS) remnant generates a short duration ($\sim 10 - 100$ms) GW signal. The power spectrum of post-merger GW signal presents a structured power spectrum which arises at $\sim 1 - 4$ kHz and is characterized by dominant oscillation frequency f_{peak} due to quadrupole oscillation in the fluid and, in additional to this, by secondary peaks generates by non linear coupling between certain oscillation modes [46][47][48] and references therein. The structure of NS outcome is strongly affected by EoS, thus the oscillations of PMNS remnant are linked to EoS describing the double neutron star system [12].

The solution of Tolman-Oppenheimer-Volkoff equations (section 1.1.4) provides maximum mass M_{max} of non-rotating neutron star and corresponding radius R_{max} for the given EoS. Numerical relativity simulations have proven that, for a given total binary mass M_{tot}, the dominant oscillation frequency peak of post-merger phase of NS coalescence scales with NS radii of given mass [49].

In view of the coming GW observations from binary NSs with the advanced interferometers, this empirical relation $R_{NS} - f_{peak}$ provides us the possibility to constrain the $M - R$ relation and consequently the EoS when the post-merger GW frequency is *directly* observed. The works [50] [51] highlights the relation between the frequency peak of the post-merger and total mass of binary system: for a given EoS, the frequency f_{peak} in the post-merger, increases with increasing binary mass. This is understandable because the remnant becomes more compact and thus its oscillation frequency higher.
In work [52], the authors discuss on how single observation of the post-merger GW signal from delayed or prompt collapse can also constrain the threshold mass M_{thresh} for prompt collapse. The threshold mass M_{thresh} depends on EoS and represents the maxi-

mum mass beyond which the binary merger leads to a direct formation of BH. Thus, it discriminates the two scenarios of prompt and delayed collapse

$$\begin{cases} M_{tot} > M_{thres} & \text{BH formation,} \\ M_{tot} < M_{thres} & \text{NS remnant,} \end{cases}$$

and assuming that M_{thres} scales with the maximum mass M_{max} of isolated, nonrotating NSs [53]

$$M_{thres} = kM_{max}, \tag{1.94}$$

where M_{max} is determined by the EoS and obtained by integration of equations of relativistic hydrostatic equilibrium (TOV equations), while the coefficient k also depends on the EoS, or equivalently on NS properties and for this coefficient. They find a tight correlation with the compactness of the binary system $C_{max} = (GM_{max})/(c^2R_{max})$ where M_{max}, R_{max} are the maximum-mass TOV configuration.
In case of delayed collapse to BH, a measurement of total mass by in-spiral phase, well understood analytically, provides a lower limit on M_{thresh} and an upper limit for f_{peak} because the peak frequency increases with the mass of the NS remnant. Indeed, in case of prompt collapse to BH, the total mass obtained by in-spiral signal is an upper limit on M_{thresh} and thus it allows to set a limit on he maximum mass of an isolated non-rotating star [51]. In work [49], the authors have demonstrated that if two or more post-merger events, with slightly different total mass, are detected, we can employ the observed f_{peak} to determine maximum mass of cold, non-rotating neutron stars to within 0.1 $M_{\odot}$ and the corresponding radius to within a few percent.

It is important to underline that the measurement of dominant GW frequency f_{peak} requires a large signal-to noise ratio because it arises outside of the most sensitive range of gravitational wave interferometers, thus the detection of this type of signals will be possible for nearby events.

In this part of paragraph, we describe in more details the gravitational spectral properties. In the recent paper, L. Rezzolla and K. Takami (2016) [8], present the analysis of a large sample of neutron star binary merger simulations associated to different EoS, in order to extract the spectral features of gravitational wave signals which bring the signature of EoS of matter at nuclear density. At the same time, they summarize the results of previous authors works on post-merger GW signal. The authors consider an initial coordinate separation of the stellar centers of 45 km (which proved almost four orbits before the merger) for all models. They focus the analysis on simulation of GW

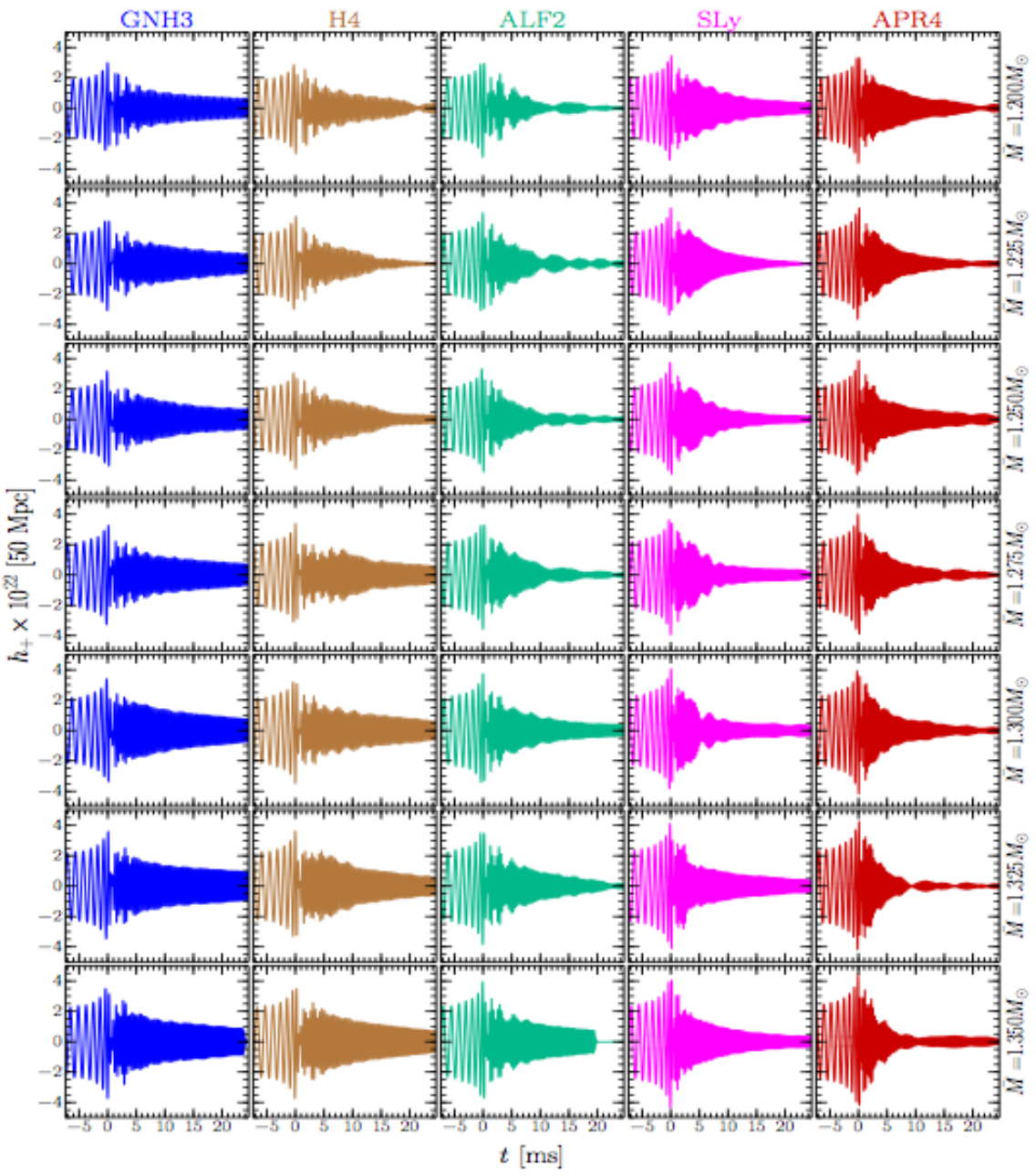

Figure 1.15: Simulations of gravitational waveforms for some cold-EoS binaries. Each column and its respective color, refers to given EoS, while each row corresponds to the gravitational masses $\bar{M} \equiv (M_1 + M_2)/2$ where M_1, M_2 are star masses of the binary system. All simulated neutron star systems, considering different EoSs, form a long-lived HMNS in the post-merger phase with $t \geq 20$ ms. See the reference [8] for more details.

signals by an hyper massive neutron star (HMNS) which is formed after binary neutron star coalescence and it survives at least $t_{HMNS} \approx 25$ ms before to collapse to black

hole (BH). Five different EoSs are considered for the simulation: GNH3, H4,ALF2 (*stiff* EoSs), SLy, APR4 (*soft* EoSs). For each one, ten equal-mass binaries are considered with average gravitational mass $\bar{M} \equiv (M_1 + M_2)/2$ at infinite separation in the range between $\bar{M} = (1.200 - 1.500)\ M_\odot$.
In the simulations also four unequal-mass binaries are included with $\bar{M} = 1.300\ M_\odot$ and mass ratio $q \equiv M_1/M_2 \simeq 0.93$ and $\bar{M} = 1.275\ M_\odot$ and $q \simeq 0.82$ for GNH3 (stiff) and SLy (soft) EoSs. The sample is completed by two equal-mass binaries with masses $\bar{M} = 1.338, 1.372\ M_\odot$ and described by the the hot LS220 EOS. Detailed informations on all the models and their properties are collected in [8].
The cold nuclear physics EoSs are adequate to represent the state of NS matter prior to the merge. After contact of two objects, due to the large shocks and heating processes involved, the pressure and density of tow neutron stars are function of temperature. So it is necessary to use "hybrid EoS" which include these thermal effects.

The Figure 1.15 shows the gravitational waveform evolution for some binary systems of equal mass and their nuclear-physics EoSs. Moving along each column, we have a specific EoS which is distinguished by different colours, while each row refers to a given initial gravitational mass. We can observe that in-spiral and post-merger phases are separated by *transient period* of $t \in [-1, 4]$ ms. Although it is very short, during this period the remnant readjusts its structure after the collision of two objects.
Moreover, the transient phase is followed by a period of $\sim 10\ ms$ characterized by oscillations in power spectrum of post-merger GW signal at different frequencies. This period anticipates the stage in which the HMNS reaches a "stationary" state and its frequency increases slowly with time as a consequence of GW losses.
For each EoS (fixed the column in Figure 1.15), the amplitude of the signal in the post-merger phase increases with mass. This is rather easy to understand: the gravitational wave amplitude is proportional to quadrupole moment of mass distribution of NS and large masses will produce large changes in the quadrupole moment. The only exception to this behaviour is represented by the APR4 EOS, which is particularly soft at high densities and hence yields an HMNS which rapidly becomes almost axisymmetric.
In the same figure, moving along a row among different EoSs but with same $\bar{M}$, the GW amplitude decays in the post-merger phase and the rate at which this happens depends inversely on the mass and on the stiffness: high-mass binaries with soft EoSs (SLy and APR4) show a large damping in amplitude (e.g., binary APR4-q10-M1325), while low-mass binaries with stiff (GNH3, H4 and ALF2) show a much small damping (e.g., binary GNH3-q10-M1300). This depends on the fact that HMNSs with larger masses (and not ultra-soft) will tend to maintain the bar-mode deformation for longer times [54].

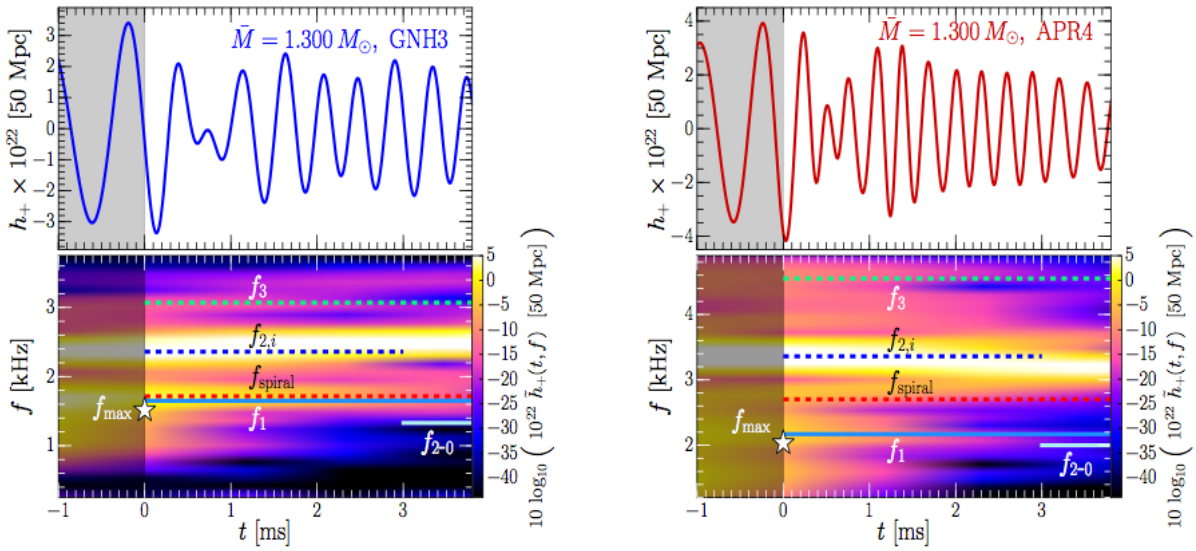

Figure 1.16: Two examples of GW emission related to transient phase $t \in [-1, 4]$ms. The gray-shaded rectangle includes the GW emission $\sim$ 1ms before the merger. The top panels show gravitational strain $h_\times$ for a type of stiff EoS (GNH3) and soft EoS (APR4) both with $\bar{M} = 1.300 M_\odot$. The both cases refer to a source at 50 Mpc. On the bottom, there are two corresponding spectrograms and the horizontal lines indicates the various frequency peaks right after the merger [8].

In Figure 1.16, Rezzolla and Takami focus on the spectral features of GW signals emitted few milliseconds after the merger and how these spectral properties evolve considering a timescale much longer than *transient* one (gray-shaded area), i.e., $\sim$ 25 ms after the merger. Top panels of Figure 1.16 report two examples of the strain of GW h_+ referring to source at 50 Mpc, for a stiff EoS (GNH3) and a soft EoS (APR4) with $\bar{M} = 1.300 M_\odot$; on the bottom the corresponding spectrograms are reported.
These last show different features in frequency spectrum marked by different colors and horizontal lines and that can be summarized as:

- the frequencies f_{max} was first introduced in Ref.[55] as instantaneous GW frequency at the merger, i.e., at GW amplitude maximum. Read *et al.* in Ref.[55] and later Takami *et al.* in Ref.[9] also,have shown that these frequencies are relates to dimensionless tidal deformability parameter Λ of the two stars

$$log_{10}\left(\frac{f_{max}}{Hz}\right) \approx 4.2423 - 0.1546\Lambda^{1/5} - log_{10}\left(\frac{2\bar{M}}{M_\odot}\right) \tag{1.95}$$

$$\Lambda \equiv \frac{\lambda}{\bar{M}^5} = \frac{2}{3}\bar{k}_2\left(\frac{\bar{R}}{\bar{M}}\right)^5 \tag{1.96}$$

where $\bar{k}_2$ is the mode l=2 dimensionless tidal Love number, $\bar{R} \equiv (R_1 + R_2)/2$ average radius and $R_{1,2}$ are the radii of the non-rotating neutron stars associated with each binaries. This behaviour is similar to *"I-Love-Q"* relations [56] [57] [58] which was brought up for isolated neutron stars.
I-Love-Q relations are relations between the moment of inertia (I), the tidal deformability (or tidal *Love* number) and the quadrupole moment (Q) of compact objects such as neutron stars and approximately do not depend on internal structure and thus equation of state. These relations become exact in the limit as compact stars become BHs.

- In Ref.[59], Stergioulas *et al.*, studied nonaxisymmetric oscillation modes in mergers of compact object binaries and the associated gravitational wave emissions. The outcome of compact object mergers can lead to either prompt collapse to black hole (BH) or hypermassive compact object (hypermassive neutron star, HMNS) which collapse to BH after few milliseconds. In case of HMNS, a non nonaxisymmetric object is generated with transient deformations such as a bar-like shape, spiral arms and quasiradial and nonaxisymmetric oscillations of the matter. Considering HMNS as an isolated gravitating fluid, they studied its oscillation modes through the Fourier transforms of the evolved variables and reveal that the oscillations identified in the fluid are in direct correspondence with peaks in the GW spectrum (obtained through the quadrupole formula). From the comparison of analysis of the dynamics of the fluid and GW spectrum of different EoSs, focusing on dominant oscillation mode m = 2 of post-merger remnant, they associated specific frequency peaks in GW spectrum with the nonlinear components (see Figure 3 - Figure 8 in Ref.[59]). In particular, the dominant oscillation mode m= 2 of post-merger remnant (fluid) forms a triplet whose side bands are due to nonlinear coupling to the fundamental quasiradial m=0. A corresponding triplet of frequencies is identified in it so that the highest frequency peak f_2 coincides with l=m=2 mode and also f_1 and f_3 with side bands. The frequency f_{2-0} coincides with difference between quadrupole mode m=2 and quasiradial mode m=0, f_{2+0} coincides with sum of these two modes.
  During the *transient* phase, as the spectrograms show in Figure 1.16, the f_2 is labelled by $f_{2,i}$ to distinguish from values of frequency peak f_2 present in quasi-

stationary evolution of the GW signal.

- the frequencies f_1, f_2, f_3 were introduced by Takami, Rezzolla and Baiotti in Refs.[54],[9] and represent the main peak of the PSDs measured in those references. Despite of f_{max}, these frequency peaks are a features of PSDs.
  In Ref.[9], a toy model is proposed in order to explain the relation $f_2 \simeq (f_1 + f_3)/2$ and the frequency f_3 is predicted as $f_3 = 2f_{2,i} - f_1$ where the quantities $f_{2,i}, f_1$ are measured from the data.

- the frequency f_{spiral} was first introduced in Ref. [60] and refer to the contribution to the GW signal coming from a "rotating pattern of a deformation of spiral shape". Shapes in gauge-dependent quantities such as the rest-mass density are essentially impossible to measure in numerical-relativity calculations, thus it is not possible to measure these frequencies in calculations. Hence, the values reported are those predicted from the analytic prescription given in Ref.[12] (cf., Eq. (2) of [12]). In Ref. [12], it is reported that the f_{spiral} peak can be roughly reproduced in a toy model, but no details are given within.

Considering much longer timescale ∼25 ms (same EoSs in Figure 1.16), it is possible to highlight how spectral peaks change from transient phase to *quasi-stationary* phase:

- the frequency $f_{2,i}$ present in transient phase, evolves in f_2 when reaches quasi-stationary phase.

- the frequency f_{2-0} has a small power during the transient phase but becomes significant in the following phase and only for stiff EoSs and for a limited time period (see, e. g., GNH3, H4 and ALF2).

- the frequency f_{spiral} has a different behavior for stiff and soft EoSs: as the figures show, f_{spiral}, during the transient phase is the *same* as the frequency f_1 in quasi-stationary one for stiff EoSs (i. e., GNH3, H4 and ALF2); for soft EoSs (APR4, SLy) f_{spiral} is present at higher values of frequency.

- for all analyzed EoSs, three frequencies appear during the transient phase: f_1, $f_{2,i}$, f_3.

In the Figures 1.17-1.18, we see how the author have investigated on spectral properties of full analyzed PSDs of GW signal. The Figure 1.17 reports two examples of PSD for low-mass (M= 1.200 $M_\odot$) and medium-mass (M= 1.350 $M_\odot$) binary systems; solid

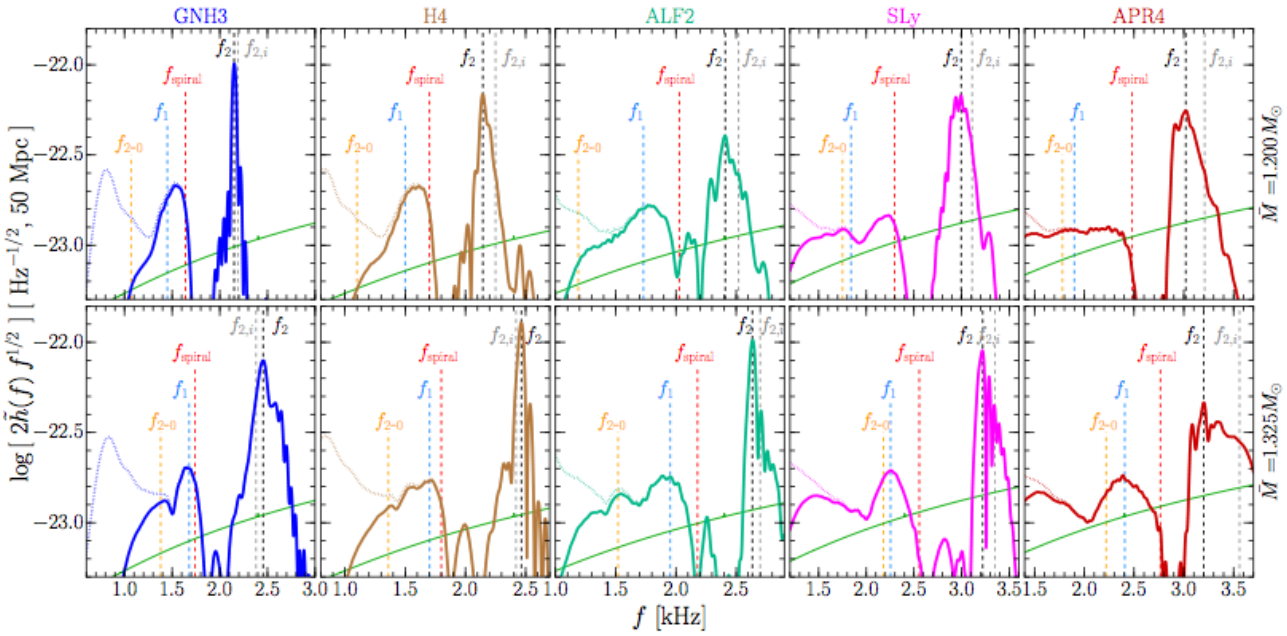

Figure 1.17: The plot shows the total PSDs of GW signal taking into account two binary systems with mass $\bar{M} = 1.200 M_\odot$ (top row) and $\bar{M} = 1.325 M_\odot$ (bottom row) for all EoSs at distance of 50 Mpc. The solid lines refer to the post-merger signal only while the dotted lines to the power during the short in-spiral. The values of the frequencies f_1, $f_{2,i}$, f_2, f_{2_0} and f_{spiral} are marked by vertical dashed lines of different colors and these values are either measured from the PSDs or estimated by numerical simulations. The green line in each plot is the sensitivity curves of Advanced LIGO[8].

lines refer to the post-merger signal while dotted lines refer to last orbit of the in-spiral phase. The frequency peaks f_1, $f_{2,i}$, f_2, f_{2-0} and f_{spiral} have different colors and are marked by vertical dashed lines. From analyzed PSDs, it arises that:

- all analyzed EoSs show a distinctive peak corresponding to f_2 frequency (black color) and given by an analytic expression.
- the $f_{2,i}$ frequencies (grey color) give a small contribution to total PSD, in fact these frequencies are short lived with a small contribution to total GW signal.
- the frequency peaks f_1 and f_{spiral} are not so different for stiff EOSs GNH4 and H4 but a evident difference, indeed, is present in case of soft EOSs, e.g., ALF2, SLy and APR4.
- the behaviour of the f_{2-0} frequencies is less clear. If we consider waveform such as SLy EOS, for which f_{2-0} is comparable and not significantly different from f_1 then

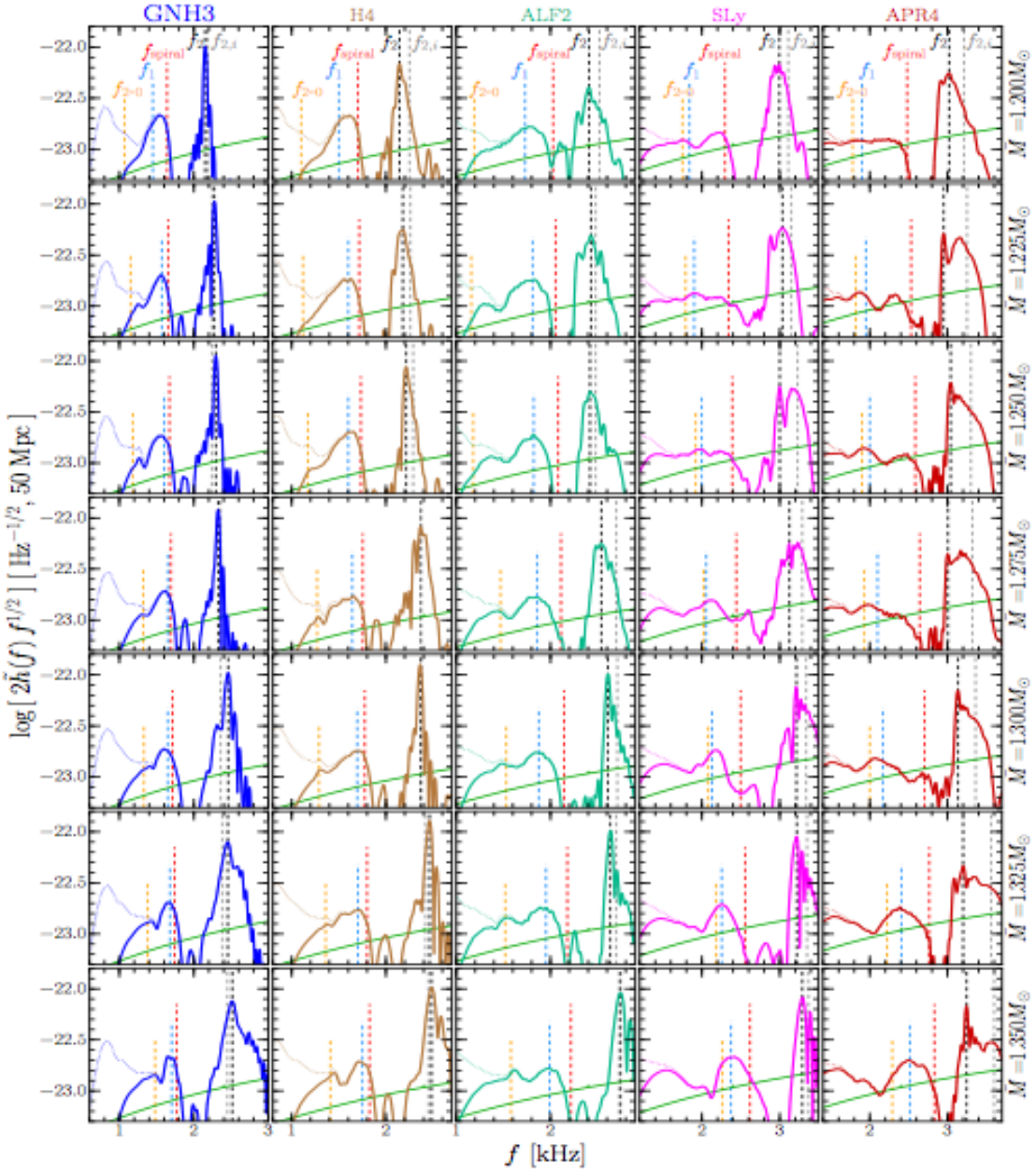

Figure 1.18: The same set of EoSs for binaries in Figure 1.15 is reporters here. The frequencies f_1 f_{spiral} are similar taking into account the stiff EoSs (e.g., GNH3, H4) but these frequencies became different in case of soft EoSs (e.g., SLy, APR4)[8].

these frequencies can be associated to the same power excess attributed to the f_1. In other cases, such as, for binary systems with $\bar{M} = 1.350 M_\odot$ with EOS GNH3, H4 and ALF2, they are associated to peaks with very imited power. While, in case with $\bar{M} = 1.200 M_\odot$ with EOS GNH3, H4 and ALF2 or $\bar{M} = 1.350 M_\odot$ with

EOS APR4 they are associated to peaks. The authors remember us that peak f_{2-0} comes from mode coupling and therefore its energetic contribution to PSD is less.

Spectral properties related to progenitors

In this part of paragraph, we discuss how the spectral properties of the GW signal are correlated to properties of progenitors stellar models. In previous numerical relativity studies, some of these correlations seem *universal*. This means that there is a *slightly dependence* with EoS and can be used to constrain the physical properties of two stars components and consequently, the EoS describing the binary system.

Read et al.[55] have found a relation which describes the f_{max} in terms of tidal deformability that is independent of the EoS. We remember the expression for tidal polarizability parameter k_2^T for a generic unequal-mass binary:

$$k_2^T \equiv 2\left[q\left(\frac{X_A}{C_A}\right)^5 k_2^A + \frac{1}{q}\left(\frac{X_B}{C_B}\right)^5 k_2^B\right] \tag{1.97}$$

where A, B refer to primary and secondary stars in the binary system respectively; q is mass ratio given by

$$q \equiv \frac{M_B}{M_A} \leq 1, \qquad X_{A,B} \equiv \frac{M_{A,B}}{M_A + M_B} \tag{1.98}$$

$C_{A,B} \equiv M_{A,B}/R_{A,B}$ are compactnesses of two stars while $k_2^{A,B}$ are the $\mathrm{l} = 2$ dimensionless tidal Love numbers.

For a given NS mass, each EOS can be identified by two useful macroscopic characteristic quantities: R the stellar radius of an isolated non-rotating NS and Λ the dimensionless quadrupole tidal deformability [55]:

$$\Lambda \equiv \frac{2}{3} k_2 \left(\frac{R}{M}\right)^5 \tag{1.99}$$

where k_2 is the quadrupole Love number. Now, if two components have the same mass $M_A = M_B$, then $k_2^A = k_2^B = \bar{k}_2$, q=1 and $X_A = X_B = 1/2$ and expression (1.97) becomes

$$k_2^T \equiv \frac{1}{8} \bar{k}_2 \left(\frac{\bar{R}}{\bar{M}}\right)^5 \tag{1.100}$$

and using the expression (1.99), k_2^T is given by

$$k_2^T \equiv \frac{1}{8}\bar{k}_2\left(\frac{\bar{R}}{\bar{M}}\right)^5 = \frac{3}{16}\Lambda \tag{1.101}$$

In case of an equal-mass case, the $l = 2$ dimensionless tidal coupling constant k_2^T is related to tidal deformability by [9]

$$\lambda = \frac{16}{3}k_2^T M^5 \tag{1.102}$$

Rearraging the eq.(1.100)

$$k_2^T \equiv \frac{1}{8}\bar{k}_2\left(\frac{\bar{R}}{\bar{M}}\right)^5 \qquad \Longrightarrow \qquad \frac{16}{3}k_2^T \bar{M}^5 \equiv \frac{2}{3}\bar{k}_2\bar{R}^5$$

and comparing the right side with eq.(1.102), we obtain

$$\lambda \equiv \frac{2}{3}\bar{k}_2\bar{R}^5 \tag{1.103}$$

$$\Lambda \equiv \frac{\lambda}{\bar{M}^5} \tag{1.104}$$

which is another way of expressing the tidal Love number for equal-mass binaries.
At this point, the tidal deformability for equal-mass component is reduced to:

$$k_2^T \equiv \frac{1}{8}\bar{k}_2\left(\frac{\bar{R}}{\bar{M}}\right)^5 = \frac{3}{16}\Lambda = \frac{3}{16}\frac{\lambda}{\bar{M}^5} \tag{1.105}$$

Figure 1.19 report the relation between the mass-weighted frequencies at amplitude maximum f_{max} and the tidal deformability k_2^T given by:

$$\begin{aligned} \log_{10}\left[\left(\frac{f_{max}}{Hz}\right)\left(\frac{2\bar{M}}{M_\odot}\right)\right] &\approx a_0 + a_1(k_2^T)^{1/5} \\ \log_{10}\left(\frac{f_{max}}{Hz}\right) &\approx a_0 + a_1(k_2^T)^{1/5} - \log_{10}\left(\frac{2\bar{M}}{M_\odot}\right) \end{aligned} \tag{1.106}$$

where the coefficients are:

$$a_0 = 4.186, \qquad a_1 = -0.195. \tag{1.107}$$

In the Figure 1.19, the black dashed line refers to fit of eq.(1.106) with coefficient values given by 1.107 while the black solid line is the fit given by Eq.(24) of [9] where the

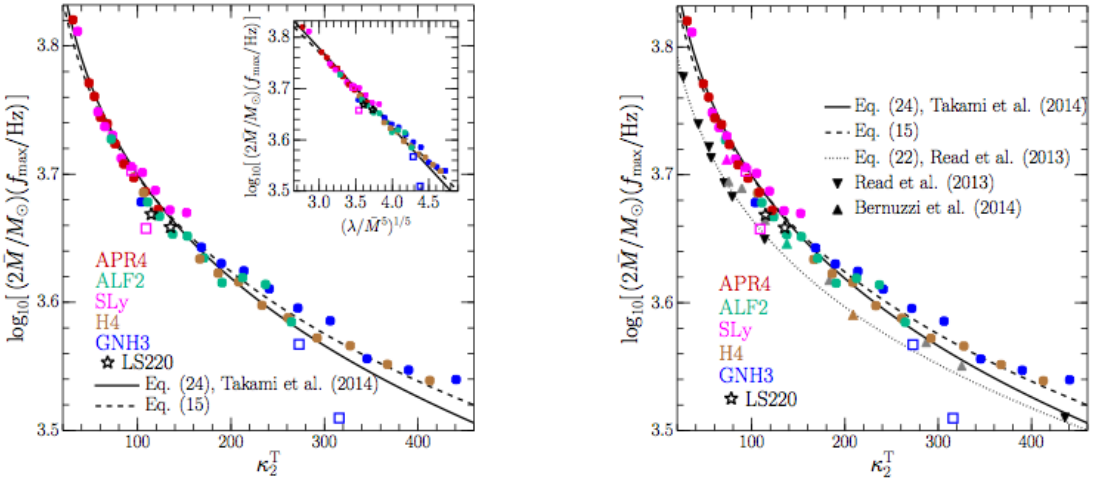

Figure 1.19: Both plots show the mass-weighted frequencies at amplitude maximum f_{max} in function of the dimensionless tidal deformability k_2^T. Filled colored circles refer to equal-mass binaries with different cold EOSs, the empty squares to the unequal-mass binaries, and the stars to the hot-EOS binaries. The black solid line is the fit given by Eq. (24) of [9] while the black dashed line is given by Eq.1.106 with updated coefficients. The inset highlights the linear dependence of f_{max} in terms of $(\lambda/\bar{M}^5)^5$[8].

coefficients have values equal to:

$$a_0 = 4.242, \qquad a_1 = -0.216. \tag{1.108}$$

The fit of the data shows a tight "universal" relation between frequency at peak amplitude and the tidal deformability. However, APR4 and GNH3 EoSs for unequal-mass (empty squares) binary systems with $q \approx 0.8$ do not follow the same behavior. The authors claim that, this could be due to small mass ratios because of dynamics and so GW emission is different for the same EoS and equal-mass systems. In these cases, the merger necessarily happens at lower frequencies as the tidal interaction is amplified and the lower-mass star is disrupted.

Another correlation comes from spectral analysis between low-frequency peak f_1 and stellar compactness of binary system $\mathcal{C} \equiv \bar{M}/\bar{R}$. The left panel of Figure 1.20, reports this relation and the solid black line represents the "universal" relation first reported in [9] and expressed as a cubic polynomial (cf., Eq. (25) of Ref. [9])

$$f_1 \approx b_0 + b_1\mathcal{C} + b_2\mathcal{C}^2 + b_3\mathcal{C}^3 \; kHz, \tag{1.109}$$

where the fitting coefficients are given by

$$b_0 = -22.07, \qquad b_1 = 466.62,$$
$$b_2 = -3131.63, \qquad b_3 = 7210.01. \tag{1.110}$$

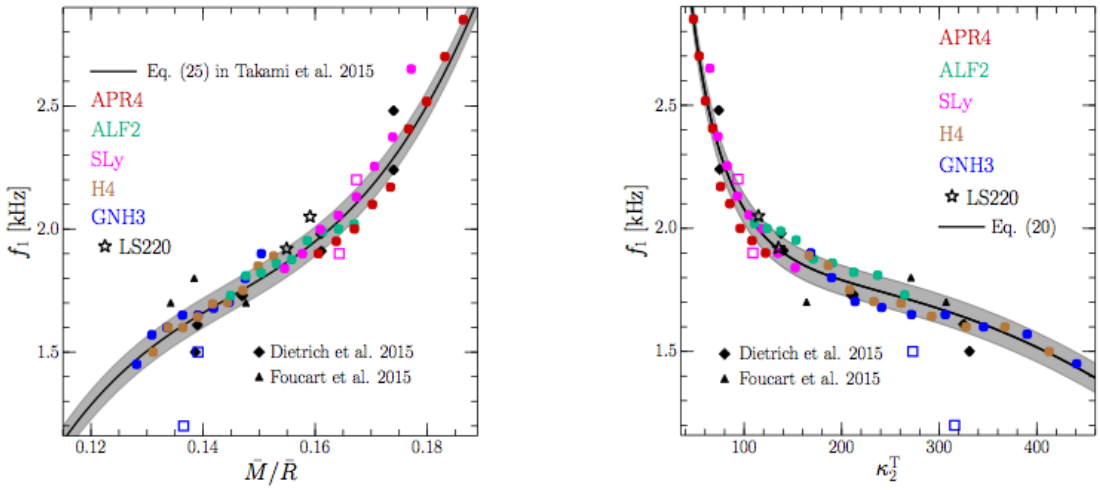

Figure 1.20: The symbol convention is the same to that in Figure 1.19. The left plot shows the dependence of f_1 from the average stellar compactness $\mathcal{C} = \bar{M}/\bar{R}$. The black diamond and triangles are results of [10] [11]. The left plot highlights the quasi-universal relation between f_1 and dimensionless tidal deformability k_2^T [8].

In the Figure 1.20, the symbols refer to a given mass and the frequencies grow with mass, i.e., for each EOS the smallest f_1 frequency corresponds to the smallest mass and the largest frequency to the largest mass. In the same Figure, black diamonds and triangles refer to f_1 peak of the data taken from Refs. [10] [11], respectively. These distance from fit and Takami *et al.* confer this behaviour to the fact that the values of f_1 do not distinguish from f_{spiral}. The right panel of Figure 1.20 reports another correlation between f_1 and tidal deformability where the data are fitted by third-order polynomial expansion of the dimensionless tidal deformability $(k_2^T)^{1/5}$:

$$f_1 \approx c_0 + c_1(k_2^T)^{1/5} + c_2(k_2^T)^{2/5} + c_3(k_2^T)^{3/5}\ kHz, \tag{1.111}$$

with

$$c_0 = 45.195, \qquad c_1 = -43.484,$$
$$c_2 = 14.653, \qquad c_3 = -1.6623. \tag{1.112}$$

Now, we consider the correlations of $f_{2,i}$ and f_2 frequencies with the stellar properties in Figure 1.21. As we saw previously, these frequencies correspond to the same fundamental l=m=2 mode of oscillation and $f_{2,i}$ is present during the transient phase while f_2 on longer timescale period. In the left panel, a fitting function is shown in terms of the dimensionless tidal deformability respectively

$$f_{2,i} \approx 6.401 - 1.299(k_2^T)^{1/5}\ kHz,$$
$$f_2 \approx 5.832 - 1.118(k_2^T)^{1/5}\ kHz, \tag{1.113}$$

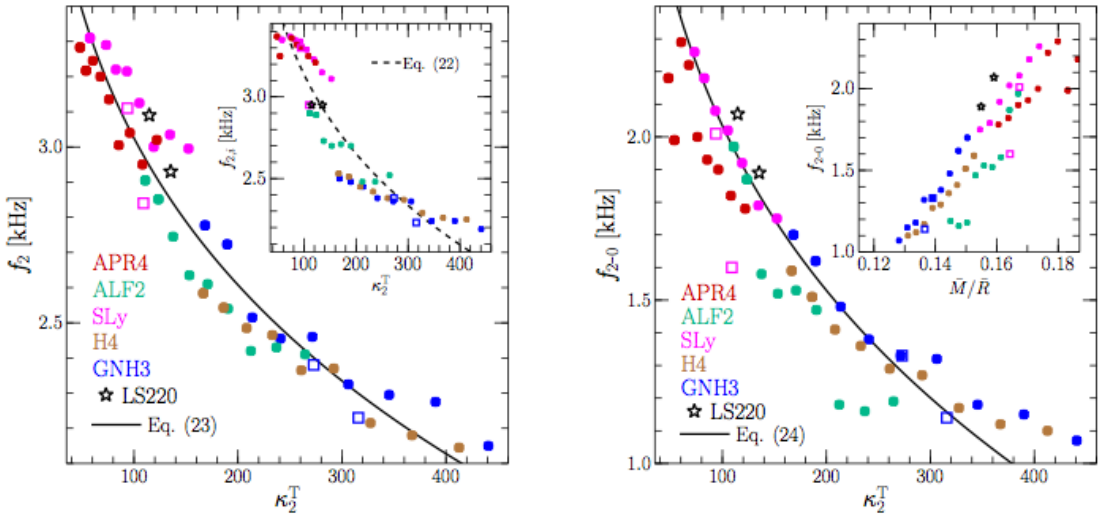

Figure 1.21: The same symbol convention of Figure 1.19 is used for both plot. In the right and the left plots, values of f_2 and f_{2-0} peak frequencies are reported as function of the dimensionless tidal deformability k_2^T. The black solid line in both cases refers to linear fit of Equation 1.113 and 1.114. The left inset shows $f_{2,i}$ frequencies as function of k_2^T while the right inset reports f_{2-0} frequencies as a function of the average compactness [8].

The right panel of Figure 1.21 shows the correlation between the f_{2-0} frequencies and the tidal deformability $(k_2^T)^{1/5}$, reporting a linear fit:

$$f_{2-0} \approx 5.424 - 1.350(k_2^T)^{1/5}\ kHz. \tag{1.114}$$

I want to remember, as discussed above, that f_{2-0} is given by the difference between the f_2, measured from PSDs, and $f_{m=0}$ that can be estimated from the analysis of the data of the simulations (e.g., via the oscillation frequencies of the central rest-mass density or of the lapse function).

Finally, in Figure 1.22 the quadratic two-dimensional fit in terms of the compactness and average gravitational mass of the binary for f_{spiral} is reported :

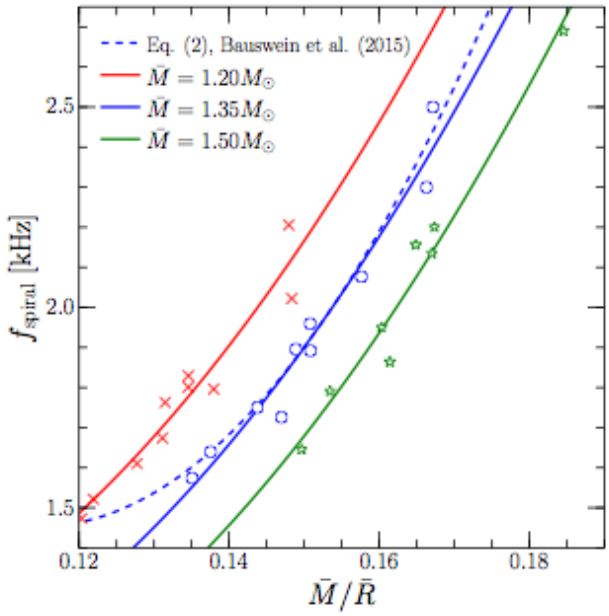

Figure 1.22: The different colors and their corresponding symbols refer to three binary systems $\bar{M} = 1.200, 1.350, 1.500\ M_\odot$. The three solid lines are two-dimensional quadratic fits of the data analyzed by Rezzolla and Takami [8] while the blue dashed line is the one given by Eq. (2) of [12].

$$f_{spiral} \approx d_0 + d_1\mathcal{C} + d_2\mathcal{C}^2 + d_3\bar{M} + d_4\bar{M}^2 + d_5\mathcal{C}\bar{M}\ kHz, \tag{1.115}$$

where

$$\begin{aligned} d_0 &= 3.28, & d_1 &= -8.68, & d_2 &= 174, \\ d_3 &= -2.34, & d_4 &= 0.99, & d_5 &= -13.0. \end{aligned} \tag{1.116}$$

The three solid lines in Figure 1.22 represent two dimensional fit of the data for binaries with $\bar{M} = 1.200, 1.350, 1.500 M_\odot$ while the blu dashed line refers to Eq. (2) in [12] for equal-mass binaries with $\bar{M} = 1.350 M_\odot$:

$$f_{spiral} \approx 6.16 - 82.1\mathcal{C}^2\ kHz \tag{1.117}$$

1.3.2 Electromagnetic emission: Gamma ray burst

Gamma-ray bursts are among the most fascinating events in the Universe, and the most luminous events in the sky. Their isotropic energy is of the order of $10^{51} - 10^{53}$ erg, emitted typically in few tens of seconds (see Figure 1.23). GRBs were discovered at the end of the 60s, by the American Vela spy satellites, devoted to monitoring the compliance of the Soviet Union (and other nuclear-capable countries) with the 1963 "Partial Test Ban Treaty". This discovery was kept secret by the American militaries until 1973.

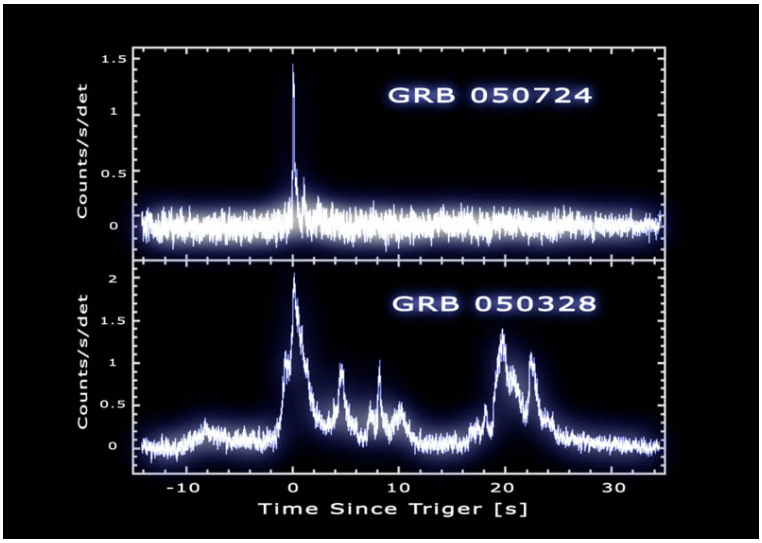

Figure 1.23: A short GRB (top) generates a single pulse of γ-rays, which often lasts for a small fraction of a second. Long GRBs (bottom) often generate several pulses, and can last for many seconds to several minutes.

The first systematic study on the nature of GRBs was performed thanks to the BATSE experiment, on-board the NASA *Compton Gamma−Ray Observatory* (CGRO). BATSE had an unprecedented sensitivity and a uniform response to all sky directions. It was particularly suited to perform systematic studies of GRBs with a good control of the angular coverage. BATSE showed that:

- GRBs are isotropically distributed (suggesting a cosmological origin);
- GRBs can be classified in *short* bursts (γ-ray duration $\lesssim$2 sec, Figure 1.23), and *long* bursts ($\gtrsim$2 s, Figure 1.23).

A real breakthrough, though, happened in February 1997, when the *Beppo*SAX satellite (Satellite per Astronomia X) detected a GRB 970228: when the X-ray camera

was pointed towards the direction of this burst, it detected a fading X-ray emission, the so-called GRB *afterglow*. Another major breakthrough occurred when the event GRB 970508 was detected. This event was localized within four hours of its discovery, allowing research teams to begin observations much sooner than any previous burst. Absorption lines were identified which allowed the identification of the GRB host galaxy and the measurement of its redshift: at a redshift of z$\approx$ 0.8, it represented the proof that GRBs are extragalactic events.

The mission that has given the highest contribution to GRB studies is *Swift*, which has been launched in 2004. Swift performs immediate ($\sim$ 60 s) X-ray and optical follow-up observations of GRBs detected with Burst Alert Telescope (BAT), on-board the same satellite. The trigger alerts are also immediately distributed for optical, near-infrared and radio observations with ground-based telescopes. Swift was designed mainly to study the early afterglow by filling the gap left by BeppoSax between the prompt emission, and the late afterglow.

Afterglow

The *afterglow* is a common feature in both short GRBs and long GRBs. It is typically observed as a slowly fading multi-wavelength emission, extending from X-rays down to optical and radio wavelengths. Typical X-ray afterglow light curves follow a "*steep-flat-steep*" behavior, with the emitted X-ray flux decreasing as a power law with time (Figure 1.24).

The most popular model for the GRB afterglow emission is the so-called *fireball* model. In this model, a huge release of γ-ray energy in a short timescale (tens of second) generates a relativistic expanding fireball, composed by e^+-e^- pairs, and photons. The non-thermal spectra of the GRB prompt and afterglow emissions suggest that synchrotron emission is the main radiation mechanism. The internal energy of the fireball is thought to be converted in energy of relativistic electrons (then that radiate via synchrotron emission), through *shocks*:

- *internal shocks*, between contiguous shells within fireball, generate the prompt radiation;
- an *external shocks*, generated when the fireball impacts the interstellar medium, generates the afterglow.

The radiation from a relativistic source is beamed within an angle of Γ^{-1} (where Γ

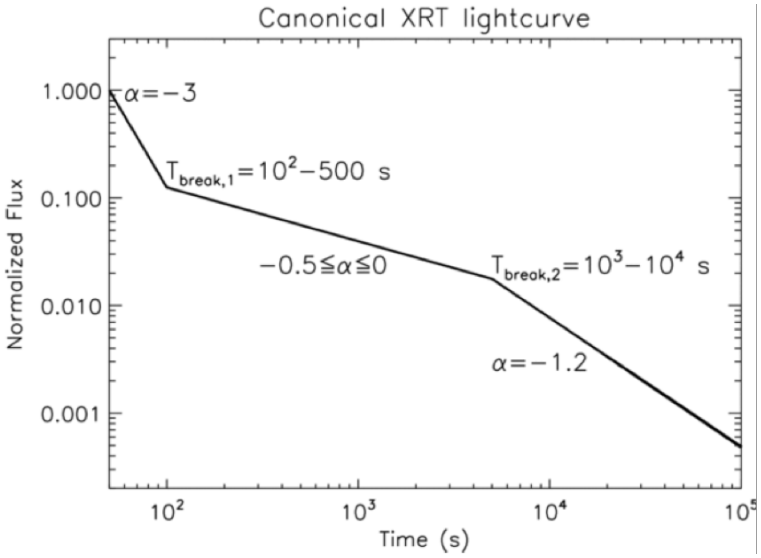

Figure 1.24: The X-ray flux from a GRB afterglow decreases with time as a power-law, t^{α}, with $\alpha \approx -3$ at short timescales, during the prompt-to-afterglow transition phase; $\alpha \approx 0$ during the plateau; and $\alpha \approx -1.2$ during the "normal" afterglow phase. In some cases, at later times, a jet break may be observed ($\alpha \approx -2$).

is the Lorentz factor of the source, which for GRBs is typically $\Gamma \approx 100$). Thus, a distant observer sees radiation only from a region within Γ^{-1} from its line of sight, and the observed photon energies are boosted into the γ-ray band. As the fireball impacts the inter-stellar medium and starts decelerating, Γ starts decreasing with time. The synchrotron radiation is expected to soften, and its peak frequency to decrease with time. Thus, while initially most of the radiation is emitted in the γ-ray range (GRB prompt emission), the peak of the emission progressively evolves into the X-rays, UV, optical, and radio bands (afterglow emission, Figure 3). A larger and larger fraction of the emitting region becomes observable, and when $\Gamma \approx \theta^{-1}$, where θ is the angular size of the GRB jet, a "jet break" is observed in the afterglow light curve.

Progenitors

Although there is no direct evidence about the nature of the central engine, it is nevertheless accepted that the real distinction between the two main categories of GRBs, long and short, is on their progenitors. *Long GRBs* are associated with the collapse of fast rotating stars, while *short GRBs* are widely thought to result from mergers of neutron star binaries or neutron star-black hole binaries Figure 1.26. In both scenarios, a stellar-mass black hole with an accretion disk is formed, and the emission of GWs is

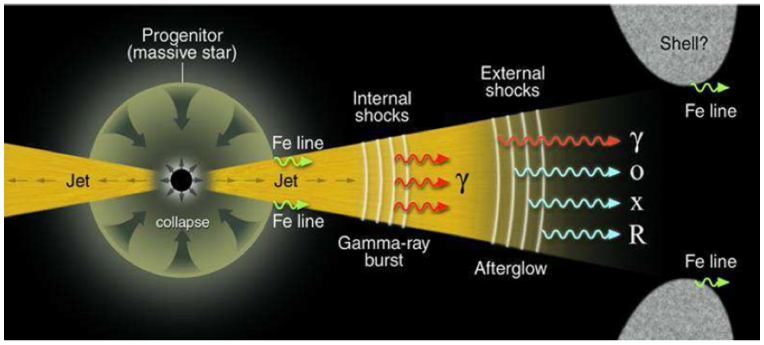

Figure 1.25: Fireball model

expected to accompany the GRB.

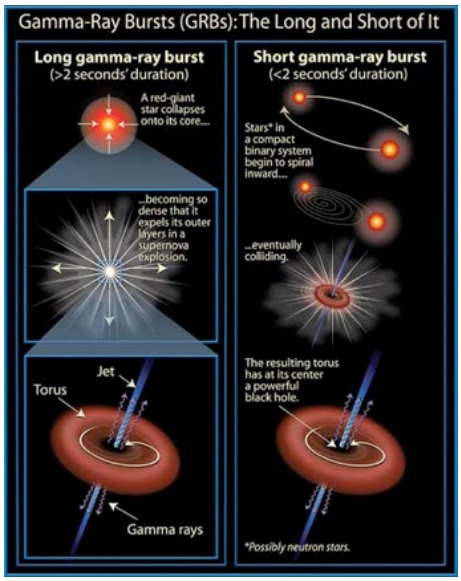

Figure 1.26: GRB progenitor scenarios

Collapsar

Collapsars, massive stellar collapses leading to a long GRB, require a high core rotation rate. The high rotation is required to form a centrifugally supported disk around a central, possibly spinning, black hole, to power a GRB jet. A high rotation rate may be conducive to the development of bar or fragmentation instabilities in the collapsing core or/and in the massive disk. The asymmetrically infalling matter also perturbs the black hole's geometry, which leads to ring-down gravitational radiation.

Binary coalescence

The candidates for short GRB are mergers of compact objects such as NS-BH or NS-NS binary systems. While the coalescence of BH-NS leads to a BH with a possible massive accretion disk, BNS merger can have different remnants as we seen in section 1.3.
A new scenario for SGRB, "time-reversal" scenario, is proposed by Ciolfi and Siegel [61]. The idea of time-reversal scenario is that the short GRB is generated by collapse of a supramassive NS and before it, around the NS is formed an optically thick environment consisting of a photon-pair nebula and an outer shell of baryon-loaded ejecta. If one side, the jet goes through this environment, on the other side, the spin-down radiation diffuses outward on much longer timescales and accumulates a time delay that allows to observe the SGRB before the long-lasting X-ray signal. The formation of SMNS as central engine supports the presence of long-lived central source which pumps energy on much longer timescales explaining the duration of X-ray afterglows and its long-lasting plateaus [62].

Chapter 2

The scenarios of advanced LIGO and Virgo detector sensitivity

Chapter 2 focuses on general properties of GW interferometric detectors, their spectral and directional sensitivity and on properties and advantages of networks of such detectors. We overview the operating principle of the detectors and their peculiarities, and provide a general description of the detectors of advanced generation which are operating (the twin detectors of the Laser Interferometer Gravitational Observatory, USA) or are close to operation (Virgo detector, Italy). The general features of the spectral sensitivity of the detectors are reviewed, with reference to different noise sources which limit the operating sensitivity of the detectors.
Following, we will see the benefits of a network of many detectors. It brings crucial advantages with respect to a single detector for transient GW searches: in fact, the network increases the capability to discriminate between GWs and noise, enables the reconstruction of the GW source sky position and allows a sensitivity to both GW polarizations.
In the last part, we will show the result of first observation run of Advanced LIGO detectors giving a general description of detected GW signals by binary BH merger, and the plan of future observations of the detector network.

2.1 Interferometric detectors

In the weak-field approximation of General Relativity, the space-time metric $g_{\mu\nu}$ can be described as [63][64][6]:

$$g_{\mu\nu} = \eta_{\mu\nu} + h_{\mu\nu}, \tag{2.1}$$

$\eta_{\mu\nu}$ is the Minkowski metric describing flat space and $h_{\mu\nu} << 1$ is the small perturbation to the metric due to the gravitational wave. The resulting theory is called *linearized theory*. In the transverse-traceless gauge (TT-gauge), this perturbation can be understood as a strain in space-time:

$$h_{\mu\nu}(z,t) = \begin{pmatrix} 0 & 0 & 0 & 0 \\ 0 & -h_+ & h_\times & 0 \\ 0 & h_\times & h_+ & 0 \\ 0 & 0 & 0 & 0 \end{pmatrix} \tag{2.2}$$

where h_+ and $h_\times$ are the only two physical degrees of freedom of the gravitational wave which correspond to the two possible polarization states *plus* and *cross*, respectively and the angle between the two polarization states is $\pi/4$.

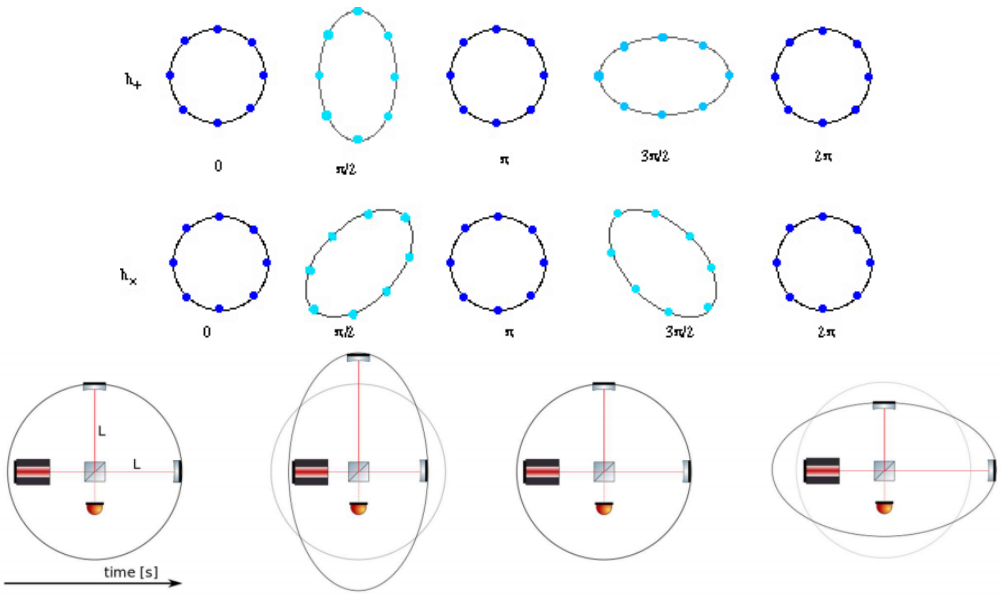

Figure 2.1: Effect on particle ring (top plot) and on gravitational wave interferometer after passage of a gravitational wave (bottom plot).

In Figure 2.1 it is illustrated the behavior of a gravitational wave, where we consider a ring of *free* particles in the (x, y) plane to $h_+, h_\times$ polarizations and along z-direction a gravitational wave impinging perpendicularly on a ring of particles. The effect of GW passage is that distance between particles is stretched and compressed causing a tidal deformation of the circular ring into an elliptical ring with the same area. Thus, the distance between them increases and decreases alternately of the same quantity according to the wave polarization:

$$\frac{\Delta L}{L} = \frac{1}{2}h_+, \tag{2.3}$$

this is the reason why a gravitational wave is said to cause a strain in space. The distance variation expected as a consequence of the gravitational wave passage can be evaluated in terms of the mass quadrupole moment Q[1]. The amplitude of gravitational wave h, can be written as [6]:

$$h_{jk}(t,d) = \frac{2G}{c^4 d}\left[\frac{d^2}{dt^2}Q_{jk}(t - r/c)\right], \tag{2.4}$$

d is the distance bettwen the source and observer, Q_{jk} is the reduced quadrupole moment related to the mass density of the source $\rho(x,t)$:

$$Q_{jk} = \int d^3x\rho(x,t)\left(x_j x_k - \frac{1}{3}r^2\delta_{jk}\right), \tag{2.5}$$

where δ_{jk} is the Kronecker delta-function. The quadrupole moment of a body of mass M and size R is approximately $Q \sim \epsilon MR^2$ and its second time derivative

$$\ddot{Q} \sim \epsilon\frac{MR^2}{T^2}, \tag{2.6}$$

where ϵ is a measure of the asymmetry of the mass distribution and T the typical timescale of the system. Thus, inserting the latter equation in eq.(2.4), replace $v = R/T$ as the source's internal velocity and rearranging the equation, we have

$$h = \frac{G\ddot{Q}}{c^4 d} \approx \epsilon\frac{G}{c^2}\frac{M}{d}\left(\frac{v}{c}\right)^2. \tag{2.7}$$

Being $G/c^2 = 7.4 \times 10^{-28}$ m/kg a small factor, only astrophysical sources such as compact binaries (containing white dwarfs, neutron stars, and black holes), neutron stars and collapsing stellar cores, can generate gravitational radiation strong enough to be detectable on Earth. For a mass $M \sim M_\odot$, $d = 15$ Mpc, the expected GW amplitude is:

$$h \approx 10^{-21}. \tag{2.8}$$

[1]We have not contribution from the monopole and dipole terms: the monopole term is due to the energy-mass of the system which is preserved while the dipole source is related to the center of mass of the system, which does not change its state of motion for the momentum conservation if the system is isolated. So the first terms contributing to the GW amplitude is the quadrupole is that of quadrupole term.

An interferometric gravitational-wave detector acts as a transducer to convert the space-time perturbations into a measurable signal. GW interferometers are modified Michelson laser interferometer with two orthogonal arms whose mirrors serve as gravitational test masses. A beam splitter mirror divides the incident laser beam into two equal components sent into the two arms of the interferometer. Fabry-P*é*rot resonant cavity, formed by two mirrors acting as *free falling* test masses, is present in each arm in order to increase the optical length and therefore amplifies the tiny distance variation caused by GW passage. The two beams are reflected by mirrors located at the end of the arms and recombined on the beam splitter where the two laser beams interfere. A part of recombined beam is sent to a photodetector where its intensity is measured. If a GW is passed, length of the two arms is changed and, therefore, the optical path length also. This produces a very small phase shift between the beams and, thus, a variation of the luminous intensity, which is proportional to the wave's amplitude.
Defining the differential displacement as $\Delta L = \delta L_x - \delta L_y$ where $L_x = L_y = L$ the lengths of two orthogonal interferometer arms, the interferometer displacement, as discussed above, is given by $\Delta L = hL$ where h is linear combination of $h_+, h_\times$ (see eq.(2.56)) and it is the gravitational wave strain amplitude projected onto the detector. For example, an interferometer with arm length of 3 km responds to a gravitational wave amplitude of $h \sim 10^{-21}$ with a distance shift of

$$\Delta L \sim hL \sim 3 \times 10^{-18}\ m. \tag{2.9}$$

Actually a network formed by three ground based detectors exists. The Laser Interferometer Gravitational Observatory (LIGO)[65] consists of two detectors, one located in Hanford (H1, Washington State) and the second in Livingston (L1, Louisiana State) both characterized by arm lengths of 4 km. The Virgo (V1) [66] interferometer is located in Cascina, near Pisa, and its arms are 3 km long.
Others interferometers with shorter arms have been built in Germany and Japan, GEO600 [67] and TAMA, respectively, 600 m and 300 m arm long. More km-scale detectors are planned for the medium-long term: in Japan, KAGRA [68] (formerly the Large-Scale Cryogenic Gravitational-wave Telescope, or LCGT [69] [70]), will be the first km scale laser interferometer GW detector, whose mirrors will be operated at cryogenic temperature (20 K), and India, LIGO-India [71].
In the past years LIGO, GEO and Virgo have performed joint data acquisitions but no gravitational waves have been detected. Successively, a upgraded [72] of first generation detector has been made with the aim of improving the initial detectors sensitivity by a

factor of 10, which means increasing the observed volume of 1000 times. This upgrade phase has given rise to the second generation of gravitational wave detectors [73], Advanced LIGO (aLIGO) [74] and Advanced Virgo (AdV) [75], which started to open up gravitational-wave astronomy with the direct observation of gravitational waves from merger of binary black hole system (see section 2.4).
The Einstein Telescope (ET) [76] is a third generation GW detector for which the construction of a new research infrastructure is being proposed in Europe. The goal is to mprove one order of magnitude the sensitivity of Advanced LIGO, Advanced Virgo and KAGRA [77]. There are many technological challenges to be faced to make this a reality. To do this, an underground infrastructure will host three nested laser interferometers with 10 km arm length forming an equilateral triangle and potentially a xylophone configuration (two independent detectors covering different frequency ranges) [73].

2.1.1 Principle of detection

In this section we give the general idea of operating principle of a gravitational wave interfeormeter. A simple Michelson interferometer is shown in fig.(2.2): the two mirrors, considered in free falling condition, are the two test masses and are located at distance l_1 and l_2 from the beam splitter which separates the light beam in two equal beams which propagate back and forth through the arms. The difference in the optical path length between the two arms causes a phase shift in the recombined beam on photodetector. In the right plot of fig.(2.2) we report the formalism adopted to treat the principles of the operation of detector interferometer.

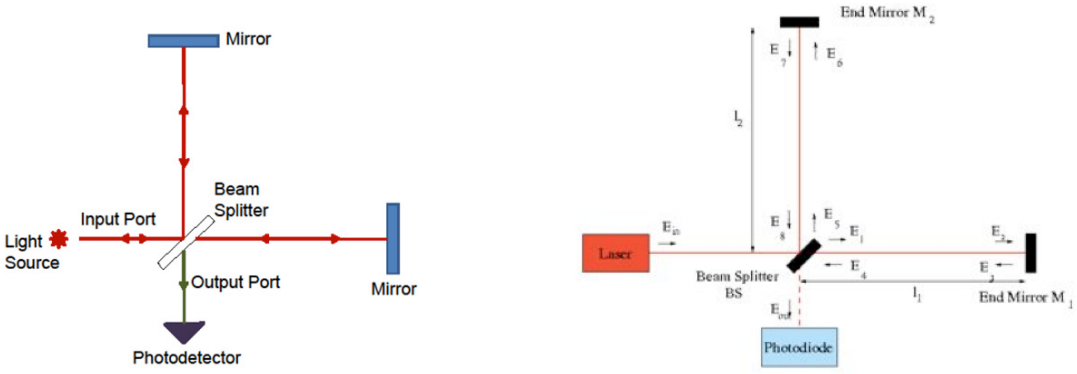

Figure 2.2: Michelson interferometer layout [13].

We define with E_{in} e E_{out} the electromagnetic field at the input and output of the Michelson interferometer:

$$E_{in} = E_0 e^{i(\overrightarrow{k}_L \cdot \overrightarrow{r} - \omega_L t + \phi_L)} \tag{2.10}$$

where E_0 is the wave amplitude of laser beam, ω_L is tthe laser pulsation, ϕ_L initial phase and $k_L = 2\pi/\lambda_L$ is the wave vector with λ_L the beam wavelength.
The electromagnetic fields inside the two arms are:

$$\begin{aligned} E_1 &= t_{BS} E_{in} & E_5 &= i r_{BS} E_{in}, \\ E_2 &= e^{-ikl_1} E_1 & E_6 &= e^{-ikl_2} E_5, \\ E_3 &= i r_1 E_1 & E_7 &= i r_2 E_6, \\ E_4 &= e^{-ikl_1} E_3 & E_8 &= e^{-ikl_2} E_7, \end{aligned} \tag{2.11}$$

t_{SB}, r_{SB} refer to transmission and reflection coefficients of the beam splitter while , r_1, r_2 are the reflection coefficients of mirrors.
The output signal and output power on photodetector are [78][79]:

$$E_{out} = i r_{BS} E_4 + t_{BS} E_8 \qquad\qquad P_{out} = |E_{out}|^2. \tag{2.12}$$

Replacing the relations of E_4 and E_8:

$$E_4 = i r_1 t_{BS} E_{in} e^{-ikl_1} \qquad\qquad E_8 = -r_2 r_{BS} E_{in} e^{-ikl_2}, \tag{2.13}$$

we have that output signal is given by:

$$E_{out} = i r_{BS} E_4 + t_{BS} E_8 = t_{BS} r_{BS} E_{in} (-r_1 e^{-ikl_1} - r_2 e^{-ikl_2}), \tag{2.14}$$

and output power given by

$$\begin{aligned} P_{out} &= |E_{out}|^2 = t_{BS}^2 r_{BS}^2 E_{in}^2 \left[(r_1^2 + r_2^2) + 2 r_1 r_2 \cos(2k \cdot \Delta l) \right] \\ &= P_{in} t_{BS}^2 r_{BS}^2 (r_1^2 + r_2^2) \left[1 + \frac{2 r_1 r_2}{r_1^2 + r_2^2} \cos(2k \cdot \Delta l) \right] \\ &= P_{in} t_{BS}^2 r_{BS}^2 (r_1^2 + r_2^2) \left[1 + C \cos(2k \cdot \Delta l) \right], \end{aligned} \tag{2.15}$$

where $\Delta l = l_1 - l_2$ is the difference between arms lengths. We observe that the output

power depends on a variation of arm lengths. The quantity:

$$C = \frac{2r_1 r_2}{r_1^2 + r_2^2},$$

is the *contrast* of the interference pattern at the output of the interferometer. It is a marker of impurities of optical surfaces, indeed it depends on reflection coefficients of mirrors. The power of the output signal can be written as:

$$P_{out} = P_{in} r_{BS}^2 t_{BS}^2 (r_1 + r_2)^2 (1 + C \cos \Delta\phi_L), \tag{2.16}$$

with

$$\Delta\phi_L = 2k_L \Delta l = 2\frac{2\pi}{\lambda_L}\Delta l, \tag{2.17}$$

which is the phase shift of two light beams recombined on beam splitter due to different optical path length in the two arms Δl, and λ_L is wave length of laser beam.
The suitable interferometer working point is the destructive interference (*dark fringe* condition), where the signal to noise ratio is maximized:

$$2k_L \Delta l = (2n+1)\pi \qquad n \in \mathbb{N}. \tag{2.18}$$

Thus, an ideal interferometer is characterized by mirrors with same reflection coefficients $r_1 = r_2 = r$ and completely reflected $r \sim 1$ (without loss of light) and the beam splitter mirror transmits and reflects the same amount of light this means $r_{BS} = t_{BS} = \sqrt{2}/2$. In these conditions, a good interferometer is characterized by value of C near to unit.

Let us study the effect of a gravitational wave impinging on the Michelson interferometer and how the strength of gravitational wave is related to path variation of the two light beams. Consider a plane monochromatic wave $h_{\mu\nu}(z,t)$, $h(z,t) = h_+(z,t)$ with frequency ν which propagates along z axis, perpendicularly to the interferometer plane whose arms are oriented along x and y axes with lengths l_1 and l_2

$$h_{\mu\nu}(z,t) = h_+ e^{i\omega t} = h_0 e^{i\omega t}. \tag{2.19}$$

Its passage generates a variation of arm lengths and the two beams recombine on the beam splitter with a time shift $\Delta\tau$

$$\Delta\tau = \Delta\tau_x - \Delta\tau_y, \tag{2.20}$$

where $\Delta\tau_x$, $\Delta\tau_y$ are the light travel time for the x, y arms. This time shift is related to the optical path difference Δl_{tot}

$$\Delta l_{tot} = \frac{1}{2} c \Delta\tau, \tag{2.21}$$

and Δl_{tot} is given by

$$\Delta l_{tot} = \Delta l + \Delta l_{gw}, \tag{2.22}$$

where $\Delta l = l_1 - l_2$ and Δl_{gw} length variation due to gravitational wave passage. Thus, the phase shift is given by:

$$\Delta\phi_L = 2\frac{2\pi}{\lambda_L}\Delta l_{tot} = \frac{2\pi c}{\lambda_L}\Delta\tau. \tag{2.23}$$

In order to see how a gravitational wave detector works, we can recall the Special Theory of Relativity considering a ray of light which connects a sets of points separated by $ds^2 = 0$. First of all, considering two neighboring space-time events linked by light beam, their interval is given by [79]:

$$ds^2 = 0 = g_{\mu\nu}dx^\mu dx^\nu = [\eta_{\mu\nu} + h_{\mu\nu}(t)]dx^\mu dx^\nu = -c^2dt^2 + [1 + h(z,t)]dx^2. \tag{2.24}$$

The time shift between the two arms is [80]:

$$\Delta\tau = \Delta\tau_x - \Delta\tau_y = \frac{2}{c}(l_1 - l_2) + \frac{1}{2}\frac{h_0}{i\omega}e^{i\omega t_0}(e^{i\omega\frac{2l_1}{c}} + e^{i\omega\frac{2l_2}{c}} - 2), \tag{2.25}$$

assuming that the two arms have the same length $l_1 = l_2 = l_0$

$$\Delta\tau = \frac{h_0}{i\omega}e^{i\omega t_0}(e^{i\omega\frac{2i\omega l_0}{c}} - 1) = h_0\tau_0 e^{i\omega t_0}\frac{\sin(\frac{\omega l_0}{c})}{\frac{\omega l_0}{c}}, \tag{2.26}$$

where $\tau_0 = 2l_0/c$. Thus, from eq.2.23 the phase of the output beam is:

$$\Delta\phi_L = \frac{2\pi}{\lambda_L}h_0\tau_0 e^{i\omega t_0}\frac{\sin(\omega l_0/c)}{\omega l_0/c}. \tag{2.27}$$

Putting the latter in equation (2.16), we have linked the detector output power with the gravitational signal. The order of magnitude of the detectable frequency at which the interferometer could be sensitive, can be estimated using the expression which link the frequency with the interferometer arm length

$$\nu_{cut} = \frac{2\pi c}{l_0} \tag{2.28}$$

So, if we want to detect a gravitation signal by pulsar which occurs at $\sim$ 100Hz , we need an interferometer with 3000 km long arm. This is clearly not technically possible to be built on Earth. Thus, to face this, Fabry-Pérot optical resonant cavities are mounted in the interferometer arms. A Fabry-Pérot cavity consists of by two mirrors. Use of these cavities allows to amplify the optical path of the light inside the interferometer, without modifying the arm length.

2.2 Main noise sources of an interferometer detector

The sensitivity of a gravitational wave detector is characterized by the *power spectral density* (PSD) of its noise contributions. The power spectrum density is defined as the Forier transform of auto-correltaion (Wiener-Khinchin theorem)[79]:

$$P_s(f) \equiv \frac{1}{\sqrt{2\pi}} \int_{-\infty}^{\infty} R(\tau) e^{-i2\pi f\tau} d\tau, \tag{2.29}$$

where $R(\tau)$ is the auto-correlation of time series.

The output signal $s(t)$ of the interferometer is given by two components:

$$s(t) = h(t) + n(t), \tag{2.30}$$

$n(t)$ noise of detectors and $h(t)$ GW signal. In the absence of any gravitational wave signal, the detector output is just an instance of noise n(t), $s(t) = n(t)$. We assume the noise to be stationary. This assumption is not completely valid in the case of real gravitational wave detectors; however, if the time scales of operation mode are not much larger than typical observation time scales, stationarity could be used as a working rule [15]. The auto-correlation function of the noise is [6]:

$$R(\tau) \equiv \langle n(t) n(t+\tau) \rangle, \tag{2.31}$$

where the average is over possible realizations of the system [2]. If the detector output is a stationary noise process, i.e., its performance is independent of time, then auto-correlation R depend only by τ.

A Gaussian stochastic process $n(t)$ is characterized by average value $\langle n(t) \rangle$ that, in case

[2] In our case, a time average on time interval T.

of a stationary noise, is a constant and can be set to zero with a constant shift of $n(t)$ [6]. In general, if we have a knowledge of behaviour of the noise at time t, this allow us a little information of the noise at time $t+\tau$ with shift time τ large enough, so that for $|\tau| \to \infty$, $R(\tau)$ tends to zero rather fast. In case of white noise for which the noise at time t and following time $t+\tau$ are uncorrelated, so far $\tau \neq 0$, we have $\langle n(t)n(t+\tau)\rangle = \langle n(t)\rangle\langle n(t+\tau)\rangle = 0$ and $R(\tau) \sim \delta(\tau)$ [6]. Thus, the auto-correlation function goes to zero for very fast for $\tau \to \pm\infty$ and this is required in order to perform a Fourier transform.

The function $S_n(f)$ is known as *noise spectral density* (or the noise spectral sensitivity, or the noise power spectrum). Considering positive frequencies $f > 0$, we define *single-side or one sided noise spectral density* $S_n(f)$:

$$\frac{1}{2}S_n(f) \equiv \int_{-\infty}^{\infty} R(\tau)e^{i2\pi f\tau}d\tau. \tag{2.32}$$

where the factor $1/2$ is by convention. $R(\tau)$ is real, this implies

$$S_n(-f) = S_n^*(f),$$

and the invariance for time translation $R(-\tau) = \langle n(t)n(t-\tau)\rangle = \langle n(t)n(t+\tau)\rangle = R(\tau)$ implies:

$$S_n(-f) = S_n(f).$$

Inverting the equation (2.32), we have that the auto-correlation function $R(\tau)$

$$R(\tau) \equiv \langle n(t)n(t+\tau)\rangle = \frac{1}{2}\int_{-\infty}^{\infty} S_n(f)e^{-i2\pi f\tau}df, \tag{2.33}$$

and for $\tau = 0$

$$R(0) \equiv \langle n^2(t)\rangle = \frac{1}{2}\int_{-\infty}^{\infty} S_n(f)df = \frac{1}{2}\int_{0}^{\infty} S_n(f)df. \tag{2.34}$$

The Fourier transform of $n(t)$ is

$$\widetilde{n}(f) \equiv \int_{-\infty}^{\infty} n(t)e^{-i2\pi ft}dt, \tag{2.35}$$

and using this in equation (2.31) and putting the result in equation (2.32), for a stationary noise process we have :

$$\langle \widetilde{n}(f)\widetilde{n}^*(f')\rangle = \frac{1}{2}S_n(f)\delta(f-f'). \tag{2.36}$$

The latter explain the name PSD given to $S_n(f)$ and the two equations (2.36) and (2.32) are equivalent definitions of $S_n(f)$ in case $\widetilde{n}(f)$ exist.
If $R(\tau) \sim \delta(\tau)$, the equation (2.32) gives $S_n(f)$ as frequency independent and we have white noise. Otherwise, $S_n(f)$ depending on frequency and we have colored noise and an example could be a noise which goes as $1/f$ and PSD has a power-law behavior $S_n(f) \sim 1/f^{\gamma}$ [6].
The amplitude spectral density or the noise amplitude is defined simply as the square root of the power spectrum $\sqrt{S_n(f)}$ and its dimension is $\mathrm{Hz}^{-1/2}$.

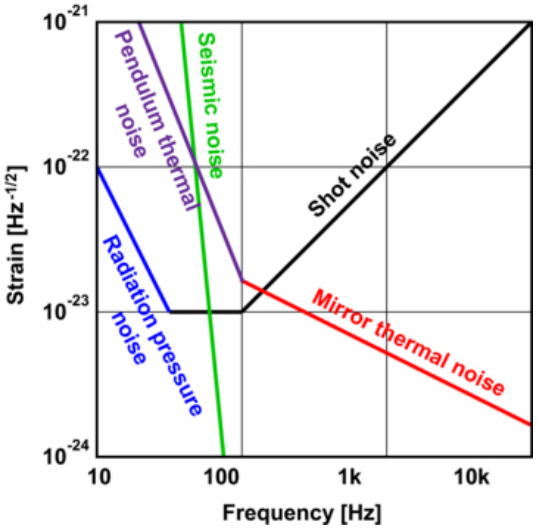

Figure 2.3: Strain sensitivity of a standard interferometer with contributions of major noise sources and corresponding frequencies at which they arise [14].

The tiny displacements induced by astrophysical events ($\Delta L \sim 10^{-18}$ m), demand a high sensitivity of interferometers, which means reducing all possible environmental disturbances. The sensitivity of ground-based interferometers is limited from different noise sources. The position of the test masses can fluctuate due to local perturbations, such as *seismic noise* and other ground-born mechanical noise, *thermal noise* associated with the test masses and their suspensions. Other noise sources affect the detected signal without a real mirror displacement and are due to the quantum nature of light: *quantum noise* which appears at high frequency as *shot noise* in the photocurrent from the photodiode while at low frequencies it manifests as *radiation pressure noise* due to momentum transfer to the test masses from the photons when using high laser powers

[73]. Each of these source will be briefly described below and more details about these topics are discussed in [79][14][73][81] and references therein. Since the of interferometer to displacement, or equivalently gravitational wave strain, is frequency dependent, it is necessary to represent the limiting detector noises as functions of frequency normalized by the interferometer response [82].

Seismic noise

The seismic noise is due to the movements of the Earth's crust driven by wind, ocean waves and human activity. The displacement due to seismic noise is give by

$$\widetilde{x}_{seismic}(f) \sim 10^{-7}\frac{1}{f^2} \;\; m/\sqrt{Hz}, \tag{2.37}$$

and corresponds to spectral density (in therms of strain, assuming an arm length of 3 km)

$$\widetilde{h}_{seismic}(f) \sim 10^{-10}\frac{1}{f^2} \;\; 1/\sqrt{Hz}. \tag{2.38}$$

The seismic noise arises at low frequencies $<$ 10 Hz, at frequencies around 0.2 Hz the seismic spectrum is dominated by the microseismic peak due to ocean waves impinging onto the continental plates [83].
The seismic noise is reduced by suspending the test masses of the interferometer with multiple stage seismic isolation systems made of a pendulum/spring. For a simple pendulum, transfer function of the motion of the pendulum decreases as $1/(\mathrm{f})^2$ above the resonant frequency of the system, the effective way of minimized the seismic noise contribution is to employ more pendulums with lower resonant frequencies [73].
Let us consider a mass, m, attached to a spring of stiffness, k with dissipation coefficient, b. The transfer function between the ground motion, x_g and the motion of the mass, x_m is [83][78]

$$H(\omega) = \frac{x_m(\omega)}{x_g(\omega)} = \frac{\omega_0^2}{\sqrt{(\omega_0^2-\omega^2)^2+\omega^2\gamma^2}} \tag{2.39}$$

where $\omega_0 = \sqrt{k/m}$ is the resonant angular frequency and $\gamma = (b/m)$ is the damping constant. The ground motion and mass motion are identical at low frequencies ($\omega \ll \omega_0$), thus transfer function becomes unity $H(\omega) \sim 1$ and the the mass and ground move together. At high frequencies $\omega \gg \omega_0$, the vibrations of the test mass are attenuated by a factor $H(\omega) \sim \omega_0^2/\omega^2$ (in the limit of low damping). This is an effective strategy

to make an isolation above a few hertz. The seismic isolation system of advanced Virgo (AdV) [84] comprises multiple ($\simeq 7$) stacks of low frequency ($\simeq 0.1$Hz) vertical isolators, and a combination of an inverted pendulum and pendulum stages for horizontal isolation. The advanced LIGO (aLIGO) [85], adopts a variety of active and passive isolation stages [83][73].

Thermal noise

Thermal noise is produced by microscopic fluctuations of particles forming every physical system in thermodynamical equilibrium. At steady-state temperature T, the energy equipartition theorem assigns to each degree of freedom a mean energy of $k_BT/2$ where k_B is the Boltzmann constant. Because of the interactions between the microscopic elements, this energy is subjected to fluctuations that produce random oscillations of macroscopic observables. This phenomenon is called thermal noise and is described by the *Fluctuation-Dissipation theorem* which represents a link between a generic dissipative mechanism and thermal fluctuations [86][87]. In particular, in an interferometer, it induces uncertainty in the position and displacement of mirrors. Let us consider a linear system in thermodinamic equilibrium T. If it is subjected to external force $F_{ext}(f)$, il will move with a velocity $v(f)$ and its equation of motion is:

$$F_{ext}(f) = Zv(f), \tag{2.40}$$

where the function $Z(f)$ is the impedance. The theorem derived by H. B. Callen et al. [86] states that the power spectrum of $F^2_{thermal}(f)$ of the minimal fluctuating force acting on the system is given by [79]:

$$F^2_{thermal}(f) = 4k_BT\Re(Z(f)), \tag{2.41}$$

where $\Re(Z)$ is the real (i.e. dissipative) part of the impedance. This theorem gives an estimation of thermal noise component without a knowledge of nature of microspic processes which generate the dissipation.
The thermal noise affects different component of interferometer: the mirror, making up a bulk substrate and layers of optical coating material, and the suspension structures as wires/fibers. There is a host of thermal noises [77]: *Brownian noise* manifests as thermally-excited body modes in the mirror and pendulum modes in the suspension fibers; *thermoelastic noise* causes the motion and displacement of the mirror due to temperature fluctuations which, causes fluctuations of the mirror refractive index. Thus,

the choice of material for mirror and suspension fiber is important for suppression of the ramaining thermal noises.

Quantum noise

Quantum noise plays a very special role in gravitational wave interferometers. First of all, quantum noise is fundamental limiting noise in most of the the detection frequency band of interferometers. Secondly, the quantum noise is due to quantum nature of photons. Two different noise mechanisms contribute to quantum noise [83]:

- ***Photon shot noise***

  As we discussed before, a gravitational interferometer works in dark fringe, this means that the two light beams, coming from two orthogonal arms, recombine in destructive way at the beam splitter. Therefore, in normal operation and in absence of any strong gravitational waves or external disturbance acting on the mirrors, there will be no light at the output port and on the photodiode. Otherwise, light is present at the output of the interferometer due to a change of differential arm length of the Michelson interferometer. Due to the fact that the number of photons of laser beam arriving at a photodetector over any period of time is statistically uncertain, its detection on the photodiode generate the so called *shot noise* which can be modeled using a Poisson distribution.
  Let be N the number of photon. If $N >> 1$, the Poisson distribution can be approximate by Gaussian distribution with a standard deviation $\sigma = \sqrt{N}$. Each photon has an energy of $\hbar\omega = 2\pi\hbar c/\lambda$. If P_{out} is the power at the output of the interferometer then the number of photon at the output will be:

  $$\bar{n} = \frac{\lambda}{2\pi\hbar c} P_{out}, \tag{2.42}$$

  with λ the wavelength of laser.

  If the laser power at the output P_{out} is half of input power P_{in}, then the mean power of photons is given by [79]:

  $$N = \frac{\lambda}{2\pi\hbar c} \frac{P_{in}}{2} \tau, \tag{2.43}$$

  where τ is the measurement interval. Since, we are using the output power to monitor the position of the test mass/mirror, it is natural to consider the statistical

power fluctuation as fluctuations on the differences of the test masses position given by

$$\sigma_{\delta L} = \frac{\sigma_N}{N} / \frac{1}{P_{out}} \frac{dP_{out}}{dL} = \sqrt{\frac{\hbar c \lambda}{4\pi P_{in} \tau}}, \tag{2.44}$$

where the numerator of this fraction is the fractional photon number while the denominator is the fractional output power change per unit position difference. Considering $dP_{out}/dL = (2\pi/\lambda)P_{in}$, the change in mirror position difference is $\delta L = Lh$, so we can interpret the brightness fluctuations as gravitational wave noise

$$\sigma_h = \frac{\sigma_{\delta L}}{L} = \frac{1}{L}\sqrt{\frac{\hbar c \lambda}{4\pi P_{in} \tau}}. \tag{2.45}$$

Thus the spectral density for a two-side spectrum is independent of frequency:

$$h_{shot}(f) = \frac{1}{L}\sqrt{\frac{\hbar c \lambda}{2\pi P_{in}}}. \tag{2.46}$$

The photon shot noise in h is described by white amplitude spectral density. Therefore, the shot noise can be reduced improving $L\sqrt{P_{in}}$ and its amplitude order is:

$$\tilde{h}_{shot}(f) \simeq 10^{-23} \frac{1}{\sqrt{Hz}} \tag{2.47}$$

- ***Quantum radiation pressure noise***

When the laser beam hints a mirror, the photons transfer momentum onto the mirror, this means that the light beam acts as radiation pressure force on the test mass. The fluctuation of the number of photons induces fluctuations in the radiation pressure force. This *quantum radiation pressure noise* can be considered as a form of back-action noise. The laser beam generates a force when it impinges on mirror and after is reflected by this. This force is proportional to power of laser $F_{rad} = P/c$. This noisy force is applied to each mirror in the arm producing a fluctuation of test mass and it is due to shot noise fluctuation in the power P. In terms of an amplitude spectral density is:

$$F(f) = \sqrt{\frac{2\pi\hbar P_{in}}{c\lambda}}, \tag{2.48}$$

independent of frequency. The power fluctuations in the two arms is anti-correleted [79], thus the radiation pressure noise is given by

$$h_{rp}(f) = \frac{2}{L}x(f) = \frac{1}{mf^2L}\sqrt{\frac{\hbar P_{in}}{2\pi^3 c\lambda}}, \tag{2.49}$$

where the function

$$x(f) = \frac{1}{m(2\pi f)^2}F(f) = \frac{1}{mf^2}\sqrt{\frac{\hbar P_{in}}{8\pi^3 c\lambda}} \tag{2.50}$$

is the displacement of each mass m due to the fluctuating radiation pressure with power $P_{in}/2$.

We have seen that there are two sources of noise associated to quantum nature of the light: shot noise which decreases with the power laser and radiation pressure noise, indeed, grows with the power. At the output of the interferometer we have the so called optical readout noise, given by the quadrature sum:

$$h_{o.r.o.}(f) = \sqrt{h^2_{shot}(f) + h^2_{rp}(f)}. \tag{2.51}$$

Because of the radiation pressure term is proportional to $h_{rp} \propto 1/f^2$, it is dominant at low frequencies, while the shot noise is independent of the frequencies ("white noise") and dominates at high frequencies [79]. So, we could improve the sensitivity at high frequency increasing the power in input into the two arms but this means increases the contribution of radiation pressure noise at low frequencies. However, for a particular frequency of operation f_0, a minimum noise spectral density exists when the power P_{in} is chosen to have an optimal value P_{opt} in order that $h_{shot}(f_0) = h_{rp}(f_0)$ and the two sources of optical noise are minimized. However, for a particular frequency of operation f_0, there will be an optimal chosen power P_{in}

$$P_{opt} = \pi c\lambda m f^2. \tag{2.52}$$

Putting P_{opt} expression in equation of $h_{o.r.o.}$, we have:

$$h_{QL}(f) = \frac{1}{\pi fL}\sqrt{\frac{\hbar}{m}}. \tag{2.53}$$

This sensitivity limit is known as the *Standard Quantum Limit* (SQL) and is due to the Heisenberg Uncertainty Principle, in its position and momentum formulation It

is possible to reduce the noise at a tuned range of frequencies, when dominated by either radiation-pressure noise or shot noise, by altering the noise distribution in the two quadratures of the vacuum field. This effect can be achieved "by squeezing the vacuum field" [73].

2.3 Response of a ground based interferometer

The gravitational wave strain of interferometer is given by eq. 2.3

$$h(t) = \frac{\delta L}{L},$$

where δL is the variation of the arm length produced by the passage of gravitational wave. However, it exists a mathematical formalism which links the contribution of gravitational waves to the scalar output of the detector [6]

$$h(t) = D^{ij} e^{A}_{ij}(\widehat{\mathbf{n}}) h_A(t), \tag{2.54}$$

with

$$F_A(\widehat{\mathbf{n}}) = D^{ij} e^{A}_{ij}(\widehat{\mathbf{n}}) \tag{2.55}$$

where F_A is the *antenna pattern* function of the two polarizations and $e^{A}_{ij}(\widehat{\mathbf{n}})$ is the polarization tensor (with $A = \times, +$, labeling the cross and plus polarizations). Thus, the response of the detector to the gravitational wave strain is given by

$$h(t) = \frac{\delta L}{L} = F_+(\theta, \phi, \psi) h_+(t) + F_\times(\theta, \phi, \psi) h_\times(t), \tag{2.56}$$

expliciting $F_+(\theta, \phi, \psi)$ and $F_\times(\theta, \phi, \psi)$ with respect to source position in the sky plane, we have that the two antenna pattern response functions of the interferometer to the two polarizations of the wave are:

$$F_+(\theta, \phi, \psi) = \frac{1}{2}(1 + \cos^2\theta)\cos 2\phi \cos 2\psi - \cos\theta \sin 2\phi \sin 2\psi, \tag{2.57}$$

$$F_\times(\theta, \phi, \psi) = \frac{1}{2}(1 + \cos^2\theta)\cos 2\phi \sin 2\psi + \cos\theta \sin 2\phi \cos 2\psi, \tag{2.58}$$

where the angles (θ, ϕ) are source position and ψ is the polarization angle which is the rotation angle in the sky frame, see Figure 2.6.

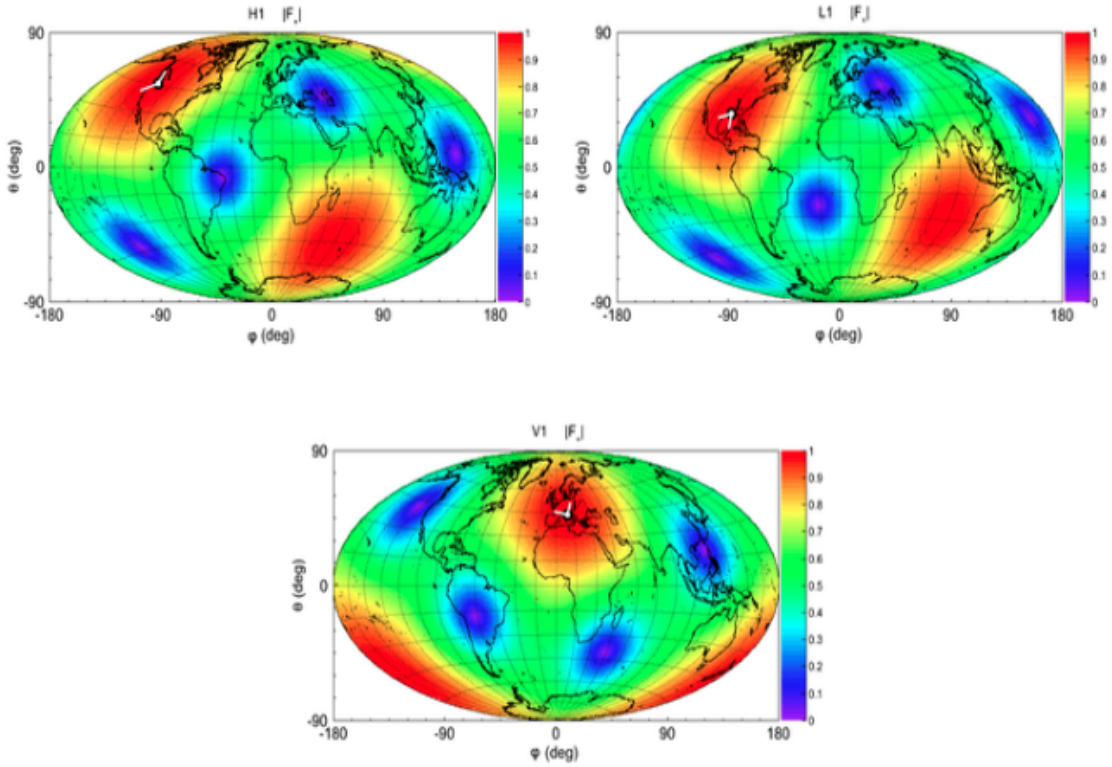

Figure 2.4: The antenna pattern F_+ of LIGO and Virgo interferometers as function of the sky coordinates (θ, ϕ)

The antenna pattern depends on source position (θ, ϕ) of gravitational wave and on geometry of the detector. Depending on the choice of frame (x' , y' , z'), the expression of the antenna pattern is generalized as above in order to take into account further rotation by the angle ψ . Note that any dependence of F_+ and $F_\times$ on time is neglected and this approximation is true as long as the signal duration within the detector bandwidth is much shorter than the Earth rotation period. The gravitational wave interferometer have a *blind direction*, this means $F_+ = 0$ and $F_\times = 0$, when the angles are $\psi = \pi/4$ and $\theta = \pi/2$.

The two polarizations $h_{+,\times}$ of the radiation from an inspiraling binary, a rotating neutron star are a simple form [6]:

$$h_+ = h_0 \frac{1+\cos^2\iota}{2}\cos\Phi(t),$$
$$h_\times = h_0 \cos\iota \sin\Phi(t), \tag{2.59}$$

where h_0 is an is an overall amplitude, $\Phi(t)$ is the signal's phase and ι is the angle between the line of sight and the characteristic direction in the source (e.g., the orbital or the spin angular momentum). In this case, the response of interferometer depends on inclination angle and takes a particularly simple form [15]:

$$h(t) = F_+ h_+ + F_\times h_\times = A h_0 \cos[\Phi(t) - \Phi_0], \tag{2.60}$$

where

$$A = (A_+^2 + A_\times^2)^{1/2}, \quad \tan\Phi_0 = \frac{A_\times}{A_+}, \quad A_+ = \frac{1}{2}F_+(1+\cos^2\iota), \quad A_\times = F_\times \cos\iota.$$

From definition of A, it assumes values in the range between $[0, 1]$. In particular, when the angle $\iota = 0$, it assumes maximum values, while in the orbital plane of the binary system or rotating object, $\iota = \pi/2$, the value is the minimum.

Before to conclude this paragraph, it is important to highlight that a gravitational interferometer can not to observe both independent polarizations of a gravitational wave at the same time, rather it measures a linear combination of the two that depends on the geometry of the detector and source direction. Furthermore, with a single detector we can not determine the position of the source in the sky. The output of a single detector is given by eq.(2.56) which depends on four unknown parameters: the two polarizations of wave $h_+(t)$, $h_\times(t)$ and source position (θ, ϕ). To solve these quantities, we need a network of al least three interferometers because we have three functions $h_i(t), i = 1, 2, 3$ and two independent delay times and so we can solve for $h_+(t), h_\times(t), \theta$ and ϕ [6][15].

So a more uniform sky coverage is obtained if the GW search is performed on networks of differently aligned detectors. The sky coverage of a network of N observatories is well quantified in the Dominant Polarization Frame (DPF): system of reference in which F_+ and $F_\times$ are orthogonal. The mathematical formalism of the DPF is explained in reference [88]. In DPF formalism, it is introduced a N-dimensional space, where each dimension represents a particular detector. In this space, each network vector has N components. So, we have:

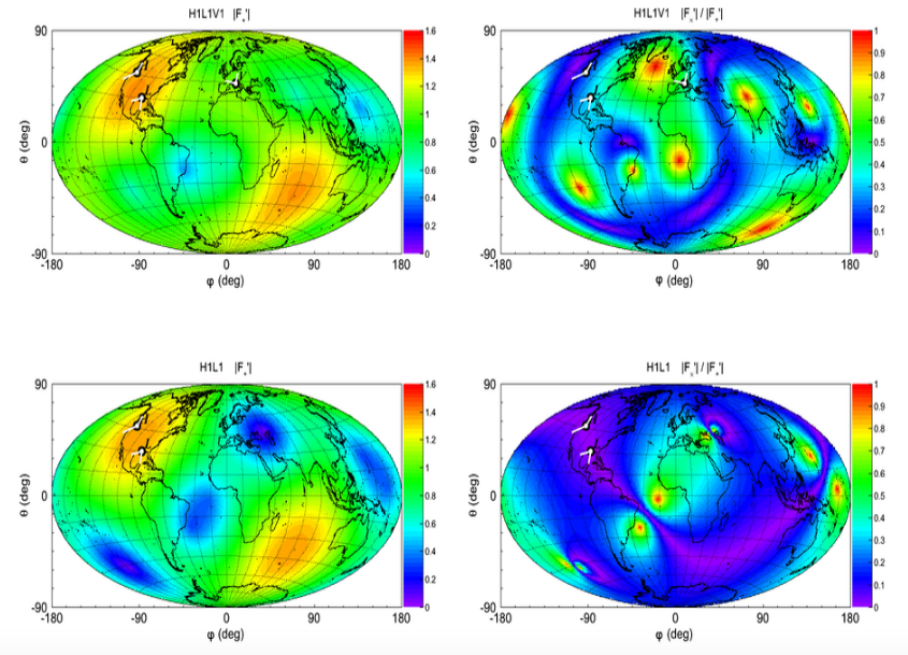

Figure 2.5: The top and bottom plots show the magnitude of $\mathbf{F}_+$ and of $\mid \mathbf{F}_+ \mid / \mid \mathbf{F}_\times \mid$ for H1L1V1 and H1L1 networks.

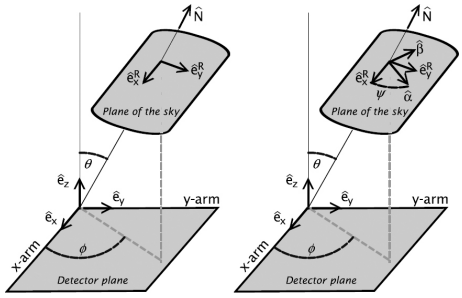

Figure 2.6: The relative orientation of the sky and detector frames (left panel) and the effect of a rotation by the angle ψ in the sky frame (right panel) [15].

$$\mathbf{F}_+ = \{F_{1,+}, F_{2,+}, ..., F_{N,+}\},$$
$$\mathbf{F}_\times = \{F_{1,\times}, F_{2,\times}, ..., F_{N,\times}\}, \tag{2.61}$$

The components of two vectors are the antenna patterns of the N detectors in the network. For two vectors, we have:

$$\mathbf{F}_+ \cdot \mathbf{F}_\times = \sum_{n=1}^{N} F_{+,N} F_{\times,N} = 0, \qquad 0 \leq \frac{\mid \mathbf{F}_+ \mid}{\mid \mathbf{F}_\times \mid} \leq 1, \tag{2.62}$$

with $\mid \mathbf{F}_{+(\times)} \mid = \left(\sum_{n=1}^{N} F^2_{+(\times),N}\right)^{1/2}$. The plots on Figure 2.5 show that a network of al least three detectors H1L1V1 differently aligned, improves the coverage of shy regione with respect to a single detector. On the other hand, if we observe the two plots of $\mid \mathbf{F}_+ \mid / \mid \mathbf{F}_\times \mid$ for H1L1V1 and H1L1, we can observe that the sensitivity to the wave polarization increases.

Sky localization

The first method to localize a GW source by network of interferometer is given by *triangulation* using the observed time delays between sites [89] [90].

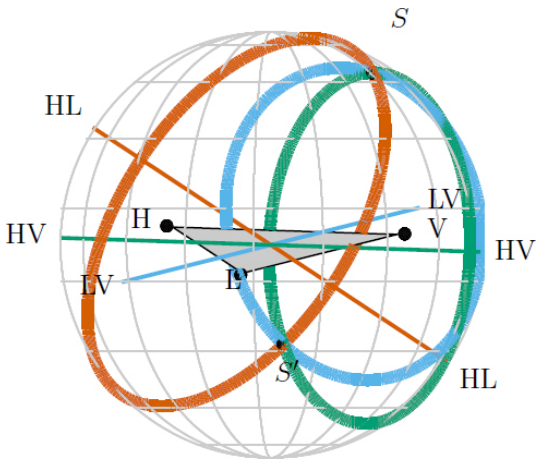

Figure 2.7: Source localization by triangulation for the aLIGO-AdV network [16]. Black dots indicate the detector location LIGO Hanford (H), LIGO Livingston (L) and Virgo (V). The locus of constant time delay (with associated timing uncertainty) between two detectors forms an annulus on the sky concentric about the baseline between the two sites (labeled by the two detectors). For three detectors, these annuli may intersect in two locations. One is centered on the true source direction S, while the other S' is its mirror image with respect to the geometrical plane passing through the three sites. For four or more detectors there is a unique intersection region of all of the annuli.

Localization accuracy will be dominated by the timing accuracy in the detectors as well as the separation between sites. The timing uncertainty in each detector is estimated to be [91] [92]

$$\sigma_t = \frac{1}{2\pi\rho\sigma_f}, \tag{2.63}$$

where ρ is expectation value of the SNR in the given detector whose values is ~ 8 for single-detector SNR threshold while σ_f is the effective bandwidth of the signal in the detector, typically of order 100 Hz. Thus, putting these values in the equation, we have that timing accuracy is on the order of 10^{-4} sec. However, this model does not include other aspects such as information from the signal amplitudes across the detector network, uncertainty in the emitted gravitational waveform, instrumental calibration accuracies, and correlation of sky location with other binary parameters.

If we consider only two detector in the network, as Figure 2.7 shows, we have an annulus on the sky whose center is on the ideal line joing the two detector sites. Adding a third interferometer we have three annuli for each detector site couple and their intersection identifying two sky regions: S point which is the source position and the S' which is the so-called mirror position. To solve this ambiguity, there are some solutions. For example, it is possible to add another detector to the network outside of the plane defined by the other three interferometer. Another solution, it could be to use information of signal amplitude and phase. With four or more detectors, timing information alone is sufficient to localize to a single sky region

2.4 Spectral sensitivity

In the last decade, many efforts have been made in design and construction of gravitational wave interferometers in order to improve the sensitivity of these detectors allowing us to observe such gravitational waves. So, in the first observing run (O1) of the Advanced LIGO detectors, from September 12, 2015 to January 19, 2016, gravitational waves from binary black hole mergers are observed *directly* [93]: two unambiguously identified signals, each one with a statistical significance exceeding 5σ and a third with an 87% probability of being astrophysical.

On September 14, 2015 at 09:50:45 UTC, the LIGO Hanford, WA, and Livingston, LA, observatories detected the first coincident signal GW150914 [94]. The initial detection was performed by low-latency searches for generic gravitational-wave transients [95] and was reported within three minutes of data acquisition by coherent Wave Burst (cWB) pipeline. Subsequently, matched-filter analyses that use a bank of relativistic templates (covering the mass range from 1 $M_\odot$ to 99 $M_\odot$) of compact binary waveforms

which model the evolution of binary compact objects [ref of CBC pipeline] recovered GW150914 as the most significant event from each detector. Consistent within the 10-ms intersite propagation time, the events have a combined signal-to-noise ratio (SNR) of 24. As the time-frequency map of figure 2.9 reports, the duration of gravitational signal is about 0.2 s which corresponds to last 8 cycles of binary evolution sweeping from 35 Hz to 235 Hz in the sensitivity frequency band of the detectors and observing an increase in time of frequency and amplitude with a gravitational wave peak strain of 1.0×10^{-21} $1/\sqrt{Hz}$. The estimated total mass of final black hole is $M = 62.3^{+3.7}_{-3.1}\ M_{\odot}$ in source frame with $m_1 = 36.2^{+5.2}_{-3.8}\ M_{\odot}$ the mass of heaviest black hole and $m_2 = 29.1^{+3.7}_{-4.4}\ M_{\odot}$ the mass for secondary black hole. The estimated total energy converted in gravitational wave energy is $M = 3.0^{+0.5}_{-0.5}\ M_{\odot}c^2$.

A second BH detection was observed on December 26, 2015 at 03:38:53 UTC and in this case the mass of BH remnant was $M = 20.8^{+6.1}_{-1.7}\ \mathrm{M}_{\odot}$ [96]. The gravitational wave candidate GW151226 was initially identified within 70 s by an online matched-filter analysis for binary coalescences. Later, off-line matched-filter analyses reconfirm the detection of gravitational wave signal with a network signal-to-noise ratio of 13. Both searches identified GW151226 as a highly significant event. In the source frame, the masses of two black holes are $m_1 = 14.2^{+8.3}_{-3.7}\ M_{\odot}$ and $m_2 = 7.5^{+2.3}_{-2.3}\ M_{\odot}$, with $1.0^{+0.1}_{-0.2}\ M_{\odot}$ radiated via gravitational wave. The signal lasts in the LIGO frequency band about 1 s, during which the frequency increased over approximately 55 cycles from 35 Hz to 450 Hz reaching a peak gravitational wave amplitude of $3.4^{+0.7}_{-0.9} \times 10^{-22}\ 1/\sqrt{Hz}$. Because of its small strain amplitude and time-frequency morphology different from first gravitational wave signal, GW151226 is not detected by generic transient searches that initially identified GW150914. However, both of these signals were observed with false alarm rates lower than 1 per $2{\times}10^5$ *years* and a significance greater than 5σ (this value is estimated by analysis of compact binary coalescence (CBC) group of LIGO-Virgo collaboration).

In addition a third candidate event, LVT151012, consistent with a BBH merger was observed on October 12, 2015 at 09?54:43 UTC with a combined matched-filter SNR of 9.7 and with a significance corresponding to false alarm rates of 1 per 2 *years*. Due to its low significance less than 2σ, the LIGO and Virgo collaborations did not claim this event as a gravitational-wave signal but as a trigger event. Detector characterization studies ruled out instrumental noise or environmental artifact as sources of this event. Thus, it is more likely to be a gravitational wave signal. The masses of two black holes are $23^{+18}_{-6}\ M_{\odot}$ and $13^{+4}_{-5}\ M_{\odot}$ while the final remnant black hole has a mass of $35^{+14}_{-4}\ M_{\odot}$ with $1.5^{+0.3}_{-0.4}\ M_{\odot}$ converted in gravitational wave energy.

The table in Figure 2.8 reports the main estimated parameters of the three most

significant event [93]. The luminosity distance of the source is inversely proportional to the amplitude of the signal (for more details see Chapter 4 of [6]). The two events GW150914 and GW151226 have similar estimated luminosity distances: $D_L = 420^{+150}_{-180}$ Mpc with redshift $z = 0.09^{+0.03}_{-0.04}$ and $D_L = 440^{+180}_{-190}$ Mpc with redshift $z = 0.09^{+0.03}_{-0.04}$ respectively. In case of LVT15102, the inferred distance is greater $D_L = 1000^{+500}_{-500}$ Mpc with redshift $z = 0.20^{+0.09}_{-0.09}$. Although the distance of two gravitational wave events are comparable, the total mass of two binary black hole systems are different: in case of GW151226, the estimated total mass is lower than GW150914 mass producing thus a gravitational wave signal intrinsically quieter and with a SNR lower than GW150914. However, for all cases, there is an uncertainty for the distance not negligible. This depends on the degeneracy between the distance and the inclination of binary system which also affects the signal amplitude.

The estimated values of sky area for each events reported in table, are larger for quieter events and as it is expected [97][98], the sky area is expected to scale inversely with the square of the SNR.
Sky localization of a gravitational wave by detector network is primarily obtained by the difference of measured time of arrival of the signal at the interferometer sites. The observed amplitude and phase of the signal in two detectors are used to reduce the sky localization and to reconstruct the distance of the source and binary orientation (with additional information coming from the signal amplitude and phase [99][91][100]). As discussed in previous section, the capabilities of the sky localization source improves adding a third detector to the network.

The mergers of binary black hole systems reach gravitational wave luminosities very high. The peak luminosity values for GW150914, LVT151912 and GW151226 are: $3.6^{+0.5}_{-0.4} \times 10^{56}$ erg s^{-1}, $3.1^{+0.8}_{-0.8} \times 10^{56}$ erg s^{-1} and $3.3^{+0.8}_{-1.6} \times 10^{56}$ erg s^{-1}. We note that the values of peak luminosities are not different among them unlike the energy radiated via gravitational wave which is inversely proportional to total mass of the system [44] $P \propto \mu^2$ with $\mu = (m_1 m_2)/(m_1 + m_2)$ reduced mass.

The detection of gravitational waves from coalescence of three BBHs, allows us to test the predictions of general relativity for binary coalescence waveforms. Several tests of general relativity were performed using GW150914, as reported in [101]. One of these, performed also to GW151226, was a parametrized test for the consistency of the observed waveform with a general relativity based waveform model. As report the Figure 2.10, because of the total mass of GW151226 is lower than GW150914, the cycles which pass the frequency band of interferometer are more than GW150914 those ($N_{cyc} \propto M_{ch}^{-5/3}$) and this provided the possibility to better constrain the post-Newtonian (PN) coefficients

describing the in spiral phase of binary system evolution.

Event	GW150914	GW151226	LVT151012
Signal-to-noise ratio ρ	23.7	13.0	9.7
False alarm rate FAR/yr^{-1}	$< 6.0 \times 10^{-7}$	$< 6.0 \times 10^{-7}$	0.37
p-value	7.5×10^{-8}	7.5×10^{-8}	0.045
Significance	$> 5.3\sigma$	$> 5.3\sigma$	1.7σ
Primary mass $m_1^{\rm source}/{\rm M}_\odot$	$36.2^{+5.2}_{-3.8}$	$14.2^{+8.3}_{-3.7}$	23^{+18}_{-6}
Secondary mass $m_2^{\rm source}/{\rm M}_\odot$	$29.1^{+3.7}_{-4.4}$	$7.5^{+2.3}_{-2.3}$	13^{+4}_{-5}
Chirp mass $\mathcal{M}^{\rm source}/{\rm M}_\odot$	$28.1^{+1.8}_{-1.5}$	$8.9^{+0.3}_{-0.3}$	$15.1^{+1.4}_{-1.1}$
Total mass $M^{\rm source}/{\rm M}_\odot$	$65.3^{+4.1}_{-3.4}$	$21.8^{+5.9}_{-1.7}$	37^{+13}_{-4}
Effective inspiral spin $\chi_{\rm eff}$	$-0.06^{+0.14}_{-0.14}$	$0.21^{+0.20}_{-0.10}$	$0.0^{+0.3}_{-0.2}$
Final mass $M_{\rm f}^{\rm source}/{\rm M}_\odot$	$62.3^{+3.7}_{-3.1}$	$20.8^{+6.1}_{-1.7}$	35^{+14}_{-4}
Final spin $a_{\rm f}$	$0.68^{+0.05}_{-0.06}$	$0.74^{+0.06}_{-0.06}$	$0.66^{+0.09}_{-0.10}$
Radiated energy $E_{\rm rad}/({\rm M}_\odot c^2)$	$3.0^{+0.5}_{-0.4}$	$1.0^{+0.1}_{-0.2}$	$1.5^{+0.3}_{-0.4}$
Peak luminosity $\ell_{\rm peak}/({\rm erg\,s}^{-1})$	$3.6^{+0.5}_{-0.4} \times 10^{56}$	$3.3^{+0.8}_{-1.6} \times 10^{56}$	$3.1^{+0.8}_{-1.8} \times 10^{56}$
Luminosity distance $D_{\rm L}$/Mpc	420^{+150}_{-180}	440^{+180}_{-190}	1000^{+500}_{-500}
Source redshift z	$0.09^{+0.03}_{-0.04}$	$0.09^{+0.03}_{-0.04}$	$0.20^{+0.09}_{-0.09}$
Sky localization $\Delta\Omega$/deg^2	230	850	1600

Figure 2.8: Main parameters of GW150914, GW151226 and LVT151012 events [17].

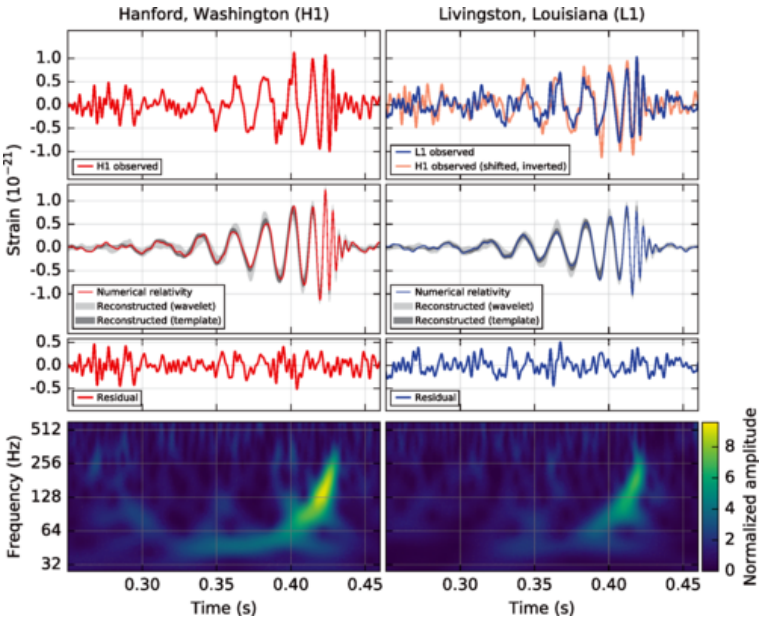

Figure 2.9: (Top) Gravitational wave strain of event GW150914 in L1 and H1 detectors. (Bottom) Time-Frequency representation of the data, showing the increase of the frequency over time.

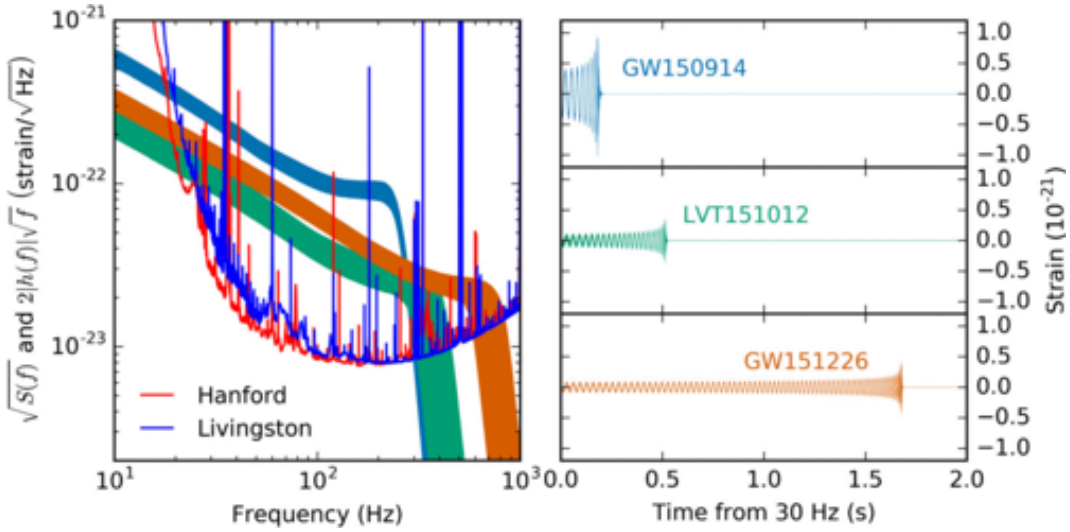

Figure 2.10: The left plot reports the spectral density in term of strain noise of H1, L1 detectors [18].

2.5 Transient noise in advanced gravitational wave detectors

The Advanced LIGO detectors came online in September 2015 after a period of upgrade of different interferometer components in order to improve the sensitivity by factor 10 (*design sensitivty*) with respect of initial LIGO detectors [74]. During the first observational run O1, the strain sensitivity was improved by 3-4 factor with respect to past configuration across the most sensitive frequency band between 100 Hz and 300 Hz [82]. The improvement in sensitivity corresponds to a gain of about 30 times in observable volume of space for BBH mergers. The left plot of figure 2.10 shows the amplitude spectral density, $\sqrt{S(f)}$, in terms of strain $\sqrt{Hz}$ for L1 and H1 detectors. In the same plot, the waveform of GW150914, GW151226 and LVT151012 are overlapped with different colors. The expected signal-to-noise ratio (SNR) ρ of a GW signal $h(t)$, is given by:

$$\rho^2 = \left(\frac{S}{N}\right)^2 = 4\int_0^\infty df \frac{|\widetilde{h}(f)|^2}{S_n(f)} = \int_0^\infty \frac{(2\widetilde{h}(f)\sqrt{f})^2}{S_n(f)} d\ ln(f), \tag{2.64}$$

where $\widetilde{h}(f)$ is is the Fourier transform of the signal. The right hand of the formula allow us to connect the relative amplitudes to the SNR of the events: the area between the signal and detector noise curve is the SNR of gravitational wave event.

As we seen in Chapter 1, the time evolution of gravitational wave signal of a binary system increase in amplitude and frequency (chirp signal) when the two objects approach

each other reaching the maximum of signal amplitude at the merger of two bodies. After the merger, the amplitude of the signal decreases as the remnant object rings down to equilibrium. In the frequency domain, during in-spiral phase, the amplitude of the signal decreases followed by a slower drop during merger and then a steep decrease during the ringdown phase. From the plot, the amplitude curve GW150914 of light blu color is significantly larger than the other two events and at the merger, the gravitational-wave signal is above the noise curves of interferometer. We note that the fall of amplitude after the merger occurs at different frequencies for three events. As mentioned above, this depends on different duration of signal in frequency band of interferometer and in turn, of the mass of binary system. In other words, the light BBH systems GW151226 and LVT151012 have low amplitude but last more cycles with respect to GW150914 as the right plot of Figure 2.10 shows.

In this part of the section, we would like to give a general idea about the *transient noise* and how it is treated in the data. This topic is widely discussed in [102] and references therein. In the section 2.2, we briefly examined the different contributions to stationary noise background of detector: seismic noise at low frequencies, thermal noise at mid frequencies and photon shot noise at high frequencies. However, the detector strain data also contain non-stationarity and non-Gaussian noise transients due to a variety of instrumental or environmental mechanisms and to complicated couplings between them. These noise artifacts have different duration and morphologies, many of these have a specific features [19]. The noise glitches manifest as a variation in shape and level sensitivity of detector noise curves in function of the time and arise in the frequency range where astrophysical transient signals are expected. The transient noises are classified [19]:

- *Uncorrelated noise*
  - **Anthropogenic noise** sources due to human activity or infrequent ground motion or noise from other nearby locations (monitored by accelerometers, seismometers, and microphones).
  - **Earthquakes** generate ground motion at low frequencies , from 0.03 to 0.1 Hz (monitored by seismometers).
  - **radio frequency modulation** used to control optical cavities, sometime producing glitches for a fault in the electronic system (vetoed).
  - **Blip transients** are short noise transients with a symmetric 'teardrop' shape

in time-frequency space and appear typically in frequency range between 30 and 250 Hz (no clear correlation to any auxiliary channels has yet).

- *Correlated noise sources*
  - **Potential electromagnetic noise** due to lightning, solar events and solar-wind driven noise (monitored by radio receivers and magnetometers).
  - **Cosmic ray showers** generated when a highly energetic cosmic ray impacts the Earth's atmosphere producing electromagnetic radiation and charged particle cascades. Observations of a coincident cosmic ray shower in two detectors is highly unlikely. However, a cosmic-ray detector is monitored at LIGO-Hanford.

The estimate of background trigger rate due to noise transients occurring simultaneously at detectors is performed by *time-shift* techniques [95] [103]. This consists of translating time data of one detector with respect to other detector's data by no physical time delay (so called *time lags*) with time duration greater than light travel time between the detectors (in case of Livingston and Hanford site this difference is 10 ms). These instances of data are analyzed, and each trigger can not be due to real GW passage but they are glitches, see Figure 2.12.

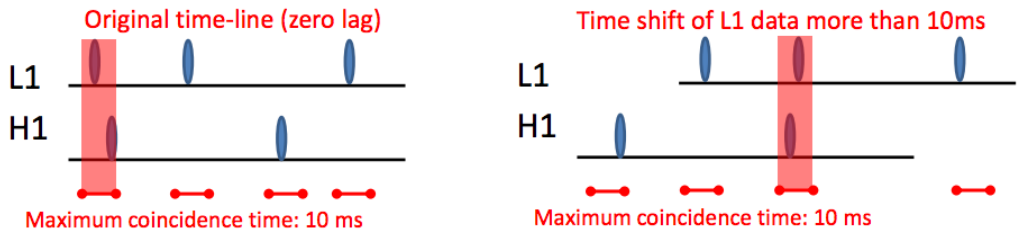

Figure 2.11: Sketch of time shift techniques.

The coincident triggers generated by many time lags of the data, produce a distribution of background triggers due to coincidence of transient noises. The estimation of background is a crucial point for significance of the gravitational wave event which is the probability that the noise produces a fake event (the *false alarm rate*).

The instrument behaviour and environmental conditions of detectors are monitored by *auxiliary channels*, an array of sensors which also record the operating point and the state of control system of detectors [104]. When a noise source in auxiliary channels and also a coupling between these channels and the gravitational wave strain data are

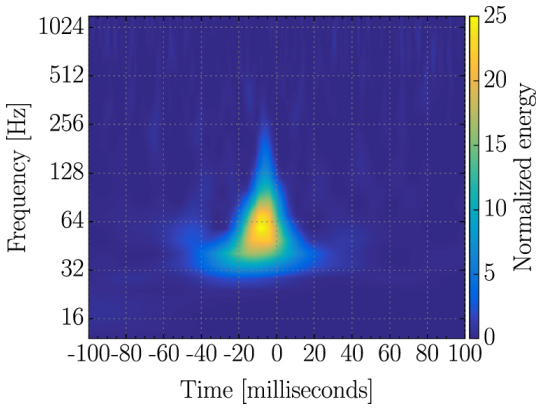

Figure 2.12: The plot show a typical shape of blip transient in a normalized spectrogram of the LIGO-Livingston channel. The color bar is excess signal energy of data normalized by an estimated power spectral density [19].

identified, a *data-quality veto* is created descarding these data from the search to reduce the background. There are two types of data quality applied as vetoes: data quality *flags* which esclude period of data whose duration can be of seconds or hours and refer to known noise couplings; data quality *triggers* are vetoes of short duration produced by algorithms that identify significant statistical correlations between a GW transient and transient noise in auxiliary channels. In turn, data quality are applied as vetoes in different categories which depend on type of problem or on search's background. The *category 1* groups data quality flags collecting times at which a component of detector not operating in its nominal configuration and for this reason they are identically defined for all transient searches.
Another category is *category 2* where data quality flags refer to times where noise source with known physical coupling to h(t) appears.
There is a third category, *category 3*, for data quality triggers, which are statistically generated, and for data quality flags where the coupling mechanism is not understood.

2.6 Observing scenario: plans for future observations

The search of gravitational wave will see an operating network of gravitational interferometers in the future years. In this section, we discuss briefly what will be observation plans of the gravitational network.

Transient gravitational wave signals from binary black hole mergers have been identified in the twin Advanced LIGO detectors during the first observational run O1 from

September 12, 2015 to January 19, 2016. The sensitivity reached by two gravitational interferometers is shown in Figure 2.13 by light blue band corresponding to an observational burst range of 40 - 80 Mpc [16].

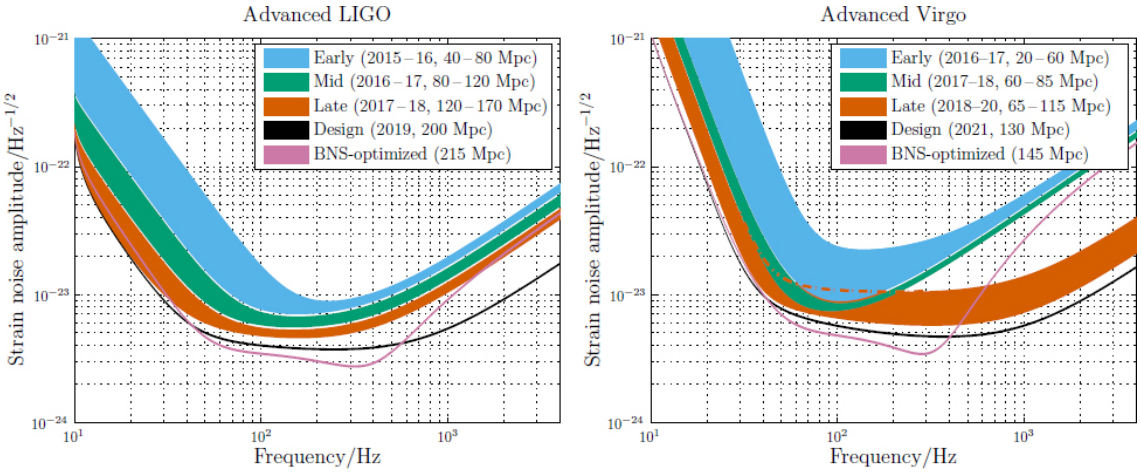

Figure 2.13: The left and right plots report strain sensitivity as a function of frequency of Advanced LIGO (aLIGO) and advanced Virgo (AdV) respectively. The different color belts, in both interferometer, indicate the sensitivity which will reach (unlike O1 already reached) by interferometers during their commissioning phases. During the different stages of commissioning (colored belts), the sensitivity is improved up to final design sensitivity target to which correspond the optimized sensitivity curve (pink curves) for binary NS searches [16].

The second observation run O2 started on November 30, 2016. This will last till end of August a six-month run to which Virgo will join in spring 2017. The aLIGO performance is expected to be similar to the mid band (green) in Figure 2.13 with burst range of 40 - 80 Mpc and range of 80-120 Mpc for BNS. The AdV range may be similar to the early band, about 20 - 60 Mpc for BNS and 20 - 40 Mpc for burst signals.

The third observation run O3 will last a nine-month between 2017-2018 with three detectors. The sensitivity performance of aLIGO and AdV will be similar to the late and mid bands of Figure 2.13 respectively, with BNS ranges of 120 - 170 Mpc and 60 - 85 Mpc, and burst ranges of 75 - 90 Mpc and 40 - 50 Mpc.

Starting from 2019, the three-detector network with aLIGO detectors will have a sensitivity curve similar to the design curve of 200 Mpc while AdV operating similarly to the late band at 65-115 Mpc, eventually reaching the design sensitivity circa 2021. Probably in 2022, the H1L1V1 network will have full sensitivity (aLIGO at 200 Mpc, AdV at 130 Mpc) with joining of fourth detector LIGO-India to network. The four-site network incorporating LIGO-India at design sensitivity will improve the sensitivity and source localization over the whole sky.

Chapter 3

Coherent Wave Burst pipeline: detection of gravitational wave bursts using minimal assumptions

This chapter describes the coherent WaveBurst (cWB) pipeline, unmodeled data-analysis pipeline developed to search for transient of gravitational radiation.

The Burst search bases on "eyes wide open" approach to detecting GW transient, this means minimal assumption on knowledge of the morphology of the signal. This strategy is more robust against uncertainties in the GW signature especially when there is not a knowledge about physics of the source.
In this context, cWB pipeline has been developed into the LIGO and Virgo collaboration; this data analysis algorithm does not make a priori assumptions on the signal waveforms. The pipeline identifies coincident candidates in data from GW detectors and reconstructs the associated GW waveform using a likelihood analysis. In general, the analysis typically done by performing a time-frequency (TF) decomposition of the data combining them in order to obtain a TF power map. A transient event is identified as a cluster of "hot" pixels in the TF maps with power above the baseline detector noise.

With the term *burst*, we refer to signal whose duration is between $10^{-3} - 10^{3}$ sec. In this category, the astrophysical processes such as coalescence of compact objects as black hole, neutron star, white dwarf (well-modelled known sources), core-collapse of supernova, star-quakes and pulsar glitches; speculative sources, e.g., cosmic string cusps (not-well-modelled known sources) are included. Some systems are difficult to model because the involved dynamics are complicated or as in the NS case the equation of state

of matter at nuclear densities are unknown. Therefore, to target this kind of signal a data analysis algorithm based on minimal assumptions on the source or accurate models is required. This approach is called *eyes wide open* approach.
However, on the other hand, this unmodeled search is affected by noise signal due to non-gaussian detector noise fluctuations which can mimic a real gravitational wave signal. Thus, generic GW burst search requires techniques that can descriminate signals from background noise fluctuations (*false alarm*) without prior knowledge of the signal waveform. For this reason, the *coherent* analysis is required: the data from all the detectors in the network are combined in a unique stream using both amplitude and phase information. A GW signal in the data stream of each detector will be built up coherently when those streams are combined, while coincident noise fluctuations can be eliminated based on their (non-)correlation between detectors. In general, the analysis perform a decomposition of the data in time-frequency domain using wavelets or short Fourier transforms, and identifying clusters of pixels in time-frequency maps with significant excess power. Several independent pipelines based on these ideas have been used in the analysis of initial LIGO - Virgo data.
The coherent Wave Burst (cWB) pipeline [105][106][107] is an algorithm of data analysis developed into the LSC collaboration that does not make a priori assumptions on the signal. It is based on a C++/ROOT [108] algorithm which identifies coincident events in data from the detectors of the networks and reconstructs the gravitational wave signal associated with these events using a likelihood analysis.
The cWB pipeline consists of three main steps pointed out in Figure 3.1:

Data conditioning For each detector in the considered network, filters are applied to the data in the wavelet domain to remove "predictable" components in the input series time, due to well know noise source. A data-whitening procedure is subsequently applied on the data.

Construction of TF clusters The whitened data is decomposed at different multiple TF resolutions. The most energetic TF pixels identified at each decomposition level are collected. The algorithm looks for sharing common regions of time-frequency map at different decomposition levels grouping in a super-clusters. The TF pixels above threshold defined by whitened procedure are selected at each decomposition level. Then algorithm searches for cluster coherent, in frequency and time, across the detectors.

Generation of coherent triggers The generation of coherent (or network) trig-

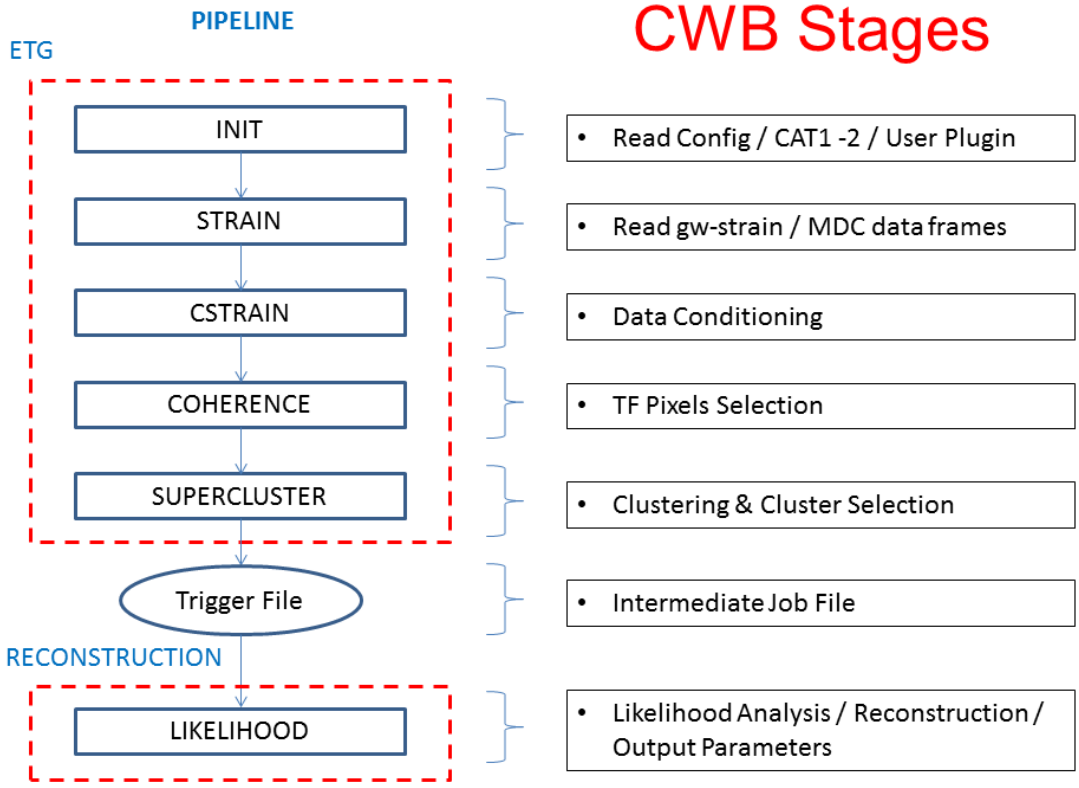

Figure 3.1: Main steps of the coherent wave burst (cWB) pipeline.

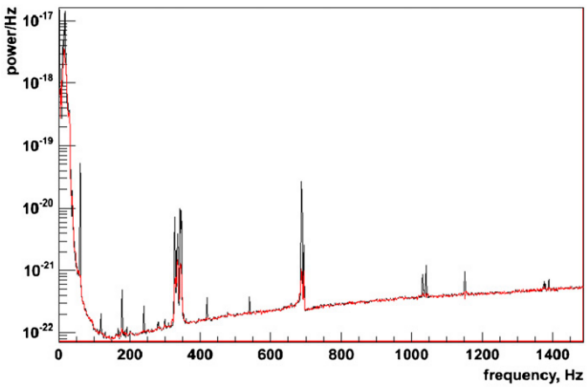

Figure 3.2: Power spectra noise of LIGO Hanford detector (black line) and after the application of LPE filter (red line). The LPE filter removes spectral lines but preserves the power spectral density of the noise floor.

ger bases on constrained maximum likelihood approach. For each trigger it proceeds with the reconstruction of the associated GW burst parameters. Selection cuts are applied on the triggers in order to improve the confidence of GW candidate events excluding triggers due to noise fluctuansions.

In the following, we describe these three stages in more details.

3.1 Data conditioning

The first step of the cWB data-conditioning procedure bases on application of the linear prediction error filter (LPE filter). The LPE filters are used to identifies and remove predictable components from the analyzed time series, such as known spectral lines of detector PSD at specific frequencies. In cWB, this is performed by so-called Regression algorithm [109]. The LPE stage is performed for each detector in the wavelet domain following these steps:

- wavelet decomposition of the time series x(t): x(t) $\rightarrow$ w(f,t) for each band of frequency or layer;
- construction and application of LPE filter F(f) individually to each wavelet layer;
- a set of filters F(f) removes predictable components in the wavelet layers producing whitening data w'(t);
- inverse wavelet transformation is applied on w'(t), obtaining filtered time series x' (t).

It highlights that, although the application in the wavelet domain of the LPE filter removes spectral lines, this, at the same time, preserves the coloured structure due to the detector sensitivity (PSD), see Figure 3.2.

3.2 Construction of Time-Frequency clusters

For the construction of pixel clusters on time-frequency (TF) map, the coherent Wave Burst pipeline decomposes the data stream, of each detector in the network, at different (dT, dF) resolution level. As reported in Figure 3.3, the different time and frequency resolutions give a different representation and characterization of the signal. The wavelet transform employed by cWB pipeline is the Wilson-Daubechies-Meyer, which is described in [110].The use of this time-frequency decomposition of the data has some advantages: a reduced spectral leakage and high TF resolution.

Once performed the TF transformation of the data for each (dt, df) level, the cWB algorithm identifies group of pixels on the TF map. We call *black* pixels if the corresponding energy is above a threshold which depends on the noise level, otherwise we call *white* pixels. For each detector and TF level, both black and white pixels are aggregated in *clusters*. The black pixels taking part of the cluster must lie within a given TF window with respect to at least another black pixel in the set and they are called *core* pixels. Indeed, in the cluster we include the white pixels which share share one side or one vertex with the considered pixel. The white pixels of a cluster are called *halo* pixels, see the Figure 3.4. Core and halo pixels in a cluster represents an trigger by a detector at the related time-frequency resolution. A cluster is considered by cWB algorithm if it includes pixels from two adjacent resolutions in each detector in the network.

At this point, these clusters are combined in *super-clusters* at the network level and the pipeline selects the optimal TF resolution level at which a network event has been identified. The selection of optimal level depends on the energy content and on the consistency among the detectors. The clusters reconstructed at the optimal TF resolution are the candidates for the generation of coherent network triggers.

Moreover, cWB pipeline can perform a *multi-resolution* analysis (MRA): it selects time-frequency pixels with significant energy excess and coherent power across the detectors at several time-frequency resolutions, so to build a representation of GW candidate events by a cluster of the most significant multi-resolution pixels. The multi resolution analysis is used for our purpose.

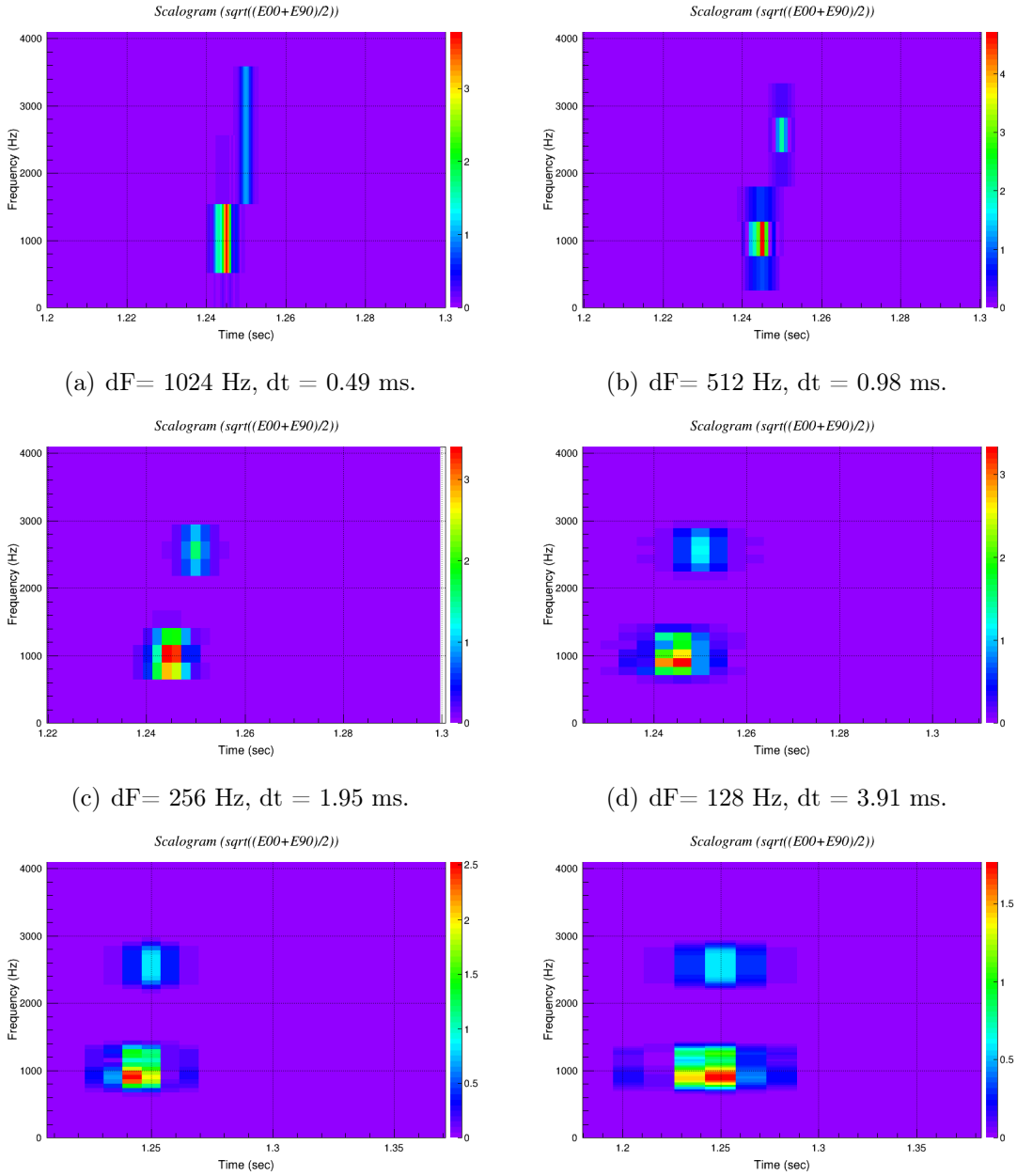

(a) dF= 1024 Hz, dt = 0.49 ms.

(b) dF= 512 Hz, dt = 0.98 ms.

(c) dF= 256 Hz, dt = 1.95 ms.

(d) dF= 128 Hz, dt = 3.91 ms.

(e) dF= 64 Hz, dt = 7.81 ms.

(f) dF= 32 Hz, dt = 15.62 ms.

Figure 3.3: In time-frequency maps is reported the GW signal of late in-sparal and post-merger phases for a delayed collapse to black hole scenario taking into account the waveform model SHT-M2.0-S (see chapter 4). The coalescence of two neutron stars forms a hypermassive neutron star generating a dominant frequency peak at ∼2.6 kHz. The signal is reconstructed by cWB tool at different time and frequency resolutions.

3.3 Selection of coherent triggers

Network triggers are coherently reconstructed from super-clusters applying a constrained maximum-likelihood approach [106] [107]. The likelihood maximization is performed in

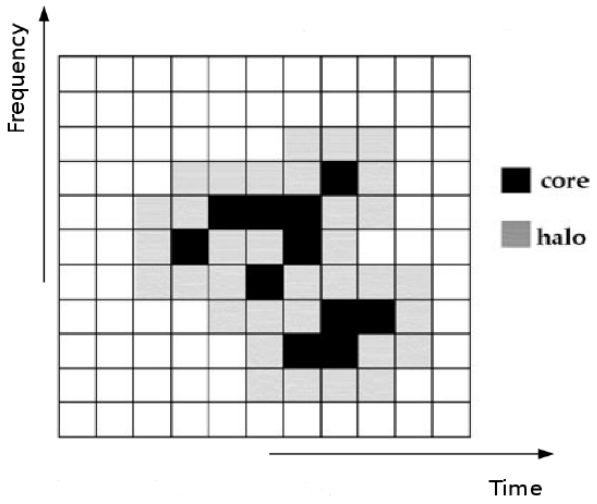

Figure 3.4: Artistic representation of a cWB TF cluster: black pixels represent the core of the cluster while the grey one the halo of it.

the formalism of the Dominant Polarization Frame (DPF) explained in [88]. In case of Gaussian quasi-stationary noise and in the wavelet (time-frequency) domain, the likelihood functional $\mathcal{L}$ is given by [106]:

$$\begin{aligned}\mathcal{L} = \mathcal{L}(i,j,\theta,\phi) &= \sum_{k=1}^{K}\sum_{i,j=1}^{N}\left[\frac{\omega_k^2[i,j]}{\sigma_k^2[i,j]} - \frac{(\omega_k[i,j]-h_k[i,j])^2}{\sigma_k^2[i,j]}\right] \\ &= \sum_{k=1}^{K}\sum_{i,j=1}^{N}\frac{1}{\sigma_k^2[i,j]}\left[2\omega_k[i,j]h_k[i,j] - h_k^2[i,j]\right], \end{aligned} \tag{3.1}$$

where K and N are respectively the number of the detectors in the network and pixels of the time-frequency area selected by algorithm, respectively and the time i and frequency j index run over this time-frequency region of the map. The quantities $\omega_k[i,j]$ refer to detector data, $h_k[i,j]$ is the detector response to GWs and $\sigma_k$noise standard deviation. The detector response (discussed in the section 2.3) is given by

$$h_k[i,j] = F_{+,k}h_+[i,j] + F_{\times,k}h_\times[i,j]. \tag{3.2}$$

We remember that the antenna pattern $F_{+,k}(\theta,\phi)$ and $F_{\times,k}(\theta,\phi)$ are function of source position and $h_+[i,j], h_\times[i,j]$ are the two polarizations of the gravitational wave signal in the wave frame. Introducing the data vector and antenna patterns vector

$$\mathbf{w}[i,j] = \left\{ \frac{w_1[i,j]}{\sigma_1[i,j]}, ..., \frac{w_K[i,j]}{\sigma_K[i,j]} \right\}, \tag{3.3}$$

$$\mathbf{f}_{+(\times)[i,j]} = \left\{ \frac{F_{1+(\times)}[i,j]}{\sigma_1[i,j]}, ..., \frac{F_{K+(\times)}[i,j]}{\sigma_K[i,j]} \right\}, \tag{3.4}$$

we write the likelihood $\mathcal{L}$ as:

$$\begin{aligned} \mathcal{L} &= \mathcal{L}_+ + \mathcal{L}_\times \\ &= \sum_{\Omega_{TF}} [2(\mathbf{w}\cdot\mathbf{f}_+)h_+ - |\mathbf{f}_+|^2 h_+^2] + \sum_{\Omega_{TF}} [2(\mathbf{w}\cdot\mathbf{f}_\times)h_\times - |\mathbf{f}_\times|^2 h_\times^2] \end{aligned} \tag{3.5}$$

where the indices i,j are replaced by Ω_{TF} which refers to the area of time-frequency map. The antenna pattern vectors $\mathbf{f}_+$ and $\mathbf{f}_\times$ are defined in the dominant polarization wave (DPF) where they are orthogonal to each other: $(\mathbf{f}_+ \cdot \mathbf{f}_\times) = 0$. We observe that GW waveforms are the solutions of the equations 3.5:

$$h_+ = \frac{(\mathbf{w}\cdot\mathbf{f}_+)}{|\mathbf{f}_+|^2} \qquad\qquad h_\times = \frac{(\mathbf{w}\cdot\mathbf{f}_\times)}{|\mathbf{f}_\times|^2}. \tag{3.6}$$

Thus, the maximum likelihood statistic is:

$$L_{max} = \sum_{\Omega_{TF}} \left[\frac{(\mathbf{w}\cdot\mathbf{f}_+)}{|\mathbf{f}_+|^2} + \frac{(\mathbf{w}\cdot\mathbf{f}_\times)}{|\mathbf{f}_\times|^2} \right] = \sum_{\Omega_{TF}} [(\mathbf{w}\cdot\mathbf{e}_+)^2 + (\mathbf{w}\cdot\mathbf{e}_\times)^2], \tag{3.7}$$

where $\mathbf{e}_{+(\times)}$ are the unit vectors

$$\mathbf{e}_+ = \frac{\mathbf{f}_+}{|\mathbf{f}_+|} \qquad\qquad \mathbf{e}_\times = \frac{\mathbf{f}_\times}{|\mathbf{f}_\times|}. \tag{3.8}$$

Thus, we have the the maximum likelihood statistic for a given time frequency location (i, j), $L_m(i,j)$, maximiming likelihood functional over the source coordinates (θ, ϕ). The maximization of this statistic determines the likelihood time-frequency map L, used to reconstruct the event.

After the coherent triggers are identified, one has to reconstruct the parameters of the GW bursts associated with the triggers, including the reconstruction of the source coordinates, the two GW polarizations, the individual detector responses and the maximum likelihood statistics of the triggers.

In case in which the detector noise is Gaussian noise and stationary, the maximum likelihood L_{max} is the only statistic needed to detect and select the GW events and

threshold on L_{max} controls the false alarm probability. In case of real data, as we discussed in section 2.5, the instrumental and environmental noises can mimic a GW event, thus additional selection cuts should be applied to distinguish genuine GW signals from transient noises. These selection cuts verify the consistency of the reconstructed responses in the detectors and the cWB algorithm computes them starting from the elements of the likelihood. The likelihood calculated over the network provides a direct estimate of the coherent and incoherent power contributions to the total energy and bases on the likelihood matrix L_{mn}. The likelihood matrix is a quadratic form (see eq.3.1)

$$L_{max} = \sum_{mn} L_{mn} = \sum_{mn} w_m (e_{+,m} e_{+,n} + e_{\times,m} e_{\times,n}) w_n, \tag{3.9}$$

where m and n indices run over the detectors in the network. It can be splitted in coherent E_c energy detected by the network given by sum of off-diagonal terms (m≠n) and incoherent E_i energy given by sum of diagonal terms (m=n). To distinguish genuine GW signals from the noise glitches, it is useful to introduce the network correlation coefficients

$$c_c = \frac{E_c}{|E_c| + E_n} \tag{3.10}$$

where E_n is the energy of the null stream given by the energy of residual noise after the reconstructed signal energy is subtracted from the total energy of the signal. The gravitational wave signal are coherent and their values of residual energy is small i.e. $E_c >> E_n$ and $c_c \sim 1$. While in case of glitches, they are not coherent and $E_c << E_n$ and $c_c << 1$.

The statistic E_c is an important estimator because depends on cross-correlation terms between the detectors pairs [107]. It is used for the construction of the burst detection statistic defined as

$$\eta_c = \left(\frac{c_c E_c K}{K - 1} \right)^{1/2}, \tag{3.11}$$

where K is the number of detector and η_c is an estimator of the network coherent signal-to-noise ration for correlated GW signals detected by different detectors in the network.

Chapter 4

Simulations of gravitational waves by binary neutron star coalescences from different scenarios

In the first section of *chapter 4*, we describe the catalog of numerical relativity waveforms analyzed in this thesis and computed by Numerical Relativity Group of Trento University. The catalog collects GW waveforms of binary NS systems whose merger produces a BH or HMNS/SMNS; or a stable NS. The GW waveforms are simulated at a reference distance of 100 Mpc including equal and un-equal mass systems. The search is targeted to reconstruct GW signals from the post-merger phase in the frequency range (768 - 4096) Hz performing a uniform distribution in distance.

4.1 Catalog of sources

In the first chapter, we argued about the possible scenario after the merger of two neutron stars depending on the EoS and the involved masses of two NSs. The binary neutron star merger can lead to different scearios [111]:

- a prompt collapse to BH;
- a formation of hypermassive NS (HMNS), with mass above the maximum mass for uniformly rotating configuration which survives few ms up to ∼100 ms before to end up in a BH;
- a long-lived NS which it could be either supramassive (SMNS), with mass above the allowed maximum mass for non-rotating configurations with a life-time of minutes

or longer time, indefinitely stable NS.

We do not have a precise knowledge of the mechanism that supports the structure against the collapse. It is believed that in case of HMNS, the key role lies in the differential rotation [112] where the core is faster than the outer layers and collapse when enough differential rotation is removed via GW emission or electromagnetic torques. In case of SMNS, indeed, its structure is supported by uniform rotation and collapses when enough angular momentum is carried away via magnetic dipole radiation and GWs. However, simulations (see Kastuan et al. [113]) point out that, for both scenarios, the support is due to the outer layers rotating slightly below the Kepler velocity while the core spins more slowly than the envelope.

The aim of this thesis is the reconstruction of GW signal produced by the oscillating massive NS remnant of the BNS merger. We analyzed a catalog of numerical relativity waveforms simulated by Numerical Relativity (NR) Group of Trento University. The technical details of the NR simulations, specific configurations and conditions of each type of nuclear physics EOSs related to binary NS systems and the results of these waveform models are detailed and widely discussed in references reported in Table 4.1. Full discussion of the NR simulations is beyond the scope of the present Thesis. We report here only a general description.

The equation of state (EoS) employed for the simulations are divided in five different types (details in the following references and therein): Lattimer-Swesty (LS) EoS [117][118], Shen-Horowitz-Teige (SHT) EoS [119][120], Akmal-Pandharipande-Ravenhall (APR) EoS [121], H4 [122] and MS1 [123] .
The LS EoS uses a compressible liquid drop model with a Skyrme force [118] including the effects of interactions and degeneracy of the nucleons outside nuclei and also taking into account the nuclear deformations and the phase transitions from nuclei to uniform nuclear matter at values of subnuclear densities.
The SHT EoS employs a relativistic mean-field model for uniform matter at intermediate and high density for a wide range of temperatures, densities, and proton fractions.
APR EoS treats a three-nucleon interaction with a transition in NS matter to a phase with neutral pion condensation at a baryon number density of 0.2 fm^{-3}. For this model, neutron stars have a layer with a thickness on the order of tens of meters where the density changes rapidly from that of the normal to the condensed phase and considers the possibility of core make up dense nucleon matter and quark matter.
The H4 and MS1 EoS are obtained within a relativistic mean field approach, and H4 includes hyperons. Wolfgang and Galeazzi in their work [113], employ a variant with

Model	Ref.	M_b [$M_\odot$]	M_∞[$M_\odot$]	τ_{MNS}[ms]	f_{peak} [kHz]	M_{BH} [$M_\odot$]
SHT-M2.0-I	[113]	4.01	1.80	>16.9	2.47	...
SHT-M2.0-S	[113]	4.01	1.80	>9.4	2.66	...
SHT-M2.2-I	[113]	4.39	1.95	prompt	...	3.73
LS220-M1.5-I	[113]	3.12	1.41	8.6	3.24	2.65
LS220-M1.5-S	[113]	3.12	1.41	7.7	3.17	2.67
LS220-M1.7-I	[113]	3.46	1.54	prompt	...	2.98
LS220-M1.8-I	[113]	3.62	1.61	prompt	...	3.14
APR4-HM	[114]	3.18	1.43	<1	...	2.79
H4-M1.5	[115]	3.04	1.40	12	2.67	2.47
H4-q08	[115]	3.04	1.54, 1.26	25	2.69	2.50
H4-M1.4	[111]	2.92	1.35	22	2.54	2.49
H4-q09	[111]	2.92	1.42, 1.28	28	2.55	2.42
APR4-LM	[114]	2.66	1.22	SMNS	3.17	...
APR4-UM	[114]	3.01	1.42, 1.29	SMNS	3.30	...
APR4-q09	[111]	2.98	1.42, 1.28	SMNS	3.24	...
MS1-M1.45	[111]	2.91	1.35	stable	2.03	...
MS1-q09	[111]	2.91	1.41, 1.28	stable	2.09	...
SHT-M1.5-I	[116]	3.03	1.40	stable	2.04	...

Table 4.1: Parameters of binary NS models: M_b is the total baryonic of system; M_∞ is the gravitational mass of each star at infinite separation; τ_{MNS} is the life-time of SMNS and HMNS unlike the prompt collapse to BH for which the final mass M_{BH} is reported; f_{peak} is the frequency of dominant oscillation peak in GW spectrum corresponding to l=m=2 modes. The label I and S denote irrotational and spinning NSs, UM refers to un-equal mass system and q to mass-ratio. The binary NS systems are generated at 100 Mpc. (From Tringali et al. 2017, in preparation).

incompressibility modulus K = 220 MeV (for this reason LS220) and for the two different nuclear physics EOSs, SHT and LS220, incorporate thermal effects and composition (electron fraction). In Figure 4.4 we report an overview of analyzed GW waveforms simulated at 100 Mpc and time-freqeuncy map for each EoS. We will come back to this in section 4.2.

The catalog contains four binary NS system which collapse to BH right after the merger: SHT-M2.2-I, LS220-M1.7-I, LS220-M1.8-I and APR4-HM. In all other cases, we have a short-lived HMSN, collapsing to BH in a few ms after merger; or long-lived NS remnant which can be SMNS (i.e collapse time $\gg$ 1 s), or indefinitely stable NS. The main parameters of binary systems and of the NS remnant are listed in Table 4.1: the gravitational

mass M_∞ of the isolated NS; the total baryonic mass M_b of each systems; the life-time τ_{MNS} of massive NS outcome; the frequency of dominant peak f_{peak} of GW spectrum and the final mass of BH. Note that model labels are chosen in order to facilitate the correspondence with the original references.

The models span in a wide range of mass values including equal and un-equal mass. The latter are labeled with the value of mass ratio q and UM label. The model of [113] are labelled by S and I referring to spinning (initial NS spins are aligned to the orbital angular momentum) and irrotational BNS systems, respectively; while all the others are irrotational. In the catalog magnetized models [111],[115] are included, however the effect of magnetic field are negligible for the purposes of the present analysis.

The time τ_{MNS} is the life-time of massive NS remnant defined as the difference between t_{BH}, which is the (coordinate) time the apparent horizon first appears, and t_m which is the time at which the separation is null and the stars merge reaching the first maximum of the rest mass density. The times reported in Table for the first two BNS models (forming a HMNS) refer to duration of their simulations because they end before the collapse to a BH.

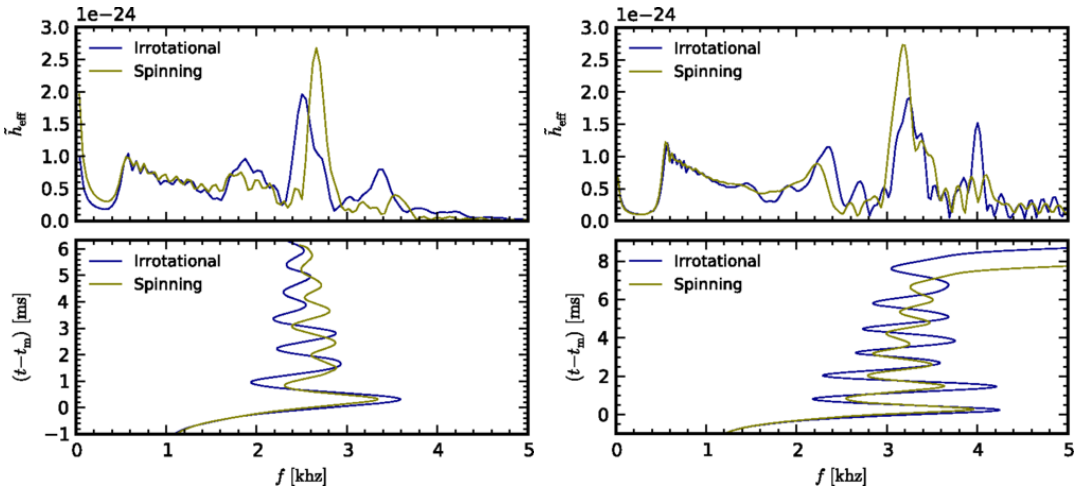

(a) SHT-M2.0-S EoS (b) LS220-M1.5-S EoS

Figure 4.1: (Top panel) GW strain spectrum at distance of 100 Mpc and (bottom panel) evolution of the corresponding instantaneous frequencies for spinning (green line) and not spinning (blue line) SHT-M2.0 and LS220-M1.5 models.

In Figures 4.1 we report the GW spectra (top panels) and the evolution of instantaneous frequencies (bottom panels). We consider, as examples, the spinning and irrotational models SHT and LS220. On the y-axis of top panels, they report $\tilde{h}_{eff}$ given by:

$$\tilde{h}_{eff} = \tilde{h}(f) f^{1/2}, \tag{4.1}$$

where $\tilde{h}(f)$ (see eq. 4.5) is the Fast Fourier transform (FFT) of GW signal and $f^{1/2}$ the frequencies. The GW spectral features are discussed in section 1.3.1 and in the Table 4.1, we report the values of dominant frequencies peak due to oscillation of quadrupole mode m=2. In Figure 4.1 for SHT and LS220 models, the GW strain spectrum $\tilde{h}_{eff}$ of spinning NSs is shifted with respect irrotational and the frequency shift is smaller than the width of the peak. This is due to the fact that the maximum instantaneous frequency reached during the merger is slightly smaller for the spinning models, which is related to the weaker radial oscillation (for more details see [113]).

4.2 Simulation of astrophysical populations of sources

In this chapter we want to describes the detection efficiency of the cWB pipeline in the configurations chosen for this specific search. Here, we want give an explanation of how the stage of simulation of NS binary waveforms works generating different (waveform) triggers. It consists on injecting simulated waveforms on simulated detector data.

cWB injections

We perform a uniform distribution in distance. Using cWB tool to injected the NR waveforms, we choose eleven values of distance in the range of 0.88 - 28.28 Mpc: [0.88, 1.25, 1.77, 2.5, 3.53, 7.07, 10, 14.14, 20, 28.28] Mpc. For each fixed distance, the tool injects a number of times the waveform on the each detector simulated data. In our analysis, cWB tool performs one injections of the BNS waveform every 100 sec. The injections have been distributed isotropically in the sky, see Figures 4.2(c) and 4.2(d), but at fixed distance, Figure 4.2, to technically simply the analysis to estimate the tools efficiency, that is calculated has function of distance.
In the chapter 2, we see that the interferometer's response depends on combination of two polarizations $h_+, h_\times$ and in turn the two polarizations depend on inclination angle ι of the orbit plane with respect the observer. As the Figure 4.2(b) shows, we performed a random distribution of this inclination angle for all binary NS waveforms including all possible orientation of the binary system.

The frequency range of the post-merger search is between 768-4096 Hz because our aim of this work, is to reconstruct post-mergere phases of the signal (this is better discussed in Chapter 5). The resolution levels of time-frequency map for post-merger

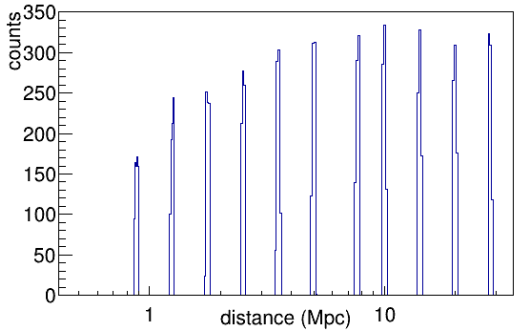

(a) Distribution in distance.

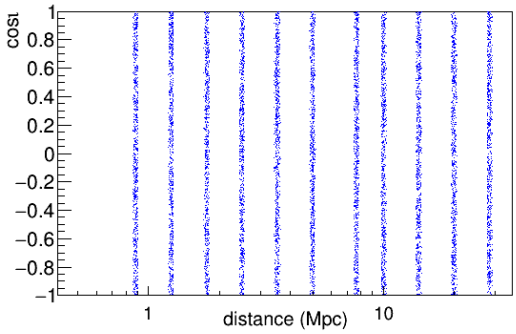

(b) Cosine distribution of ι angle at each distance

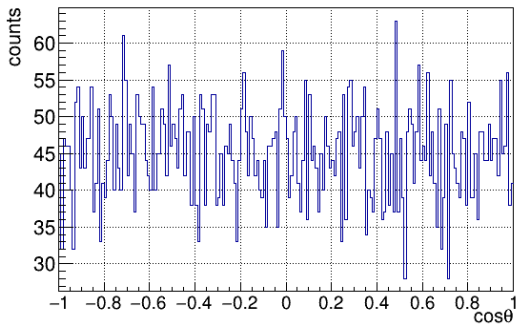

(c) Cosine distribution of θ angle.

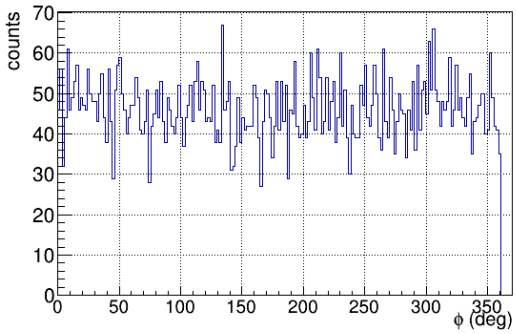

(d) Distribution of ϕ angle.

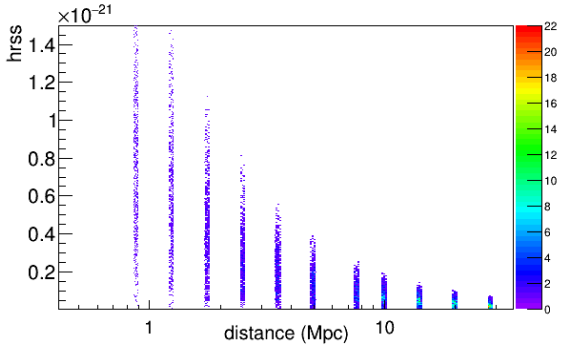

(e) Injected amplitude h_{rss} as function of distance values.

Figure 4.2: Parameters of injections of numerical relativity waveforms by cWB tools for SHT-M2-0-S model.

analysis range from level 3 referring to frequency and time resolutions dF = 512 Hz, dT = 0.97 ms, up to level 7 with dF = 32 Hz and dT = 15.62 ms. In the Table 4.2 are ported the values of other setting parameters [105]:

- netRHO: coherent network signal-t-noise ratio using by cWB tool to selected cluster of pixel during production stage;

- bpp: probability for pixel selection rapresents the fraction of most energetic pixels selected from the TF map to construct events.

Configuration	level	netRHO	bpp
1	3-8	4	0.0005
2	3-7	4	0.0005
3	3-8	4	0.002
4	3-7	4	0.002
5	3-8	4	0.001
6	3-7	4	0.001

Table 4.2: Tested configuration parameters of the post-merger search. level=3 corresponds to dF=512 Hz while level = 7 and 8 refer to dF=32 Hz and dF=16 Hz, dt=31.25 ms, respectively.

As it is reported in Figure 4.3, we have tested different configurations of cWB algorithms in order to improve the capability of identification of the BNS waveform in case of delayed collapse to BH and to reduce the false alarm rate (FAR) in case of prompt collapse scenario. For each plot we report the efficiency defined as

$$\varepsilon = \frac{N_{rec}}{N_{inj}}, \tag{4.2}$$

where N_{rec} is the number of reconstructed events and N_{inj} the number of injected events by cWB tool respectively (in our case, the term *event* refers to gravitational signal of BNS system analyzed). The estimate of the standard deviation for efficiency value is given by standard deviation for a binomial distribution:

$$\sigma_\varepsilon = \frac{\sqrt{N_{rec}(1-\varepsilon)}}{N_{inj}}. \tag{4.3}$$

The simulated noise employed for the post-merger analysis is in according to design curve of advanced LIGO (aLIGO) and advanced Virgo (AdV)reported in the Figure 1 (black curve) of reference [16] corresponding to sensitivity distance of 200 Mpc and 130 Mpc for aLIGO and AdV respectively.

4.3 Injection of astrophysical waveforms

As discusse above, to develop our analysis tool of post-merger signal, we used a catalog collecting light and heavy BNS systems in which a direct collapse to BH occurs or a massive NS is formed (HMNS or long-lived NS, which, in turn, can be a SMNS or a

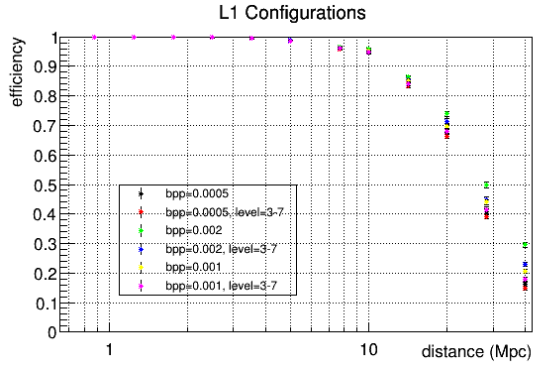

(a) Tested setups of L1 detector for delayed collapse scenario.

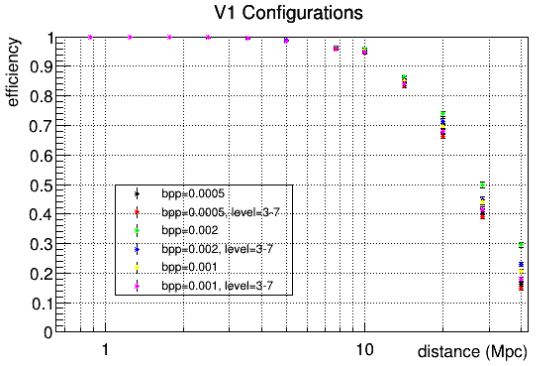

(b) Tested setups of V1 detector for delayed collapse scenario.

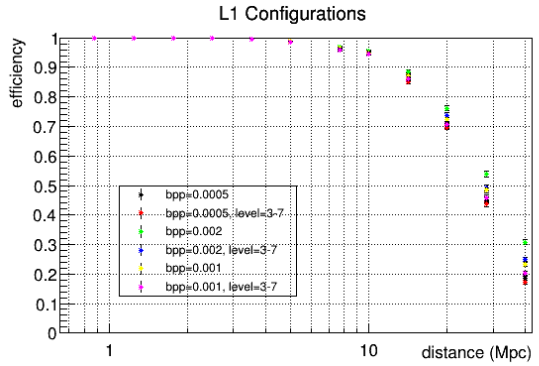

(c) Tested setups of L1 detector for prompt collapse scenario.

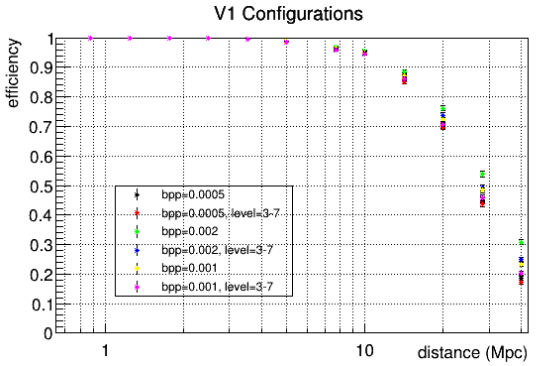

(d) Tested setups of V1 detector for prompt collapse scenario.

Figure 4.3: Tested configurations of cWB for two case studies: SHT-M2.0-S (delayed collapse to BH) and SHT-M2.2-I (prompt collapse to BH). We report the values of ε=N_{rec}/N_{inj} at each configuration as function of distances for Livingstone L1 (left) and Virgo V1 (right) detectors.

stable NS).

In Figures 4.4-4.21 we report the GW strain for h_+ component and its representation in time-frequency map for models of catalog. In order to highlight the features of signal, we chose an optimal distance values equal to $\sim$ 3 Mpc. Because of the oscillation mode m=2, l=2 turns out to be the dominant one with respect the other modes, we inject only l=m=2 mode of GW components $h_{+,\times}$.

The GW signal extracted by NR group (in Newman-Penrose formalism [124]) is given by [9]:

$$h_{+,\times} = \sum_{l=2}^{\infty} \sum_{m=-l}^{l} h^{lm}_{+,\times} \; {}_{-2}Y_{lm}(\theta,\phi) \approx h^{22}_{+,\times} \; {}_{-2}Y_{22}, \tag{4.4}$$

where ${}_sY_{lm}(\theta,\phi)$ are the spin-weighted spherical harmonics [125]. They define the power

spectral density of the effective amplitude as

$$\tilde{h}(f) \equiv \sqrt{\frac{|\tilde{h}_{+}(f)|^2 + |\tilde{h}_{\times}(f)|^2}{2}}, \tag{4.5}$$

with $\tilde{h}_{+,\times}(f)$ the FFT of two GW polarizations

$$\tilde{h}_{+,\times}(f) \equiv \int_{-\infty}^{\infty} h_{+,\times}(t) e^{-i2\pi ft} dt \tag{4.6}$$

We remember that, as discussed in section 1.3.1, the dominant frequency peaks of NS remnant in GW spectrum are due to quadrupole oscillation mode m=2 and in turn these form a triplet of frequency peaks generating by nonlinear coupling to the fundamental quasiradial m=0.

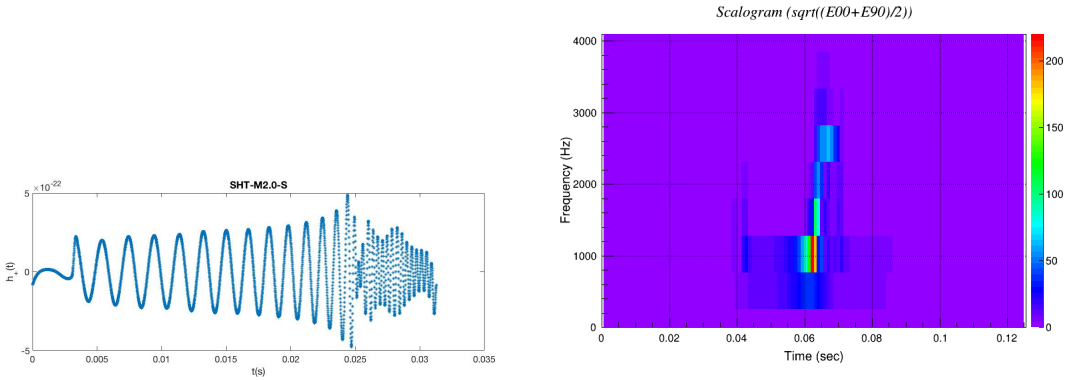

Figure 4.4: Gravitational wave strain h_+ of oscillation mode m=l=2 at distance100 Mpc for waveform model SHT-M2.0-S and TF map at optimal distance of $\sim$ 3Mpc.

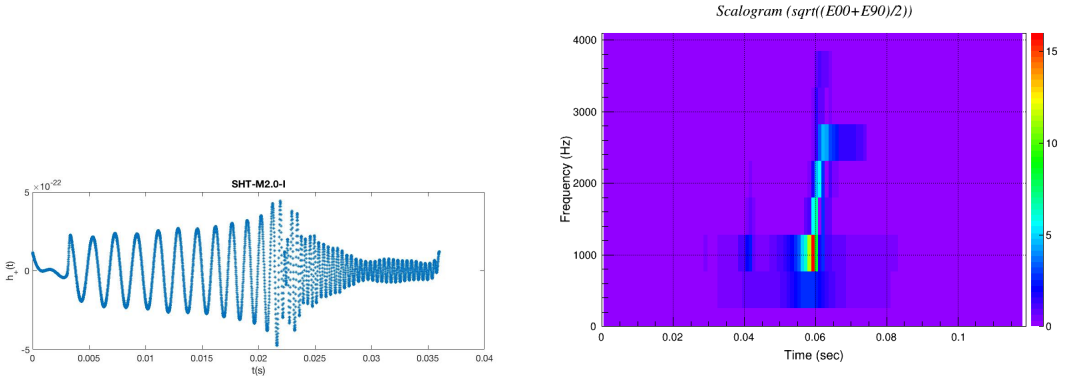

Figure 4.5: Same plots for waveform model SHT-M2.0-I.

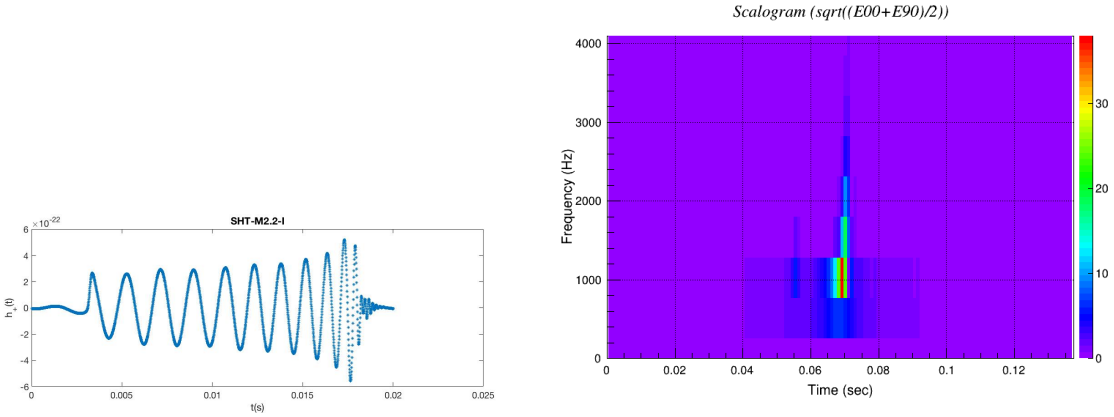

Figure 4.6: Same plots for waveform model SHT-M2.2-I.

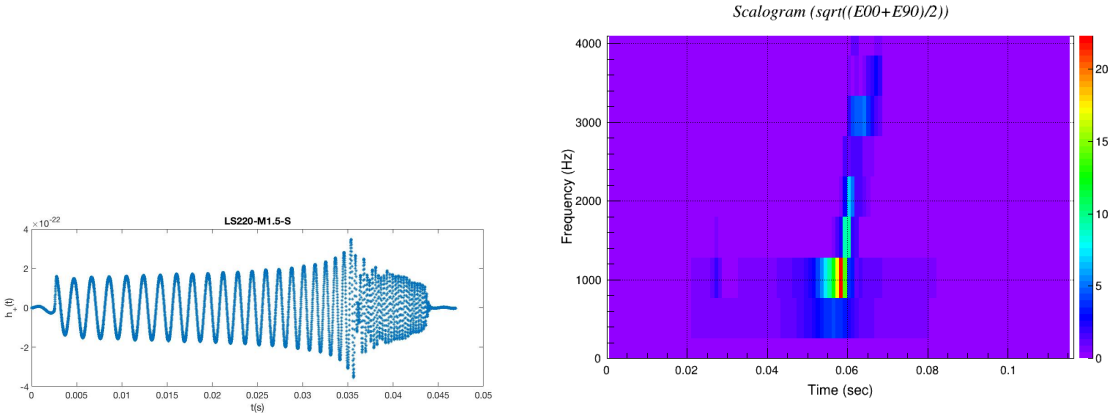

Figure 4.7: Same plots for waveform model LS220-M1.5-S.

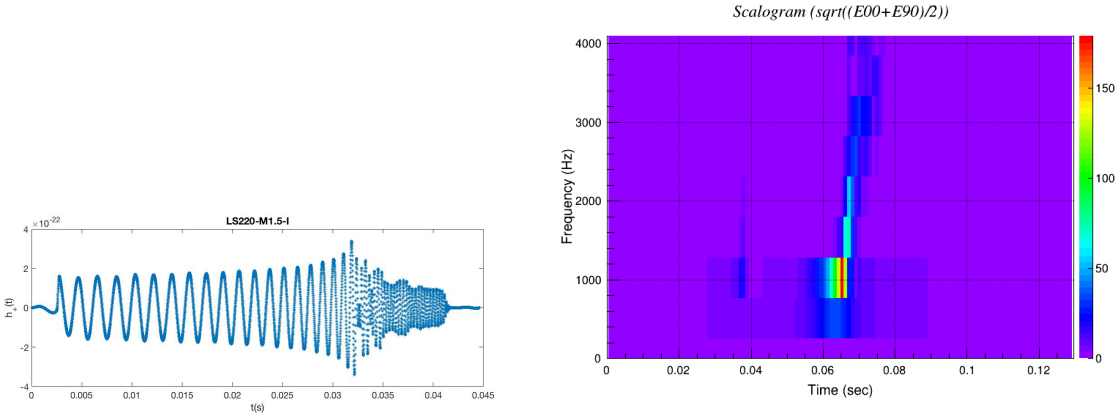

Figure 4.8: Same plots for waveform model LS220-M1.5-I.

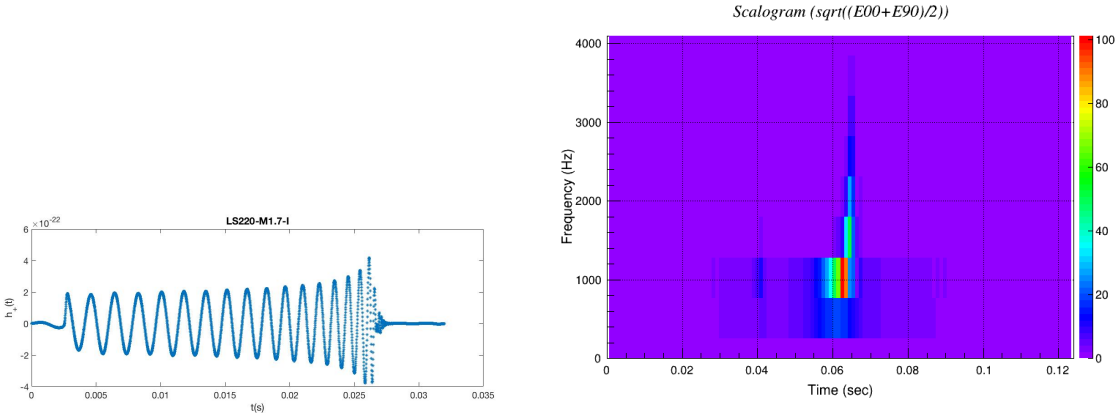

Figure 4.9: Same plots for waveform model LS220-M1.7-I.

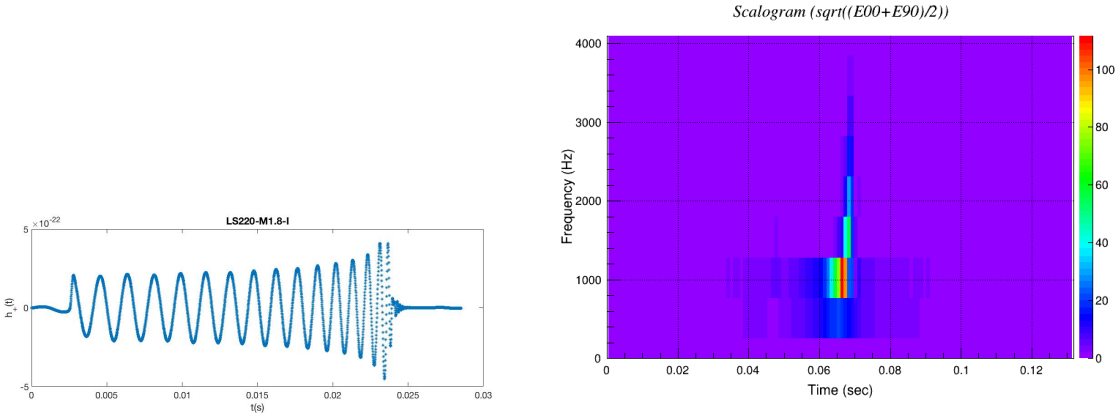

Figure 4.10: Same plots for waveform model LS220-M1.8-I.

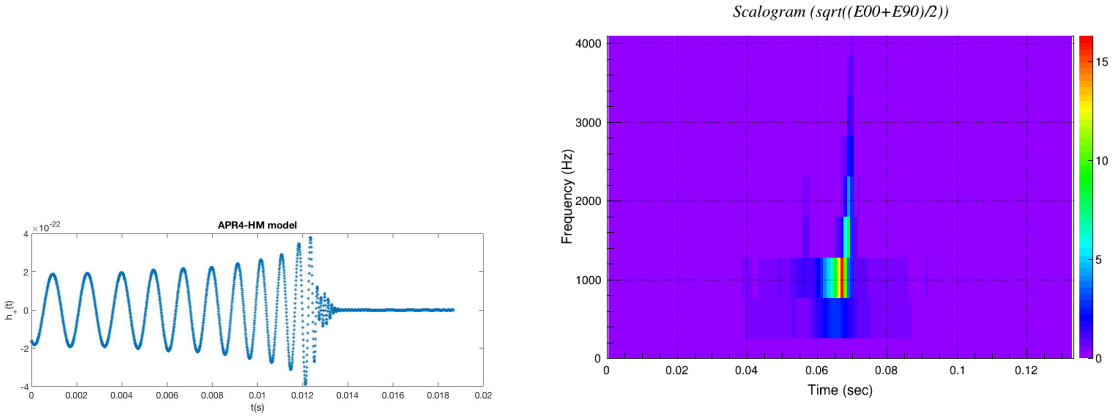

Figure 4.11: Same plots for waveform model APR4-HM.

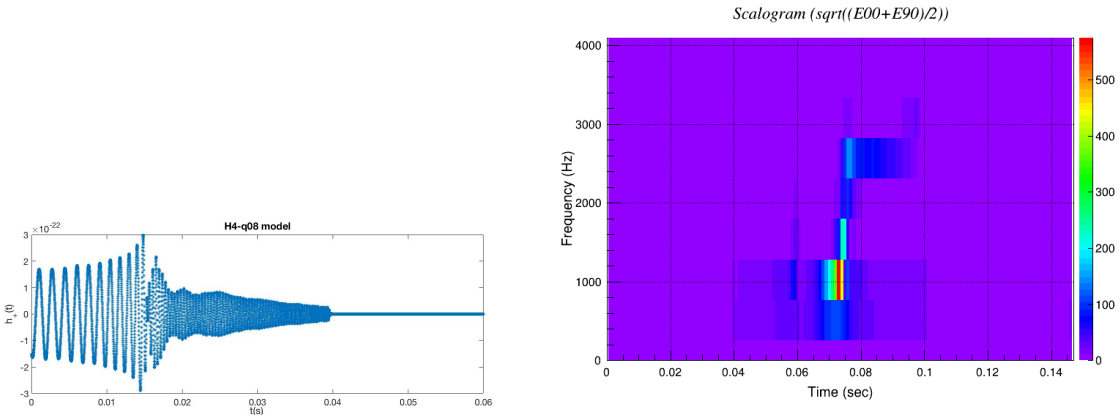

Figure 4.12: Same plots for waveform model H4-q08.

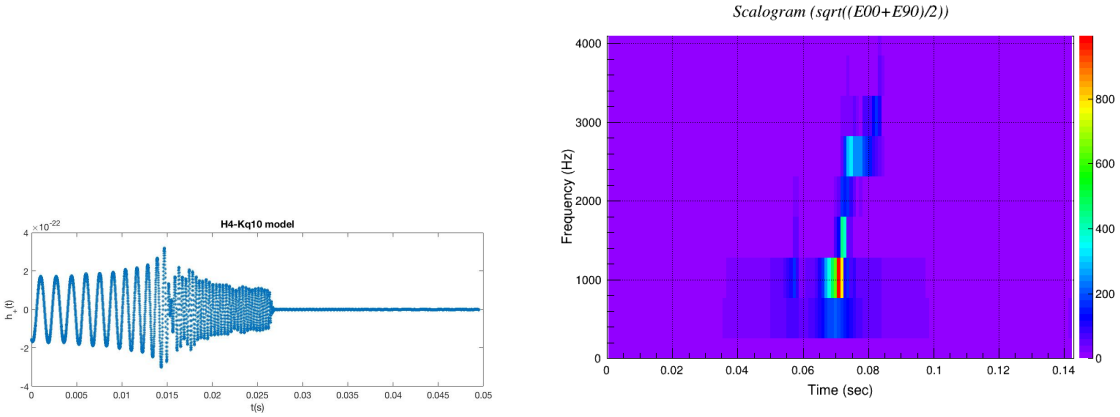

Figure 4.13: Same plots for waveform model H4-M1.5.

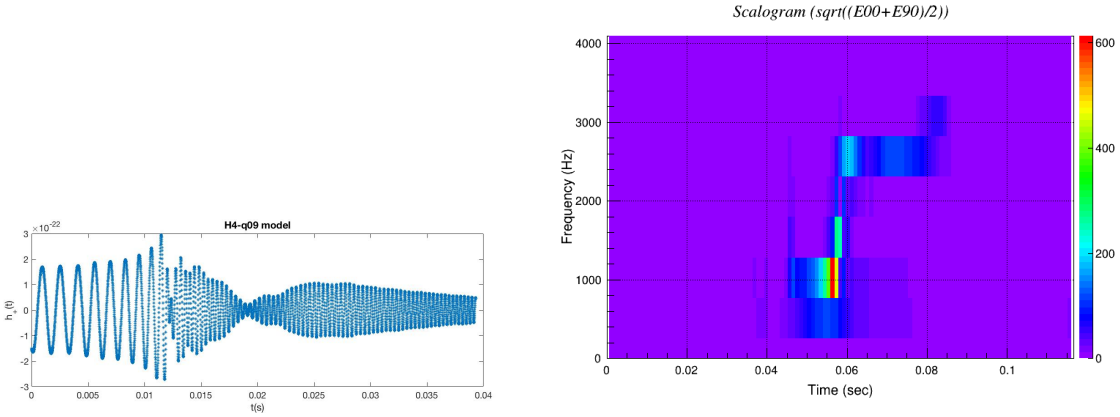

Figure 4.14: Same plots for waveform model H4-q09.

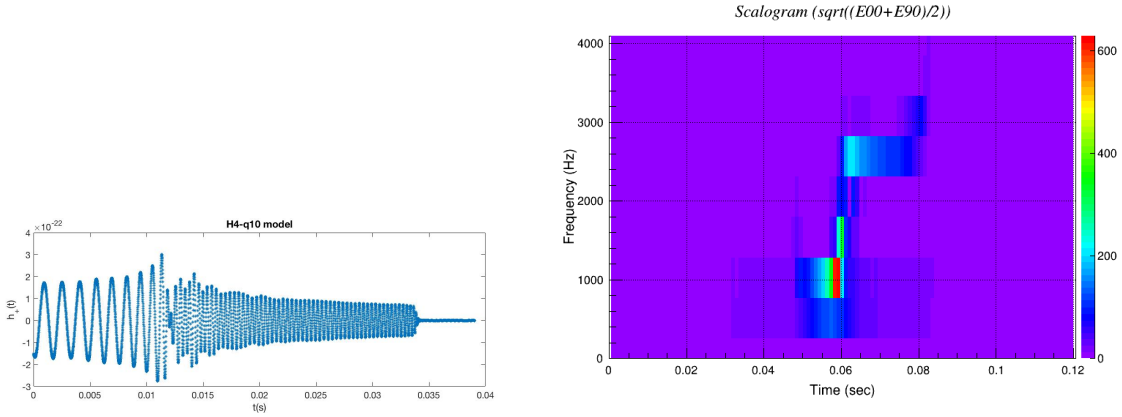

Figure 4.15: Same plots for waveform model H4-M1.4.

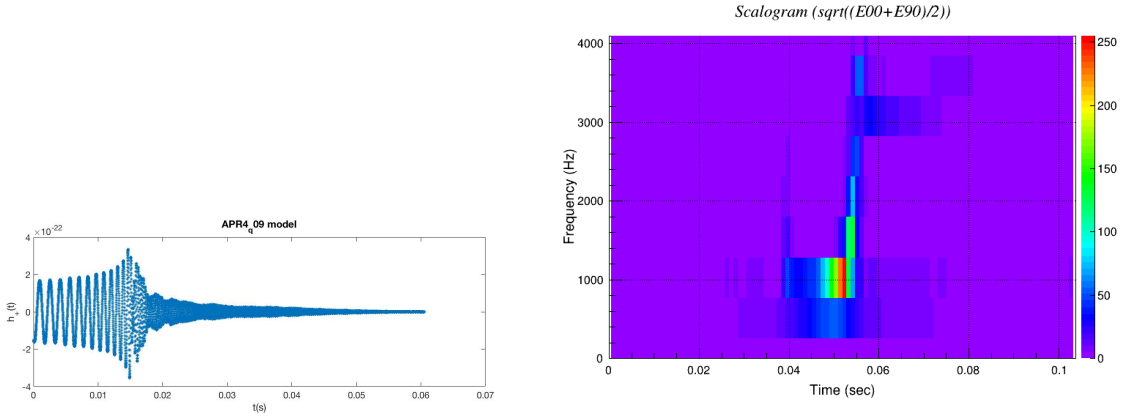

Figure 4.16: Same plots for waveform model APR4-q09.

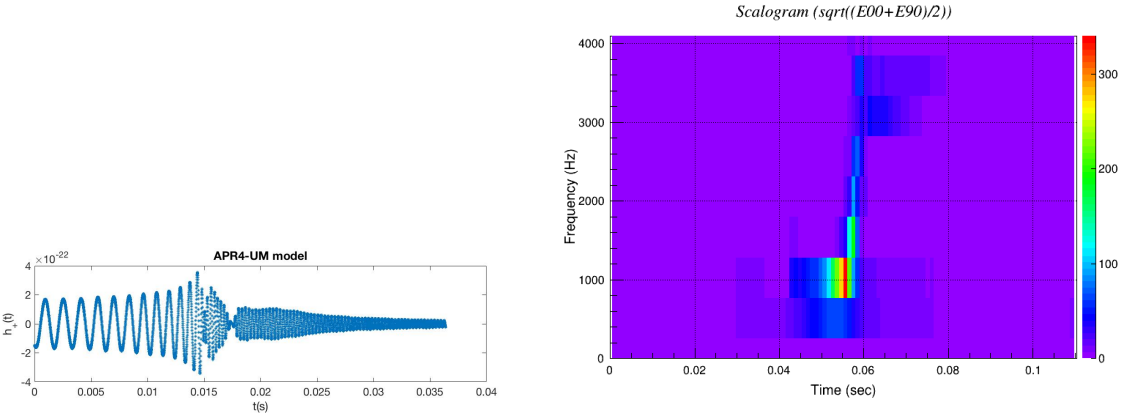

Figure 4.17: Same plots for waveform model APR4-UM.

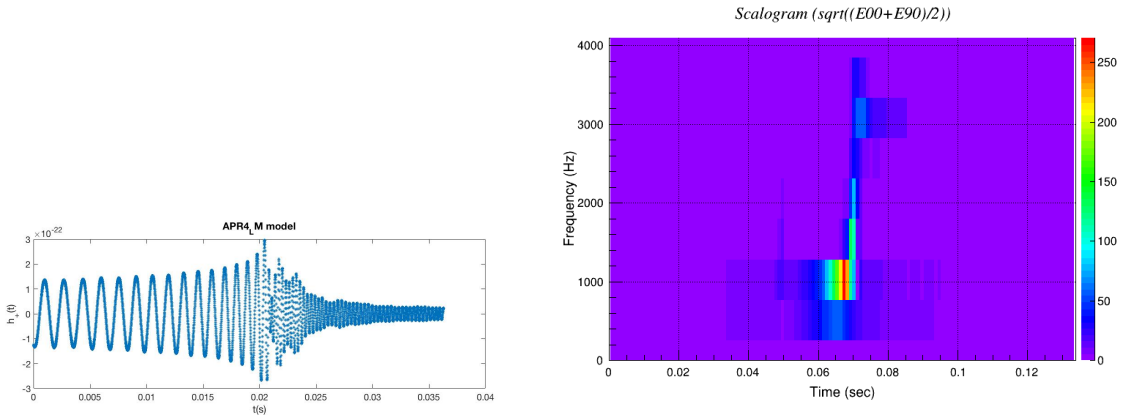

Figure 4.18: Same plots for waveform model APR4-LM.

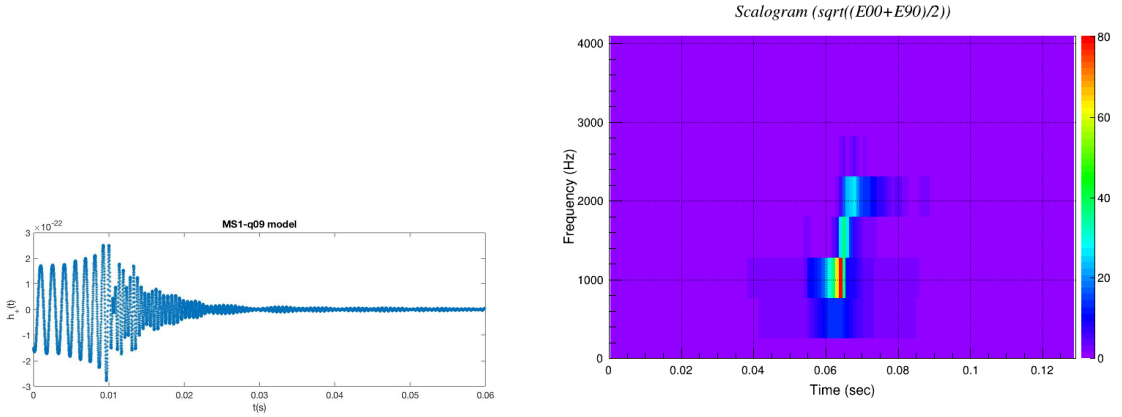

Figure 4.19: Same plots for waveform model MS1-q09.

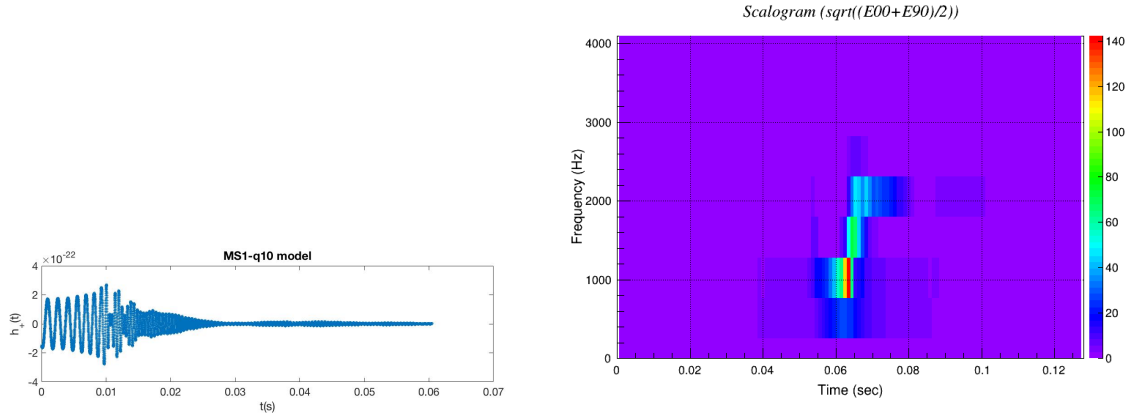

Figure 4.20: Same plots for waveform model MS1-M1.45.

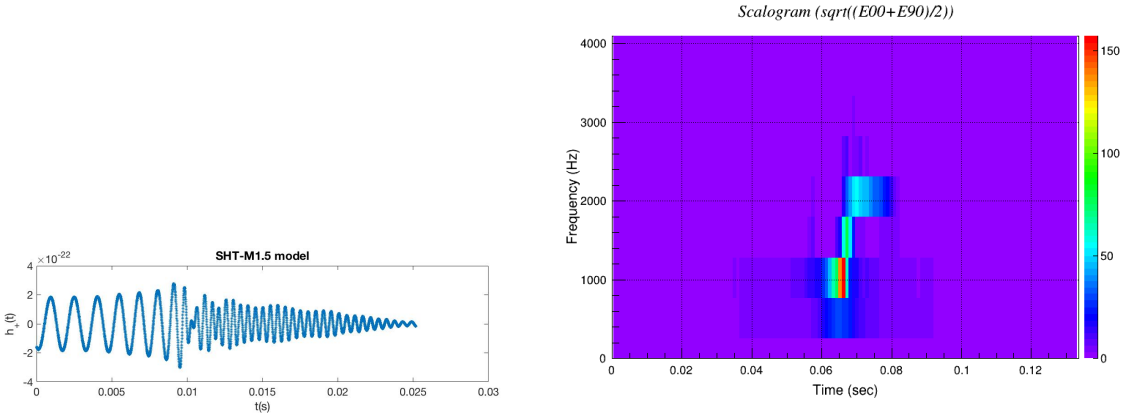

Figure 4.21: Same plots for waveform model SHT-M1.5.

Chapter 5

Tool for reconstruction of neutron star post-merger signals

In *chapter 5*, we describe the method developed to select and to characterize the post-merger signals. For each candidate event by by BNS system, the tool discriminates post-merger signals generated by HMNSs or long-lived NSs from the prompt collapse (to a BH) case at fixed statical significance. The discrimination criteria are based on the investigation of signal in the different time-frequency regions. In case a PM signal from BNS coalescence is found, the tool estimates its main parameters, such as the dominant frequency peak.

5.1 General view of procedure about the reconstruction of post-merger phase

The follow up procedure to reconstruct the post-merger phase performs a coherent wave burst (cWB) multi resolution analysis in frequency band (768-4096) Hz. The choice of low frequency value 768 Hz is motivated by the fact that we want to analyze and reconstruct the post-merger signal of gravitational waveform of each binary system, and as we have seen in section 1.3, GW signals from remnant NSs arise at frequencies higher than $\sim 1\ kHz$. Therefore in this analysis of post-merger, we decided to focus on late in-spiral phase and post-merger one. Furthermore, the band frequency region including in-spiral phase, should reconstruct the whole gravitational signal with SNR due to in-spiral signal and this could miss the post-merger part being a faint signal respect to the entire one.
Before going further, we introduce a couple of definitions used in this chapter. The time-

frequency (TF) map is the time frequency representation using the Wilson-Daubechies time-frequency transform [110]. The map representation is sketched in Figure 5.1(a). Each pixel is identified by vertical and horizontal lines corresponding to *slices* and *layers* respectively as figure 5.1 shows. Pixel dimensions in frequency and time domain are the resolution of the map.
In Table 5.1, we report the lower and upper frequency values of each corresponding layer, its central frequency and the number of layers N, respectively. The latter (see eq.(5.1)) is related to the TF map resolution, in this case dT = 0.98 ms and dF = 512 Hz. The central frequency of layer pixel is equal to N*dF. Instead, for the first and last pixel of map (in our case, layer 0 and layer 8), their frequency widths are equal to dF/2 (128 Hz and 3968 Hz, respectively).

Layer	**Frequency Range (Hz)**	**Central Frequency (Hz)**
0	0 - 256	128
1	256 - 768	512
2	768 - 1280	1024
3	1280 - 1792	1536
4	1792 - 2304	2048
5	2304 - 2816	2560
6	2816 - 3328	3072
7	3328 - 3840	3584
8	3840 - 4096	3968

Table 5.1: It is reported the number of layers, their frequency range and central frequency for TF map with resolution dF= 512 Hz.

Once cWB tool performs a multi resolution analysis in (768-4096) Hz, the following step is the division of the time-frequency map (TF map) for each reconstructed event. The time frequency map of the signal is performed at fixed resolution dF= 512 Hz and dT= 0.98 ms. An example of TF map for SHT-M2.0-S waveform model with a PM is reported in Figure 5.2. The aim of analysis is the identification of the signal of NS remnant, in order to analyze the corresponding portion of the map and to perform parameter estimation. As Figure 5.2 shows, cut in time and frequency are applied to the TF map to divide it in four quadrants labelled with Roman numeral I, II, III, IV clockwise. The value chosen as cut in frequency domain, *freq_cut*, is 1280 Hz (it corresponds to edge pixel). From the map, we observe that layers below freq_cut value, contain the part of the signal generated by late in-spiral/merge phase; therefore the choice of 1280 Hz is the most appropriate to separate the post-merger phase from merger one. We will explain the procedure to define time cut later. Then, similarly, the region III

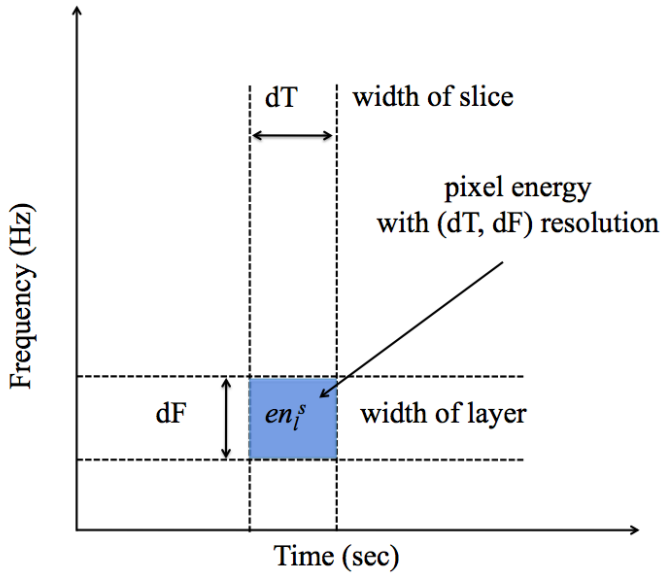

(a) Representation of time-frequency map.

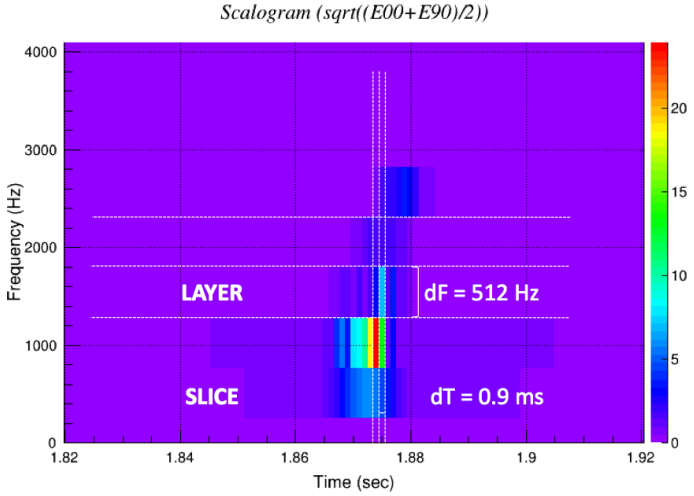

(b) Time-frequency map.

Figure 5.1: The top plot is a schematic view of T-F map. Dimension of each pixel are the time dT and frequency dF resolution of the map. On the bottom, it is reported a TF map for reconstructed GW signal including post-merger for SHT-M2.0-S model. On the map, time dT=0.98 ms and frequency dF= 512 Hz resolutions are reported together to slices and layer.

of the TF map is studied to improve the capability to figure out the morphology of the event reconstructed.

The following step is the analysis of the third quadrant in order to extract the frequency informations of the reconstructed signal such as the dominant frequency peak seen in the section 1.3.1. A specific analysis in frequency is performed using different resolution of the reconstructed map so that spectral features can be obtained.

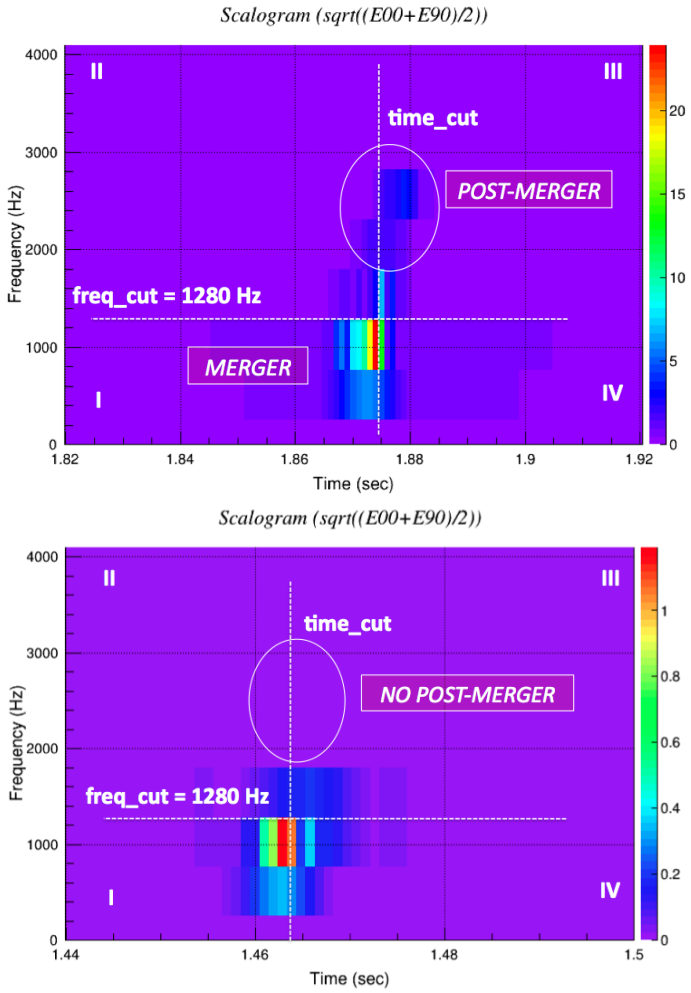

Figure 5.2: Two examples of TF map for GW signals in L1 detector reconstructed by cWB pipeline referring to SHT-M2.0-S waveform model corresponding to a binary system with HMNS remnant. Both maps report the division in four quadrants. The vertical and horizontal dot line are the freq_cut and time_cut computed by tool. On the top an event with post merger phase reconstructed, on the right ones with it missed.

In this section, we discuss about procedure of post-production analysis built to compute the value of the parameter time_cut used to divided the T-F map of each reconstructed event. Starting from T-F map of reconstructed event in each single detector, the first step of cWB tool is to compute the energy of the layers. The number of layers is related to frequency resolution of the map:

$$N = \frac{Rate}{2 * dF}, \tag{5.1}$$

where *Rate* is the sampling rate equal to 8129 Hz and dF= 512 Hz is the frequency resolution map choosen.

The energy of layer En_l is defined by

$$En_l = \sum_s en_{ls} \tag{5.2}$$

where l is resolution level and s time pixels, while en_{ls} is pixel energy of l-th layer s-th slice (see fig.5.1).

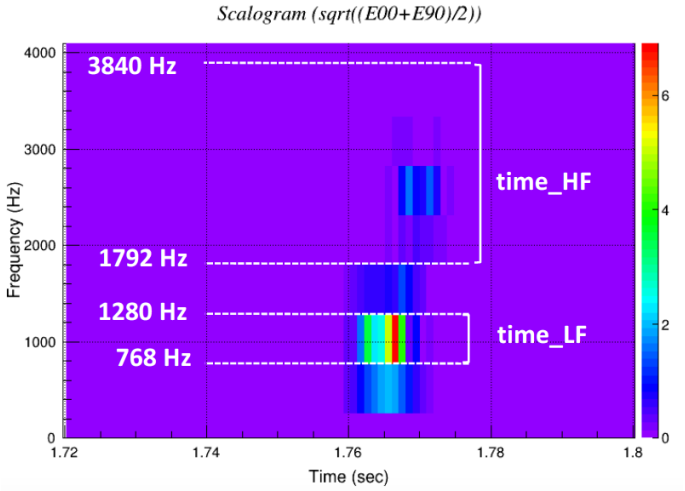

Figure 5.3: In T-F map, the two definitions of time at low frequencies 768-1280 Hz and at high frequency 1792-3840 Hz are reported.

For each layer l, a time weighted $\bar{t}_l$ by energy is computed as:

$$\bar{t}_l = \frac{\sum_{s=1}^{M} t_{pixel} \cdot en_{ls}}{En_l}. \tag{5.3}$$

At this point, the routine computes two values of time, see Figure 5.3. One at low frequency $time\_LF$ defined as the time at which the 50% of energy is reached in frequency band (768-1280) Hz and another time at high frequency $time\_HF$ as

$$time\_HF = \sum_{l=4}^{M} \frac{\bar{t}_l}{En_l}, \tag{5.4}$$

the average time weighted by energy considering frequency band (1792-3840) Hz and with l=4,..,8.

At this point, the procedure for each reconstructed event verifies the so-called *post-merger time condition*:

$$time\_HF - time\_LF > 2dT. \tag{5.5}$$

As it is reported in Figure 5.4, if the PM time condition is fulfilled, then the time_cut turns out to be the time average of time_LF and time_HF, in otherwise if this condition is not verified the time_cut is time_LF.

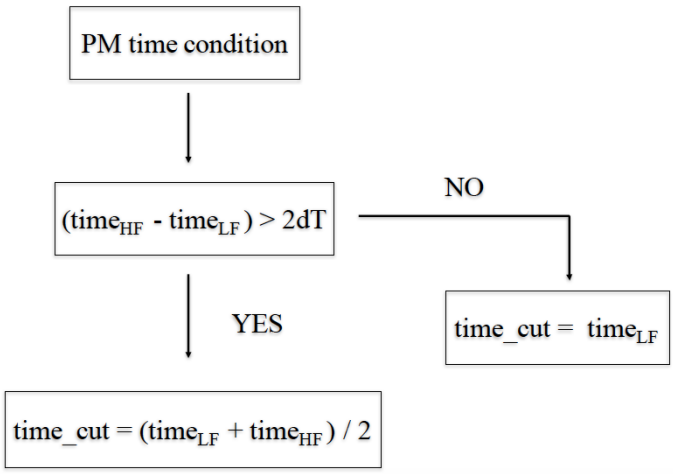

Figure 5.4: The diagram summarizes the procedure to calculate time_cut.

After the division of the map in four quadrants, the tool proceeds with analysis of the third region which contains the post-merger signal emitted by binary system. In particular, we performed an further division of III quadrant identifying a *high frequency* part (HF) with frequencies in the range $1792 < \mathrm{f} < 4096$ Hz and *low frequency* (LF) part for frequency values in $1280 < \mathrm{f} < 1792$ Hz, respectively.
In turn, these two belts of TF map are classified as *early* and *later* taking into account the time values, time_*cut* and time_HF, computed by the tool in previous step:

$$\begin{aligned} LFE &\longrightarrow \quad 1280 < f < 1792Hz,\ time\_cut < t < time\_HF \\ LFL &\longrightarrow \quad 1280 < f < 1792Hz,\ t > time\_HF \\ HFE &\longrightarrow \quad 1792 < f < 4096Hz,\ time\_cut < t < time\_HF \\ HFL &\longrightarrow \quad 1792 < f < 4096Hz,\ t > time\_HF \end{aligned}$$

The plot of Figure 5.5(a) shows this schematic division of third quadrant and different colors refer to four parts of this TF region while the bottom plot 5.5(b) is an example of reconstructed TF map for SHT-M2.0-S model in which we point out HFE, HFL, LFE

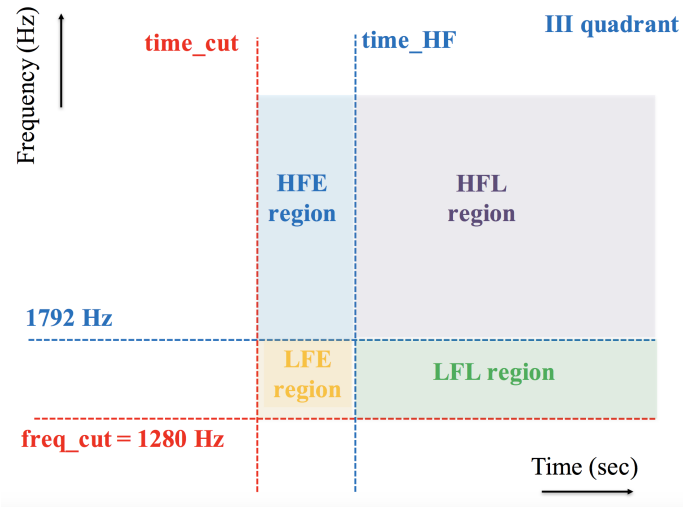

(a) The different colors indicate the four section in the portion of TF map of third quadrant: HFE (light blue), HFL (light violet), LFE(yellow) and LFL (green)

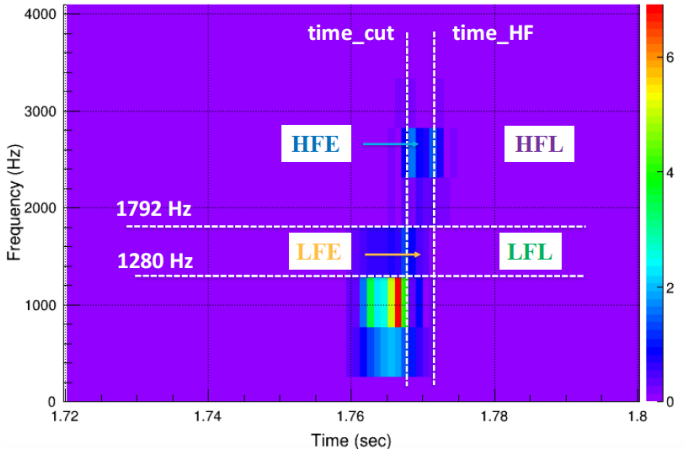

(b) Time-Frequency map of a reconstructed event for SHT-M2.0-S model in which is reported the further division of third region.

Figure 5.5: In both plots, it is sketched the further regions identifying in third quadrant of TF map of reconstructed GW signal.

and LFL sections.

For each of these regions of TF map, we compute the corresponding energy which lie within and we define two quantities of which we will discuss later: the energy En_{HF} given by sum of the pixel energies of two portions HFE and HFL and the energy energy En_{LF} given by sum of the pixel energies of LFE and LFL regions.

5.2 Criteria for discriminating an observed post-merger signal

In this section, we see the criteria using to discriminate the presence or not of a signal of post-merger phase generated by HMNS from that one by BH. At the same time, this mean to verify the capability of tool to distinguish a delayed collapse to BH from prompt collapse to BH right after merger.

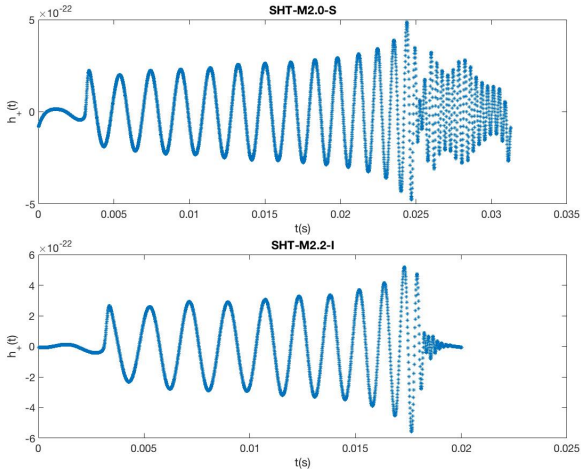

Figure 5.6: Two gravitational waveforms for a couple of SHT EoSs used as case studies are reported. Waveforms simulate a binary NS system coalescence with a prompt and delayed collapse to BH. In particular, waveform SHT-M2.0-S (on the top panel) with total mass M_{tot}= 4 $M_{\odot}$ forms HMNS which survives for $\sim$ 6ms. On the bottom panel, waveform SHT-M2.2-I (on the bottom panel) simulates a binary NS system with M_{tot}= 4.4 $M_{\odot}$ whose merger generates a BH remnant.

We use two case studies of gravitational waveforms reported in Figure 5.6 corresponding to two scenarios: SHT-M2.0-S (top panel) for a binary NS system which forms HMNS and SHT-M2.2-I for a binary NS system which collapse to BH right after coalescence of two compact objects.

As reported in previous section, the tool divides the map of each reconstructed event in four time-frequency regions. Observing both plots of Fgiure 5.2, we expect that quadrant III contains a post-merger signal in case in which a NS remnant is present and does not contain signal if a prompt collapse scenario occurs. Furthermore, the quadrant I collects the signal of last orbits of in-spiral and merger phases and instead we do not expect signal in quadrant II and IV; anyway noise fluctuations or excess of power in the late in-spiral and merger phase, can mimic signal in this part of the time frequency region. Thus, we look for post-merger signal and in order to discriminate the two scenarios, we

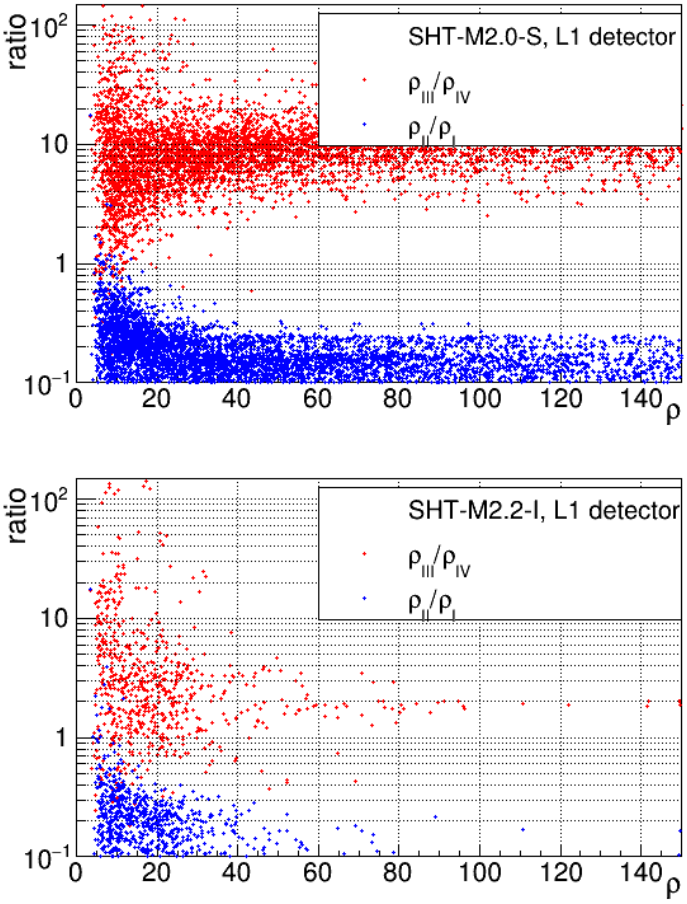

Figure 5.7: For both cases, ratio ρ_{III}/ρ_{IV} with red dots and ρ_{II}/ρ_{I} with blue dots are reported in function of coherent energy ρ for events that fulfilled the PM time condition.

calcolate the percentage of TF energy separately in each quadrant and we renormalize the value of the detection statistic ρ for each quadrant. The detection statistic ρ is an estimate of coherent energy signal-to-noise ratio (SNR) in the detector network. Thus, we define these percentage of energy as $\rho En_l/E_{tot}$ where for each region of TF map we consider the following values of frequency and time:

$$\begin{aligned} \rho_I &\longrightarrow f < freq\_cut,\ t < time\_cut \\ \rho_{II} &\longrightarrow f > freq\_cut,\ t < time\_cut \\ \rho_{III} &\longrightarrow f > freq\_cut,\ t > time\_cut \\ \rho_{IV} &\longrightarrow f < freq\_cut,\ t > time\_cut \end{aligned}$$

In Figure 5.7, we can see how delay collapse and prompt collapse to BH differ in the energy distribution in the TF map region.

In this Figure, we report the ratios ρ_{III}/ρ_{IV} (red dots) and ρ_{II}/ρ_{I} (blue dots) of the energy of respective TF regions as function of reconstructed coherent energy ρ of the BNS gravitational wave signal. Observing the two plots, thus, it is inferable that the ratio ρ_{II}/ρ_{I} does not distinguish the presence or not of HMNS in post-merger signal. The parameter, indeed, that is able to do this separation between NS and BH remnant, is ρ_{III}/ρ_{IV}. Comparing the red dots in both waveforms, as expected, at low values of ρ there is not a good discrimination, due to the fact that reconstruction of the signal is not optimal; instead for high values of detection statistic ρ, the scenario with HMNS remnant becomes clear because of we have a better reconstruction of post-merger signal by cWB tool.

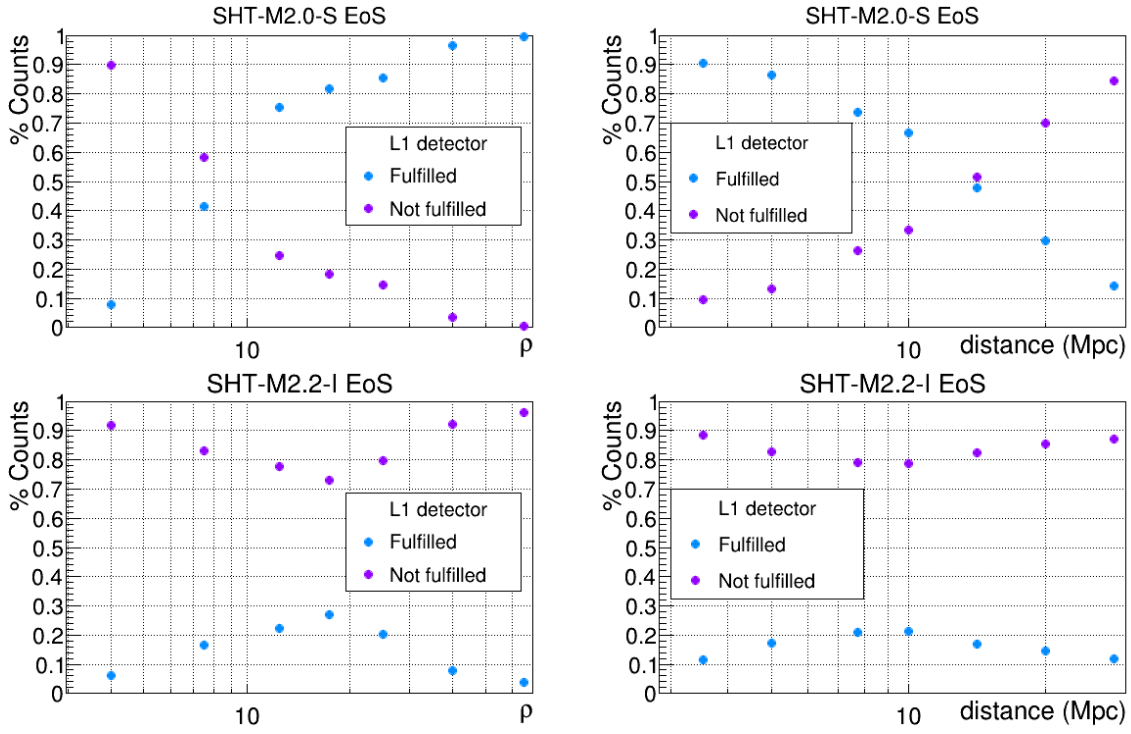

Figure 5.8: Blue dots mark the case in which the PM time condition is fulfilled while violet dots the opposite one. The same marker are showed for two case studies.

The plots in Figure 5.8 report the fraction of events that fulfil (blue dots) or not (violet dots) the PM time condition as function of reconstructed coherent energy ρ and distance values, respectively. In case of waveform SHT-M2.0-S with HMNS as remnant, in Figure 5.8 (top row), the value of $\rho \simeq 7$ is a turning point at which the behavior of

two efficiency curve changes. At values lower then $\rho \lesssim 7$, the procedure reconstructs $\sim 60\%$ event as event without post merger signal. This is in agreement with the top plot of previous Figure 5.7 where for low values of ρ and of ratio $\rho_{III}/\rho_{IV} \lesssim 0.5$, we can see that there is a dense population of event. At $\rho \gtrsim 7$, the number of event reconstructed as event with post-merger increases. This is not a surprise: the post-merger signal is faint signal with respect to whole evolution phases of binary NS system and to reconstructed it, high values of signal to noise ratio are necessary. On the left plot of Figure 5.8, we observe the same behaviour with a turning-point at distance of ∼15 Mpc: at distances greater than 15 Mpc, the events are wrongly identified without a PM signal. Unlike the delayed collapse scenario, in case of waveform SHT-M2.2-I with a prompt collapse to BH, there is a clear trend of efficiency curve as we expected: also for low value of ρ, the PM time condition is not fulfilled or rather, the tool reconstructs most of the events as events which collapse to BH. The same occurs also in case of efficiency as function of distance.

5.3 Discrimination of delayed and prompt collapse scenarios

In section 5.2 we have discussed about the discrimination of delayed collapse to BH. The first step, to claim if a GW signal by HMNS/SMNS is present or not, is done using the ratio parameter ρ_{III}/ρ_{IV}, as reported in Figures 5.7.
A further analysis is performed by studying in detail the third quadrant of TF map for each event in which the PM time condition is fulfilled. Also in this case, we take the two case studies SHT-M2.0-S and SHT-M2.2-I EoS for two scenarios. We consider the division of third quadrant in high frequency and low frequency regions defined in section 5.1. We report the behaviour of the signal energy in Figure 5.9 and 5.10. In both Figures, on the right side, we report the behaviour of another two parameter, as function of ρ_{III}/ρ_{IV}:

- percentage of the energy in TF map in frequency range 1280 - 1792 Hz and t >time_*cut* normalized to energy ρ_{III} of whole third quadrant, ρ_{LF}/ρ_{III} (black markers);

- percentage of the energy in TF map in frequency range 1792 - 4096 Hz, t >time_*cut*, ρ_{HF}/ρ_{III} (red markers).

This plot show how the energy of third quadrant is distributed in both scenario and at the same time, it is an further indicator of presence of possible GW post-merger signal. In particular, we point out that the bahaviour of ρ_{HF}/ρ_{III} and ρ_{LF}/ρ_{III} are opposite in case of delayed collapse to BH (SHT-M2.0-S) and prompt collapse to BH (SHT-M2.2-I), respectively. This does not surprise us: we remember that in the so-called high frequency part of third quadrant we expect post-merger signal of HMNS/SMNS. Of course, for low values of ρ_{III}, the two distributions are mixed, the post-merger phase is not well identified as post-merger signal and in case of prompt collapse, post merger signal can be wrongly identified.

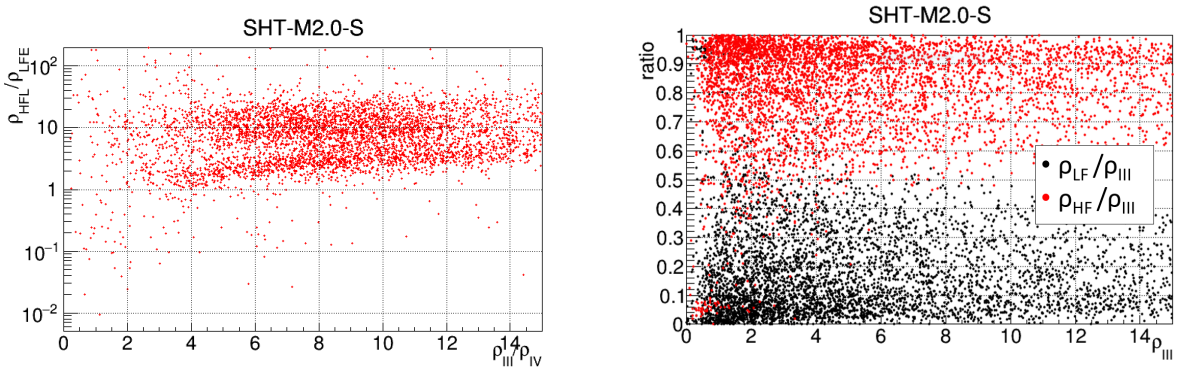

Figure 5.9: Analysis of third quadrant for SHT-M2.0-S model.

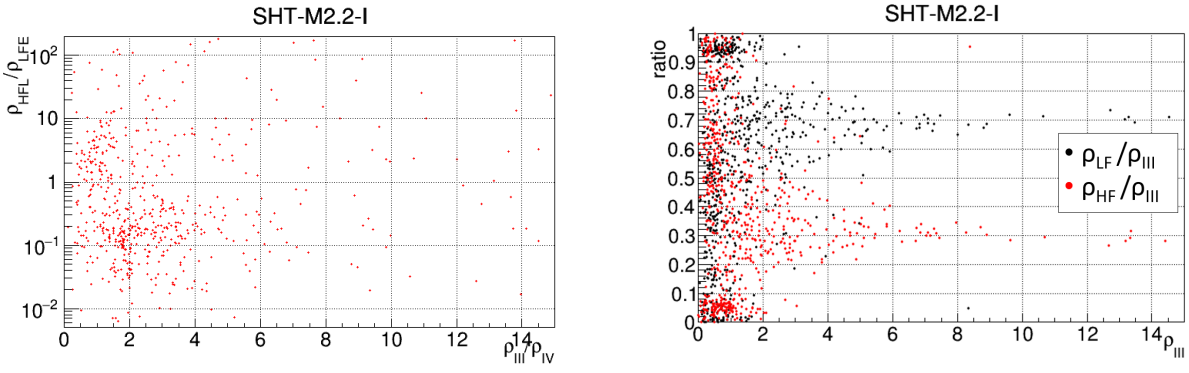

Figure 5.10: Analysis of third quadrant for SHT-M2.2-I model (reconstructed events that fulfilled PM time condition).

The left plots in Figures 5.9 and 5.10, show the behaviour of ration between ρ_{HFL} and ρ_{LFE}, ρ_{HFL}/ρ_{LFE}, as function of parameter ρ_{III}/ρ_{IV}.
We observe a trend for the case of delayed scenario for ratio values above one. We remember that the HFL is a region of third quadrant TF map at frequencies above 1792

Hz and times after the time_HF given by eq. 5.4. This ratio parameter is an indicator of presence of GW signal by HMNS or SMNS remnant and its time evolution. In case of prompt scenario, at low values of ρ_{III}/ρ_{IV}, we see a scattered behavior in contrast to other scenario and we have $\rho_{HFL}/\rho_{LFE} < 1$ except some cases in which the tool identified a post-merger scenario.

5.4 Parameter estimation for reconstructed post-merger signals

In this section we introduce the tool developed to estimate the features of post-merger signals such as the frequency of the dominant peak.

5.4.1 Frequency peak of post-merger signal

For what concerns the estimate of dominant frequency peak, we start by computing a power spectral density of the reconstructed gravitational wave. The power spectrum is estimated performing a Fast Fourier transform (FFT) on the relevant frequency range, 1280-4096 Hz. In this frequency range, the tool looks for the maximum in the power spectrum and fits a gaussian in its neighbourhood. The resulting gaussian mean is taken as the estimate of the dominant frequency peak.

Chapter 6

Results with simulated data

This chapter describes the tests aiming to characterize the performances of the algorithm on gaussian noise. We simulate data streams of advanced LIGO and Virgo detectors using their expected power spectral density at design sensitivity. We provide a first optimization of the performances by tuning the internal parameters of the algorithm. We test the capability to discriminate two possible scenarios which could occur after the merger of two neutron stars: the prompt collapse to black hole versus the formation of a supramassive neutron star or hypermassive neutron star, both collapsing to a black hole on different time scales. We remind the main steps of the procedure developed in this work to select and to characterize the NS as describe in the previous chapter:

- follow-up multi resolution analysis (MRA) by cWB pipeline in the frequency range (768-4096) Hz;
- division of TF map in four quadrants in order to collect the post-merger signal in third region of TF map using a frequency cut at 1280 Hz and time cut to separate lower frequency content earlier phase from higher frequency content post merger phase;
- studies of the third quadrant region (post-merger and higher frequency content), defining additional regions: low frequency early (LFE), low frequency later (LFL), high frequency early (HFE), high frequency later (HFL);
- analysis of the third quadrant in order to extract spectral frequency and time evolution informations of the reconstructed post-merger signal of the BNS coalescence.

Below, we report the results for two EoSs with PM signal, SHT-M2.0-S and LS220-M1.5-S, and for three EoSs with BH outcome, SHT-M2.2-I, LS220-M1.7-I and LS220-

M1.8-I. The results for the other models of the catalog are collected in section 6.3.

6.1 Discrimination of delayed versus prompt collapse to black hole: results

As discussed in chapter 5, the first estimator parameter to discriminate a delayed collapse from a prompt collapse to black hole is the ratio of the energy fraction in the quadrants III and IV, ρ_{III}/ρ_{IV}.
In the Figure 6.1 and 6.2, for LS200-M1.5-S (in which a HMNS/SMNS is formed) and for LS220-M1.7 (which simulate a prompt black hole formation scenario), we report the distribution of ratio ρ_{III}/ρ_{IV} (red point) and ρ_{II}/ρ_I (blu point) as function of detection statistic ρ.

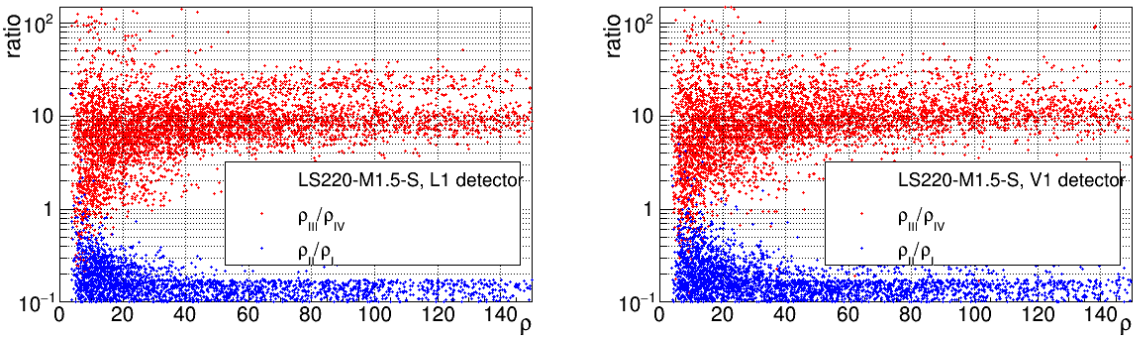

Figure 6.1: Scatter plot of ratio parameters ρ_{III}/ρ_{IV} (red points) and ρ_{II}/ρ_I (blu points) for LS220-M1.5-S EoS.

We can observe that there is not a different distribution of ρ_{II}/ρ_I (blue point) among the EoSs analyzed in our catalog and then between the two scenarios. We remember that, the quadrant I would collect the pixels turned on by last cycles of the in-spiral phase and merger phase of two NSs while in the region II we do not expect signals. However, the behaviour of ratio ρ_{III}/ρ_{IV} is different for delayed and prompt collapse to BH, indeed the post-merger signal is collect in the third quadrant. Thus, for high values of detection statistic ρ (ρ>20), the scenario with HMNS remnant becomes clear due to a better reconstruction of PM signal by cWB tool.
In principle this is what we expect and it is graphically summarized in two Figures 6.3 and 6.4, where we report the values of ρ_{III}/ρ_{IV} ratio for each analyzed EoSs of SHT model and LS220 model, respectively.
For SHT model, we observe that at low values of detection statistic, the procedure

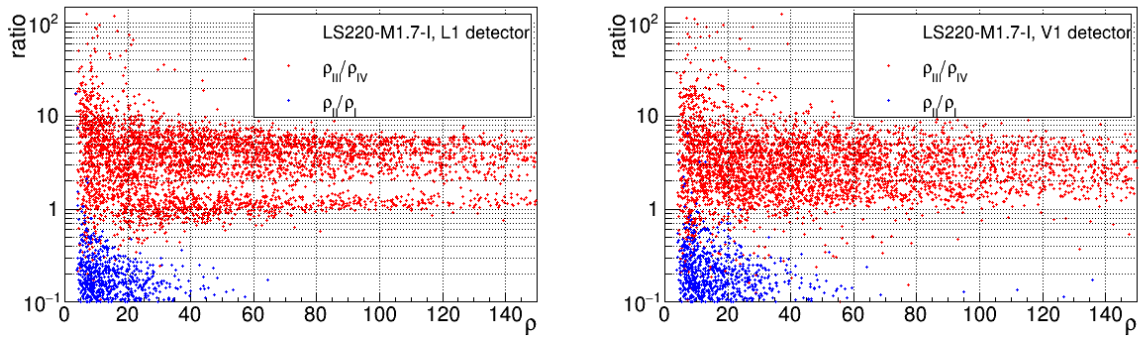

Figure 6.2: Scatter plot of ratio parameters ρ_{III}/ρ_{IV} (red points) and ρ_{II}/ρ_{I} (blu points) for LS220-M1.7-I EoS.

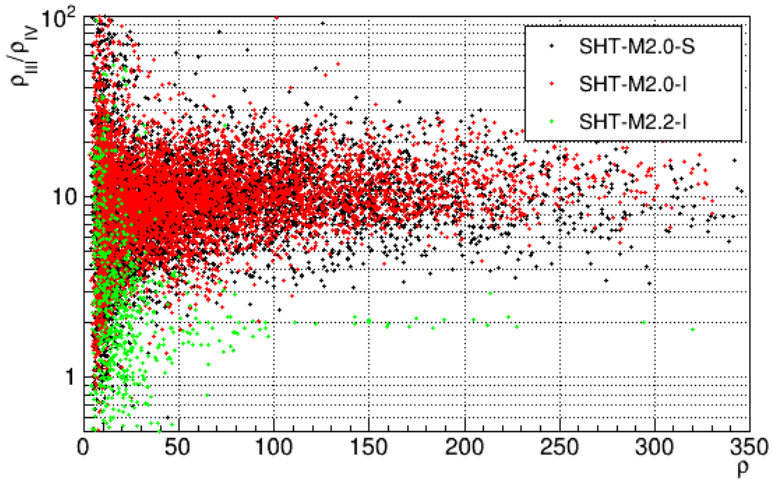

Figure 6.3: Comparison of ratio ρ_{III}/ρ_{IV} for SHT EoSs: SHT-M2.0-S (black dot), SHT-M2.0-I (red dot) and SHT-M2.2-I (green dot, BH remnant). Plot refers to Livingston detector.

identifies for prompt collapse scenario SHT-M2.2-I some events as events with a post-merger but for high values the distinction is sharp with respect the two other EoSs spinning and non-spinning SHT.

Instead in case of LS220 model the distributions of ρ_{III}/ρ_{IV} are still different in the two scenarios, but LS220-M1.7-I and LS220-M1.8-I which form BH are not as clearly separated from the delayed collapse cases as in SHT model. In particular the former model presents mean value of ρ_{III}/ρ_{IV} higher than in SHT case, and this has driven the improvement of the discrimination tool with further specific studies on the third quadrant.

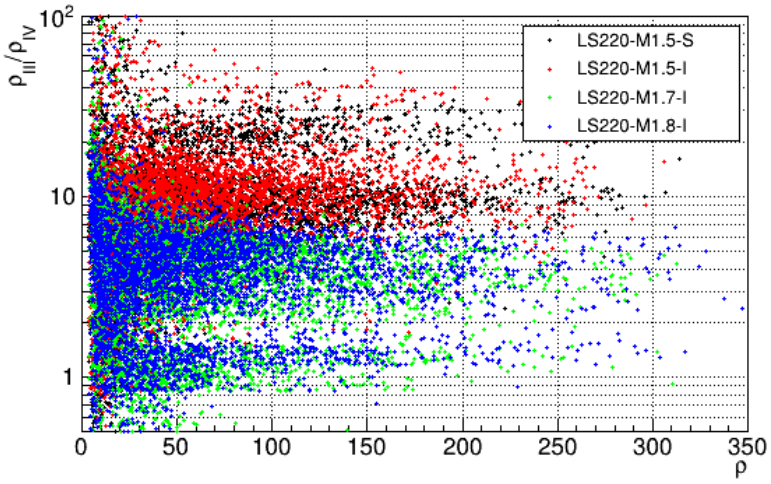

Figure 6.4: Comparison of ratio ρ_{III}/ρ_{IV} for LS220 models: LS220-M1.5-S (black dot), LS220-M1.7-I (red dot, BH remnant), LS220-M1.8-I (green dot, BH remnant). Plot refers to Livingston detector.

6.1.1 Efficiency and false alarm rate of the post-merger identification

The problematic discrimination performances on LS220-M1.7 and 1.8, are highlighted in Figures 6.5 and 6.6, where we report the efficiency of reconstruction of the tool defined by

$$\varepsilon(\alpha) = \frac{N_{rec}}{N_{inj}},$$

where α is the threshold value on ρ_{III}/ρ_{IV}, N_{rec} is the number of events fulfilling the condition of time_cut selection and of ρ_{III}/ρ_{IV} above threshold (these events point to a post merger signal). N_{inj} is instead the number of injected events (waveform) analyzed by cWB algorithm; the efficiency is estimated as function of the distance at which the injections are performed. The estimate of the standard deviation for efficiency value is given by:

$$\sigma_\varepsilon = \frac{\sqrt{N_{rec}(1-\varepsilon)}}{N_{inj}}. \tag{6.1}$$

For the two models with PM signal, see Figure 6.5, we report the efficiency curves as function of simulated distance values considering Livingston and Virgo detector interferometers. For the models in which a BH is the outcome of NS merger, see Figure 6.6, we report the false positive probability (FPP) defined as the event fraction which is wrongly

identified by the tools as events possibly including post merger signal.

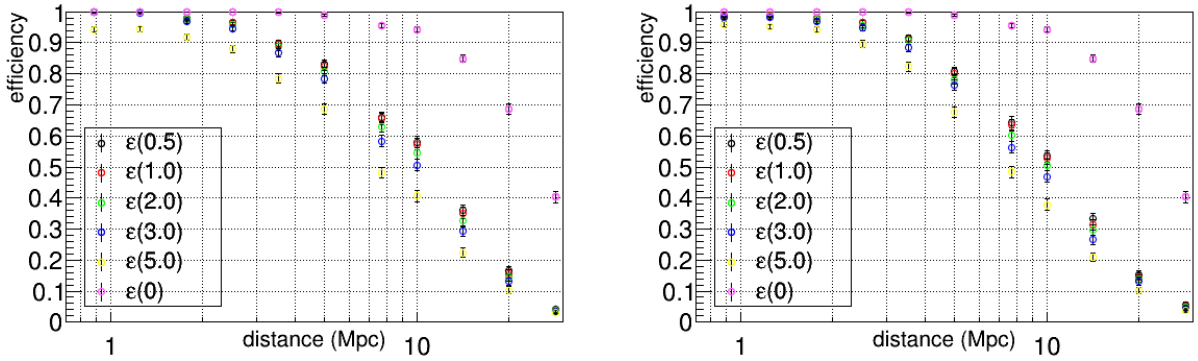

(a) SHT-M2.0-S EoS

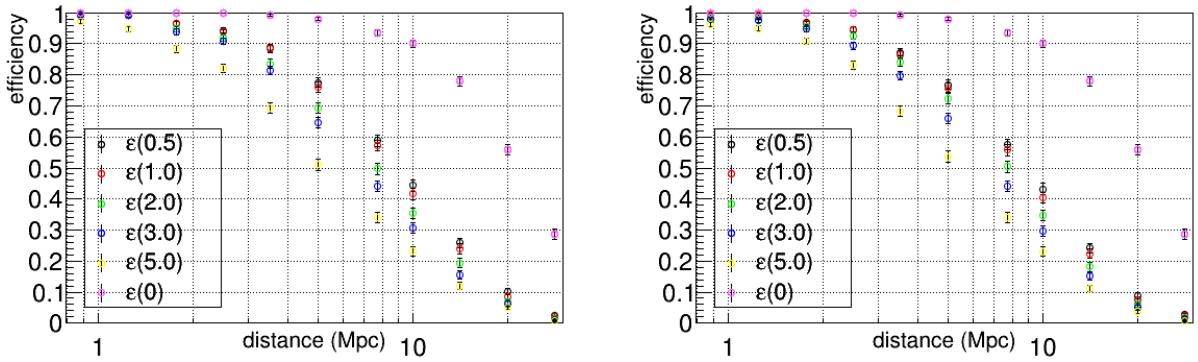

(b) LS220-1.5-S EoS

Figure 6.5: Efficiency of the tool as function of the distance for models with delayed collapse to BH scenario. The different colors refer to threshold values on ρ_{III}/ρ_{IV}. The left and right plots refer to Livingston and Virgo interferometer, respectively.

For all efficiency and FPP reported in Figures, the violet curve $\varepsilon(0)$ is the ratio of the number of events reconstructed by cWB pipeline over the number of injected events. Instead, the other colored curves point out the efficiency $\varepsilon(\alpha)$ of identification of post-merger signal above exploratory thresholds set on our ρ_{III}/ρ_{IV} parameter: $\alpha = \{0.50, 1, 2, 3, 5\}$. These values has been selected on the distributions of the ratio ρ_{III}/ρ_{IV} in the previous Figures 6.1 and 6.2, and allow to investigate the discriminating power between prompt collapse and delayed collapse to black hole. For each EoS, we report the efficiency and false positive probability for Livingston and Virgo interferometers in Figures 6.5 and 6.6; as a general comment, the results based on LIGO and Virgo GW reconstructions are compatible within the uncertainties. This is due to that the two design sensitivity PSDs of advanced detectors, are comparable at high frequencies.

Looking to the efficiency plots of Figure 6.5, we can observe as the efficiency falls

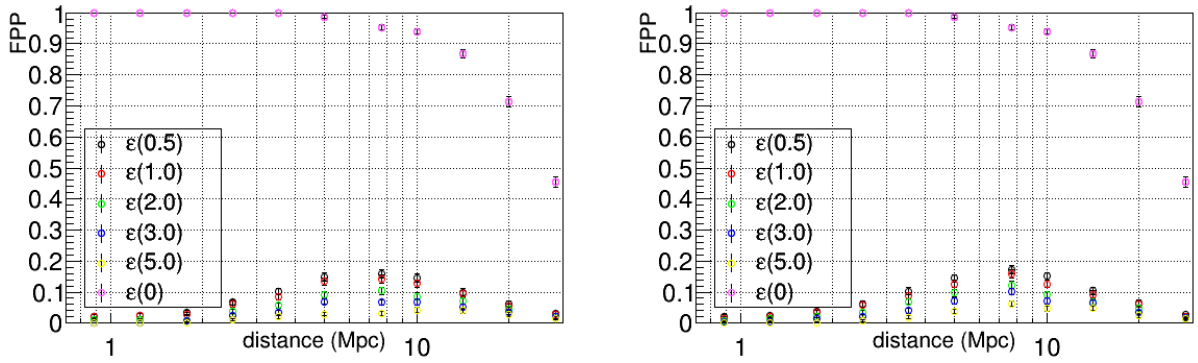

(a) SHT-2.2-I EoS

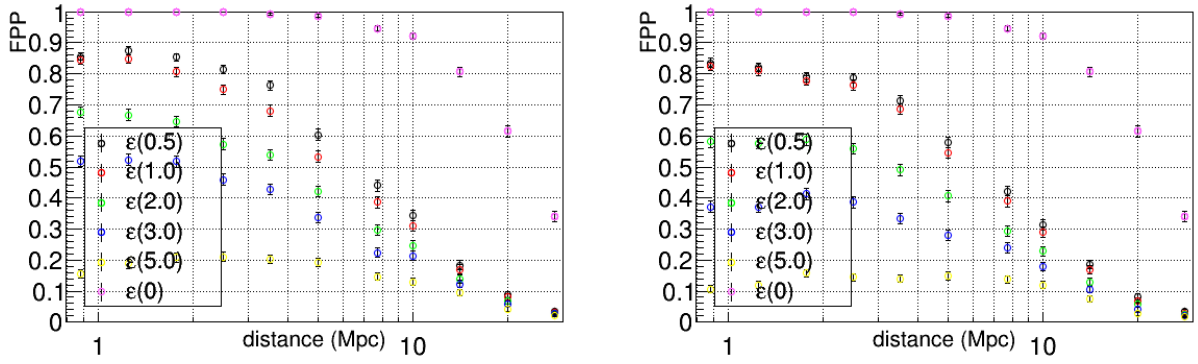

(b) LS220-1.7-I EoS

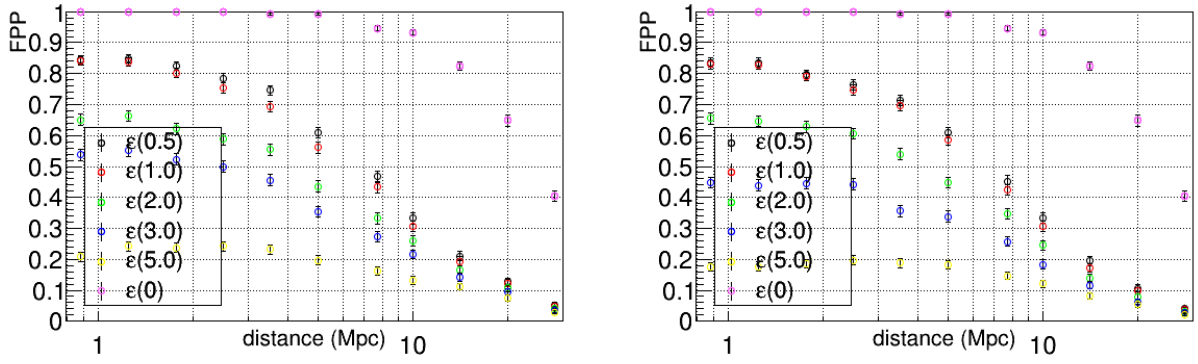

(c) LS220-1.8-I EoS

Figure 6.6: FPP of the tool as function of the distance for models with prompt collapase to BH scenario. The different color markers refer to threshold values of ρ_{III}/ρ_{IV}. The left and right plots refer to Livingston and Virgo interferometers, respectively.

at larger distances as the SNR decreases. The black and red curves, corresponding to thresholds 0.50 and 1, show a neglegible differences in efficiency of reconstruction. For example, at 10 Mpc, the developed tool identified ∼58% of injected events as event

with a post-merger signal for SHT-M2.0-S model; in case of LS220-M1.5-S model ∼44%. At higher threshold values, the efficiency decreases up to ∼10-15% with respect the threshold ρ_{III}/ρ_{IV}>0.5 at fixed distance.
For example, at 10 Mpc and for ρ_{III}/ρ_{IV}>2.0, we have that the tool identifies ∼54% of events as containing a post-merger signal for SHT-M2.0-S model, ∼36% for LS220-1.5-S model.

Figure 6.6 show the False Positive Probability using the same threshold values. If we focus on Figure 6.6(a) of SHT-M2.2-I EoS, the highest values of FPP, at distance ∼7-10 Mpc for threshold $\rho_{III}/\rho_{IV}>$ 0.5-1, is ∼16% out of ∼96% of reconstructed events and selecting $\rho_{III}/\rho_{IV}>$ 2.0 and a distance ∼10 Mpc, the tool wrongly identifies less than ∼8% of events as containing a PM signal.
For what concern the other two EoSs of the catalog with prompt collapse to BH, LS220-M1.7-I and LS220-M1.8-I, Figures 6.6(b) and 6.6(c), we see a different behavior of FPP for all threshold values on ρ_{III}/ρ_{IV}. These curves look like to that of previous waveform with delayed collapse scenario.
For value of ρ_{III}/ρ_{IV}>2.0 and at 10 Mpc, the probability to identify a fake PM signal, for both LS220-M1.7 and 1.8 models, is equal to ∼24-26% out of ∼93% of reconstructed events. We could increase the threshold on ρ_{III}/ρ_{IV} the FFP for this type of models but on the other side, the efficiency of identification of a PM signal, would drop too much, as Figure 6.5 shows.

In the following, we choose the ρ_{III}/ρ_{IV} threshold equal to 2.0 to perform a further study of the quadrant III of the TF map since this threshold alone is not enough to discriminate properly the two scenarios.

6.1.2 Analysis of third quadrant

In section 5.3, we have introduced new parameters to study the third region of the TF map for each event selected by the ρ_{III}/ρ_{IV} threshold. As in the previous paragraphs, we take into account the two case studies: SHT-M2.0-S and SHT-M2.2-I.

Figures 6.7 and 6.8 report the same parameters, ρ_{HFL}/ρ_{LFE}, ρ_{HF}/ρ_{III} and ρ_{LFE}/ρ_{III}, for the waveforms with a delayed collapse to BH LS220-M1.5-S, and with a prompt collapse to BH, LS220-M.17-I. In both Figures and for each studied EoSs, we consider the events identified as candidates possibly containing a post merger phase.

Let us focus on EoSs with a BH after BNS coalescence. We observe some differences between the light BNS system (LS220-M1.7) and the heavy BNS systems (SHT-M2.2). The first difference is the number of events identified: for SHT-M2.2-I EoS, the procedure

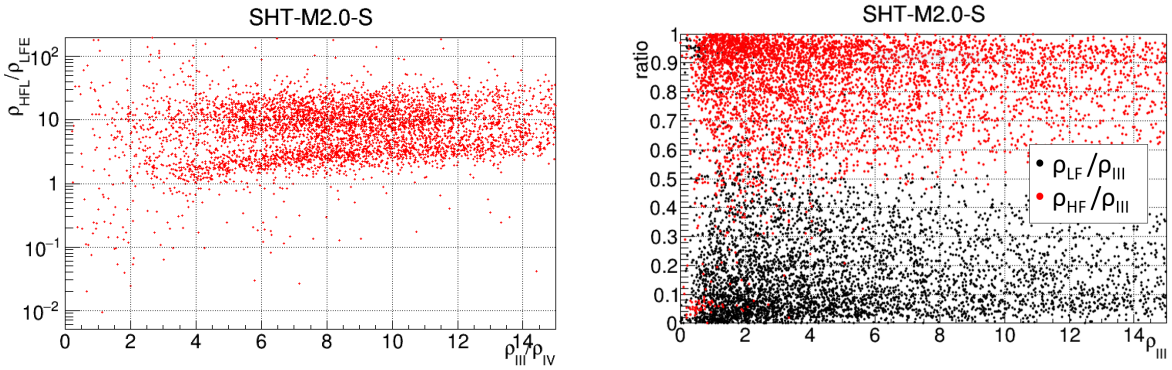

(a) SHT-M2.0-S model

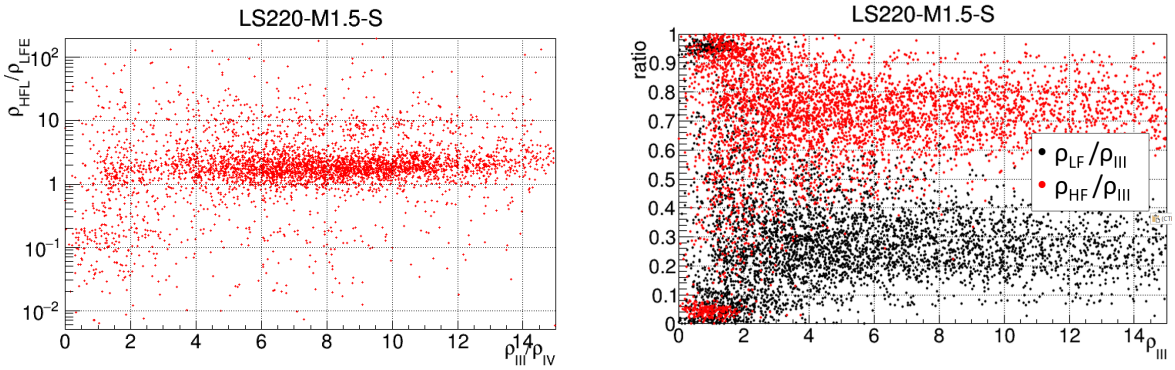

(b) LSS220-M1.5-S model

Figure 6.7: Analysis of third quadrant for two models with delayed scenario taking into account Livingston detector. Left plot: ratio ρ_{HFL}/ρ_{LFE} as function of ρ_{III}/ρ_{IV}. Right plot: ρ_{HF}/ρ_{III} (red point) ρ_{LF}/ρ_{III} (black point) parameters as function of ρ_{III}.

reconstructs a lower number of candidates with a PM phase with respect to LS220-M.17 and 1.8.

The second difference is pointed out in right plot of Figure 6.8(a), 6.8(b) and 6.8(c) in which we compare, as function of ρ_{III}, the behaviour of the energy in high frequency (ρ_{HF}/ρ_{III}) and low frequency (ρ_{LF}/ρ_{III}) regions of third quadrant of TF map. They show that, for LS220 EoSs in the prompt collapse to BH scenario, the distributions of ρ_{HF}/ρ_{III} and ρ_{LF}/ρ_{III} are clearly separated for events with $\rho_{III}>$ 4; and in this cases about 60% of energy of the region III lies in frequency band 1280-1792 Hz. In case of SHT-2.2-S, Figure 6.8(a), where the number of event recognized as candidate post-merger signal is lower than those of LS220-M1.7-I and LS220-M1.8-I, the two distributions of ρ_{HF}/ρ_{III} and ρ_{LF}/ρ_{III} are separated already at ρ_{III} circa 1.

It is important to highlight that the energy is distributed differently between the high frequency and the low frequency bands for EoSs with delayed collapse scenario and EoSs with prompt collapse scenario. Indeed, in right plots of Figures 6.7, we observe that the

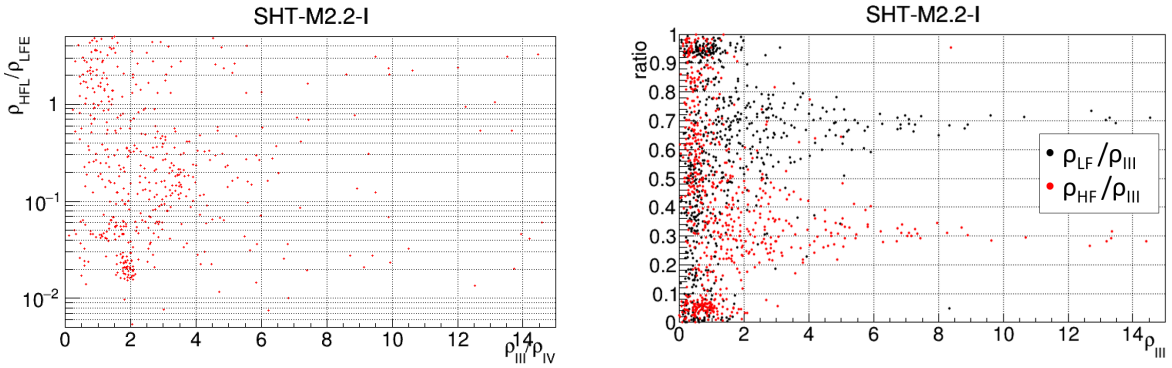

(a) SHT-M2.2-I model

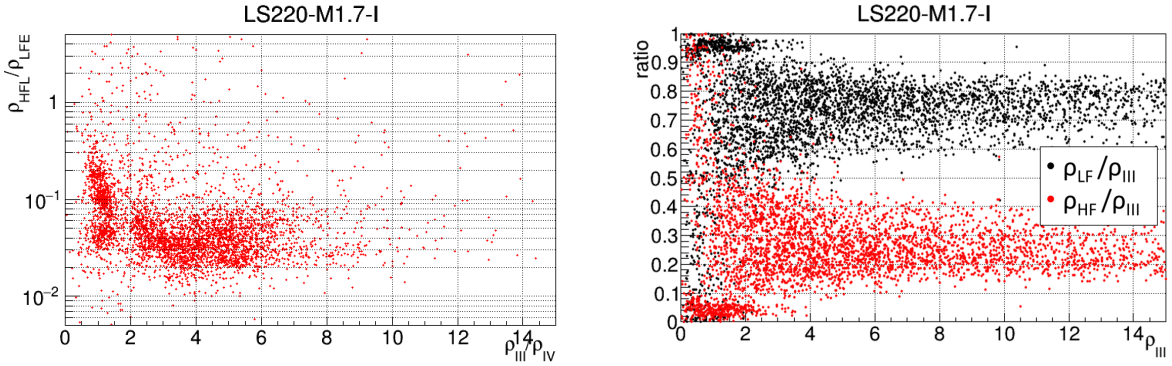

(b) LSS220-M1.7-I model

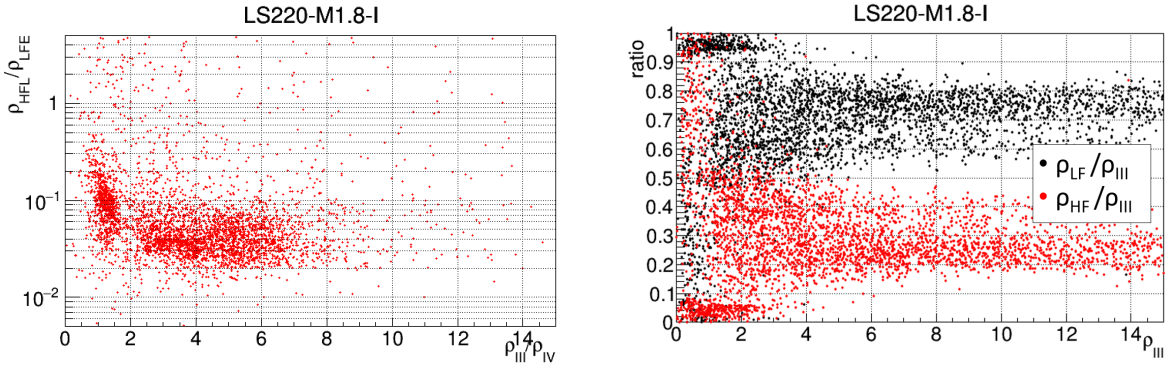

(c) LSS220-M1.8-I model

Figure 6.8: Analysis of third quadrant for all waveforms with prompt decay to black hole scenario. Left plot: ratio ρ_{HFL}/ρ_{LFE} as function of ρ_{III}/ρ_{IV}. Right plot: ρ_{HF}/ρ_{III} (red point) ρ_{LF}/ρ_{III} (black point) as function of ρ_{III}.

most of energy is in high frequency part (1792-4096 Hz) of TF map where we expect a GW post-merger signal; while in Figure 6.8 in which we report the prompt scenario case a prompt scenario, the energy is collected in low frequency region of third quadrant of TF map. Thus, the comparison of two ratios ρ_{HF}/ρ_{III} and ρ_{LF}/ρ_{III}, gives us how the

energy of III quadrant behaves for the two simulated scenarios.

Another distinctive feature of the models is given by ratio ρ_{HFL}/ρ_{LFE} [1]. As anticipated in section 5.3, this ratio is an indicator of presence of GW post-merger signal and its time with typical values above unit. As for models with a HMNS/SMNS remnant outcome after the merger of two NSs, the value of this parameter shows no significant correlation with ρ_{III}/ρ_{IV}, see left plots of Figures 6.7. Hence, the ρ_{HFL}/ρ_{LFE} provides additional information with respect the first parameter ρ_{III}/ρ_{IV}. It allows us to look also for an evolution in time of the HMNS/SMNS remnant because HFL region is the region of TF map containing PMNS signal.
In case of prompt BH collapse as outcome, models LS220-M1.7-I and LS220-M.8-I, the parameter ρ_{HFL}/ρ_{LFE} takes typical values below unit: in Figure 6.8, for both LS220 EoSs, it is order of $\sim$10%. In other words the signal energy in case of prompt collapse scenario, is collected in LFE region of TF map (right after the merger) while a negligible part occurs in HFL band.

Based on these GW waveform models, we are able to finalize a first tuning of the two thresholds for the discrimination between the prompt and delayed collapse scenarios: the threshold value 2.0 for ρ_{III}/ρ_{IV} and threshold value 0.1 for ρ_{HFL}/ρ_{LFE}. In fact, this implementation allows to reduce the false positive probability on all scenarios with a direct formation of BHs with respect to the use of the only ρ_{III}/ρ_{IV} parameter, without loosing the efficiency for all the scenarios with NS formation.
In the next sections we will refer to the full set of cut to identify events containing post merger as the term *post-merger (PM) full selection*, this includes: PM time condition and thresholds on value of ρ_{III}/ρ_{IV} and ρ_{HFL}/ρ_{LFE}.
We did not attempt to optimize this tuning at this stage, but instead we decided to test its performance over a larger set of NR waveforms and to study the estimation a posteriori of the probability that a massive NS is formed.

6.1.3 Post-merger full selection and posterior probability

At this point, we compute the efficiency and false positive probability of the our procedure of PM full selection over more NR models. In Figures from 6.9 to 6.13, we report the efficiency and FPP for single detectors (left plots) and as well as requiring the full PM condition for detector pairs (right plots).
For all EoSs, we observe that there is not a significant difference between the efficiency

[1] ρ_{HFL} is detection statistics from the latest part in the higher band of the III quadrant, ρ_{LFE} the detection statistics from the earlier part in the lower band of the III quadrant.

of any single detector and of identification in at least two detectors. Putting the latter under the spotlight, we see that the efficiency of identification in at least two detectors and that for specific couples of interferometers changes by a few percent. At frequencies higher than 1 kHz, the power spectra of design sensitivity curve of advanced Livingston and of advanced Virgo, see Figure 2.13 (black line), do not manifest a significant difference. Therefore, this reflects on the efficiency curves of detector couples which do not vary.

Let us focus on results for two EoSs with PM phase and for EoSs with prompt collapse to BH. For SHT-M2.0-S EoS (see Figure 6.9), in each detectors and for couple of detectors, the efficiency is around ∼55% at ∼ 10 Mpc, and at ∼15-20 Mpc, the efficiency is reduced to ∼10-15%. In case of LS220-M1.5-S, at ∼ 10 Mpc, we identified up to ∼30% of events with a post-merger phase.

For what concern the scenario with BHs, see Figures 6.11-6.13, considering the full PM selection in at least two detectors we achieve the best FPP values. In case of LS220-M.17-I the procedure gives a false probability to identify a PM signal equal to ∼9% at ∼ 10 Mpc for Livingston (∼12% in case of Virgo) and if we consider at least two detector the FPP is ∼8%. For the other waveform of the same EoS, FPP is ∼10% at ∼ 10 Mpc for Livingston while for Virgo, is ∼14% at the same distance; in case of at least two detectors we have more or less the same value of FPP (at same distance) ∼11%. In case of SHT-M2.2-I, the FPP, of at least two detectors, has values smaller than those of previous two waveforms: it lies below ∼7%.

We conclude that the procedure to require the full PM condition in at least two detectors automatically selects the best operating conditions, since on one side it preserves efficiency and on the other side it controls FPP at the level of the best detector and the best detector pair.

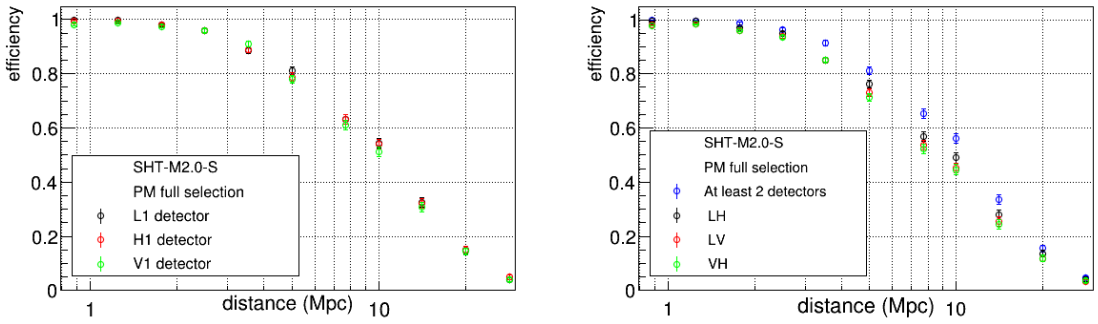

Figure 6.9: Efficiency with PM full selection for SHT-M2.0-S model.

Since our selection procedure (full PM selection) controls the efficiency and false

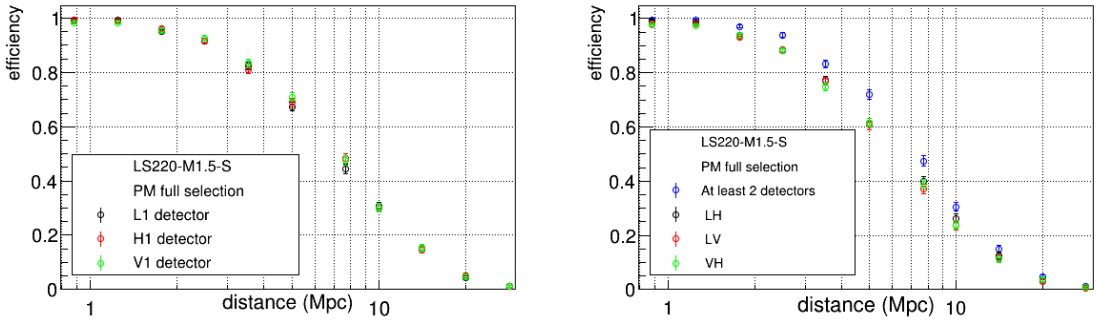

Figure 6.10: Efficiency with PM full selection for LS220-M1.5-S model.

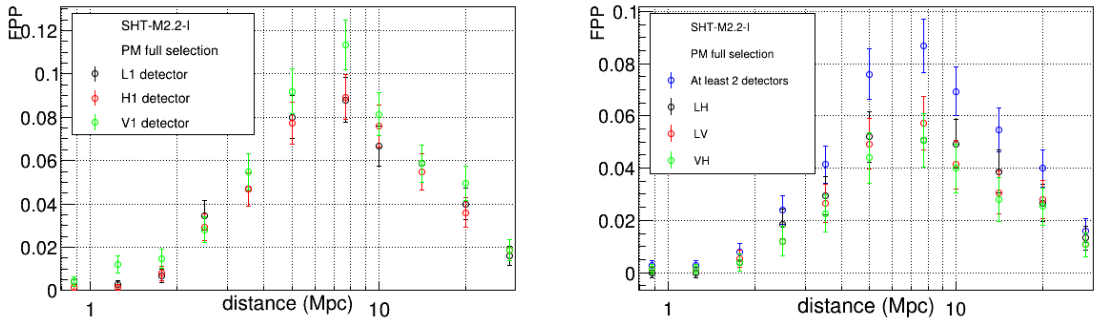

Figure 6.11: FPP with PM full selection for SHT-M2.2-I model.

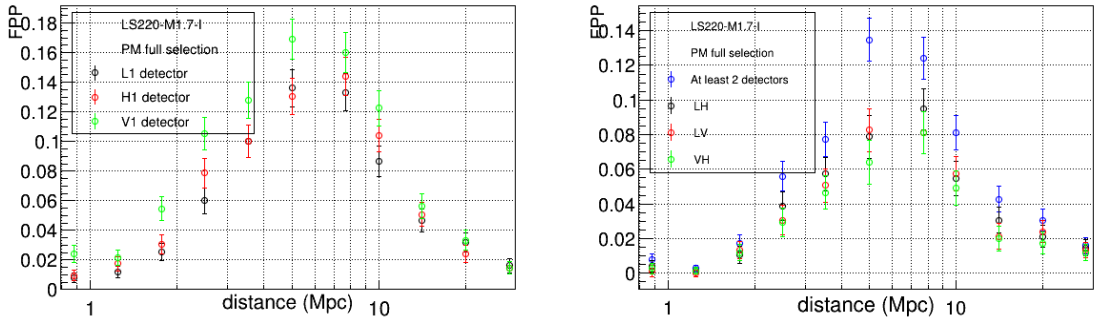

Figure 6.12: FPP with PM full selection for LS220-M1.7-I model.

positive probability for each NR waveform, it makes as well possible to provide estimates for the posterior probability that any selected candidate be truly related to HMNS or SMNS formation. We define two hypothesis considering the two scenarios studied in this thesis: BNS system with delayed collapse scenario (H_1) and BNS system with prompt collapse scenario (H_0, null hypothesis). At the same time, we point out with " + " events that passed our selection for a post-merger signal while " − " events identified as missing a post-merger signal for each waveforms. Thus, the posterior probability that a

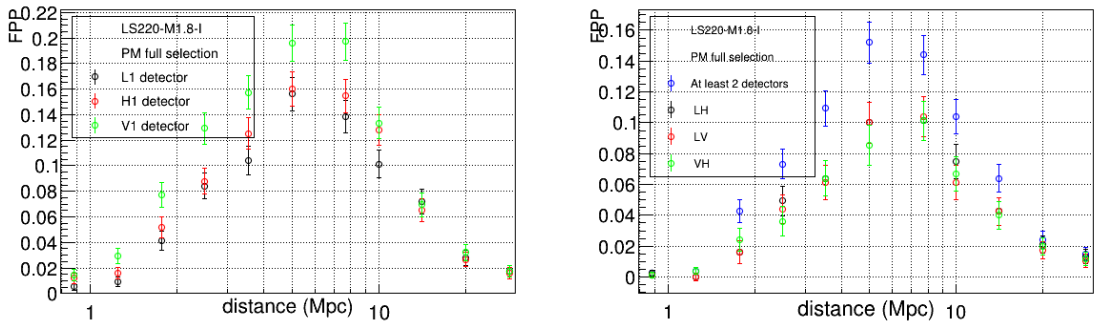

Figure 6.13: FPP with PM full selection for LS220-M1.8-I model.

NS post-merger is present in any selected candidate is given by:

$$P(H_1|+) = \frac{P(+|H_1)P(H_1)}{P(+|H_1)P(H_1) + P(+|H_0)P(H_0)}, \tag{6.2}$$

where

- $P(H_1)$ is the prior for the astrophysical model of BNS systems with a massive NS remnants;
- $P(H_0)$ is the prior for the astrophysical model of BNS systems with a prompt BH formation;
- $P(+|H_1)$ is the efficiency of detection of massive NS remnant;
- $P(+|H_0)$ is the false positive probability of detecting a PM signal in case of prompt collapse to BH.

In the following, we assume equal probability priors for the alternative hypothesis, considering $P(H_1) = P(H_0) = 0.5$ and the eq.(6.2) reduces to:

$$P(H_1|+) = \frac{P(+|H_1)}{P(+|H_1) + P(+|H_0)}, \tag{6.3}$$

Thus, we take into account the SHT and LS220 models because we have at least one waveform with a prompt collapse to BH for the same type of EoS: SHT-M2.2-I and LS220-M1.7-I, LS220-M1.8-I, respectively.
Figures 6.14 and 6.15 show the $P(H1|+)$ of SHT-M2.0-S and LS220-M1.5-S as function of distance, for all reconstructed events satisfying the PM full selection.
On the left plots of Figures, we compare the posterior probability in each single detector

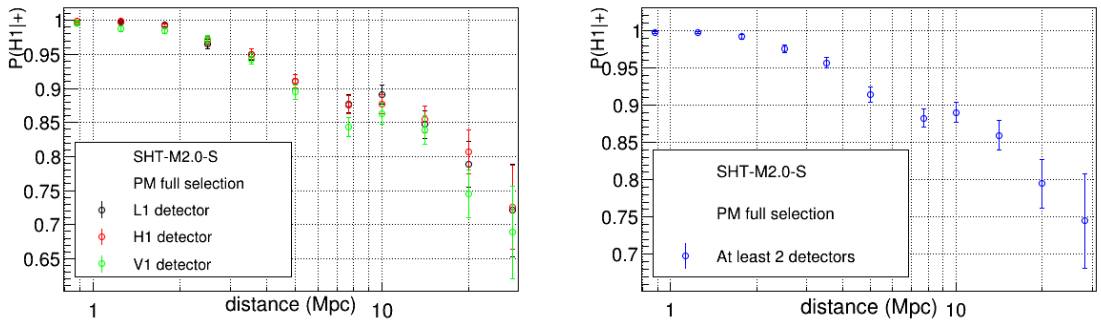

Figure 6.14: $P(H_1|+)$ of SHT-M2.0-S EoS for Livingston detector (left plot) and for at least two detectors (right plot).

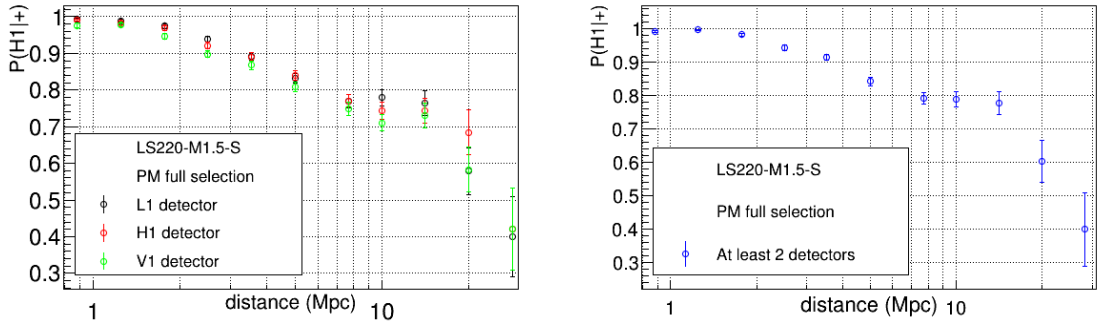

Figure 6.15: $P(H_1|+)$ of LSS20-M1.5-S EoS for Livingston detector (left plot) and for at least two detectors (right plot). The LSS20-M1.7-I EoS is used to compute the probability.

Model	M_{tot} [$M_\odot$]	$P(H_1\|+)$ d= 10 Mpc	$P(H_1\|+)$ d= 20 Mpc
SHT-M2.0-S	4.01	$(89 \pm 1)\%$	$(79 \pm 3)\%$
SHT-M2.0-I	4.01	$(89 \pm 1)\%$	$(82 \pm 3)\%$
LS220-M1.5-S	3.12	$(79 \pm 2)\%$	$(60 \pm 6)\%$
LS220-M1.5-I	3.12	$(76 \pm 2)\%$	$(53 \pm 7)\%$
LS220-M1.5-S	3.12	$(75 \pm 2)\%$	$(66 \pm 6)\%$
LS220-M1.5-I	3.12	$(72 \pm 2)\%$	$(59 \pm 7)\%$

Table 6.1: In the table, the posterior probability $P(H_1|+)$ values are reported for SHT and LS220 models. The first couple of LS220-M1.5-S and I EoS takes into account LS220-M1.7-I EoS as H_0, while the second one, LS220-M1.8-I. The values of $P(H_1|+)$ refers to distances 10 Mpc and 20 Mpc and for at least two detectors.

while on the right plots, we have the posterior probability that the BNS EoS is identified in at least two detectors of network interferometers.

Moving toward far way distances, we observe that, taking into account only one detector or at least two detectors, the two probability curves vary slightly, about few percents. For example, in case of SHT-M2.0-S EoS at 20 Mpc, $P(H1|+) \sim (81 \pm 3)\%$ (H1); while for at least two detectors we have $P(H1|+) \sim (79 \pm 3)\%$. We notice that, at higher distances, the estimate becomes more uncertain due to lower number of events selected by the tool.
At distances around of ∼10 Mpc, both posterior probability distribution for SHT and LS220 models show a plateau. To understand this behaviour, it is necessary to focus on distribution of efficiency and false positive probability.
Since SNR of signal scales inversely with distance, we expected that efficiency of identification of PM signal decreases increasing the distance.
In case of BH formation, we have a double behavior of FPP. At closer distances we expect that the signal without PM signal is properly reconstructed by the tool so the efficiency correctly decrease to zero, as at far away distances in which the SNR is extremely low at high frequency. Instead at intermediate distances, being higher the probability to wrongly reconstruct the signal, the probability to misreconstruct the events, and so misidentify the PM increase.

In Table 6.1, we report the value of posterior probability for SHT and LS220 models at fixed distances, 10 and 20 Mpc because, at greater distances, the estimate becomes more uncertain.

Finally, we see that the posterior probability values decrease for lighter systems. This is a general feature of our full PM selection procedure, which results less effective for lighter binary systems

6.2 Reconstruction of post-merger signals: results

In this section, we report the estimate of dominant post-merger frequency peak, discussed in section 1.3.1, for two waveforms: SHT-M2.0-S and LS220-M1.5-S.

6.2.1 Dominant frequency peak

As discussed in section 5.4.1, the estimate of dominant frequency peak is performed by a gaussian fit in the power spectrum of GW signal.
In Figures 6.16 and 6.17, we report the following informations on estimated frequency peak: the distribution of peak values obtained by gaussian fit for each single detector (considering all distance at which the signal is reconstructed); the scatter plot of differ-

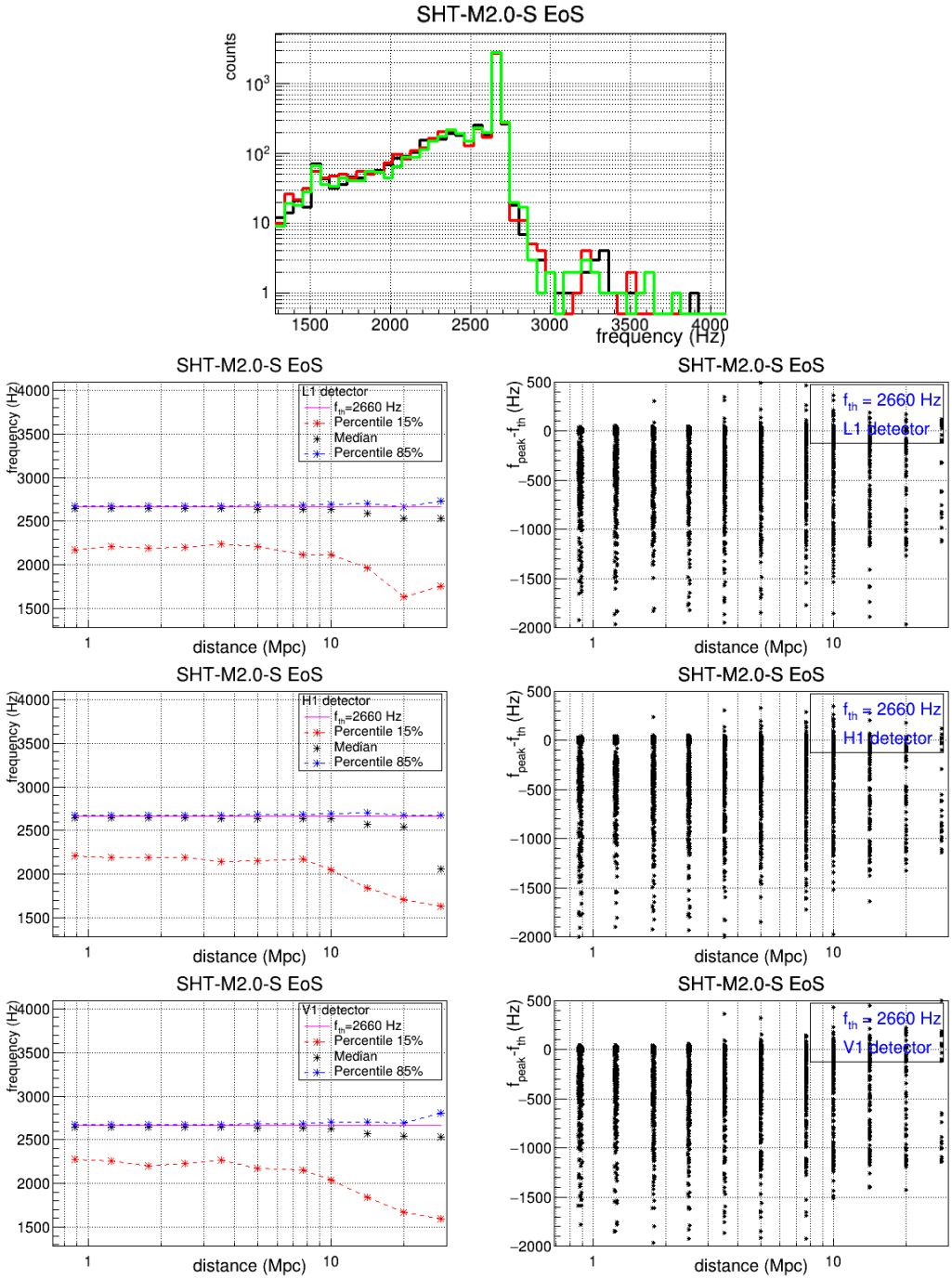

Figure 6.16: (Top) Distribution of frequency peak values for SHT-M2.0-S EoS. (Left) 15% (red dot line), 50% (black dot line) and 85% (blue dot line) percentiles of the distribution of the frequency peak estimated, as function of the distance. (Right) Scatter plot of difference frequency between estimated peak values and theoretical one, f_{th}= 2660 Hz.

ence between estimated f_{peak} and theoretical f_{th} values of frequency peak at each distance and the distribution of 15%, 50% and 85% of the distribution of the estimated frequency

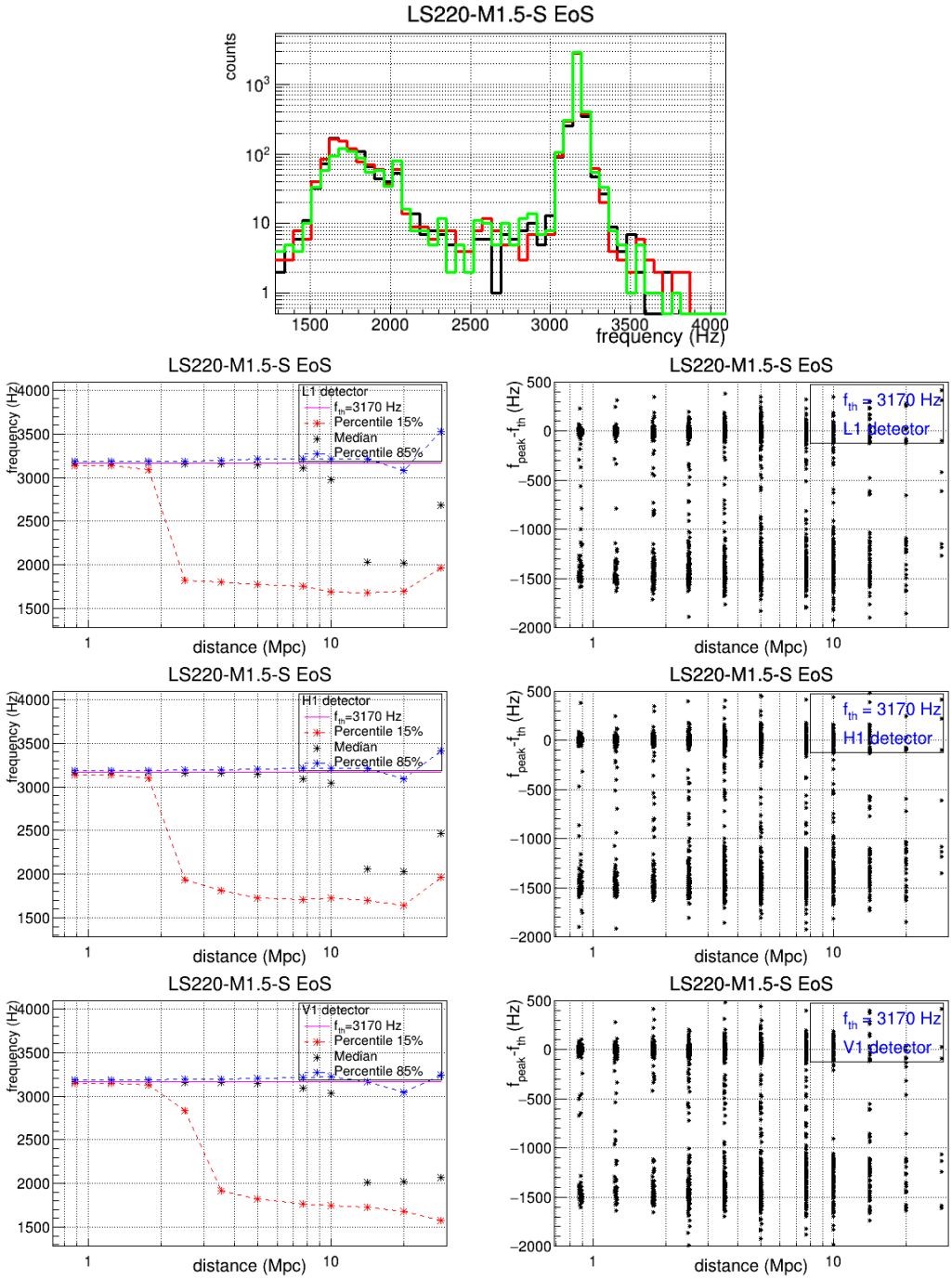

Figure 6.17: (Top) Distribution of frequency peak values for LS220-M1.5-S EoS. The color lines black, red and green refer to L1, H1 and V1 detectors, respectively. (Left) 15% (red dot line), 50% (black dot line) and 85% (blue dot line) percentiles of the distribution of the frequency peak estimated, as function of the distance. (Right) Scatter plot of difference frequency between estimated peak values and theoretical one, f_{th}= 3170 Hz.

peak.
Starting with SHT-M2.0 model keeping in mind its GW power spectrum (see Figure 4.1(a)). From histogram, we see that the peak of distribution is at ∼2.6 kHz, as we expect; while a secondary peak arise in the range between 2-2.5 kHz. Looking at the plots of percentile distributions for each detector, they point out that, up to ∼10 Mpc, the distribution of gaussian peak lies at ∼2.2 kHz which corresponds to a secondary peak in GW spectrum. Instead the median and 85% curves, turn out to be at ∼2.7 kHz deferring of one hundred Hz at distance greater than 15 Mpc.
In case of LS220-M1.5-S EoS, Figure 4.1(b) shows a GW spectrum with a dominant peak at ∼3.16 kHz but at the same time, it is populated by secondary peaks at ∼2.3 kHz and ∼4.1 kHz, but the latter is out of our range of analysis. What we observe from distribution of percentiles is that the distribution is dominate by the tail with a gaussian peak of ∼1.8 kHz. At 50%, indeed, we have a double behavior: for closer distance the peak reconstructed is that we expect but for distance greater than 10 Mpc, the reconstruction is dominated by peak at ∼1.7 kHz. This aspect is found also in the scatter plot of frequency differences as function of distance. Only the 85% of distribution of estimate of gaussian peak report the expect values at each distance.

6.2.2 Further developments on reconstruction

Once performed our multi resolution analysis in the frequency range 786-4096 Hz, our follow-up search reconstructs the gravitational signal of each BNS model with time and frequency resolution.
In order to highlight the features of post-merger signal, the future step will be reanalyzed the signal choosing another resolutions (dT, dF). This could allow to find new spectral estimators and also compute the *brightness*, that would looks like a luminosity profile of the GW signal of the NS remnant given by the energy of pixels in the frequency band 1792-4096 Hz.

The first step of the procedure provides the evolution of the post merger signal calculating the cumulative energy since the post merger time cut as function of the time. This estimation is performed in the TF map with the usual resolution dF = 512 Hz, dT = 0.98 ms. It is possible to obtain an estimation of the duration of the post-merger phase of the signal through Δt_{cum} defined as:

$$\Delta t_{cum} = t_{85} - t_{15}, \tag{6.4}$$

where t_{85}, t_{15} are time at which correspond 85% and 15% of the cumulative energy of

the map, respectively. The second step of the procedure aims to select an optimal level resolution to describe the post merger signal phase. To do that the optimal resolution is defines as the one that fulfill the condition: $2 \cdot dT_n \leq \Delta t_{cum} < 2 \cdot dT_{n+1}$ where dT_n={1.95, 3.91, 7.81, 15.62} ms is a new interval of time resolutions. If the condition is fulfilled, then the new resolution of the map is the lower value dT_n of interval.
In Figure 6.18, we show an example of this next step of analysis for a single reconstructed event. We report black and red curves (in addition to cumulative function with blu circles) as function of time and the starting point (t=0) is defined as t = time_cut. The brightness, pointing out by black markers, considers the frequency band 2304 - 4096 Hz. The red markers are the cumulative energy of the pixel on frequency band 1792-2304 Hz.
If on one hand, the curves are the cumulative energy of the map at different times, on the other hand, they point out the number of pixels *turned on* by gravitational wave signal and at the same time, the duration of the signal at high frequencies or at specific frequency range.
This implementation could give informations on possible structures of dominant frequency peak or secondary peaks and can pick informations up about the time duration of PM signal.

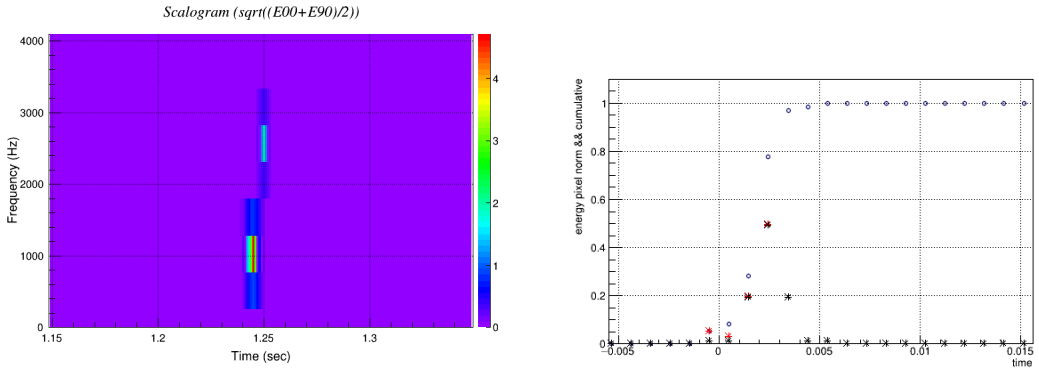

Figure 6.18: Example of post-merger signal brightness for SHT-M2.0-S model of a single event. The blu circles is the cumulative energy of the map pixels considering the frequency range 1792-4096 Hz, the red marker refer to cumulative energy of pixel in 1792-2304 Hz and for times after the time_cut; the black marker refer to cumulative energy in 2304-4096 Hz for time values after time_cut. The value t=0 sec indicates the time_cut on the map.

As previously introduced, we can have an estimation of the duration of the post merger looking at the Δt_{cum}; in Figure 6.19, we point out the distribution of this parameter for different EoS signal. For EoSs, SHT-M2.0-S, LS220-M1.5-S and MS1-q09, we

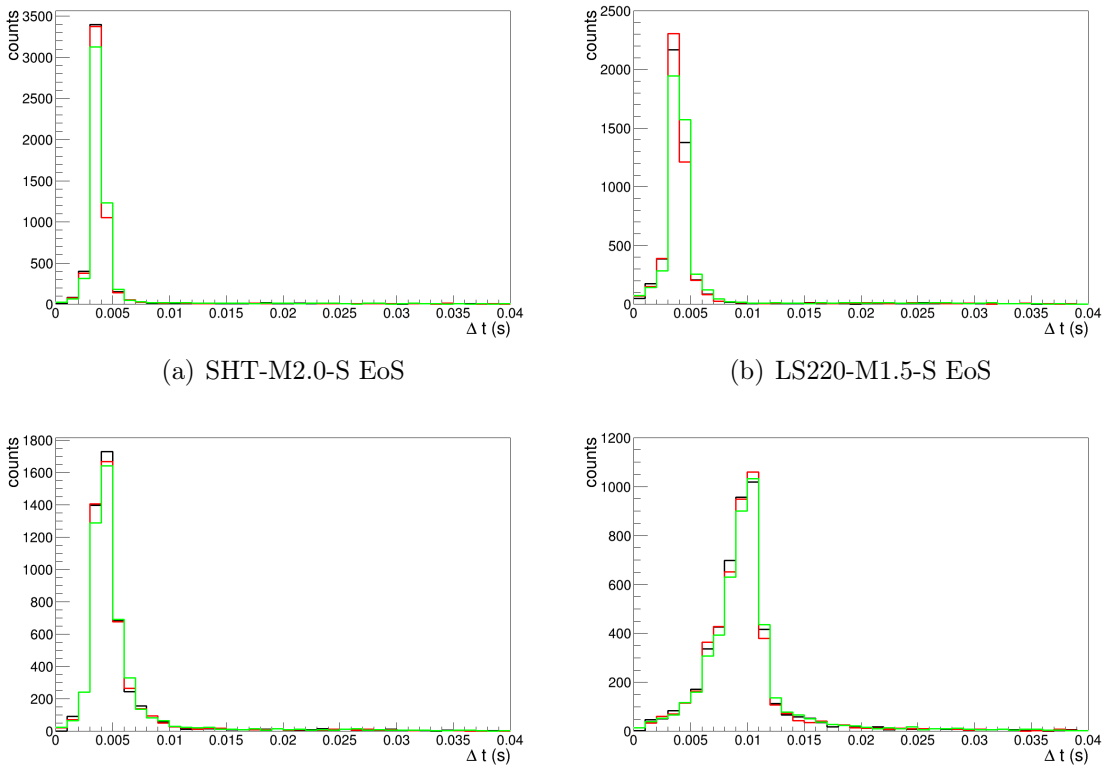

(a) SHT-M2.0-S EoS

(b) LS220-M1.5-S EoS

(c) MS1-q09 EoS

(d) H4-q08 EoS

Figure 6.19: Distribution of Δt_{cum} given by eq. (6.4) for SHT-M2.0-S, LS22-M1.5-S, MS1-q09 and H4-q08 models. The color line black, red and green refer to Livingston, Hanford and Virgo interferometers.

can observe that the duration of PM signal corresponding to its 70% of energy, is equal to ∼3-4 ms, instead, in case of H4-q08 EoS, the duration is longer ∼9-10 ms (τ_{MSN} ∼25ms, see Table 4.1). Therefore, the estimated duration of the PM GW signal can contribute to discriminate among different EoS.

6.3 Extended results on the waveform catalog

In this section, we collect the final results for the other waveform models in the catalog described in section 4.1, including efficiency, FPP and the posterior probability P($H_1|+$). In Figures 6.21, 6.23 and 6.25 we report also P($H_1|+$) for SHT-M2.0-I, LS220-M1.5-S and LS220-M1.5-I EoSs, respectively. For the latter EoS, we take into account both EoSs with BH formation right after the merger, LS220-M1.7-I and LS220-M1.8-I.

In section 4.1, we have pointed out APR4-HM EoS like a BNS system with HMNS remnant which collapse to BH within a time less than 1 ms, thus we consider it as a

prompt collapse to BH model and its efficiency behaviour confirms this.

In Tables 6.2 and 6.3, we collect the efficiency and false positive probability values for models at fixed distances 5, 10 and 20 Mpc. The models, APR4-LM, APR4-UM, APR4-q09 form a SMNS remnant while MS1-q09, MS1-M1.45, SHT-M1.5-I produce a stable NS. The efficiency and FPP values refer to the case with post merger full condition fulfilled by the signals of at least two detectors.

Taking into account the SHT and LS220 models, we observe that the efficiency of SHT EoSs are higher than LS220 EoSs.

In case of HMNS remnant, there is another remark regarding H4 models. If we consider the couple of waveforms H4-q08, H4-M1.5 and H4-q09 and H4-M1.4 models, from their Figures 6.27, 6.29, 6.31 and 6.33, we observe that the efficiency for equal mass systems is greater than the one of un-equal mass systems. This aspect is found also for MS1-M1.45 and MS1-q09 models (with a stable NS remnant) whose efficiency values are 47% and 38% at 10 Mpc, respectively.

		efficiency		
Model	M_{tot} [$M_\odot$]	5 Mpc	10 Mpc	20 Mpc
SHT-M2.0-S	4.01	(81 ± 1)%	(56 ± 2)%	(15 ± 1)%
SHT-M2.0-I	4.01	(82 ± 1)%	(57 ± 2)%	(18 ± 1)%
LS220-M1.5-S	3.12	(72 ± 2)%	(30 ± 2)%	(5 ± 1)%
LS220-M1.5-I	3.12	(66 ± 2)%	(26 ± 2)%	(4 ± 1)%
H4-M1.5	3.04	(79 ± 1)%	(45 ± 2)%	(5 ± 1)%
H4-q08	3.04	(75 ± 2)%	(35 ± 2)%	(4 ± 1)%
H4-M1.4	2.92	(82 ± 1)%	(52 ± 2)%	(8 ± 1) %
H4-q09	2.92	(81 ± 1)%	(49 ± 2)%	(7 ± 1)%
APR4-UM	3.01	(61 ± 2)%	(20 ± 1)%	(2 ± 1)%
APR4-q09	2.98	(58 ± 2)%	(16 ± 1)%	(2 ± 1)%
APR4-LM	2.66	(42 ± 2)%	(9 ± 1)%	(1 ± 1)%
SHT-M1.5-I	3.03	(83 ± 1)%	(54 ± 2)%	(11 ± 1)%
MS1-q09	2.91	(74 ± 2)%	(38 ± 2)%	(5 ± 1)%
MS1-M1.45	2.91	(80 ± 1)%	(47 ± 2)%	(8 ± 1)%

Table 6.2: Efficiency values for the case in which the signals reconstructed in at least two detector fulfill the full PM conditions. The efficiency is reported at distance of 5, 10 and 20 Mpc, respectively. The uncertainties of the measurements depend on each models (see corresponding plots in the text).

For what concerns the dominant frequency peak of GW post-merger signal, moving among the different plots of each BNS model, we observe that the gaussian fit estimate reconstructs properly the peak except for few models. In these cases, the larger spread

Model	M_{tot} [$M_\odot$]	FPP 5 Mpc	FPP 10 Mpc	FPP 20 Mpc
SHT-M2.2-I	4.39	(8 ± 1)%	(7 ± 1)%	(4 ± 1)%
LS220-M1.8-I	3.62	(15 ± 1)%	(10 ± 1)%	(2 ± 1)%
LS220-M1.7-I	3.46	(13 ± 1)%	(8 ± 1)%	(3 ± 1)%
APR4-HM	3.18	(20 ± 1)%	(11 ± 1)%	(3 ± 1)%

Table 6.3: FPP values for the case in which the signals reconstructed in at least two detector fulfill the full PM conditions. The values refer to distances of 5, 10 and 20 Mpc, respectively. The uncertainties of the measurements depend on each models (see corresponding plots in the text).

in the distributions of the estimators of the dominant PM frequency reflects the the complex spectral features of their GW emission. In letterature and as we have seen in section 1.3.1, the GW spectrum of post-merger signal is described as a spectrum with dominant frequency peak at ∼2-3 kHz. However, the spectrum could be more complex, in other words, it can be characterized by secondary peaks whose intensity is comparable to that of dominant one; furthermore, it possible to find also side-band frequency peaks. We focus on few models. For each APR4 model, see Figures 6.36, 6.38 and 6.40, we have a bimodal distribution of frequency peak estimation reflecting the structure of GW spectra characterized by secondary peak (see plots in [111], [114]) at frequency lower than dominant one. Indeed, the distribution of 85% percentile up to ∼10-15 Mpc, is dominated by expected value of dominant frequency peak while the 15% percentile distribution by secondary frequency peak.

In case of LS220-M1.5-I, see Figure 6.26, we have a large gap between 15% and 85% percentile distributions. This is due to its power spectrum characterized by secondary peaks and their side-band frequency peaks (see plot in [113]). The reconstruction of dominant frequency peak at 3240 Hz is missed since the its SNR is reduced by the spectral sensitivity cut-off at high frequency.

Also for H4-q08 and H4-M1.5 models the frequency peak estimate is missed. Probably for both EoSs, this depends on the peak in GW power spectrum (see plots in [115]) lies below the noise level at ∼2.4 kHz.

6.3.1 SHT-M2.0-I EoS

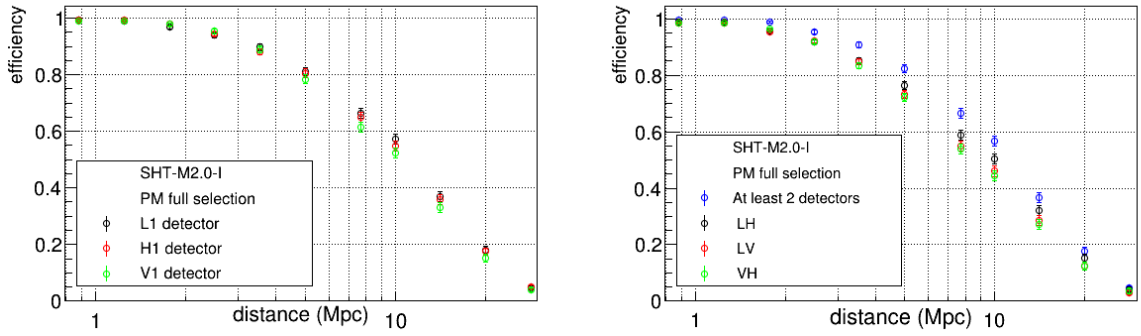

Figure 6.20: Efficiency with PM full selection for SHT-M2.0-S model.

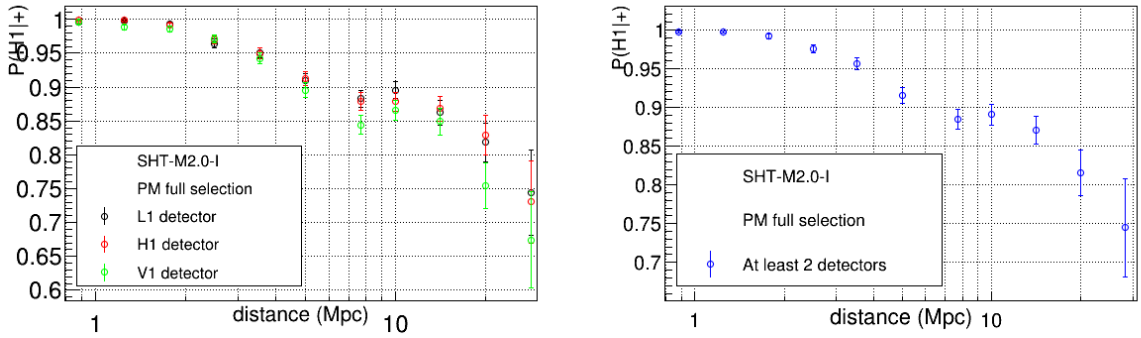

Figure 6.21: $P(H_1|+)$ of SHT-M2.0-I EoS for Livingston detector (left plot) and for at least two detectors (right plot).

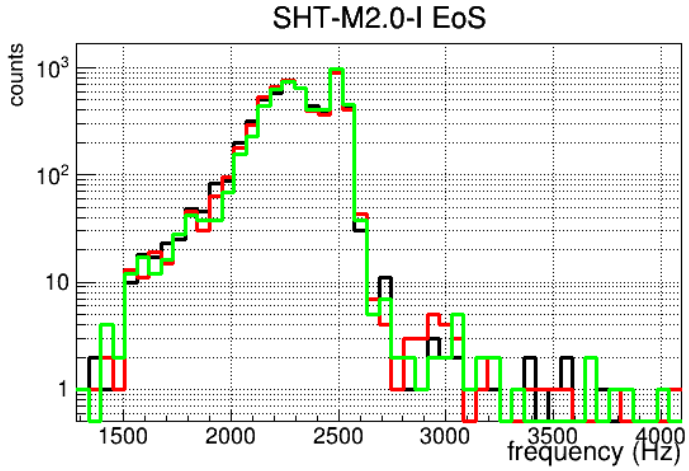

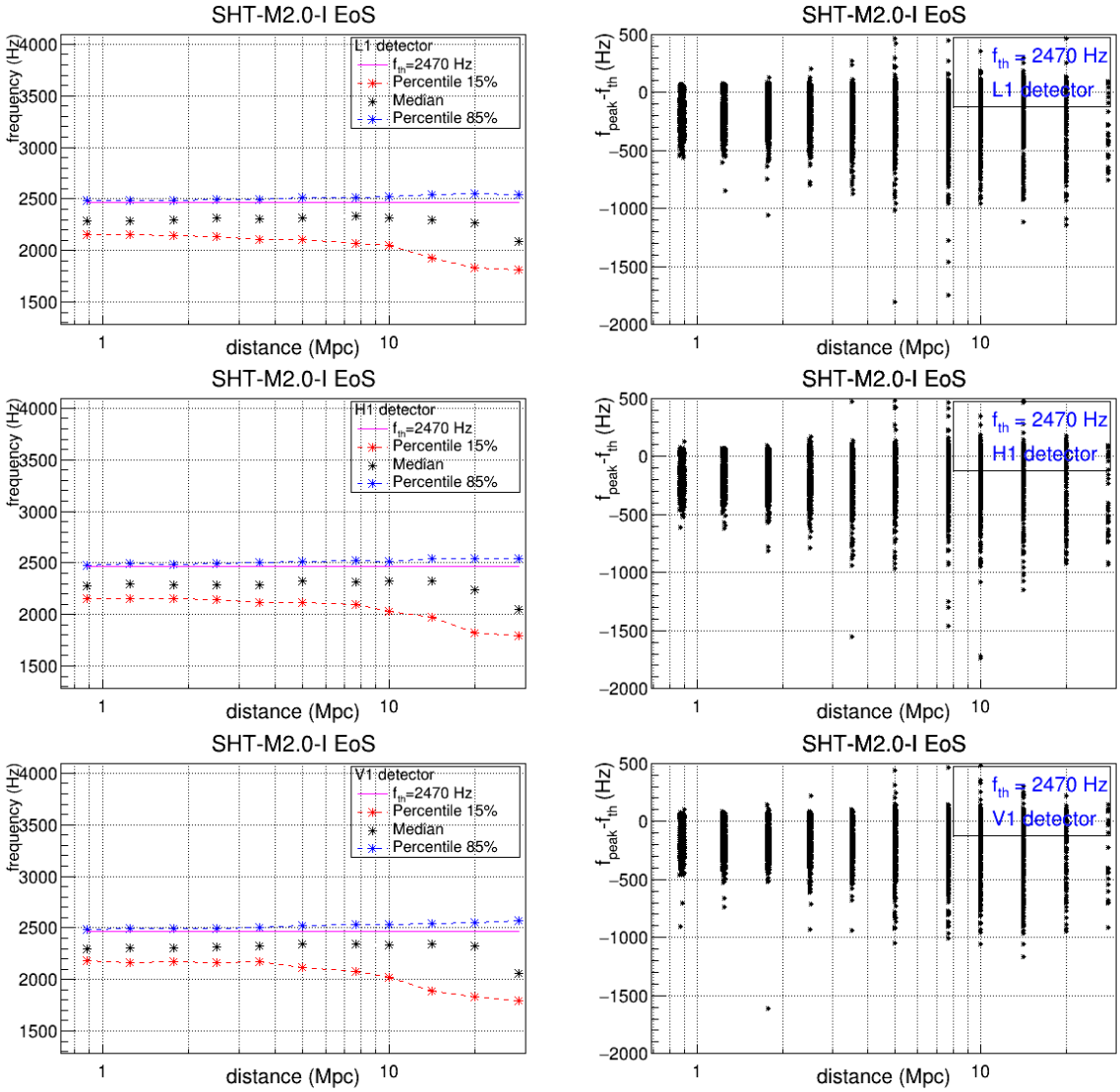

Figure 6.22: (Top) Distribution of frequency peak values for SHT-M2.0-I EoS. The color lines black, red and green refer to L1, H1 and V1 detectors, respectively. (Left) 15% (red dot line), 50% (black dot line) and 85% (blue dot line) percentiles of the distribution of the frequency peak estimated, as function of the distance. (Right) Scatter plot of difference frequency between estimated peak values and theoretical one, f_{th}= 2470 Hz.

6.3.2 LS220-M1.5-S EoS

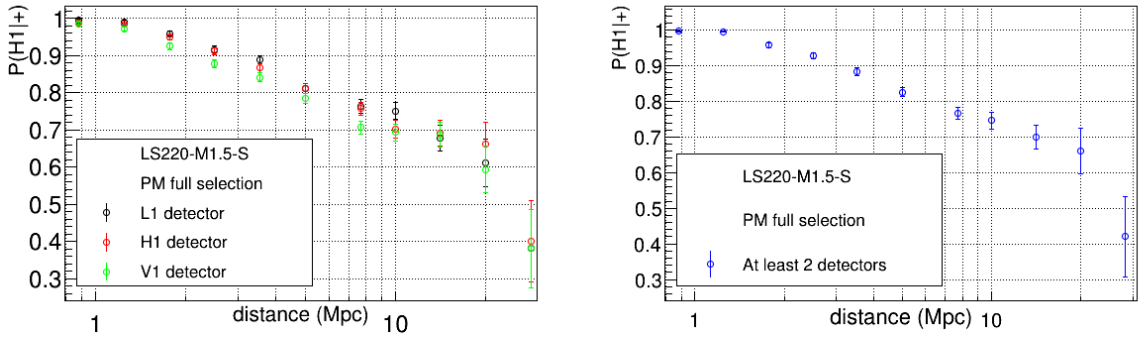

Figure 6.23: $P(H_1|+)$ of LSS20-M1.5-S EoS for Livingston detector (left plot) and for at least two detectors (right plot). The LSS20-M1.8-I EoS is used to compute the probability.

6.3.3 LS220-M1.5-I EoS

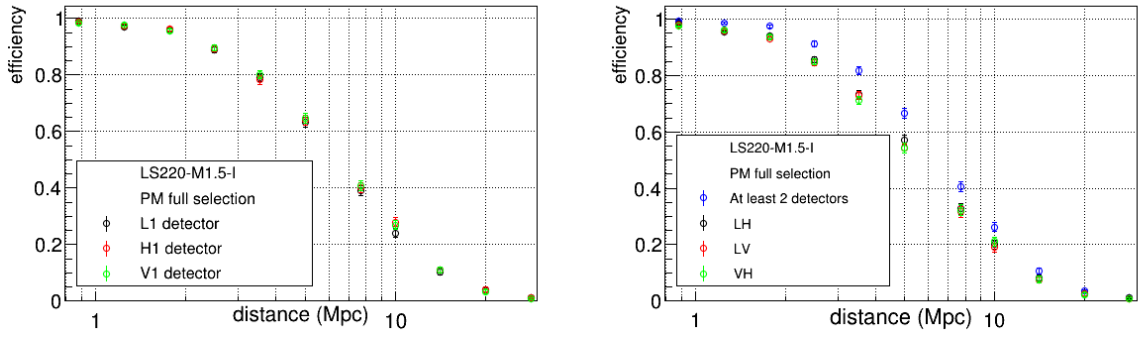

Figure 6.24: Efficiency with PM full selection for LS220-M1.5-I EoS model.

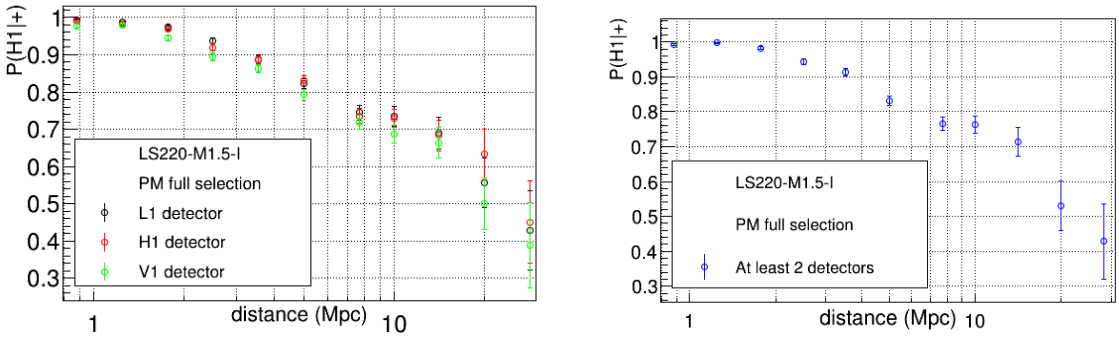

(a) LS220-M1.7-I EoS

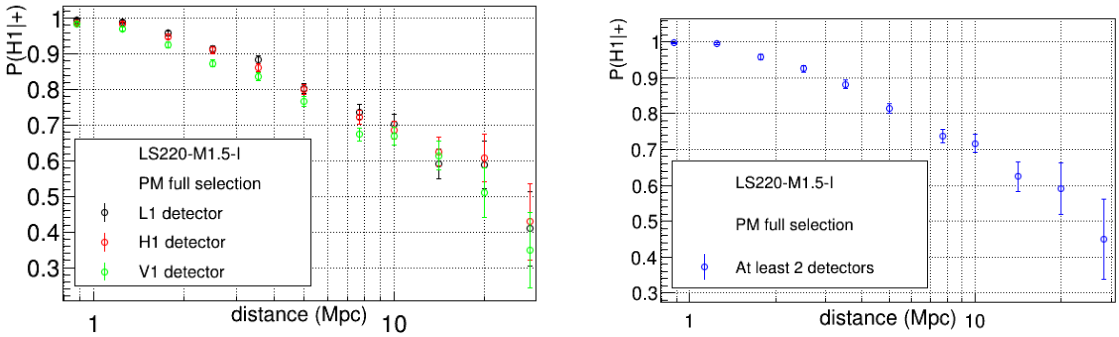

(b) LS220-M1.8-I EoS

Figure 6.25: $P(H_1|+)$ of LS220-M1.5-I EoS considering two BH models.

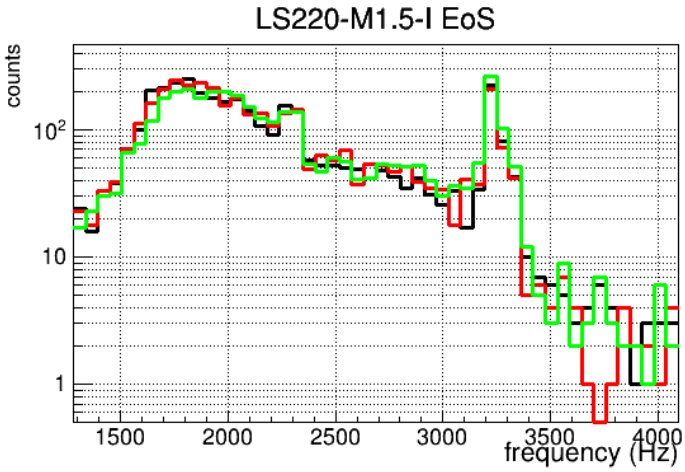

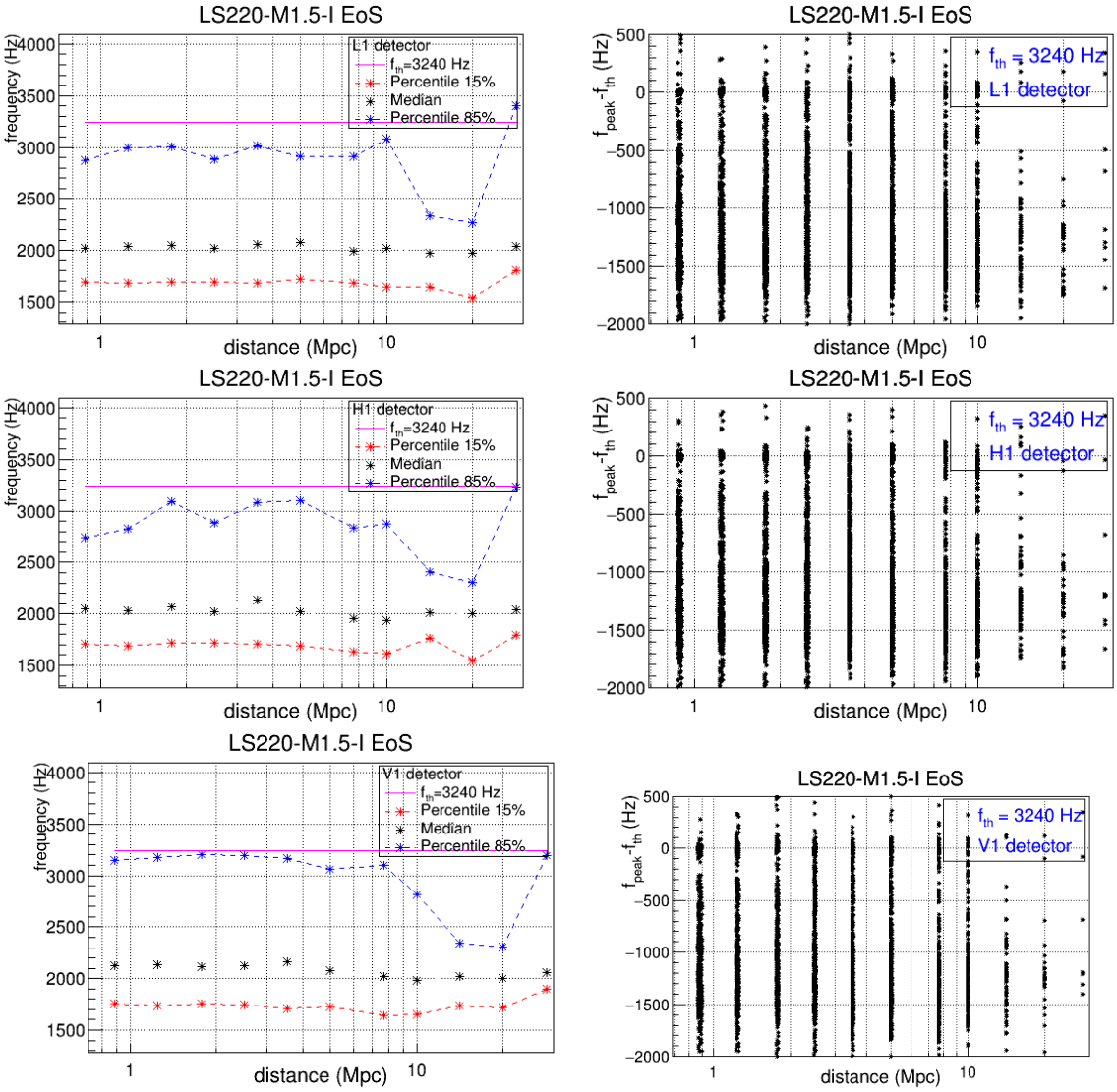

Figure 6.26: (Top) Distribution of frequency peak values for LS220-M1.5-I EoS. The color lines black, red and green refer to L1, H1 and V1 detectors, respectively. (Left) 15% (red dot line), 50% (black dot line) and 85% (blue dot line) percentiles of the distribution of the frequency peak estimated, as function of the distance. (Right) Scatter plot of difference frequency between estimated peak values and theoretical one, f_{th}= 3240 Hz.

6.3.4 H4-q08 EoS

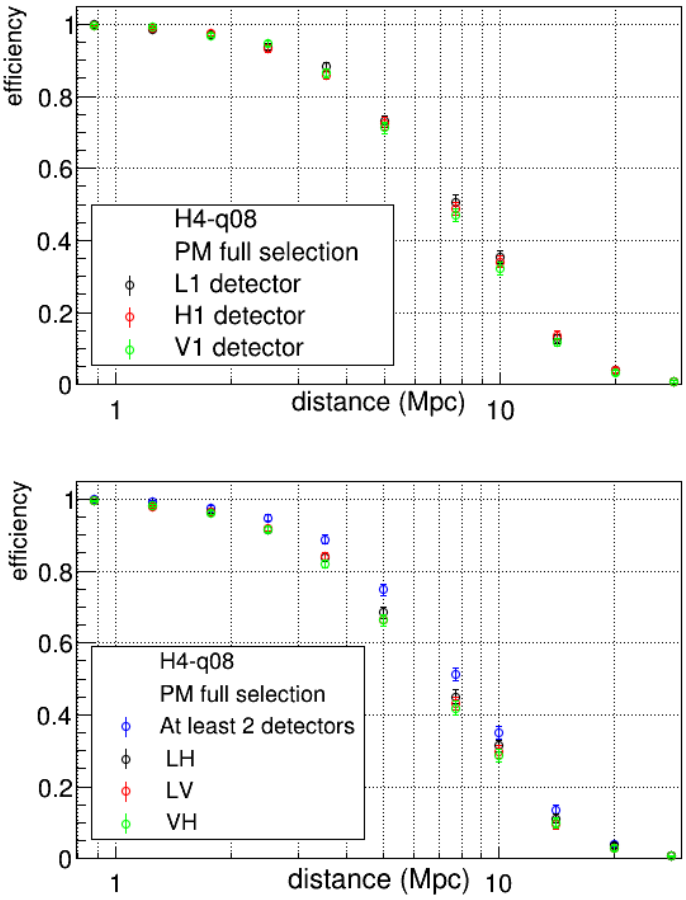

Figure 6.27: Efficiency with PM full selection for H4-q08 model.

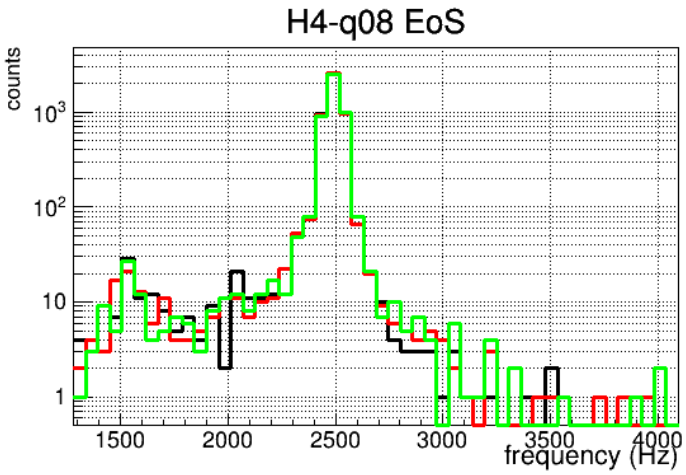

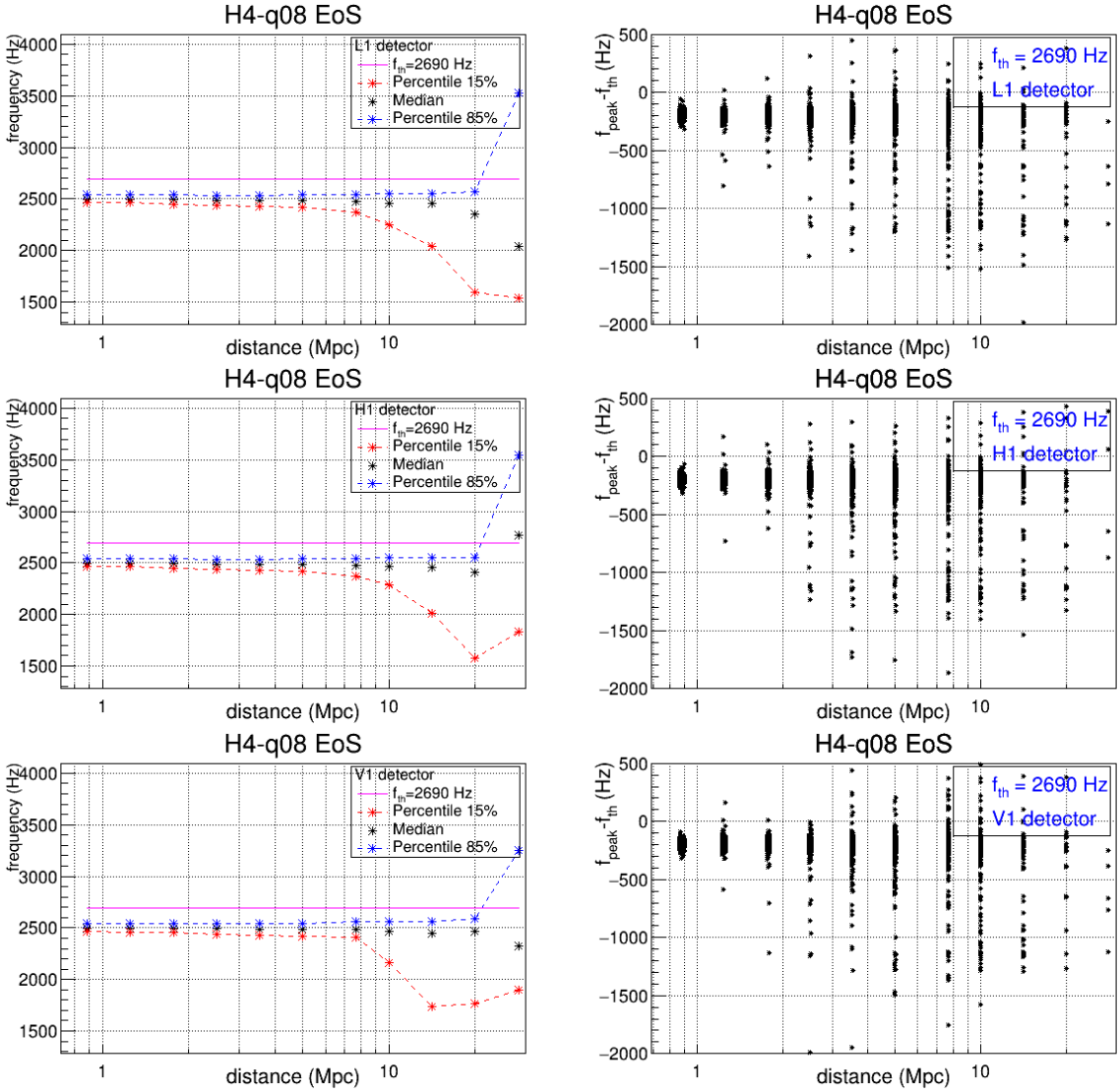

Figure 6.28: (Top) Distribution of frequency peak values for H4-q08 EoS. The color lines black, red and green refer to L1, H1 and V1 detectors, respectively. (Left) 15% (red dot line), 50% (black dot line) and 85% (blue dot line) percentiles of the distribution of the frequency peak estimated, as function of the distance. (Right) Scatter plot of difference frequency between estimated peak values and theoretical one, f_{th}= 2690 Hz.

6.3.5 H4-M1.5 EoS

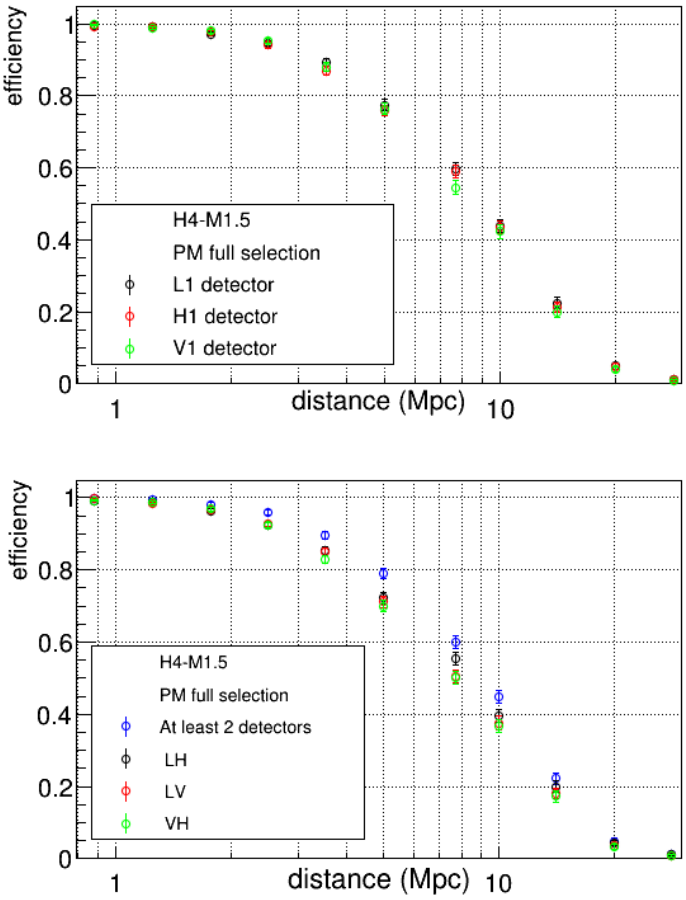

Figure 6.29: Efficiency with PM full selection for H4-M1.5model.

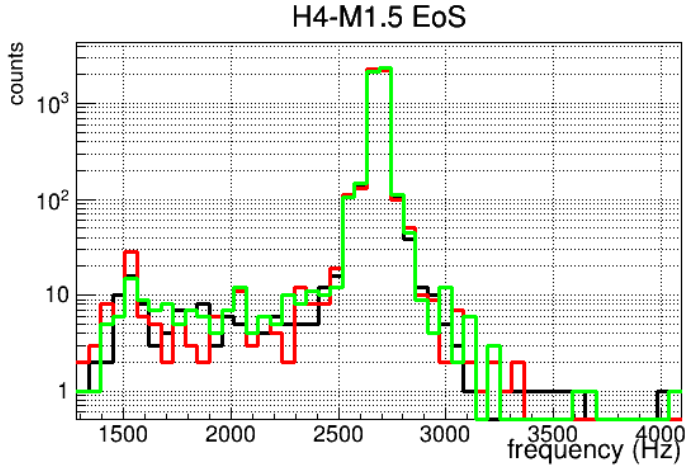

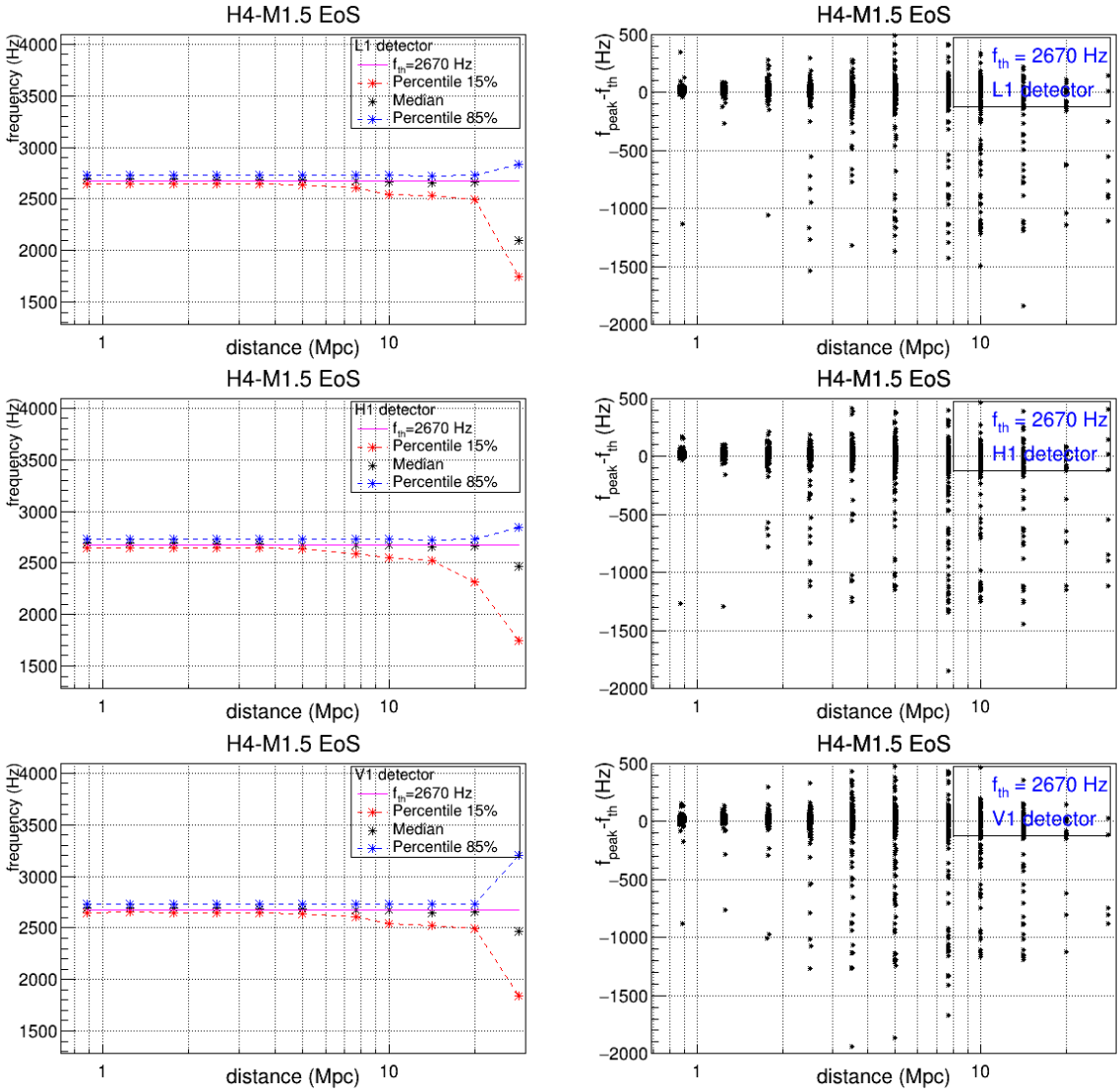

Figure 6.30: (Top) Distribution of frequency peak values for H4-M1.5 EoS. The color lines black, red and green refer to L1, H1 and V1 detectors, respectively. (Left) 15% (red dot line), 50% (black dot line) and 85% (blue dot line) percentiles of the distribution of the frequency peak estimated, as function of the distance. (Right) Scatter plot of difference frequency between estimated peak values and theoretical one, f_{th}= 2470 Hz.

6.3.6 H4-q09 EoS

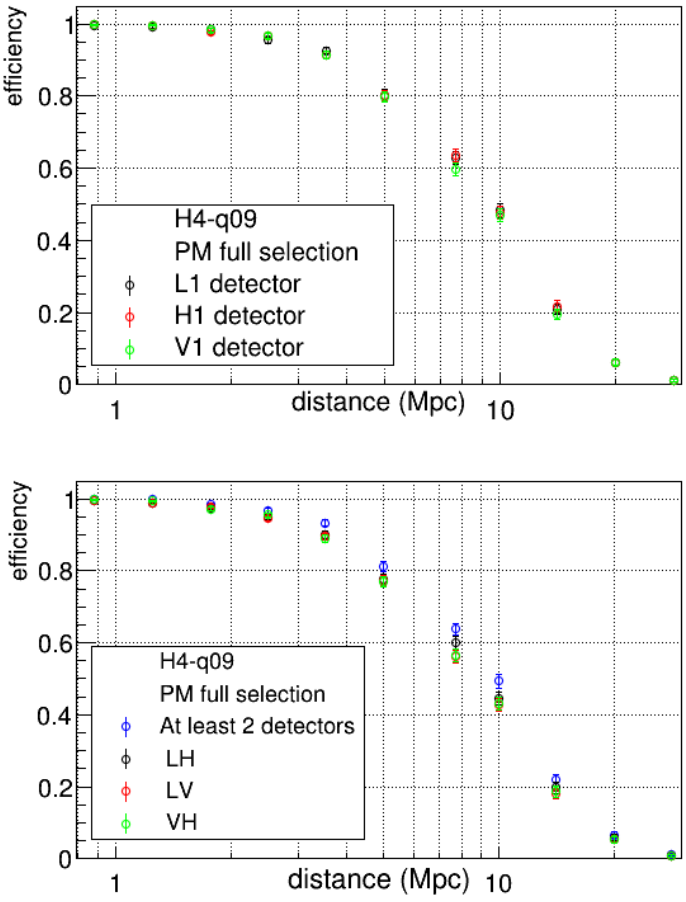

Figure 6.31: Efficiency with PM full selection for H4-q09 model.

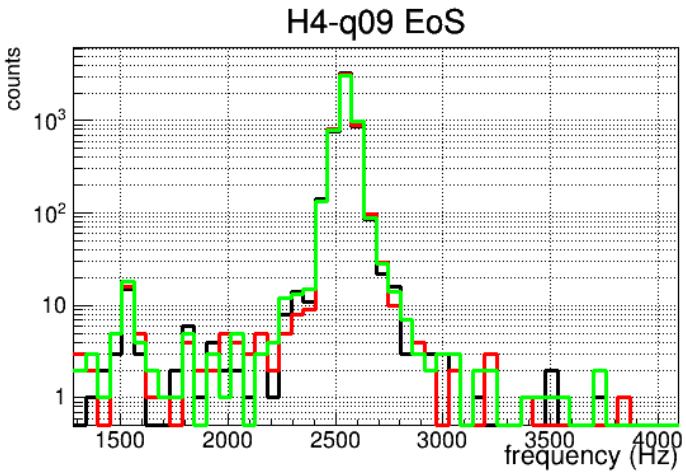

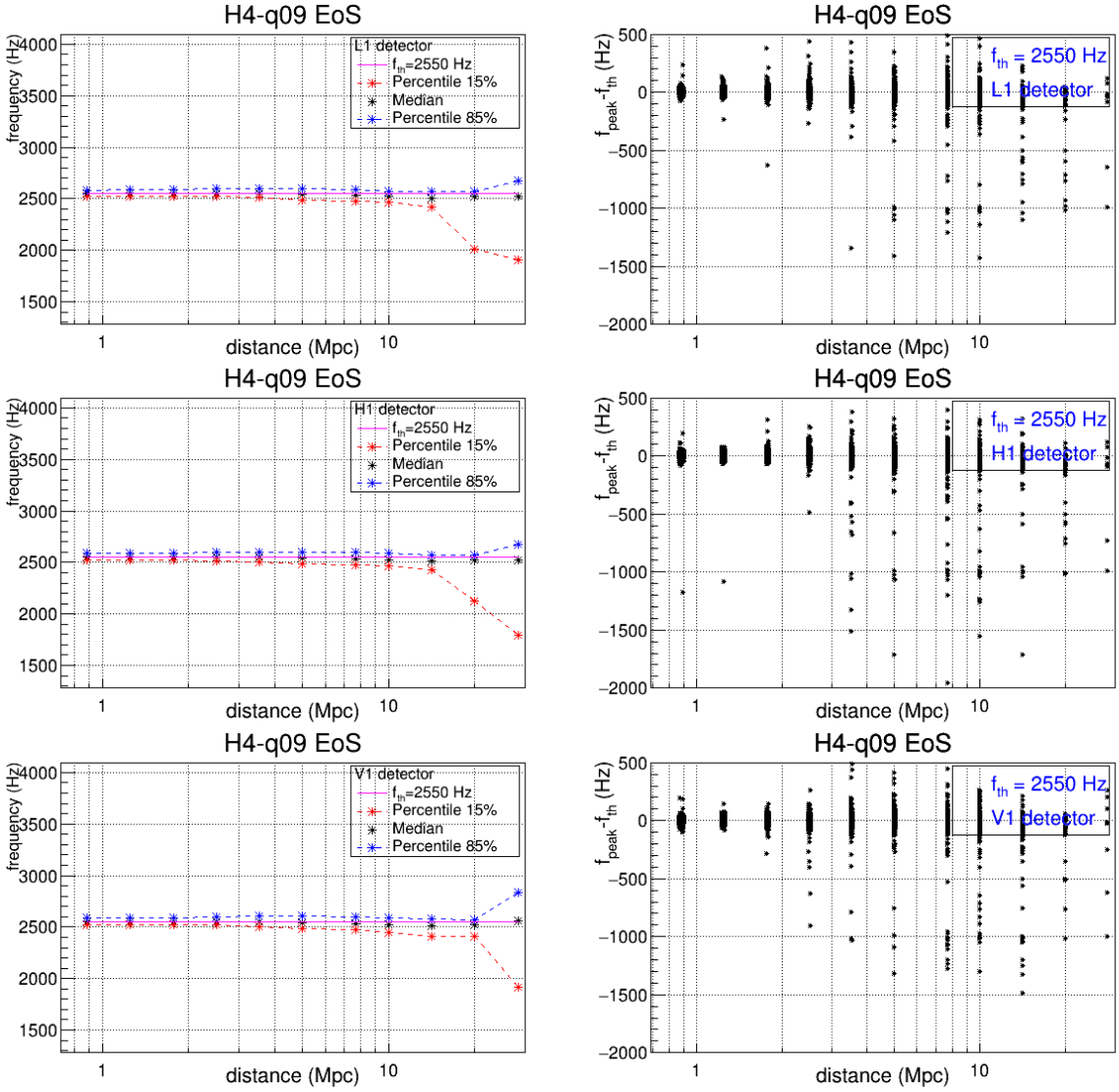

Figure 6.32: (Top) Distribution of frequency peak values for H4-q09 EoS. The color lines black, red and green refer to L1, H1 and V1 detectors, respectively. (Left) 15% (red dot line), 50% (black dot line) and 85% (blue dot line) percentiles of the distribution of the frequency peak estimated, as function of the distance. (Right) Scatter plot of difference frequency between estimated peak values and theoretical one, f_{th}= 2550 Hz.

6.3.7 H4-M1.4 EoS

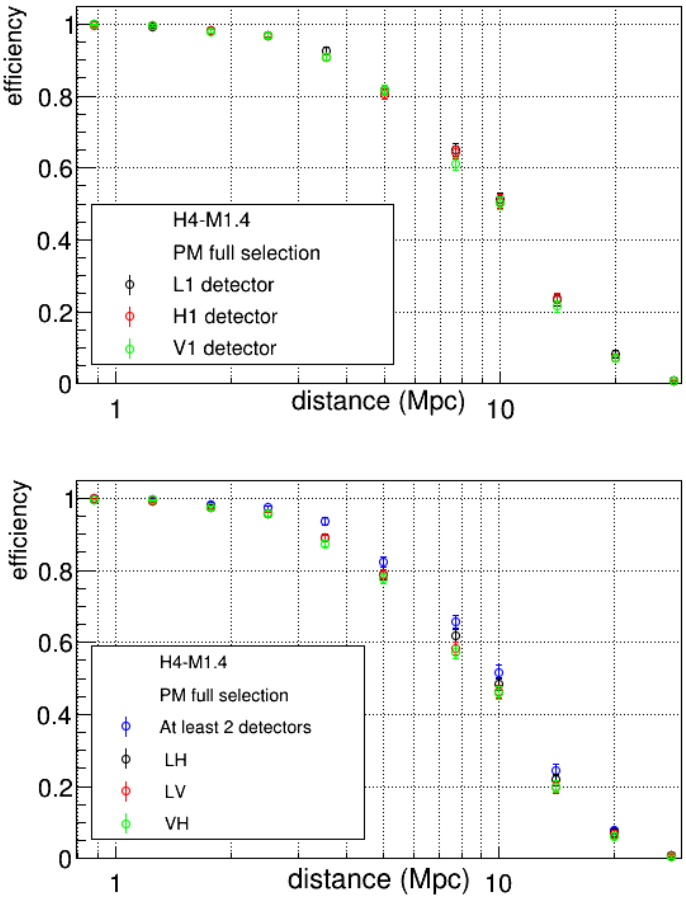

Figure 6.33: Efficiency with PM full selection for H4-q10 model.

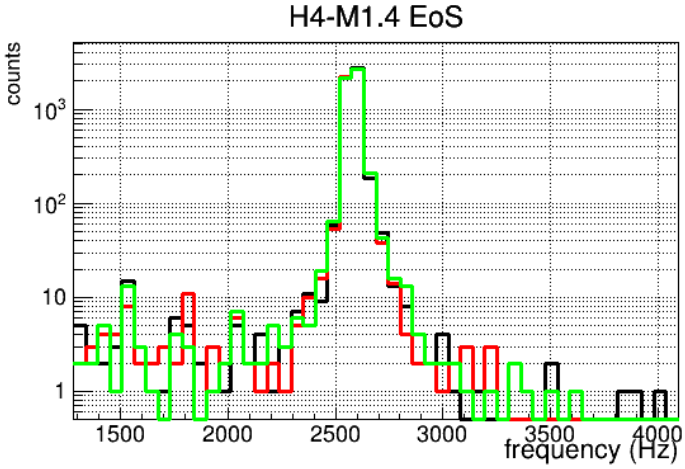

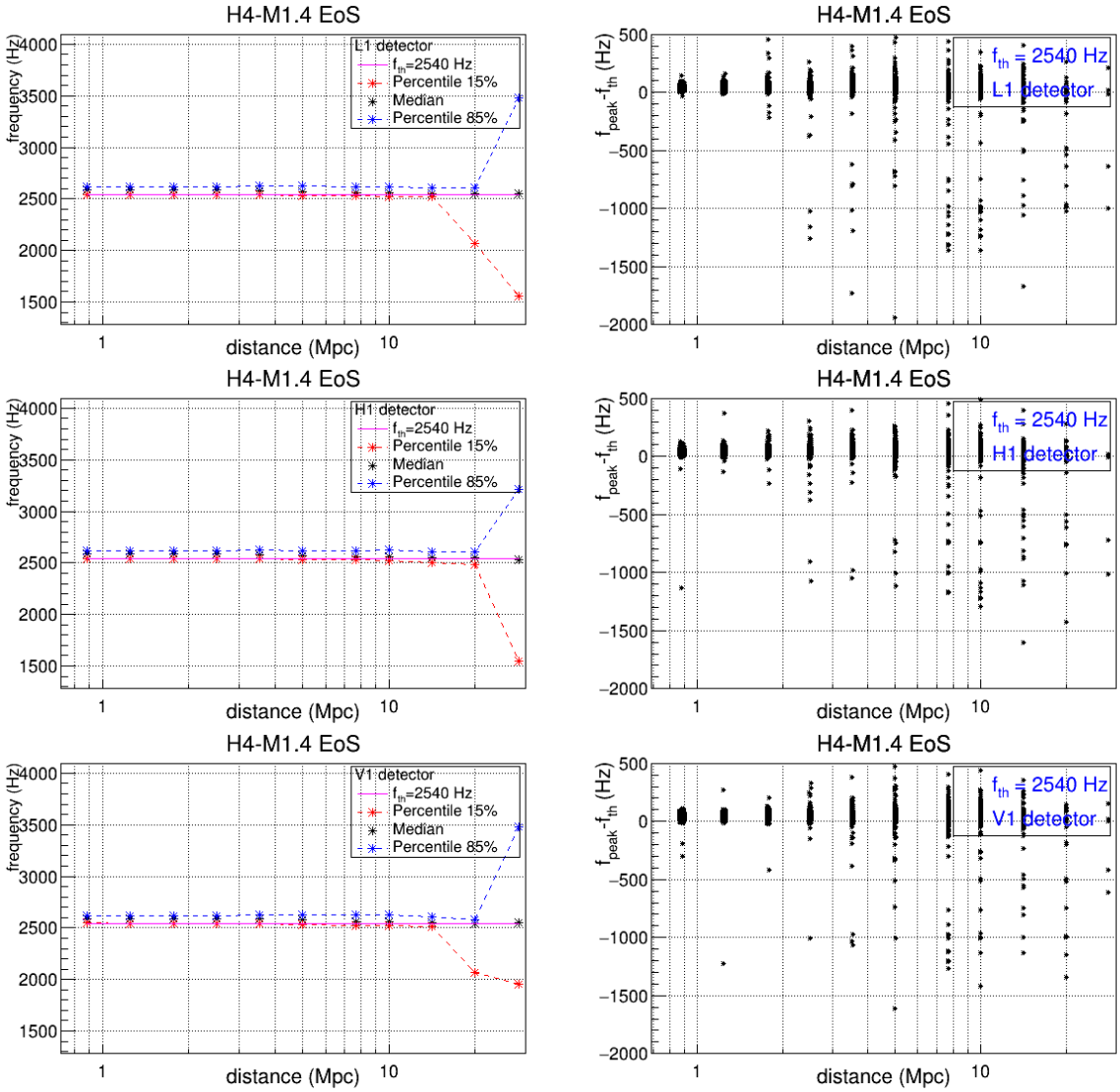

Figure 6.34: (Top) Distribution of frequency peak values for H4-M1.4 EoS. The color lines black, red and green refer to L1, H1 and V1 detectors, respectively. (Left) 15% (red dot line), 50% (black dot line) and 85% (blue dot line) percentiles of the distribution of the frequency peak estimated, as function of the distance. (Right) Scatter plot of difference frequency between estimated peak values and theoretical one, f_{th}= 2540 Hz.

6.3.8 APR4-LM EoS

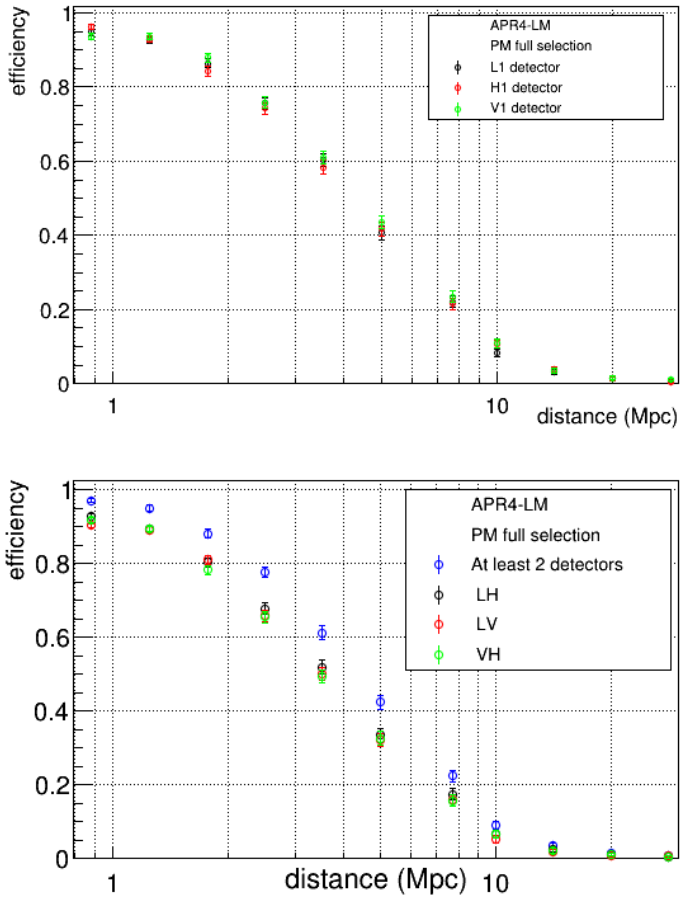

Figure 6.35: Efficiency with PM full selection for APR4-LM model.

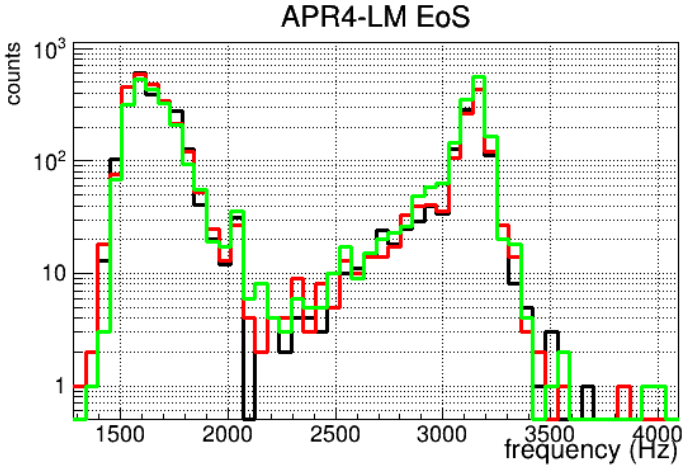

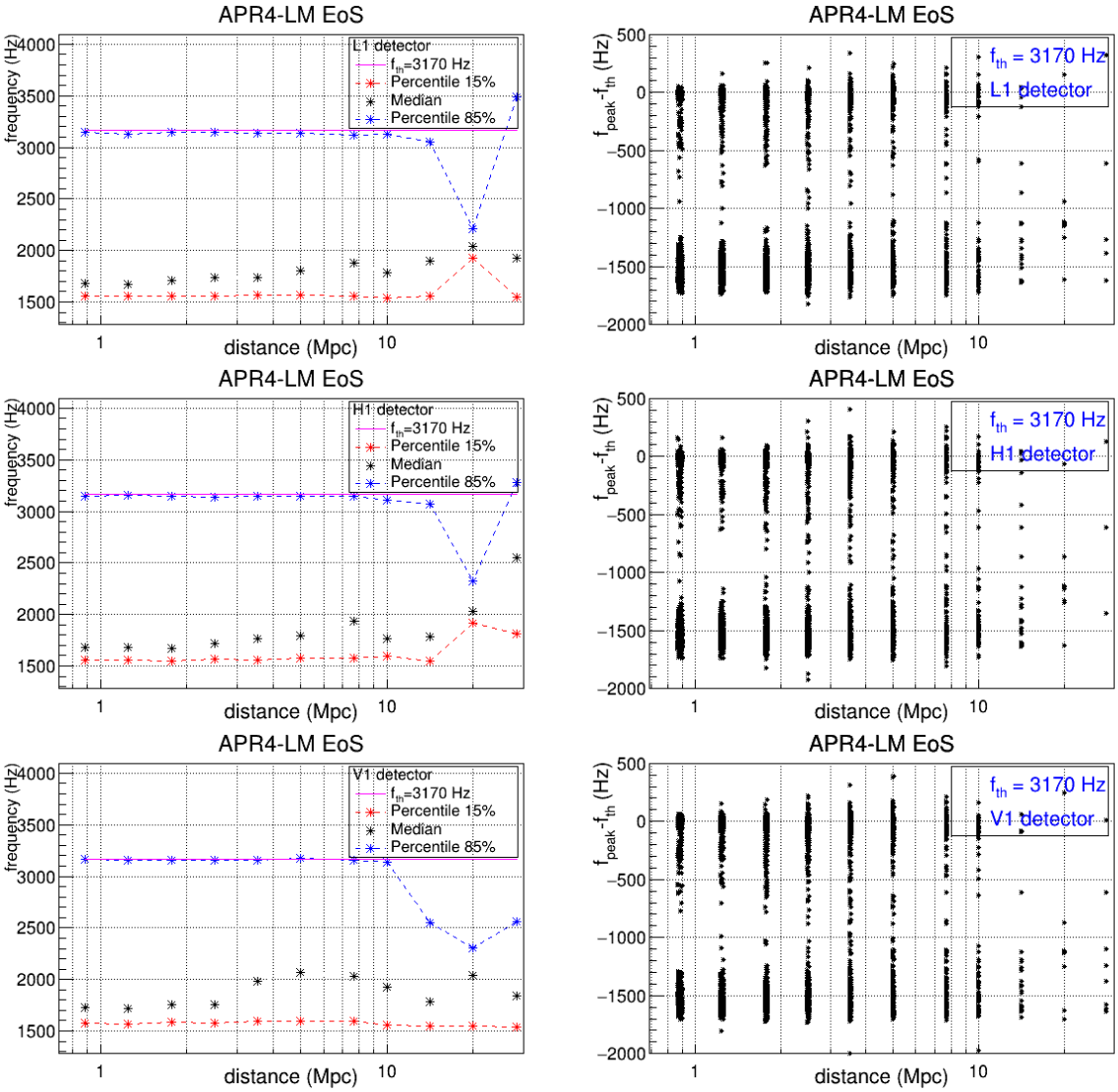

Figure 6.36: (Top) Distribution of frequency peak values for APR-LM EoS. The color lines black, red and green refer to L1, H1 and V1 detectors, respectively. (Left) 15% (red dot line), 50% (black dot line) and 85% (blue dot line) percentiles of the distribution of the frequency peak estimated, as function of the distance. (Right) Scatter plot of difference frequency between estimated peak values and theoretical one, f_{th}= 3170 Hz.

6.3.9 APR4-UM EoS

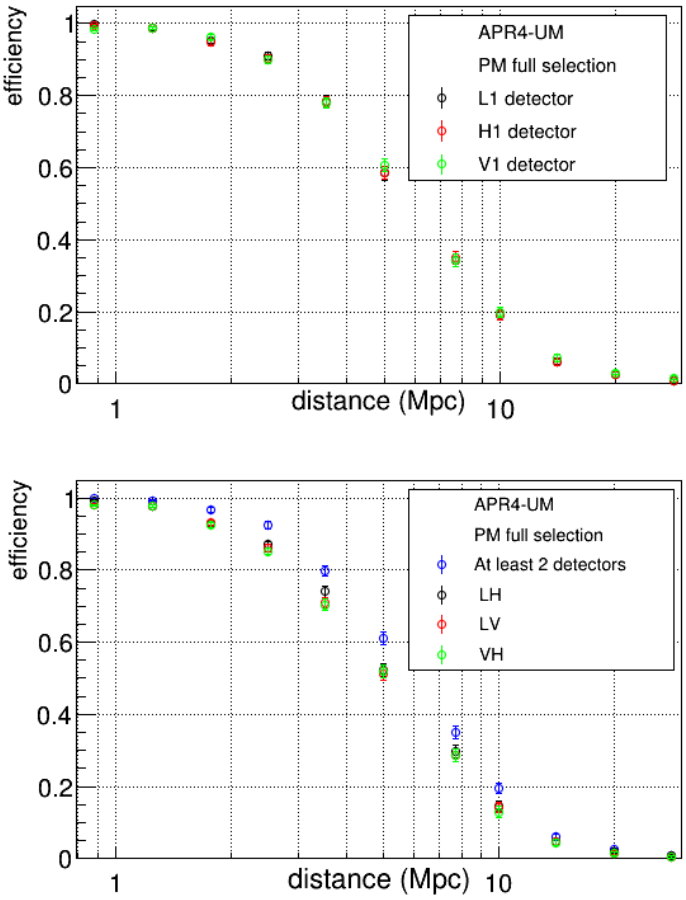

Figure 6.37: Efficiency with PM full selection for APR4-UM model.

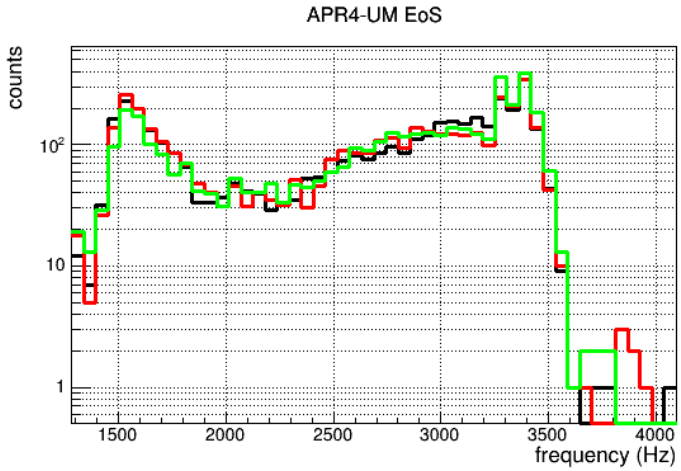

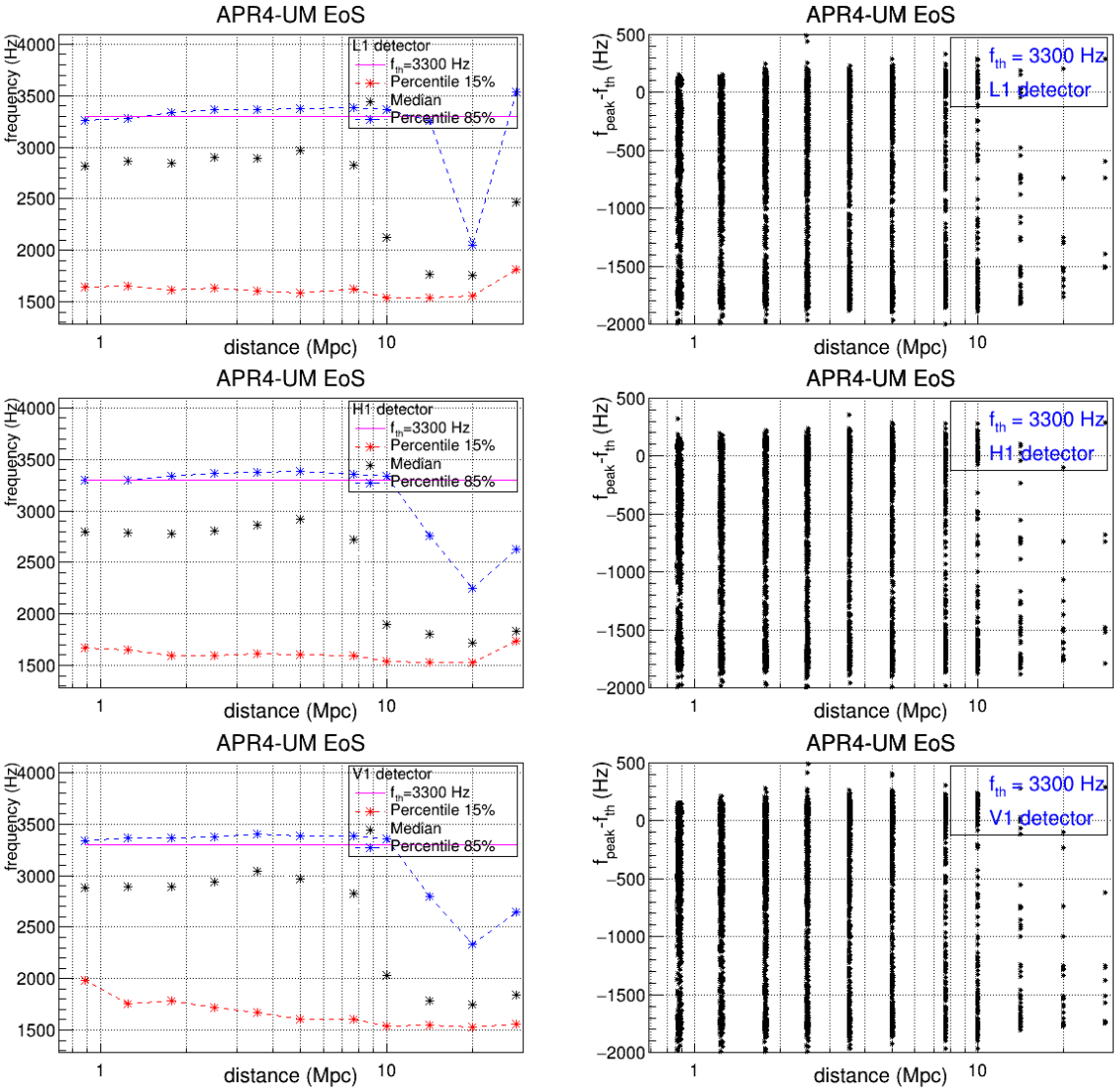

Figure 6.38: (Top) Distribution of frequency peak values for APR-UM EoS. The color lines black, red and green refer to L1, H1 and V1 detectors, respectively. (Left) 15% (red dot line), 50% (black dot line) and 85% (blue dot line) percentiles of the distribution of the frequency peak estimated, as function of the distance. (Right) Scatter plot of difference frequency between estimated peak values and theoretical one, f_{th}= 3330 Hz.

6.3.10 APR4-q09 EoS

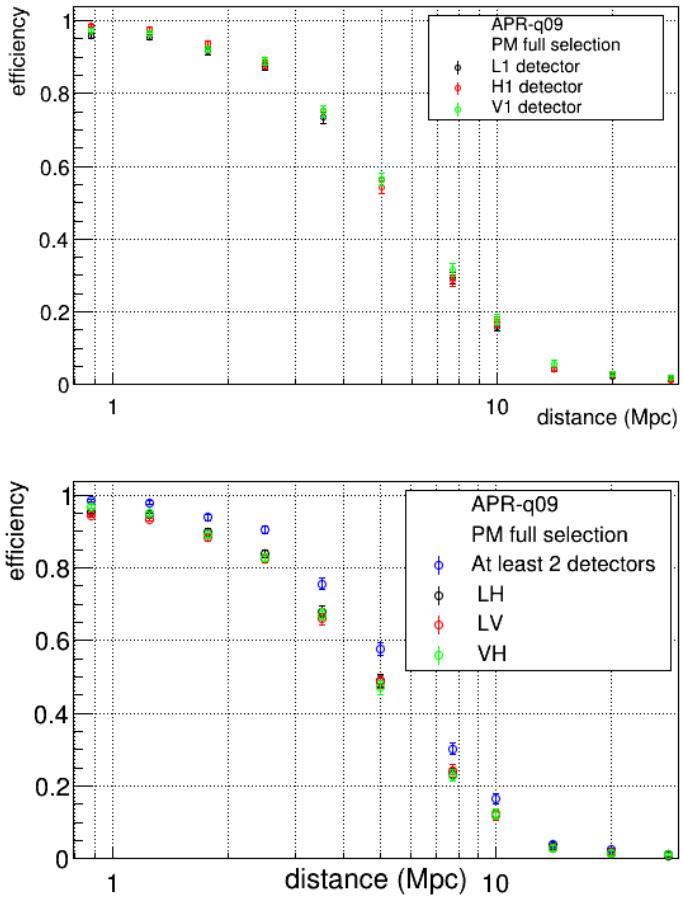

Figure 6.39: Efficiency with PM full selection for APR4-q09 model.

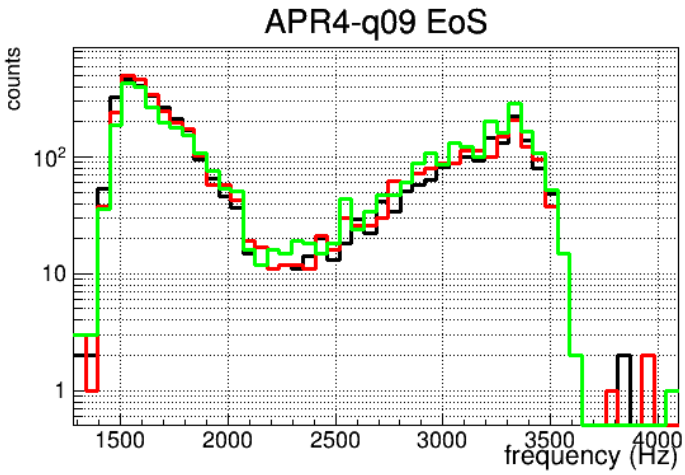

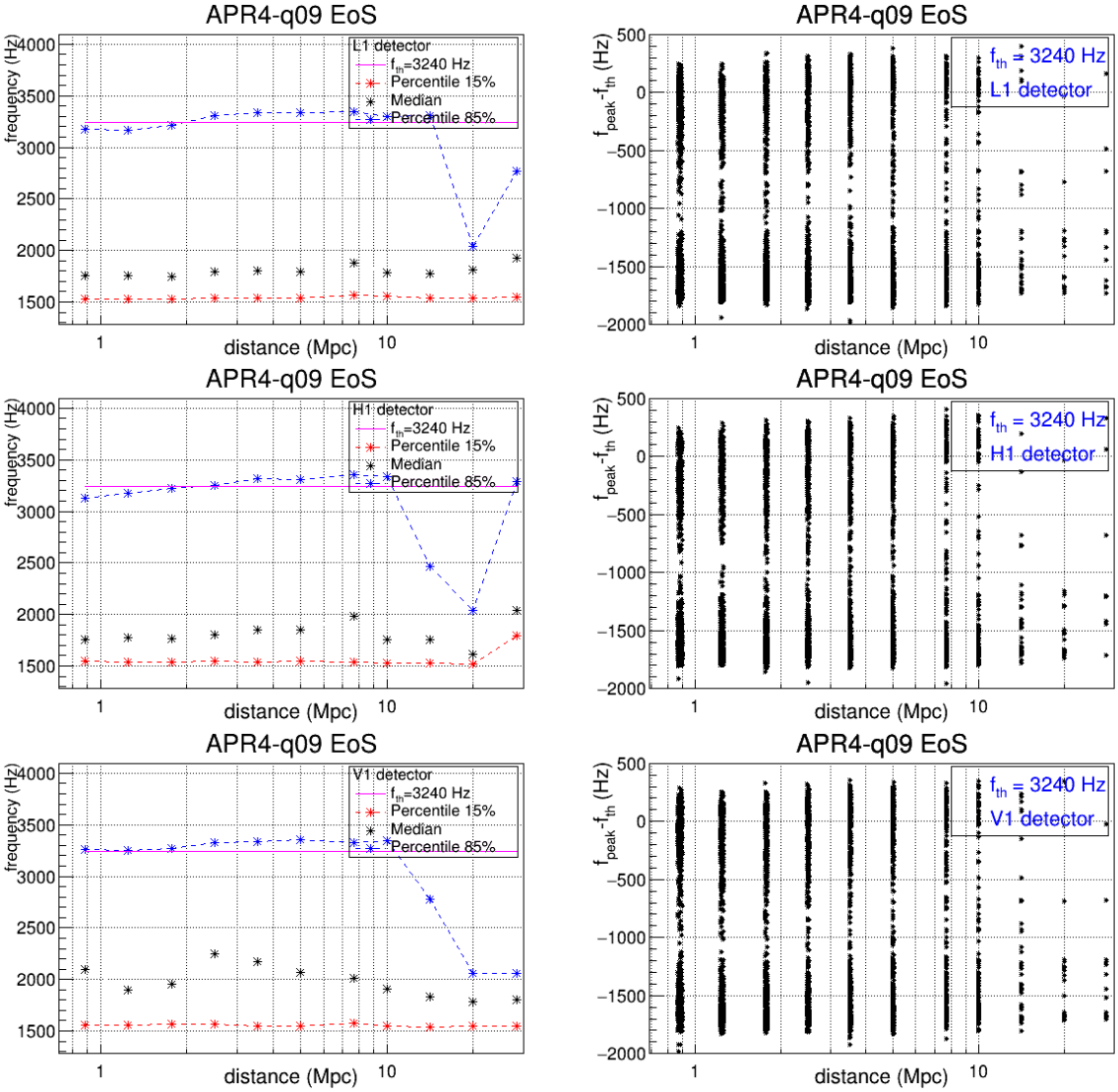

Figure 6.40: (Top) Distribution of frequency peak values for APR-q09 EoS. The color lines black, red and green refer to L1, H1 and V1 detectors, respectively. (Left) 15% (red dot line), 50% (black dot line) and 85% (blue dot line) percentiles of the distribution of the frequency peak estimated, as function of the distance. (Right) Scatter plot of difference frequency between estimated peak values and theoretical one, f_{th}= 3240 Hz.

6.3.11 MS1-q09 EoS

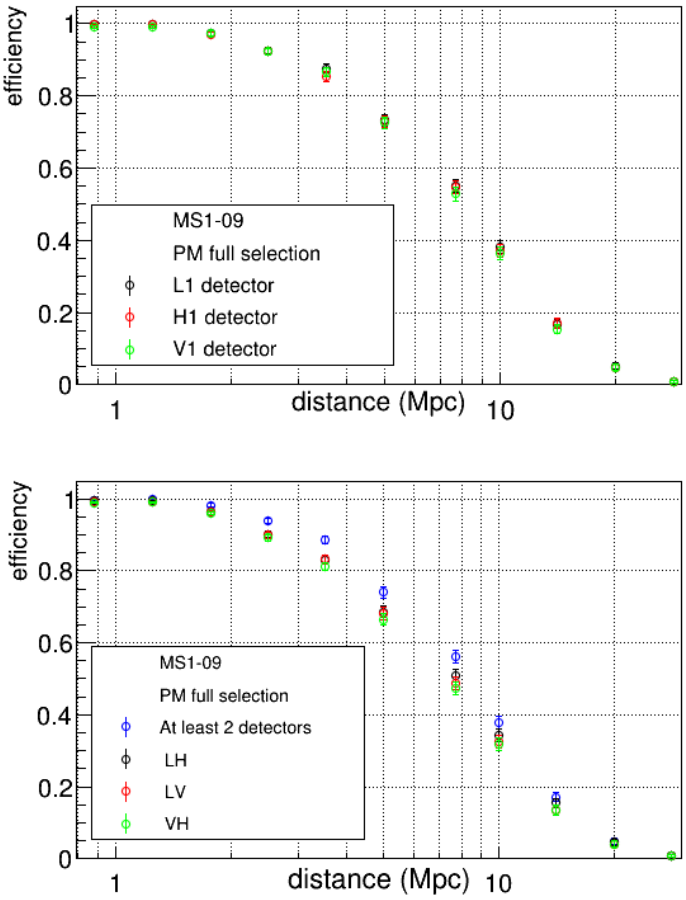

Figure 6.41: Efficiency with PM full selection for MS1-q09 model.

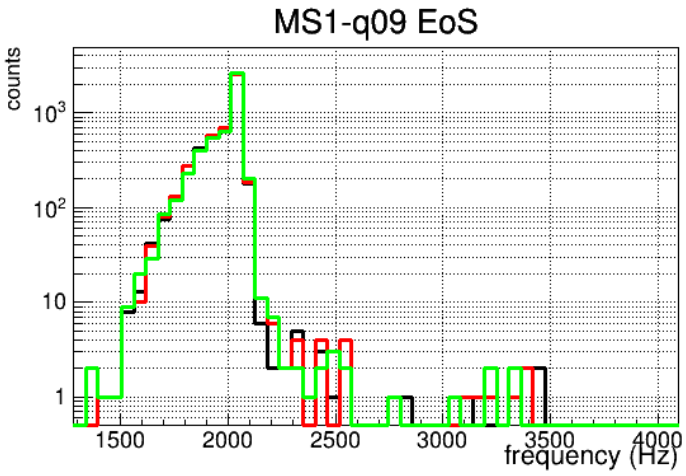

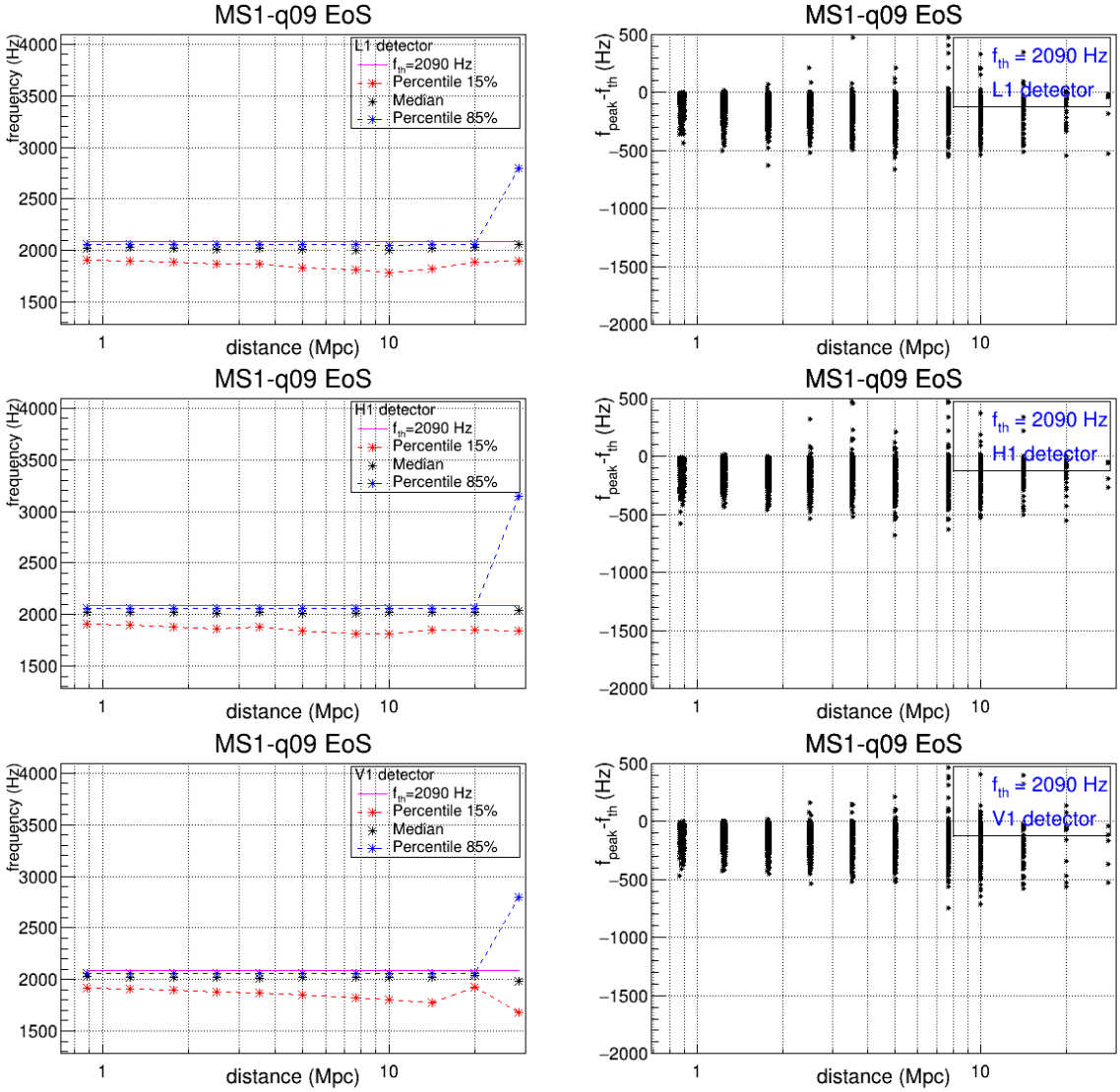

Figure 6.42: (Top) Distribution of frequency peak values for MS1-q09 EoS. The color lines black, red and green refer to L1, H1 and V1 detectors, respectively. (Left) 15% (red dot line), 50% (black dot line) and 85% (blue dot line) percentiles of the distribution of the frequency peak estimated, as function of the distance. (Right) Scatter plot of difference frequency between estimated peak values and theoretical one, f_{th}= 2090 Hz.

6.3.12 MS1-M1.45 EoS

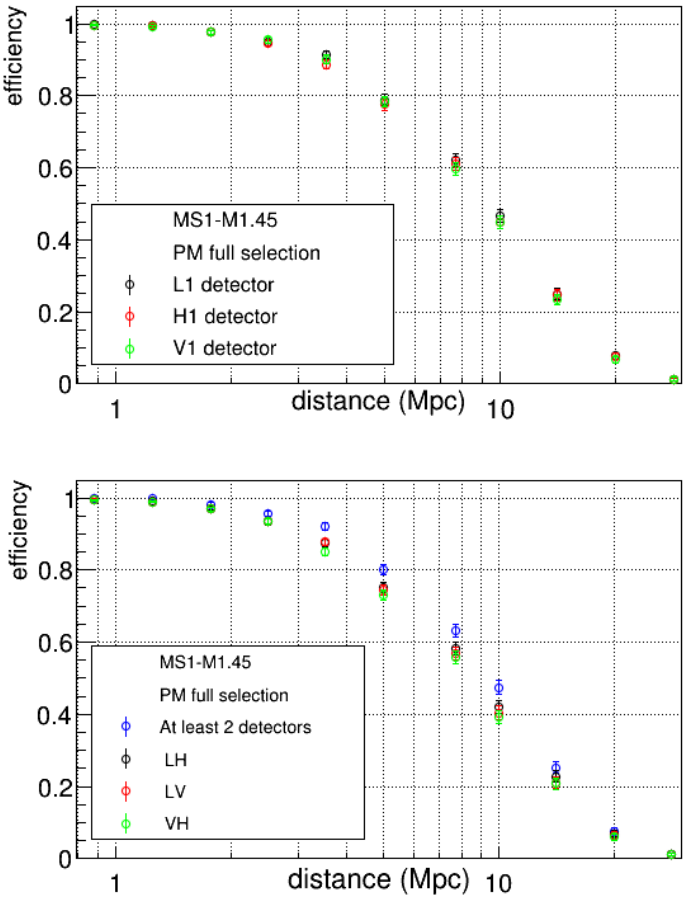

Figure 6.43: Efficiency with PM full selection for MS1-M1.45 model.

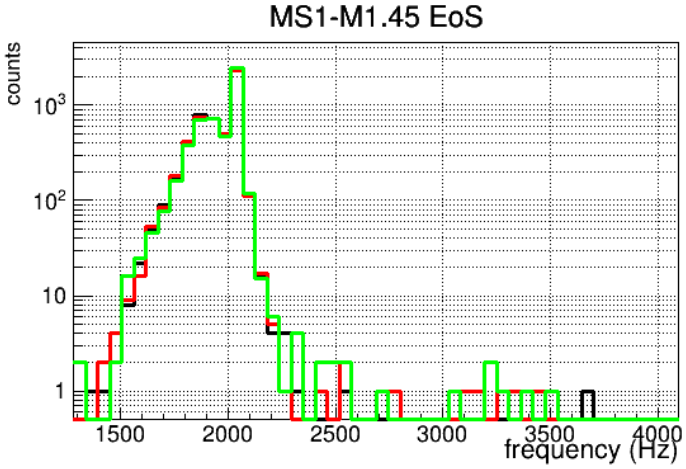

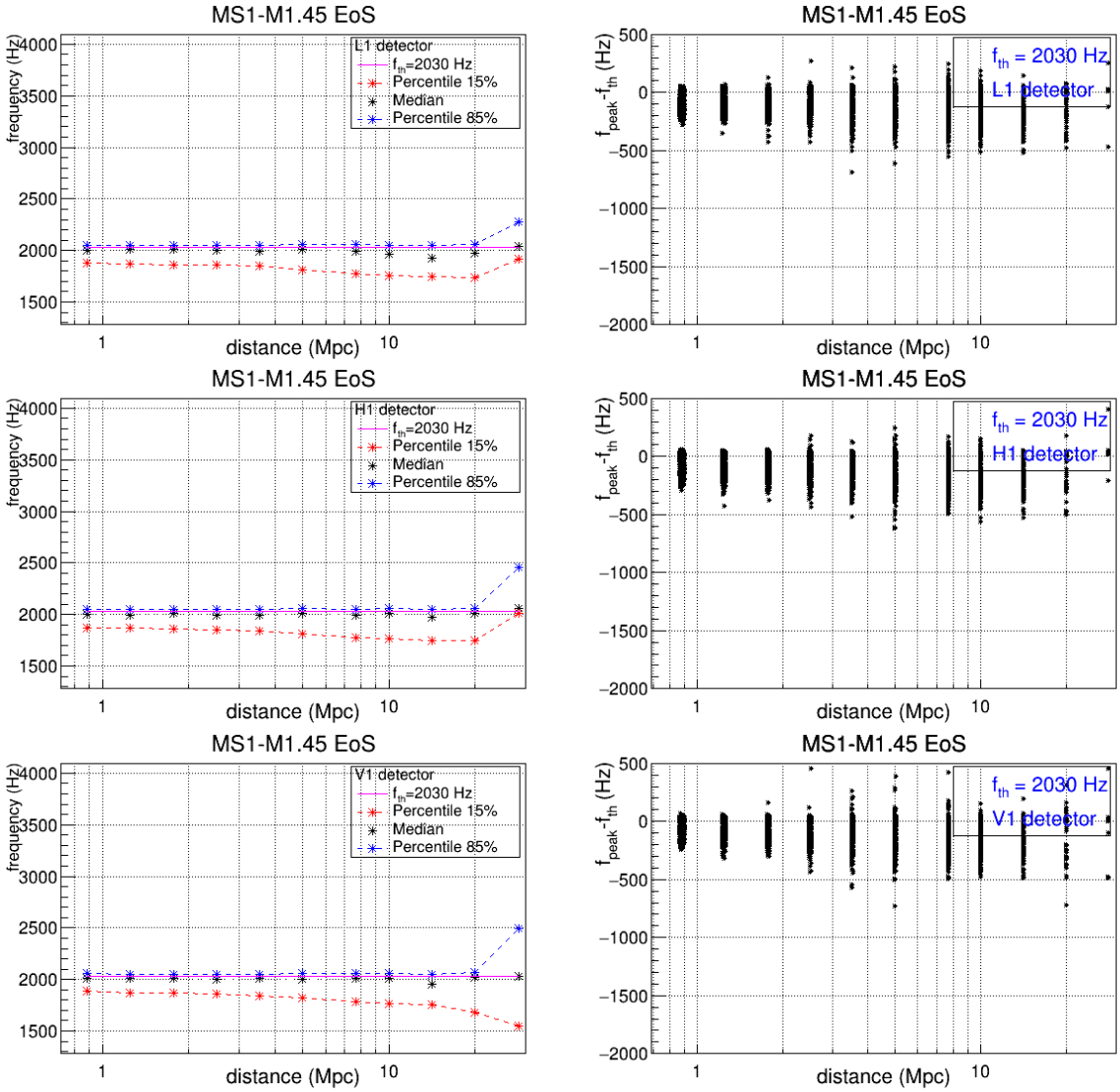

Figure 6.44: (Top) Distribution of frequency peak values for MS1-q10 EoS. The color lines black, red and green refer to L1, H1 and V1 detectors, respectively. (Left) 15% (red dot line), 50% (black dot line) and 85% (blue dot line) percentiles of the distribution of the frequency peak estimated, as function of the distance. (Right) Scatter plot of difference frequency between estimated peak values and theoretical one, f_{th}= 2030 Hz.

6.3.13 SHT-M1.5-I EoS

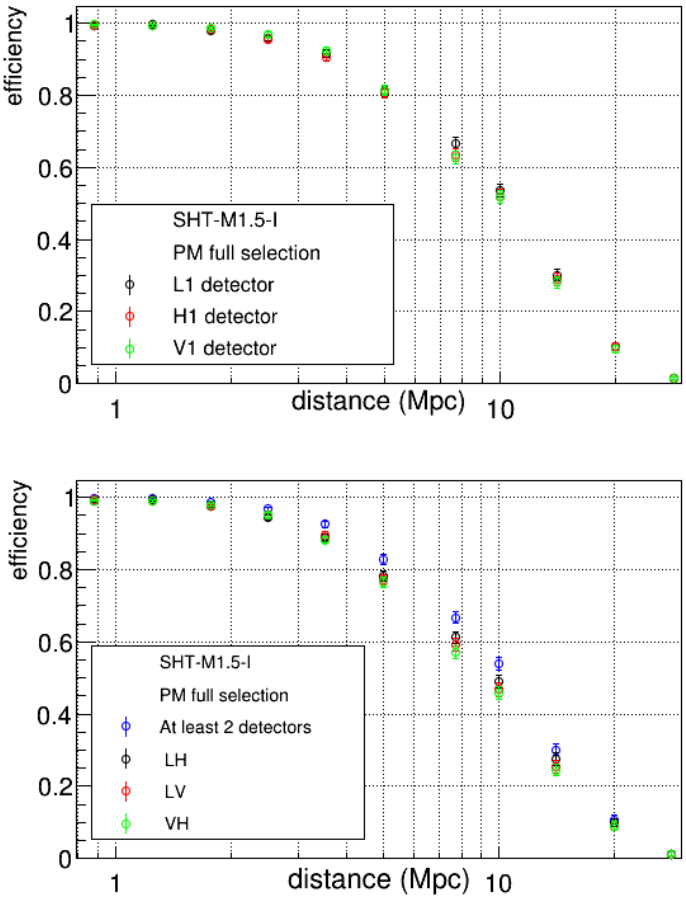

Figure 6.45: Efficiency with PM full selection for SHT-M15 model.

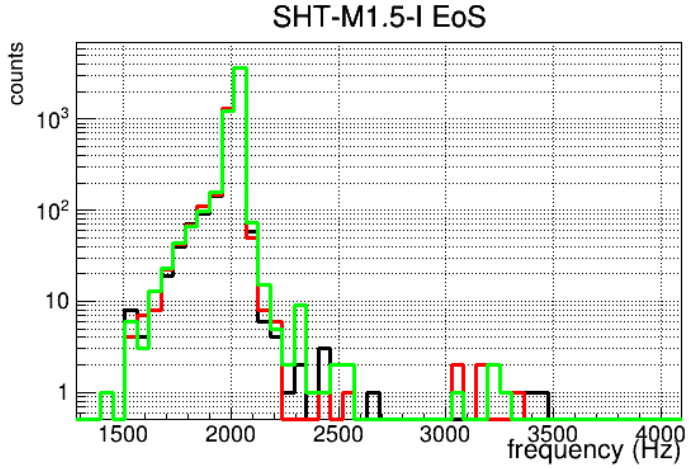

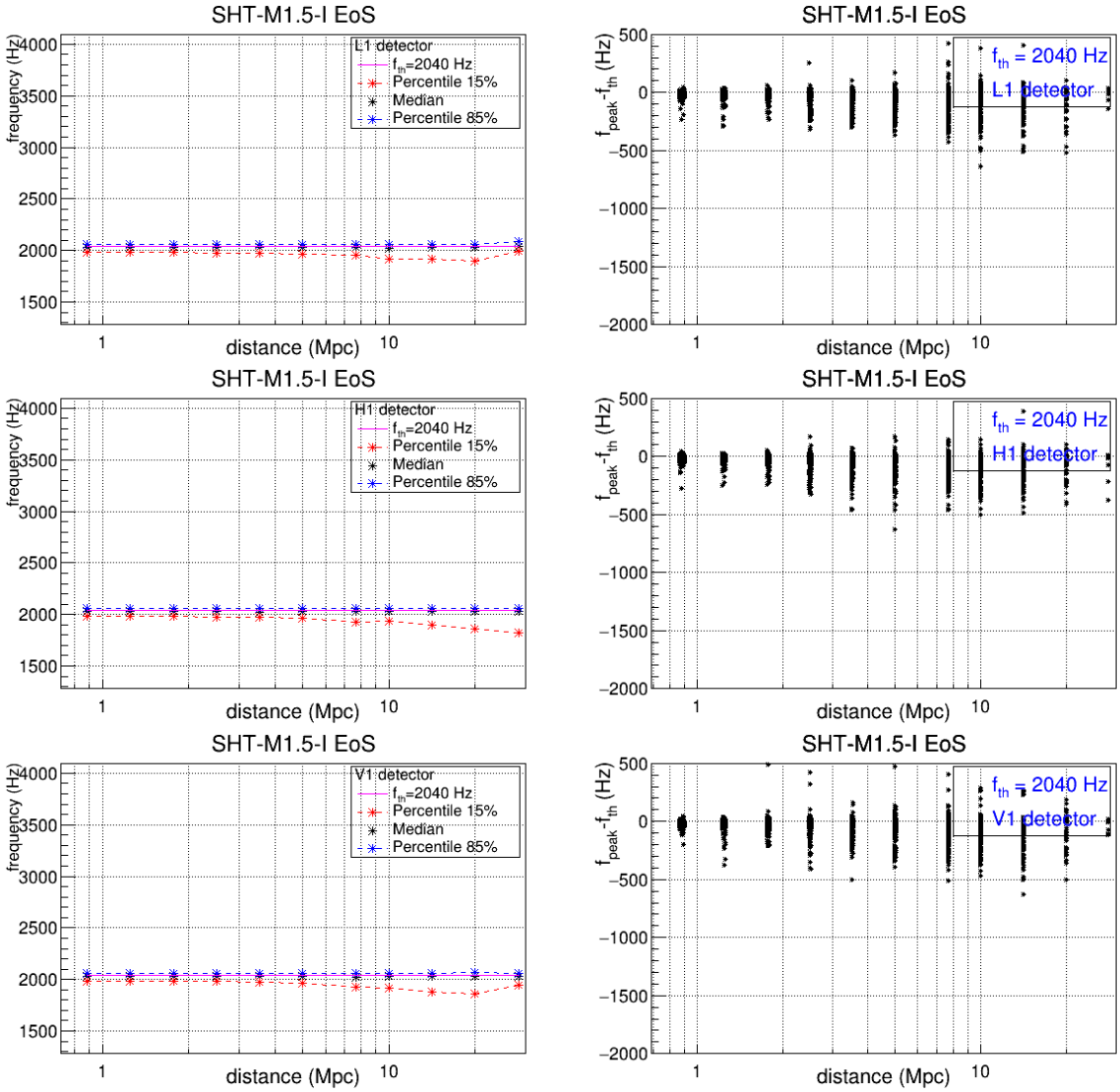

Figure 6.46: (Top) Distribution of frequency peak values for SHT-M1.5-I EoS. The color lines black, red and green refer to L1, H1 and V1 detectors, respectively. (Left) 15% (red dot line), 50% (black dot line) and 85% (blue dot line) percentiles of the distribution of the frequency peak estimated, as function of the distance. (Right) Scatter plot of difference frequency between estimated peak values and theoretical one, f_{th}= 2040 Hz.

6.3.14 APR4-HM EoS

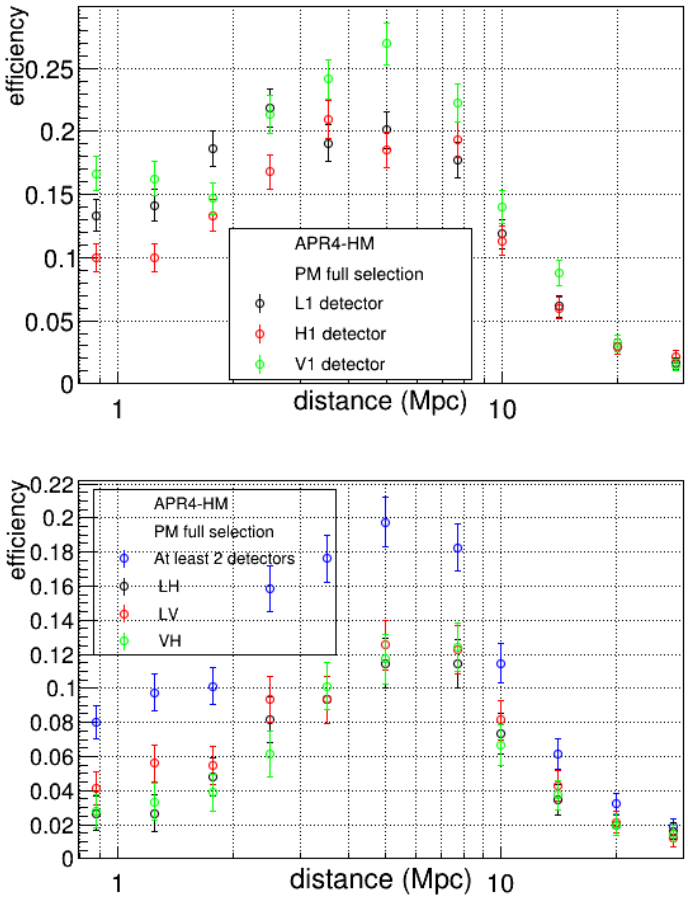

Figure 6.47: Efficiency with PM full selection for APR4-HM model.

Chapter 7

Simulation results with actual data

In this chapter, we describe a preliminary test of the performances on real data of the methods developed in this thesis. The first step is building a real data set with comparable sensitivities with respect to the simulated data used in the previous tests. To this purpose, we start from a stream of actual $h(t)$ data from the last observation run of previous generation LIGO and Virgo detectors, namely LIGO-S6 and Virgo-VSR3 runs, see Figure 7.1. The $h(t)$ stream of each detector is then scaled by a constant, to produce an effective spectral sensitivity matching the design sensitivity of advanced detectors at a reference frequency, namely 1 kHz. Since all these spectral sensitivities share a very similar spectral index in the frequency range of interest for this analysis, the scaling produces an approximate design sensitivity curve on top of which the spectral and the transient features of the actual noise are preserved.

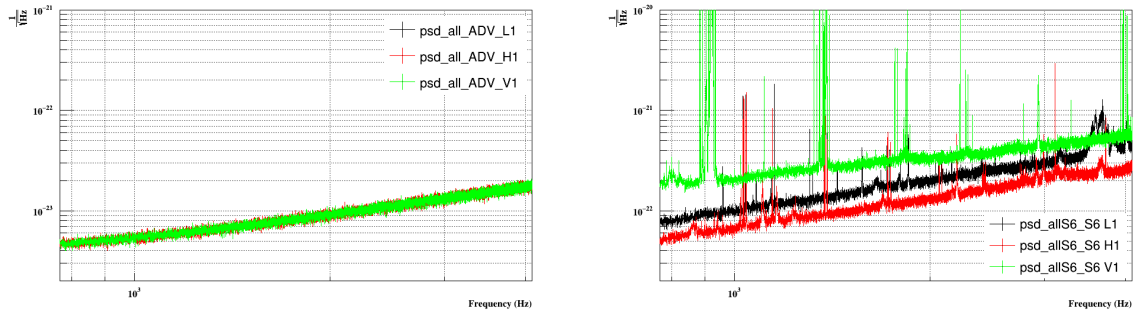

Figure 7.1: Amplitude noise spectral densities: the simulated advanced detector design sensitivity (left) compared to the actual noise of the last observation by initial generation detetors (right). By scaling the actual $h(t)$ data streams of past observations, we produce real noise data which mimick the spectral sensitivity for the advanced detectors.

We tested the method on a representative sub-set of the NR waveforms, namely

the SHT-M2.0-S and I, LS220-M1.5-S, H4-M1.5, H4-q08, MS1-M1.45, APR4-LM, SHT-M2.2-I, LS220-M1.7-I and LS220-M1.8-I. The same analysis procedures and the same parameters described in Chapter 5 have been used here. The resulting efficiencies for PM signals from NS remnant are shown in Figure 7.2, while the false positive probabilities for a NS remnant in case of prompt collapse to BH are shown in Figure 7.3. Both quantities result lower with respect to the performances achieved in simulated noise, which is something expected. The comparison of the performances is summarized in Table 7.1 and Table 7.2. At 10 Mpc the efficiencies, as defined by detection of a PM signal in at least two detectors, for real (simulated) noise range from ∼15% (30%) for LS220-M1.5-S to ∼39% (56%) for SHT-M2.0-S, while the false positive probabilities span from ∼2% (7%) for SHT-M2.2-I to ∼4% (8%) for LS220-M1.7-I. An estimate of the posterior probability of correct classification of the PM signal from a NS remnant is shown in Figure 7.4, assuming equal probability priors for the alternative models of NS remnant formation versus prompt collapse to BH.

		efficiency	
Model	M_{tot} [$M_\odot$]	5 Mpc	10 Mpc
SHT-M2.0-S	4.01	(78 ± 2)% [81%]	(39 ± 2)% [56%]
SHT-M2.0-I	4.01	(81 ± 2)% [82%]	(38 ± 2)% [57%]
LS220-M1.5-S	3.12	(60 ± 2)% [72%]	(15 ± 2)% [30%]
H4-M1.5	3.04	(75 ± 2)% [79%]	(27 ± 2)% [45%]
H4-q08	3.04	(66 ± 2)% [75%]	(15 ± 2)% [4%]
MS1-M1.45	2.91	(77 ± 2)% [80%]	(30 ± 2)% [8%]
APR4-LM	2.66	(19 ± 2)% [42%]	(2 ± 1)% [1%]

Table 7.1: Efficiency values at fixed distances of 5 and 10 Mpc, as defined by a detection of a PM signal in at least two detectors. In brackets, the values obtained using Gaussian noise as reported in Table 6.2. Uncertainties are reported in the related plots.

The results using actual noise should be considered preliminary, since no attempt to optimimize the tuning of the analysis method have been made.
The next step will be to repeat the tuning procedure of the method, to check if a different setting of relevant parameters, such as e.g. the black pixel probability, may bring some improvement in the final performances. Then the analysis will be extended to the full set of available NR waveforms.

Model	M_{tot} [$M_\odot$]	FPP 5 Mpc	FPP 10 Mpc
SHT-M2.2-I	4.39	$(1 \pm 1)\%$ [8%]	$(2 \pm 1)\%$ [7%]
LS220-M1.7-I	3.46	$(4 \pm 1)\%$ [13%]	$(4 \pm 1)\%$ [8%]
LS220-M1.8-I	3.46	$(6 \pm 1)\%$ [15%]	$(4 \pm 1)\%$ [2%]

Table 7.2: False positive probability at fixed distances of 5 and 10 Mpc, as defined by a detection of a PM signal in at least two detectors. In brackets, the values obtained using Gaussian noise as reported in Table 6.3. Uncertainties are reported in the related plots.

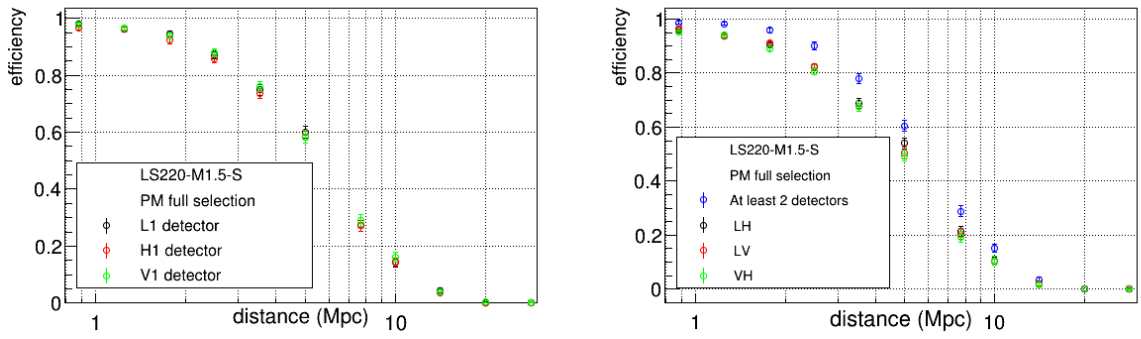

(a) LS220-M1.5-S EoS

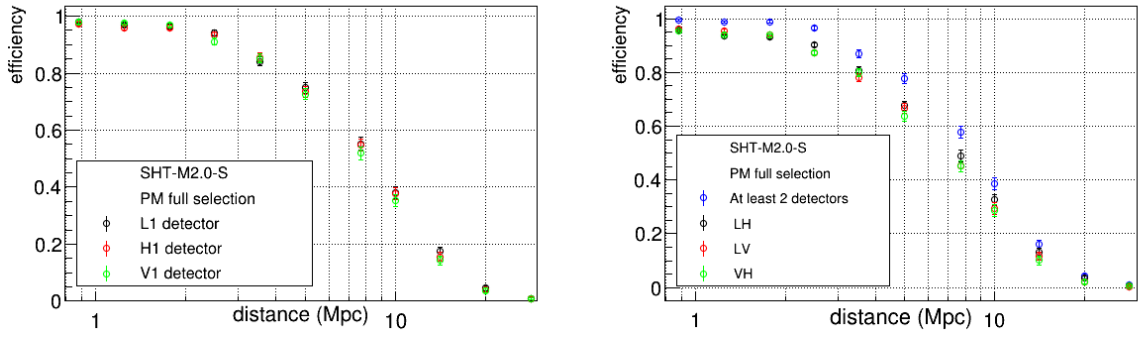

(b) SHT-M2.0-S EoS

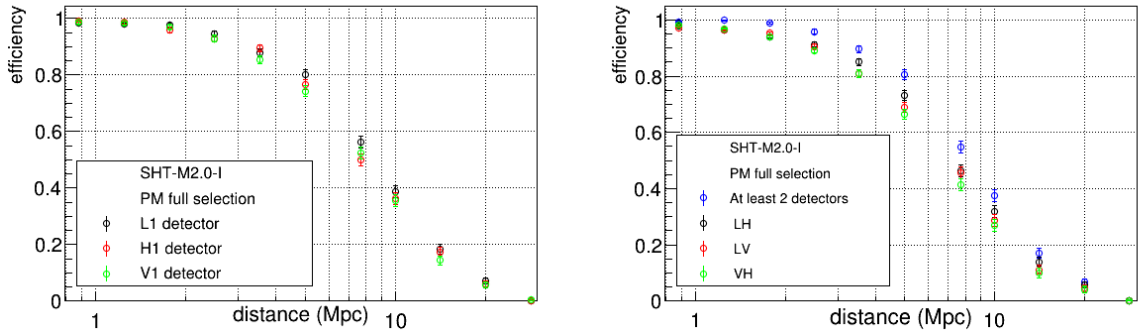

(c) SHT-M2.0-I EoS

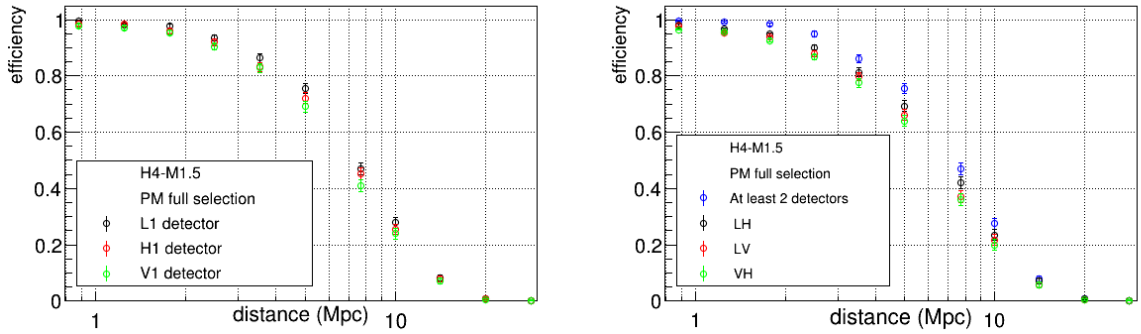

(d) H4-M1.5 EoS

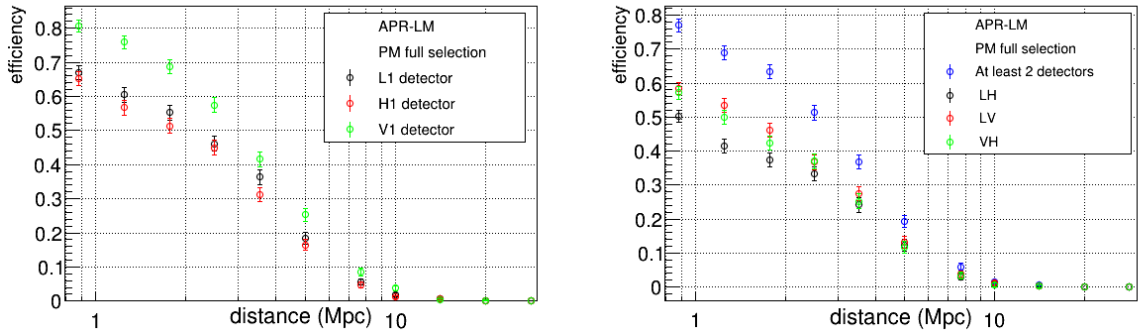

(e) APR4-LM EoS

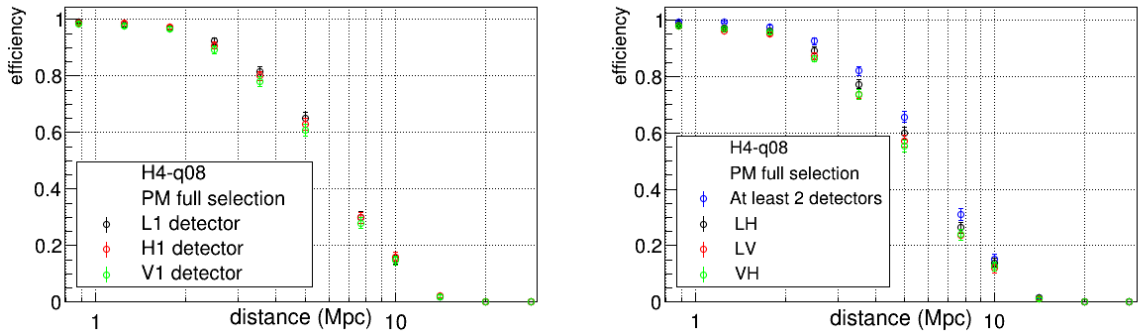

(f) H4-q08 EoS

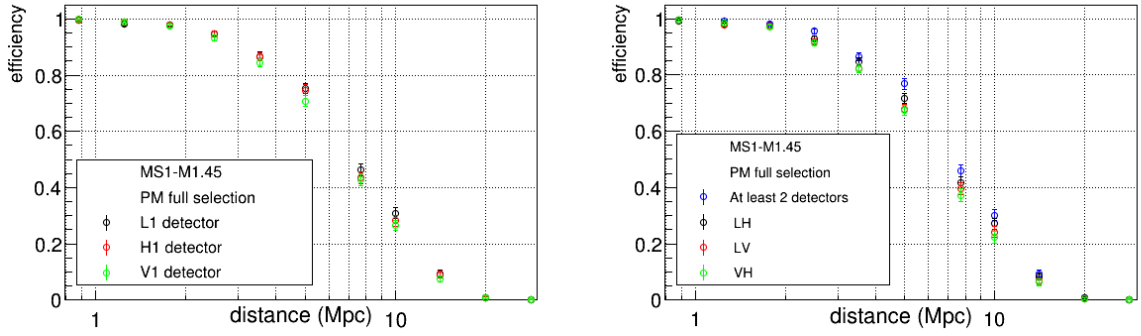

(g) MS1-M1.45 EoS

Figure 7.2: The resulting efficiencies of each detector (left) and of detector pairs (right) for a set of NR waveforms including a PM signal from a NS. The simulation uses real data scaled to mimick the design spectral sensitivity of advanced detectors.

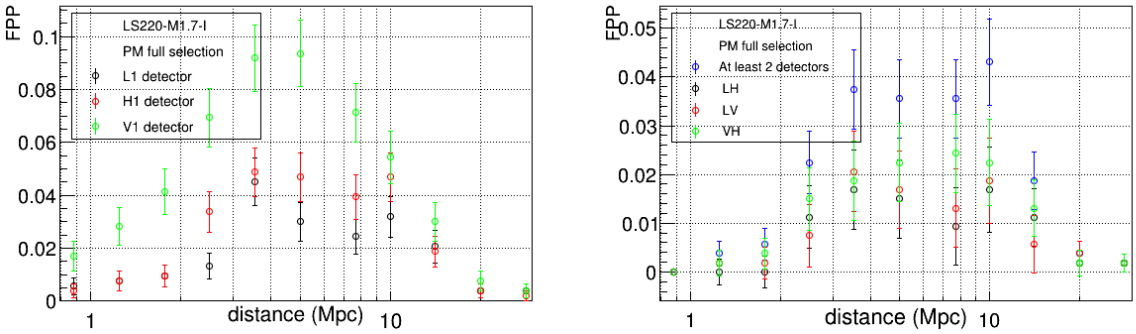

(a) LS220-M1.7-I EoS

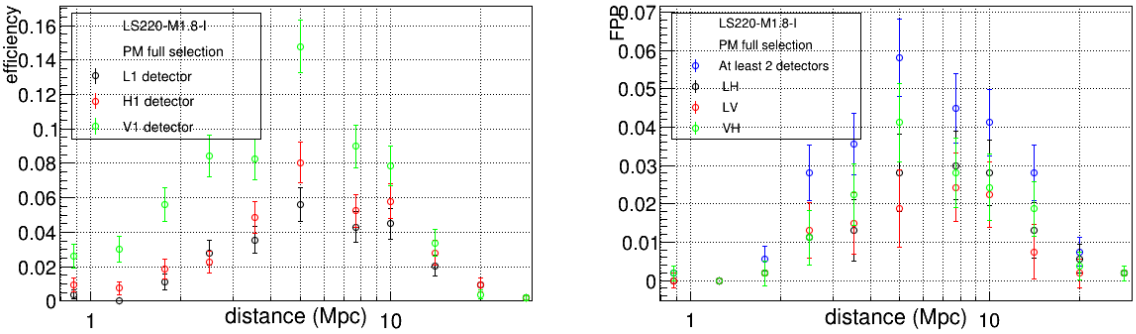

(b) LS220-M1.8-I EoS

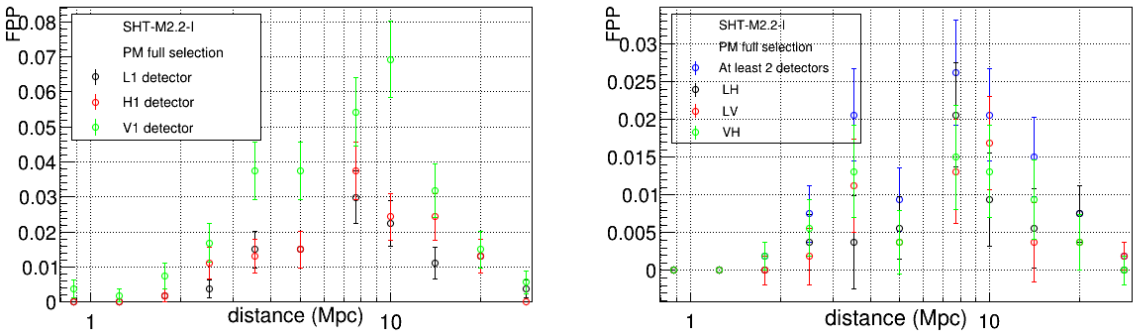

(c) SHT-M2.2-I EoS

Figure 7.3: The resulting false positive probabilities of each detector (left) and of detector pairs (right) for a set of NR waveforms showing a prompt collapse to BH. The simulation uses real data scaled to mimick the design spectral sensitivity of advanced detectors.

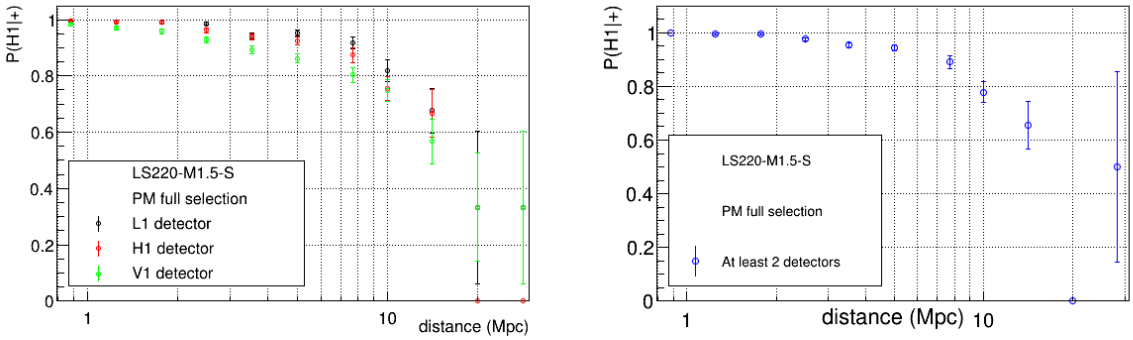

(a) LS220-M1.5-S EoS

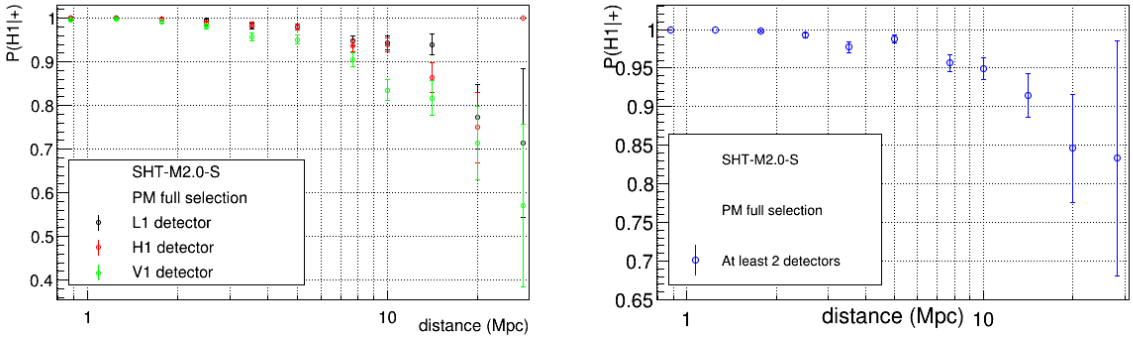

(b) SHT-M2.0-S EoS

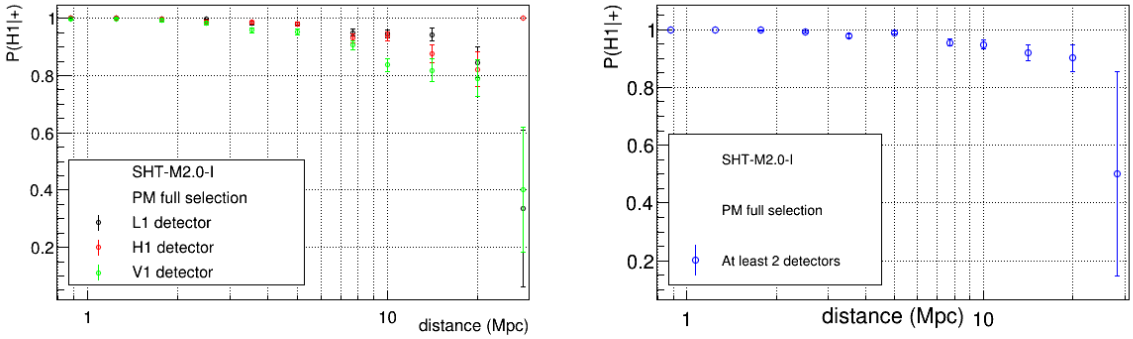

(c) SHT-M2.0-I EoS

Figure 7.4: Posterior probability of correct classification of the PM signal from a NS remnant, assuming equal probability priors for the alternative models of NS remnant formation versus prompt collapse to BH.

Conclusions

The detections of gravitational waves from mergers of binary black hole systems by the ground-based LIGO interferometers has opened to the so-called *gravitational wave astronomy*. The forthcoming addition of the advanced Virgo interferometer to the detector network will greatly improve the source sky localization and more generally the estimation of GW characteristics. The detection of new source classes, especially of Binary Neutron Star mergers, is expected in the short term.

An observation of the GW signal emitted by the coalescence of a NS binary, can constrain the equation of state of these stars in at least two ways: by investigating smaller effects on top of the signal from the inspiral phase due to the tidal deformability of the components and by characterizing the emission from the possible highly excited NS remnant after the merger. Both methods promise to probe matter up to yet unknown and unexplored supranuclear densities. In the latter case, the signal morphology cannot be accurately modeled to cover even a small part of the parameter space, hence a waveform-agnostic data analysis method is necessary.

In this context, we have developed a new data analysis tool to perform a follow-up search aiming to characterize the Post Merger signal in LIGO-Virgo data and in particular to discriminate between the two scenarios: *delayed collapse* to BH in which the merger leads first to an Hyper Massive NS or a Supra Massive NS or even a stable NS; *prompt collapse* to BH.
Our follow-up is using minimal assumptions on the expected characteristics of the detectable GW waveform, and the morphology of a candidate signal emerges from a maximum likelihood estimation of the coherent response of the detectors in the time-frequency plane. We constrain the follow-up search for NS remnant signals in the frequency band above $\sim$1.3 kHz, after the merger time, as expected by all NR models. The detectable signals are deeply constrained due to the fact that the amplitude spectral noise of the detectors in this band is proportional to frequency; therefore, we expect negligible sensitivity to BH remnant ring-down signals and a better response for the lower frequency NS PM signals. The first step of the procedure is to properly divide the interesting

time-frequency region in four quadrants, using a wavelet representation with resolution dT=0.98 ms, dF=512 Hz. A time threshold indicates when merger ends, a frequency threshold separate the upper frequency region in which PM can be expected from the lower frequency region of the late in-spiral emission. The target PM signal is searched above both thresholds by comparing the Signal-to-Noise Ratio in this time-frequency quadrant, with the SNR in the other quadrants. A second selection step is then applied by testing the SNR distribution within the PM quadrant, to improve the rejection of false positive NS PM candidates. This is accomplished by requiring a minimal ratio of candidate PM SNR at later times and above 1.8 kHz over candidate PM SNR closer to merger time and in the band 1.3-1.8 kHz. As a third step, the tool estimates main PM signal characteristics, such as the dominant frequency peak.
All the procedure has been developed and tested with a set of numerical relativity waveforms which provide both delayed and prompt collapse scenarios in full GR. Extensive Monte Carlo simulations have been performed by injecting NR signals from isotropic source distributions in the LIGO-Virgo network of advanced detectors at design sensitivity, considering simulated gaussian noise. We also accomplished a preliminary investigation on real data, rescaled from previous LIGO-Virgo observations to match the same spectral sensitivity of the previous test on simulated noise.
The efficiency of detection of a PM signal and the false alarm probability of the method has been determined as a function of source distance. The discriminating power between the prompt and delayed collapse to BH is satisfactory up to $\sim$ 10 Mpc, while at $\sim$ 20 Mpc for many waveform models the procedure looses power.
This discrimination by itself is a very important tool, since it can be exploited both to draw conclusions on single events and on collective properties of a population of events. Similarly, the estimation of main spectral characteristics of the PM GW emission shows large uncertainties at $\sim$ 20 Mpc for all waveforms. Moreover, due to the spectral features of the GW emission from APR4 and LS220 EoS, our simple estimator of the PM dominant frequency is affected by large biases even at $\sim$ Mpc distances. In addition to the spectral properties, our estimate of the duration of the PM signal can provide as well discriminating power among different EoSs.

Future developments of this work can improve the capability of identification and estimation of the PM signal. Our PM follow-up tool can be improved by implementing a multi-resolution time-frequency analysis which is expected to better reconstruct faint signals characteristics. In perspective, the composition of the information from many BNS detections will be exploited. In addition, the information from other concurrent GW analyses and from EM observations can be folded in order to improve the discrim-

inating power among different NS Equation of State. In particular, the GW inspiral signal can provide NS component masses and possibly estimate of their tidal deformability. The integration of such additional information can be accomplished by developing down-stream tools, based e.g. on model selection methods, to complement this work.

Bibliography

[1] $http://www.stellarcollapse.org/sites/default/files/table\_0.pdf$.

[2] Luciano Rezzolla and Olindo Zanotti. *Relativistic Hydrodynamics*. 2013.

[3] http://www.universetoday.com/83029/students-find-rare-recycled-pulsar/.

[4] http://astronomy.swin.edu.au/cosmos/R/Roche-lobe.

[5] H.-J. et al. Grimm. *X-ray binaries in the Milky Way and other galaxies*. *Chinese Journal of Astronomy and Astrophysics Supplement*, 3:257–269, December 2003.

[6] Michele Maggiore. *Gravitational Waves*.

[7] Nikolaos Stergioulas. *Rotating Stars in Relativity* . *Living Rev. Relativity*, 6, 2003.

[8] L. Rezzolla et al. *Gravitational-wave signal from binary neutron stars: A systematic analysis of the spectral properties* . *Phys. Rev. D*, 93:124051, Jun 2016.

[9] K. Takami et al. *Spectral properties of the post-merger gravitational-wave signal from binary neutron stars* . *Phys. Rev. D*, 91:064001, Mar 2015.

[10] F. Foucart et al. *Low mass binary neutron star mergers: Gravitational waves and neutrino emission* . *Phys. Rev. D*, 93:044019, Feb 2016.

[11] T. Dietrich et al. *Numerical relativity simulations of neutron star merger remnants using conservative mesh refinement* . *Phys. Rev. D*, 91:124041, Jun 2015.

[12] A. Bauswein et al. *Unified picture of the post-merger dynamics and gravitational wave emission in neutron star mergers* . *Phys. Rev. D*, 91:124056, Jun 2015.

[13] $https://www.learner.org/courses/physics/unit/text.html?unit=3secNum=7$.

[14] Seiji Kawamura. *Ground-based interferometers and their science reach . Classical and Quantum Gravity*, 27(8):084001, 2010.

[15] B.S. Sathyaprakash and Bernard F. Schutz. *Physics, Astrophysics and Cosmology with Gravitational Waves. Living Reviews in Relativity*, 12(2), 2009.

[16] LIGO Scientific Collaboration and Virgo Collaboration. *Prospects for Observing and Localizing Gravitational-Wave Transients with Advanced LIGO and Advanced Virgo. Living Reviews in Relativity*, 19(1):1, 2016.

[17] Abbott et al. *Binary Black Hole Mergers in the First Advanced LIGO Observing Run. Phys. Rev. X*, 6:041015, Oct 2016.

[18] J. Veitch et al. *Parameter estimation for compact binaries with ground-based gravitational-wave observations using the LALInference software library. Phys. Rev. D*, 91:042003, Feb 2015.

[19] L. K. Nuttall et al. *Improving the data quality of Advanced LIGO based on early engineering run results. Classical and Quantum Gravity*, 32(24):245005, 2015.

[20] W. J. Kaufmann III N. F. Comins. *Discovering the Universe.*

[21] A. Hewish et al. *Observation of a Rapidly Pulsating Radio Soure. Nature*, 217(5130):709–713, 1968.

[22] S. Rosswog and M. Brüggen. *Introduction to High-Energy Astrophysics.* Cambridge University Press, 2011.

[23] Feryal Özel and et al. *On the Mass Distribution and Birth Masses of Neutron Stars. The Astrophysical Journal*, 757(1):55, 2012.

[24] B. Kiziltan et al. *The Neutron Star Mass Distribution. The Astrophysical Journal*, 778(1):66, 2013.

[25] P. B. Demorest et al. *A two-solar-mass neutron star measured using Shapiro delay. Nature*, 467(1081-1083):66, 2010.

[26] J. Antoniadis et al. *A Massive Pulsar in a Compact Relativistic Binary. Science*, 340:6131, 2013.

[27] F. Crawford et al. *A Survey of 56 Midlatitude EGRET Error Boxes for Radio Pulsars. The Astrophysical Journal*, 652(2):1499, 2006.

[28] James M. Lattimer. *The Nuclear Equation of State and Neutron Star Masses. Annual Review of Nuclear and Particle Science*, Vol.62:1-515:485–515, 2012.

[29] James M. Lattimer et al. *Neutron star observations: Prognosis for equation of state constraints. Physics Reports*, 442(1-6):109–165, 2007.

[30] Frederick M. et al. Walter. *The optical counterpart of the isolated neutron star RX J185635-3754. Nature*, 389(6649):358–360, 1997.

[31] F. M. Walter, T. Eisenbeiss, J. M. Lattimer, B. Kim, V. Hambaryan, and R. Neuhaeuser. *Revisiting the Parallax of the Isolated Neutron Star RX J185635-3754 Using HST/ACS Imaging. Astrophys. J.*, 724:669–677, 2010.

[32] Lattimer. *Rapidly rotating pulsars and the equation of state*, volume 355. 190.

[33] Norman K. Glendenning. *Limiting rotational period of neutron stars. Phys. Rev. D*, 46:4161–4168, Nov 1992.

[34] Christian D. Ott. *Static Spherically-Symmetric Stellar Structure in General Relativity.*

[35] A. Smith. *Tolman-Oppenheimer-Volkoff (TOV) Stars.*

[36] Kenta et al. Hotokezaka. *Remnant massive neutron stars of binary neutron star mergers: Evolution process and gravitational waveform. Phys. Rev. D*, 88:044026, Aug 2013.

[37] Nikolaos Stergioulas. *Rotating Stars in Relativity. Living Reviews in Relativity*, 6(3), 2003.

[38] Podsiadlowski. *The Evolution of Binary Systems. http://www-astro.physics.ox.ac.uk/ podsi/.*

[39] D. Lorimer and M. Kramer. *Handbook of Pulsar Astronomy.*

[40] T. J.-L. Courvoisier. *High Energy Astrophysics. An Introduction.*

[41] A. Faber Joshua et al. *Binary Neutron Star Mergers . Living Rev. Relativity*, 15, 2012.

[42] Luc Blanchet. *Gravitational Radiation from Post-Newtonian Sources and Inspiralling Compact Binaries . Living Rev. Relativity*, 17, 2014.

[43] A. Postnov Konstantin et al. *The Evolution of Compact Binary Star Systems. Living Rev. Relativity*, 17, 2014.

[44] P. C. Peters et al. *Gravitational Radiation from Point Masses in a Keplerian Orbit. Phys. Rev.*, 131:435–440, Jul 1963.

[45] P. C. Peters. *Gravitational Radiation and the Motion of Two Point Masses. Phys. Rev.*, 136:B1224–B1232, Nov 1964.

[46] J. A. Clark et al. *Prospects for high frequency burst searches following binary neutron star coalescence with advanced gravitational wave detectors . Phys. Rev. D*, 90:062004, Sep 2014.

[47] J. A. Clark et al. *Observing gravitational waves from the post-merger phase of binary neutron star coalescence. Classical and Quantum Gravity*, 33(8), 2016.

[48] A. Bauswein et al. *Equation-of-state dependence of the gravitational-wave signal from the ring-down phase of neutron-star mergers . Phys. Rev. D*, 86:063001, Sep 2012.

[49] A. Bauswein et al. Neutron-star properties from the postmerger gravitational wave signal of binary neutron stars. *Phys. Part. Nucl.*, 46(5):835–838, 2015.

[50] A. Bauswein et al. *Measuring Neutron-Star Properties via Gravitational Waves from Neutron-Star Mergers . Phys. Rev. Lett.*, 108:011101, Jan 2012.

[51] A. Bauswein et al. *Revealing the high-density equation of state through binary neutron star mergers . Phys. Rev. D*, 90:023002, Jul 2014.

[52] A. Bauswein et al. *Prompt Merger Collapse and the Maximum Mass of Neutron Stars. Phys. Rev. Lett.*, 111:131101, Sep 2013.

[53] Kenta et al. Hotokezaka. *Binary neutron star mergers: Dependence on the nuclear equation of state. Phys. Rev. D*, 83:124008, Jun 2011.

[54] K. Takami et al. *Constraining the Equation of State of Neutron Stars from Binary Mergers . Phys. Rev. Lett.*, 113:091104, Aug 2014.

[55] J. S. Read et al. *Matter effects on binary neutron star waveforms . Phys. Rev. D*, 88:044042, Aug 2013.

[56] K. Yagi et al. *I-Love-Q relations in neutron stars and their applications to astrophysics, gravitational waves, and fundamental physics . Phys. Rev. D*, 88:023009, Jul 2013.

[57] K. Yagi et al. *I-Love-Q: Unexpected Universal Relations for Neutron Stars and Quark Stars . Science*, 314:365–368, 2013.

[58] K. Yagi et al. *I-Love-Q relations: from compact stars to black holes . Classical and Quantum Gravity*, 33:095005, 2016.

[59] N. Stergioulas et al. *Gravitational waves and non-axisymmetric oscillation modes in mergers of compact object binaries . Monthly Notices of the Royal Astronomical Society*, 418(1):427, 2011.

[60] A. Bauswein et al. *Inferring neutron-star properties from gravitational-wave signals of binary mergers . q*, 3:1, 2015.

[61] Riccardo Ciolfi et al. *Short Gamma-Ray Bursts in the "Time-reversal" Scenario. The Astrophysical Journal Letters*, 798(2):L36, 2015.

[62] A. Rowlinson et al. *Signatures of magnetar central engines in short GRB light curves. Monthly Notices of the Royal Astronomical Society*, 430(2):1016, 2013.

[63] Rana X. Adhikari. *Gravitational radiation detection with laser interferometry. Rev. Mod. Phys.*, 86:121–151, Feb 2014.

[64] Valeria Ferrari. *General Relativity.* 2015-2016.

[65] B. P. Abbot et al. *LIGO: the Laser Interferometer Gravitational-Wave Observatory. Reports on Progress in Physics*, 72(7):076901, 2009.

[66] T. Accadia et al. *Virgo: a laser interferometer to detect gravitational waves. Journal of Instrumentation*, 7(03):P03012, 2012.

[67] B. Willke and the LIGO Scientific Collaboration. *GEO600: status and plans. Classical and Quantum Gravity*, 24(10):S389, 2007.

[68] Kentaro Somiya. *Detector configuration of KAGRA: the Japanese cryogenic gravitational-wave detector. Classical and Quantum Gravity*, 29(12):124007, 2012.

[69] LCGT collaboration Kanda, Nobuyuki. *LCGT and the global network of gravitational wave detectors.* 2011.

[70] K. Kuroda and the LCGT Collaboration. *AStatus of LCGT . Classical and Quantum Gravity*, 27(8), 2010.

[71] `http://www.gw-indigo.org/tiki-index.php?page=LIGO-India`

.

[72] Stanley E Whitcomb. *Ground-based gravitational-wave detection: now and future . Classical and Quantum Gravity*, 25(11):114013, 2008.

[73] Matthew Pitkin et al. *Gravitational Wave Detection by Interferometry (Ground and Space) . Living Reviews in Relativity*, 14(5), 2011.

[74] The LIGO Scientific Collaboration. *Advanced Ligo. Classical and Quantum Gravity*, 32(7), 2015.

[75] F. Farnese et al. *Advanced Virgo: a second-generation interferometric gravitational wave detector. Classical and Quantum Gravity*, 32(2), 2015.

[76] M. Punturo et al. *AStatus of LCGT . Classical and Quantum Gravity*, 27(19):194002, 2010.

[77] Davidz Blair et al. *Gravitational wave astronomy: the current status. SCIENCE CHINA Physics, Mechanics & Astronomy*, 58(2):120402–, 2015.

[78] Ilaria Nardecchia. *Control of optical aberrations in advanced interferometric gravitational wave detectors.* PhD thesis, 2015.

[79] Peter R. Saulson. *Fundamentals of Interferometric Gravitational Wave Detectors.* World Scientific Publishing, 1994.

[80] Matone Luca. *È tude du controle global de l'interferometer central de Virgo.* PhD thesis, 1999.

[81] Stefan Ballmer et al. *New Technologies in Gravitational-Wave Detection. Annual Review of Nuclear and Particle Science*, 65(1):555–577, 10 2015.

[82] LIGO Scientific Collaboration and Virgo Collaboration. *GW150914: The Advanced LIGO Detectors in the Era of First Discoveries. Phys. Rev. Lett.*, 116:131103, Mar 2016.

[83] Giles Hammond, Stefan Hild, and Matthew Pitkin. *Advanced technologies for future ground-based, laser-interferometric gravitational wave detectors . Journal of Modern Optics*, 61(sup 1):S10–S45, 2014.

[84] Acernese and et al. *Measurements of Superattenuator seismic isolation by Virgo interferometer. Astroparticle Physics*, 33:182–189, April 2010.

[85] R. Abbott et al. *Seismic isolation for Advanced LIGO. Classical and Quantum Gravity*, 19(7):1591, 2002.

[86] Herbert B. Callen et al. *On a Theorem of Irreversible Thermodynamics. Phys. Rev.*, 86:702–710, Jun 1952.

[87] Richard F. Greene et al. *On a Theorem of Irreversible Thermodynamics. II. Phys. Rev.*, 88:1387–1391, Dec 1952.

[88] S. Klimenko et al. *Constraint likelihood analysis for a network of gravitational wave detectors. Phys. Rev. D*, 72:122002, Dec 2005.

[89] Stephen Fairhurst. *Source localization with an advanced gravitational wave detector network. Classical and Quantum Gravity*, 28(10):105021, 2011.

[90] Stephen Fairhurst. *Triangulation of gravitational wave sources with a network of detectors. New J. Phys.*, 11:123006, 2009. [Erratum: New J. Phys.13,069602(2011)].

[91] K. Grover et al. *Comparison of gravitational wave detector network sky localization approximations. Phys. Rev. D*, 89:042004, Feb 2014.

[92] Stephen Fairhurst. *Improved source localization with LIGO India. J. Phys. Conf. Ser.*, 484:012007, 2014.

[93] LIGO Scientific Collaboration and Virgo Collaboration. *Binary Black Hole Mergers in the First Advanced LIGO Observing Run. Phys. Rev. X*, 6:041015, Oct 2016.

[94] LIGO Scientific Collaboration and Virgo Collaboration. *Observation of Gravitational Waves from a Binary Black Hole Merger. Phys. Rev. Lett.*, 116:061102, Feb 2016.

[95] LIGO Scientific Collaboration and Virgo Collaboration. *Observing gravitational-wave transient GW150914 with minimal assumptions. Phys. Rev. D*, 93:122004, Jun 2016.

[96] LIGO Scientific Collaboration and Virgo Collaboration. *GW151226: Observation of Gravitational Waves from a 22-Solar-Mass Binary Black Hole Coalescence. Phys. Rev. Lett.*, 116:241103, Jun 2016.

[97] C. P. L. Berry et al. *Parameter Estimation for Binary Neutron-star Coalescences with Realistic Noise during the Advanced LIGO Era . The Astrophysical Journal*, 804(2):114, 2015.

[98] Stephen Fairhurst. *Source localization with an advanced gravitational wave detector network. Classical and Quantum Gravity*, 28(10):105021, 2011.

[99] Stephen Fairhurst. *Triangulation of gravitational wave sources with a network of detectors. New Journal of Physics*, 13(6):069602, 2011.

[100] Leo P. Singer et al. *Rapid Bayesian position reconstruction for gravitational-wave transients. Phys. Rev. D*, 93:024013, Jan 2016.

[101] LIGO Scientific Collaboration and Virgo Collaboration. *Tests of General Relativity with GW150914. Phys. Rev. Lett.*, 116:221101, May 2016.

[102] LIGO Scientific Collaboration and Virgo Collaboration. *Characterization of transient noise in Advanced LIGO relevant to gravitational wave signal GW150914. Classical and Quantum Gravity*, 33:134001, 2016.

[103] LIGO Scientific Collaboration and Virgo Collaboration. *GW150914: First results from the search for binary black hole coalescence with Advanced LIGO. Phys. Rev. D*, 93:122003, Jun 2016.

[104] A. Effleret et al. *Environmental influences on the LIGO gravitational wave detectors during the 6th science run. Classical and Quantum Gravity*, 32(3):035017, 2015.

[105] Coherent Wave Burst homepage. https://www.atlas.aei.uni-hannover.de/ wavebburst/LSC/doc/cwb/man.

[106] S. Klimenko et al. *A coherent method for detection of gravitational wave bursts. Classical and Quantum Gravity*, 25(11):114029, 2008.

[107] S. Klimenko et al. *Method for detection and reconstruction of gravitational wave transients with networks of advanced detectors. Phys. Rev. D*, 93:042004, Feb 2016.

[108] ROOT homepage. https://root.cern.ch/.

[109] V. Tiwari et al. *Regression of environmental noise in LIGO data . Classical and Quantum Gravity*, 32(16):165014, 2015.

[110] V. Necula et al. *Transient analysis with fast Wilson-Daubechies time-frequency transform . Journal of Physics: Conference Series*, 363(1):012032, 2012.

[111] Ciolfi R. et al. *General relativistic magnetohydrodynamic simulations of binary neutron star mergers forming a long-lived neutron star*. arXiv: 1701.08738, 2017.

[112] T. W. Baumgarte et al. *On the Maximum Mass of Differentially Rotating Neutron Stars . The Astrophysical Journal Letters*, 528(1):L29, 2000.

[113] K. Wolfgang et al. *Properties of hypermassive neutron stars formed in mergers of spinning binaries. Phys. Rev. D*, 91:064027, Mar 2015.

[114] A. Endrizzi et al. *General relativistic magnetohydrodynamic simulations of binary neutron star mergers with the APR4 equation of state. Classical and Quantum Gravity*, 33(16):164001, 2016.

[115] T. Kawamura et al. *Binary neutron star mergers and short gamma-ray bursts: Effects of magnetic field orientation, equation of state, and mass ratio. Phys. Rev. D*, 94:064012, Sep 2016.

[116] W. Kastaun et al. *Structure of stable binary neutron star merger remnants: A case study. Phys. Rev. D*, 94:044060, Aug 2016.

[117] J. M. Lattimer et al. *A generalized equation of state for hot, dense matter. Nuclear Physics A*, 535(2):331–376, 1991.

[118] J. F. Tondeur et al. *Static nuclear properties and the parametrisation of Skyrme forces. Nuclear Physics A*, 420(2):297–319, 1984.

[119] G. Shen et al. *Equation of state of dense matter from a density dependent relativistic mean field model. Phys. Rev. C*, 82:015806, Jul 2010.

[120] G. Shen et al. *New equation of state for astrophysical simulations. Phys. Rev. C*, 83:035802, Mar 2011.

[121] A. Akmal et al. *Equation of state of nucleon matter and neutron star structure. Phys. Rev. C*, 58:1804–1828, Sep 1998.

[122] N. K. Glendenning et al. *Reconciliation of neutron-star masses and binding of the* Λ *in hypernuclei. Phys. Rev. Lett.*, 67:2414–2417, Oct 1991.

[123] Horst Mü et al. *Relativistic mean-field theory and the high-density nuclear equation of state. Nuclear Physics A*, 606(3):508 – 537.

[124] L. Baiotti et al. *Accurate evolutions of inspiralling neutron-star binaries: Prompt and delayed collapse to a black hole. Phys. Rev. D*, 78:084033, Oct 2008.

[125] J. N. Goldberg et al. *Spin-s Spherical Harmonics and* ∂. *J. Math. Phys.*, 8:2155, Oct 1967.